Mechanisms of Serpentinite Dehydration in Subduction Zones

Constraints from the Almirez Exhumed Metamorphic Terrane

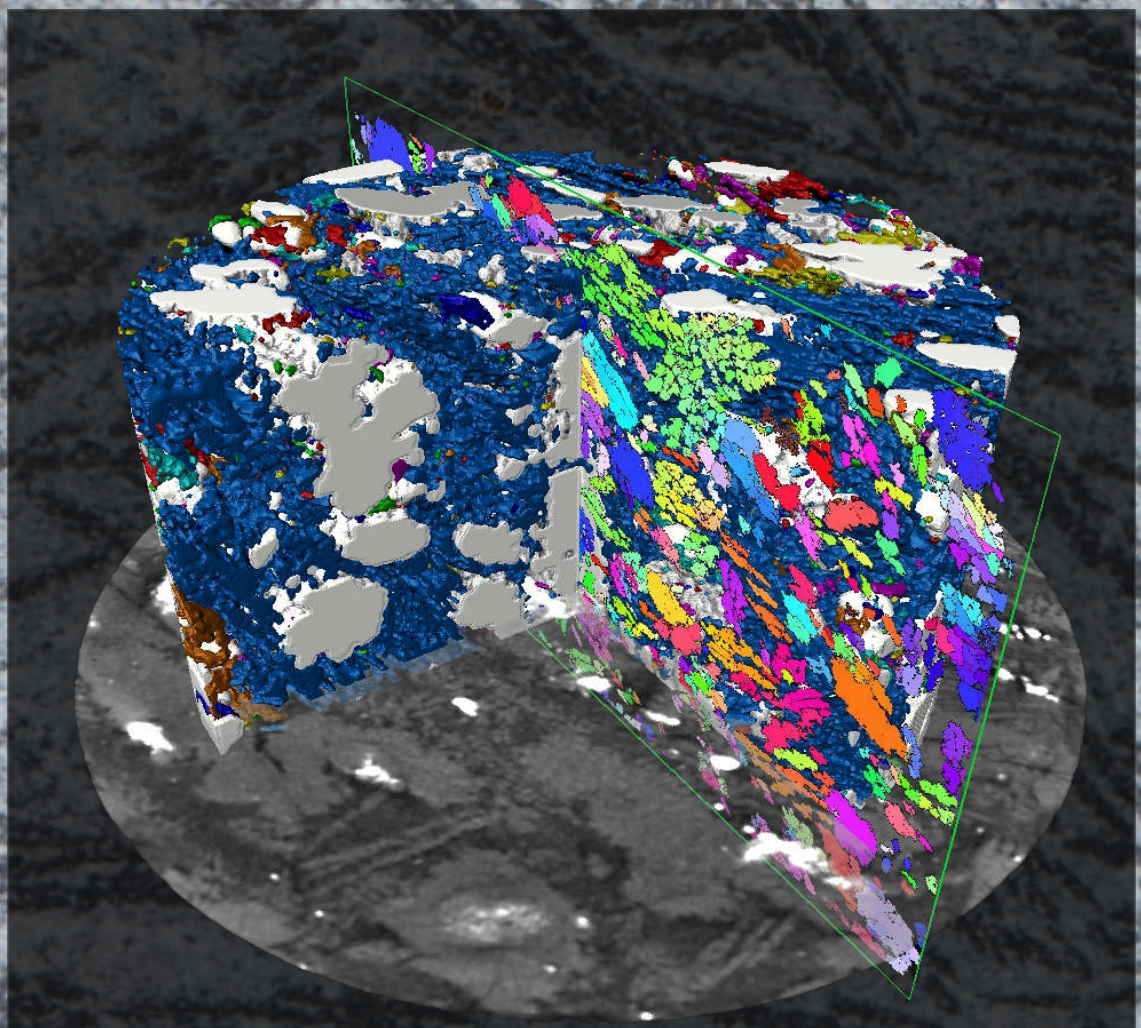

Nicole Dilissen

CSIC
IACT INSTITUTO ANDALUZ DE CIENCIAS DE LA TIERRA
ugr Universidad de Granada
Programa Doctorado Ciencias de la Tierra

Tesis Doctoral, 2019

Editor: Universidad de Granada. Tesis Doctorales
Autor: Nicole Dilissen
ISBN: 978-84-1306-167-2
URI: http://hdl.handle.net/10481/55470

MECHANISMS OF SERPENTINITE DEHYDRATION IN SUBDUCTION ZONES

CONSTRAINTS FROM THE ALMIREZ EXHUMED METAMORPHIC TERRANE

NICOLE DILISSEN

Ph.D. Thesis – Tesis Doctoral

PhD Program in Earth Sciences

Memoria de Tesis Doctoral presentada por M.Sc. en Geología Nicole Dilissen para optar al grado de Doctora por la Universidad de Granada

Esta Tesis Doctoral ha sido dirigida por el Dr. Carlos J. Garrido Marín, del Instituto Andaluz de Ciencias de la Tierra (CSIC-UGR), y el Dr. Vicente López Sánchez-Vizcaíno, del Departamento de Geología (Unidad asociada al CSIC), Universidad de Jaén.

En Granada, 22 de febrero de 2019

Funding: Research presented in this Ph.D. thesis has been funded by the EU-FP7 Marie Curie Initial Training Network "Zooming in between plates – ZIP" under grant agreement number PITN-GA-2013-604713. I also acknowledge funding from the Spanish "Agencia Estatal de Investigación" (AEI) under grants nº CGL2012-32067 and CGL2016-75224-R and "Programa de Cooperanción Internacional" grant nº PCIN-2015-053. I also acknowledge funding from the "Junta de Andalucía" research groups RNM-131, RNM-145, and RNM-374 and grant P12-RNM-3141. This research and the research infrastructures at the IACT have benefited from funding from the European Social Fund and the European Regional Development Fund.

Aan mijn ouders, an meine Eltern,

Voor al hun steun en toeverlaat ,

Für ihren unendlichen Glauben und Liebe

"A calm and modest life brings more happiness than the pursuit of success combined with constant restlessness."

Albert Einstein

Abstract

Subduction zones are the main sites of water recycling on Earth. At intermediate depth of subducting slabs, metamorphic devolatilization reactions are the principal source of fluids. A key devolatilization reaction is the discontinuous dehydration of antigorite serpentinite (Atg-serpentinite) that releases substantial amounts of water at the intermediate-depth of subducting slabs. The main aim of this Ph.D. Thesis is to constrain the dynamics and mechanisms of serpentinite dehydration and associated fluid release from observations in the exhumed Almirez ultramafic massif (Betic Cordillera, SE Spain). This massif uniquely preserves the dehydration front of the Atg-serpentinite reaction to chlorite harzburgite (Chl-harzburgite) at subarc depth of a subducting slab. The combination of field, petrological, microstructural and geochemical data sheds new light on the episodic nature and dynamics of antigorite dehydration and their relation to stress orientation and kinematics of subducting slabs, and the role of kinetics and fluid dynamics in metamorphic crystallization.

This thesis presents strong natural evidence supporting the episodic release of fluids during Atg-serpentinite dehydration to Chl-harzburgite. Detailed mapping of the Almirez reveals the alternation of Chl-harzburgite lenses with granofels and spinifex textures. The lenses have alike thicknesses, volumes and calculated time-integrated water volumes. Their precursor Atg-serpentinite lenses have thicknesses that agree well with the theoretical length scale expected for porosity wave instabilities controlled by viscous compaction (i.e., the compaction length) for permeability and viscosity values typical of Atg-serpentinite. Crystallization of granofels Chl-harzburgite was likely driven by compaction and near-equilibrium fluid drainage by porosity waves, while fluid pressure instabilities —likely induced by short-lived hydrocracking— allowed open-system arrival of external fluids that might explain the crystallization of spinifex Chl-harzburgite. The sequence of textural intervals of Chl-harzburgite probably records cyclic events of low and high fluxes that varied in extent by several orders of magnitude. This unique natural record provides the first field evidence supporting an episodic nature of the fluid release during high-P serpentinite dehydration in subducting slabs, as predicted by theoretical models of metamorphic devolatilization reactions.

For the in depth study of the texture and microstructures of Almirez Chl-harzburgite, I have investigated the 3-D microstructure of centimeter-sized olivine crystals in these rocks using correlative X-ray micro-computed tomography (μ-CT) and electron backscattered diffraction (EBSD). The new innovative technique was applied to oriented samples across the Atg-serpentinite dehydration isograd to examine the textural evolution during serpentinite dehydration to prograde peridotite and investigate its relation to the paleo-stress orientation and the kinematics of the paleo-subducting Almirez slab. Above the Atg-out isograd, Atg-serpentinite textures record the long-term shear deformation in a foliation near the slab interface. Below the Atg-out isograd, Atg-serpentinite dehydrated to unfoliated, coarse-grained Chl-harzburgite. Crystallization of granofels and spinifex Chl-harzburgite records, respectively, a sequence of slow and fast fluid draining events during serpentinite dehydration under the same orientation of the principal stresses that resulted in the shear deformation of the Atg-serpentinite. The texture of the granofels Chl-harzburgite formed by a topotactic dehydration reaction after Atg-serpentinite coupled to compaction leading to an olivine layering subparallel to the Atg-serpentinite foliation. The shape and crystal preferred orientations (SPOs and CPOs, respectively) of spinifex Chl-harzburgites are composed of clustered CPOs and SPOs that show a remarkable correlation with the orientation of the principal paleostresses, suggesting a cause-effect relationship. Oxide aggregate lineations in Chl-harzburgite and the platelet lineation of spinifex Chl-harzburgite might be correlated to along-strike fluid flow below the permeability barrier that constituted the Atg-out dehydration isograd. With this is shown that the kinematics of the slab, paleostresses, and fluid flow exert a dynamic control on the textures of Atg-serpentinite dehydrating to peridotite in subducting slabs.

In the Almirez massif, the change in fluid flow expulsion mechanism during Atg-serpentinite dehydration is exceptionally recorded in the morphological transition of olivine (i.e., in granofels vs. spinifex textures) in the prograde Chl-harzburgite. The study of rare samples of Chl-harzburgite preserving a varied-textured olivine morphology reveals the existence of composite olivine porphyroblasts made up of rounded cores mantled by coronas of tabular grains. The correlative X-ray μ-CT and EBSD study of these samples show that the morphological transition of olivine likely records the open-system arrival of highly polymerized aqueous fluids during Atg-serpentinite dehydration. Besides reaction affinity and reaction rate, the results of this study show that surface-

active molecules may play an essential role in shaping the morphology of growing crystals during metamorphic crystallization.

Keywords*: Subduction zones; antigorite serpentinite; chlorite harzburgite; Almirez massif; dehydration; episodic fluid release; compaction-driven expulsion; X-ray micro-computed tomography (μ-CT); electron backscatter diffraction (EBSD); 3-D microstructure; Shape preferred orientation (SPO); Crystal Preferred Orientation (CPO); stress; fluid flow; rounded olivine; tabular olivine; morphological transition; surfactant; inhibited growth.*

Extended abstract

Subduction zones are the main sites of water recycling on Earth. At intermediate depth of subducting slabs, metamorphic devolatilization reactions are the principal source of fluids. Despite their fundamental role in subduction dynamics, the time, flux and nature of deserpentinization fluid release are poorly constrained. A key devolatilization reaction is the discontinuous dehydration of antigorite serpentinite (Atg-serpentinite), liberating the largest amounts of slab fluids. The main aim of this PhD thesis is to constrain the dynamics and mechanisms of serpentinite dehydration fluid release from observations in an exhumed high-pressure metamorphic terrain, being the Almirez Ultramafic massif (SE Spain). This is a natural laboratory that uniquely preserves the dehydration front of the antigorite dehydration reaction into chlorite harzburgite (Chl-harzburgite) that used to be at sub-arc depth in a subducting slab. Until now, this is the only setting known worldwide to have this isograd with on both sides well-kept reactant and product. The key in studying the antigorite dehydration in this thesis lies within the differing textures observed within the dehydrated Chl-harzburgite. The combination of field data, textural, petrological, microstructural and geochemical analyses sheds more light on the episodic nature and physical mechanisms of antigorite dehydration, on its dynamics related to stress orientation and slab kinematics and on the role of its kinetics and fluid dynamics.

In a *first* chapter, this work presents evidence of the episodic fluid release and crystallization of Chl-harzburgite during Atg-serpentinite dehydration as predicted by theoretical models. The Almirez massif records the alternation of granofels and spinifex textured Chl-harzburgite lenses, with similar lens thicknesses, volumes and calculated time-integrated water volumes. Their precursor Atg-serpentinite lenses have thicknesses (~ 15–35 m) that agree well with the theoretical length scale expected for porosity wave instabilities controlled by viscous compaction (i.e., the compaction length) for typical permeability and viscosity values of Atg-serpentinite. Crystallization of granofels Chl-harzburgite is linked to this compaction-driven, near-equilibrium fluid drainage by porosity waves. This would leave behind undrained metastable serpentinite domains, trapped by the rigid and impermeable granofels Chl-harzburgite surrounding them. Fluid pressure instabilities likely induced short-lived hydrocracking in the Chl-harzburgite that

allowed open-system arrival of external fluids that might explain the textural crystallization of spinifex Chl-harzburgite. The minimum timescale of compaction-driven fluid expulsion for a 15–35 m thickness is estimated to be 10–23 yrs and can increase up to three orders of magnitude depending on fluid production rates and the order they are slower than viscous compaction rates. Fluid pressure instabilities linked to hydrocracking are estimated to last 12–70 days for linear kinetics or 14 h to 3 days for non-linear kinetics. The constrained size and shape of textural lenses provided an excellent opportunity to estimate time-integrated fluid fluxes at the Almirez massif. Unfocussed flow through porosity waves is estimated as $1 - 4\ m^3\ m^{-2}$, while focused flow through narrow zones could vary between $10^1\ m^3\ m^{-2}$ and $3 \cdot 10^3\ m^3\ m^{-2}$. The successive expulsion per textural interval herewith would have fluctuated between two orders of magnitude marking the cyclic events of low and high fluxes. This unique natural record of the Almirez thus provides the first evidence supporting the episodic nature of fluid release during high-P serpentinite dehydration by porosity waves.

A more in depth study of textures and microstructures at Almirez is presented in a *second* and *third* chapter of the thesis, for which a new microstructure analysis technique has been developed. The 3-D microstructure is reconstructed of centimeter-sized olivine crystals in rocks from the Almirez massif using combined X-ray micro computed tomography (µ-CT) and electron backscatter diffraction (EBSD). The semi-destructive sample treatment involves geographically oriented drill pressing of rocks and preparation of oriented thin sections for EBSD from the µ-CT scanned cores. The µ-CT results show that the mean intercept length (MIL) analyses provide reliable information on the shape preferred orientation (SPO) of texturally different olivine groups. Statistical interpretation of crystal preferred orientation (CPO) and SPO of olivine becomes feasible because the highest densities of the distribution of main olivine crystal axes from EBSD are aligned with the three axes of the 3-D ellipsoid calculated from the MIL analyses from µ-CT. From EBSD data multiple CPO groups are distinguished and by locating the thin sections within the µ-CT volume, SPO is assigned to the corresponding olivine crystal aggregates, which confirm the results of statistical comparison. This work demonstrates that the limitations of both methods (i.e., no crystal orientation data in µ-CT and no spatial information in EBSD) can be overcome, and the 3-D orientation of the crystallographic axes of olivines from different orientation groups can be successfully correlated with the

crystal shapes of representative olivine grains. Through this approach one can establish the link among geological structures, macrostructure, fabric and 3-D SPO-CPO relationship at the hand specimen scale even in complex, coarse-grained geomaterials.

The *second* chapter of the thesis applies the novel combined µ-CT-EBSD technique in a detailed study of oriented samples across the Atg-serpentinite dehydration isograd to investigate the textural evolution during serpentinite dehydration to peridotite and its relation to stress orientations and the kinematics of subducting slabs. Above the Atg-out isograd, Atg-serpentinite shows a prograde mylonitic foliation and a weak Shape Preferred Orientation (SPO) of oxide aggregates defining a N–S stretching lineation. The antigorite Crystal Preferred Orientation (CPO) is characterized by $[001]_{Atg}$ perpendicular to the foliation, and the poles to $(100)_{Atg}$ and $(010)_{Atg}$ distributed in a girdle-like symmetry with $[100]_{Atg}$ nearly parallel to the stretching lineation. The antigorite microstructure and CPO are consistent with deformation by dislocation creep, twinning, and dissolution-precipitation creep. These textures record the long-term shear deformation near the slab interface where the main compressive stress, σ_1, was at an acute angle to the foliation.

Below the Atg-out isograd, Atg-serpentinite dehydrated to unfoliated, coarse-grained Chl-harzburgite with granofels or spinifex textures distributed in alternating decameter-sized lenses. Crystallization of granofels and spinifex Chl-harzburgite records, respectively, a sequence of slow and fast fluid draining events during serpentinite dehydration under the same orientation of the principal stresses that resulted in the shear deformation of the Atg-serpentinite. Both textural types exhibit coarse-grained textures with systematic mineral CPOs and SPOs and microstructures without evidence of major ductile deformation. The texture of the granofels Chl-harzburgite formed by a topotactic dehydration reaction after Atg-serpentinite coupled to compaction leading to an olivine layering subparallel to the Atg-serpentinite foliation. The olivines of granofels Chl-harzburgite are rounded and display a weak CPO that can be accounted for by the topotactic reaction $<100>_{Atg}||<100>_{Ol}$ and $(001)_{Atg}||(010)_{Ol}$ after Atg-serpentinite. Similarly, orthopyroxene shows a marked CPO consistent with the topotactic reaction $(100)_{Opx}||(001)_{Atg}$ and $[001]_{Opx}||[100]_{Atg}$.

Spinifex Chl-harzburgite displays systematic mineral SPO and CPO. Spinifex olivines are tabular on $(100)_{Ol}$ and elongated along $[001]_{Ol}$ (c>b>>a), and define a ESE–WNW platelet lineation. The average texture is characterized by $[001]_{Ol,Opx}$ subparallel to a

strong ESE–WNW oxide aggregate lineation, and $[100]_{Ol,Opx}$ and $[001]_{Ol,Opx}$ within a plane of similar orientation to the Atg-serpentinite foliation. The SPOs and CPOs of spinifex Chl-harzburgites are composed of up to four orientation populations of tabular olivines, where one population is volumetrically dominant in all samples. Relative to the main orientation population, the CPO of olivine shows clustered distribution of $[100]_{Ol}$ and $[010]_{Ol}$ maxima rotated at systematic angles around $[001]_{Ol}$. These clustered CPOs and SPOs show a remarkable correlation with the orientation of the principal paleostresses. The preponderant orientation population of tabular olivines lies on the plane of maximum compression (σ_2–σ_3 plane) and has $[010]_{Ol}$ and its $(100)_{Ol}$ tabular faces nearly perpendicular to the Atg-serpentinite foliation. This population can be accounted for by oriented growth of platy crystals perpendicular to σ_1. The other populations lie in the plane perpendicular to the least compressive stress (σ_3) and the planes of maximum shear. The driving force and causes for the oriented crystallization of tabular olivine in these planes is uncertain, but their correlation with paleostresses suggests a cause-effect relationship.

Spinifex and granofels Chl-harzburgites show a marked ESE–WNW oxide aggregate lineation that differs in orientation from that of Atg-serpentinite and is approximately parallel to the intermediate compressive stress (σ_2). These lineations and the platelet lineation of spinifex Chl-harzburgite may be due to along-strike fluid flow below the permeability barrier that constituted the Atg-out dehydration isograd. The study discussed in the *second* chapter therefore shows that the kinematics of the slab, paleostresses, and fluid flow exert a dynamic control on the textures of Atg-serpentinite dehydrating to peridotite in subducting slabs.

In the *third* and last chapter, this thesis reports an exceptional record of the morphological transition of olivine formed during subduction metamorphism and high-pressure dehydration of Atg-serpentinite to prograde Chl-harzburgite. Uncommon samples of varied-textured Chl-harzburgite unveil the existence of olivine porphyroblasts made up of rounded cores mantled by coronas of tabular grains. Single olivine grains with a tabular morphology also occur in the matrix. The correlative μ-CT and EBSD study of two samples shows that tabular olivine in coronas is tabular on $(100)_{Ol}$ with $c > b >> a$, and grew in nearly the same crystallographic orientation as the rounded olivine cores. These tabular olivines strongly differ from previously described igneous and

metamorphic tabular olivines, which are tabular on the $(010)_{Ol}$ with either a > c >> b, or a ≈ c >> b. The tabular olivines overgrown on rounded olivine are most likely due to a shift from isotropic to anisotropic olivine growth caused by inhibited growth on the (100) and, to a lesser extent, (010) olivine interfaces.

Quantitative textural analysis and reaction mass balance point to a two-stage nucleation and growth process of olivine during the progress of the dehydration reaction of Atg-serpentinite to Chl-harzburgite. The first stage occurred under a low affinity and rate of the reaction and resulted in a low time-integrated nucleation rate and the isotropic growth of rounded olivine porphyroblasts. This stage was followed by a sudden increase in the affinity and reaction rate, which resulted in a relatively higher time-integrated nucleation rate of olivine and a shift from isotropic to anisotropic tabular olivine growth. The rounded and tabular olivines show differing trace element compositions that are likely due to the arrival of external fluids during the olivine tabular growth stage. Whatever the cause of the increase in the affinity and reaction rate, kinetic factors alone —due to increased nucleation rate and growth mechanisms— cannot account for the unusual morphology of olivine, which is tabular on the (100) face. Theoretical works in highly polymerized fluids predict inhibited growth on the (100) and (010) olivine interfaces due to the dissociative and molecular adsorption of water monolayers on these interfaces. It is likely that the morphological transition of olivine records the open-system arrival of highly polymerized aqueous fluids during Atg-serpentinite dehydration. Besides reaction affinity and reaction rate, surface-active molecules could play an important role in shaping the morphology of growing crystals during metamorphic crystallization.

***Key words**: Subduction zones; antigorite serpentinite; chlorite harzburgite; Almirez massif; Atg-dehydration; episodic fluid release; compaction-driven expulsion; X-ray micro computed tomography (μ-CT); electron backscatter diffraction (EBSD); 3-D microstructure; Shape preferred orientation (SPO); Crystal Preferred Orientation (CPO); stress; fluid flow; rounded olivine; tabular olivine; morphological transition; surfactant; inhibited growth.*

Resumen extendido

Las zonas de subducción son los principales contextos de reciclaje de agua en la Tierra. A una profundidad intermedia en la placa que subduce tienen lugar reacciones metamórficas de devolatilización que son la principal fuente de liberación de fluidos. Entre ellas, juega un papel clave la deshidratación discontinua de la serpentinita con antigorita, por ser la reacción que libera las mayores cantidades de fluidos. Sin embargo, y a pesar de su papel fundamental en la dinámica de la subducción, la duración, el mecanismo de flujo y la naturaleza de la liberación del fluido debidos a la deserpentinización están todavía muy pobremente establecidos.

El objetivo principal de esta tesis doctoral es contribuir al mejor conocimiento de la dinámica y los mecanismos de deshidratación de la serpentinita partiendo de las observaciones realizadas en un terreno metamórfico de alta presión exhumado: el Complejo ultramáfico del Cerro del Almirez (SE de España). Es éste un laboratorio natural en el que se preserva de manera excepcional el frente de deshidratación generado durante la reacción que dio lugar a la transformación de serpentinita con antigorita (Atg-serpentinita) en harzburgita con clorita (Chl-harzburgita) a una profundidad de sub-arco en una placa subducida. Hasta ahora, ésta es la única localidad conocida en todo el mundo en la que se preservan esta isograda metamórfica ("Atg-out") y, a cada lado de ella, los reactantes y los productos de la reacción de deshidratación mencionada. En esta tesis doctoral la clave para estudiar la deshidratación de la antigorita reside en las diferentes texturas observadas dentro de la Chl-harzburgita deshidratada: textura "granofélsica" y textura "spinifex". La combinación del análisis de datos de campo, texturales, petrológicos, microestructurales y geoquímicos arroja nueva luz sobre la naturaleza episódica y los mecanismos físicos de la deshidratación de la antigorita, sobre su dinámica, relacionada con la orientación de los esfuerzos y la cinemática de la placa que subduce, y sobre el papel de la cinética y la dinámica de fluidos.

Todas estas cuestiones son abordadas en la tesis a continuación de los tres primeros capítulos, en los que se presenta una introducción al trabajo realizado y se describe el contexto geológico de las rocas estudiadas (Capítulo 1), se enumeran los objetivos que se

ha pretendido alcanzar (Capítulo 2) y se describen las principales innovaciones metodológicas aplicadas al estudio (Capítulo 3).

En el Capítulo 4 se muestran las evidencias del carácter episódico que tuvo la liberación de fluidos durante la deshidratación de Atg-serpentinita y la cristalización de Chl-harzburgita, según lo predicho por los modelos teóricos. El macizo del Almirez registra la alternancia de lentes de Chl-harzburgita con textura "granofélsica" y lentes con textura "spinifex". Estas lentes presentan valores medios similares entre sí para el espesor, volumen y volumen de agua integrado en el tiempo. Sus correspondientes lentes precursoras de Atg-serpentinita habrían tenido espesores (~ 15–35 m) que concuerdan bien con la escala de longitud teórica esperada para las inestabilidades de las ondas de porosidad controladas por la compactación viscosa (es decir, la longitud de la compactación) para los valores típicos de permeabilidad y viscosidad de Atg-serpentinita. La cristalización de Chl-harzburgita con textura "granofélsica" estaría vinculada a este drenaje de fluido cercano a las condiciones de equilibrio, impulsado por la compactación debida a las ondas de porosidad. Durante el avance de la deshidratación, este proceso dejaría tras de sí dominios de serpentinita metaestable y sin drenar, atrapados por los dominios rígidos e impermeables de Chl-harzburgita "granofélsica" que los rodeaban. La generación de inestabilidades de la presión del fluido confinado probablemente indujo la formación de hidro-fracturas de corta duración en la Chl-harzburgita, lo que permitió la llegada al sistema abierto de fluidos externos que podrían explicar la cristalización textural de la Chl-harzburgita "spinifex". Se estima que la escala de tiempo mínima de expulsión de fluido impulsada por compactación para un espesor de 15 a 35 m es de 10 a 23 años. Esta escala de tiempo puede aumentar hasta tres órdenes de magnitud dependiendo de la tasa de producción de fluidos. Se estima que las inestabilidades de presión del fluido relacionadas probablemente con la formación de la textura "spinifex" duraron entre 12 y 70 días para cinéticas lineales y entre 14 horas y 3 días para cinéticas no lineales. Una cartografía detallada ha permitido establecer el tamaño y la forma de las lentes de Chl-harzburgita con cada uno de los tipos texturales. Estos datos brindaron una excelente oportunidad para estimar los flujos de fluido integrados en el tiempo en el macizo del Almirez. El flujo no focalizado debido a las ondas de porosidad se estima en $1 – 4\ m^3\ m^{-2}$, mientras que el flujo focalizado a lo largo de fracturas más estrechas pudo variar entre $10^1\ \ m^3\ m^{-2}$ y $3{\cdot}10^3\ \ m^3\ m^{-2}$. Si la formación de Chl-harzburgita

"granofélsica" y "spinifex" registra los flujos asociados con el drenaje del fluido por las ondas de porosidad y las fracturas, respectivamente, las lentes alternantes de ambas texturas cartografiadas en el Almirez corresponden, por tanto, a eventos cíclicos de flujos altos y bajos que varían en hasta dos órdenes de magnitud. Este registro natural único encontrado en el Almirez proporciona así la primera evidencia que respalda la naturaleza episódica de la liberación de fluidos durante la deshidratación de serpentinita en condiciones de alta presión.

En los Capítulos 5 y 6 de la tesis se presenta un estudio más profundo de las texturas y microestructuras de las rocas ultramáficas del macizo del Almirez, para lo cual se ha desarrollado un nuevo método de análisis (descrito con detalle en el Capítulo 3). La microestructura en 3-D de las rocas se reconstruye, a partir de cristales de olivino de tamaño centimétrico, utilizando una "tomografía computerizada de rayos X" (µ-CT) combinada con "difracción de electrones retrodispersados" (EBSD). El tratamiento semi-destructivo de la muestra conlleva la extracción de microtestigos de roca orientados geográficamente y la preparación de láminas delgadas para su análisis por EBSD y cuya orientación se decide a partir de los núcleos escaneados por µ-CT. Los resultados de µ-CT muestran que los análisis de la "mean intercept length" (MIL) proporcionan información fiable sobre la "orientación preferente de la forma" (SPO) de grupos de granos de olivino texturalmente diferentes entre sí. La interpretación estadística de la "orientación cristalográfica preferente" (CPO) y la SPO del olivino se vuelve factible porque la distribución de los ejes principales de los cristales de olivino, obtenidos a partir de las mayores densidades de puntos de los análisis de EBSD, se alinean con los tres ejes del elipsoide en 3-D calculados a partir del análisis MIL de los datos de µ-CT. Partiendo de los datos de EBSD, se distinguen múltiples grupos de CPO y al ubicar las secciones delgadas dentro del volumen analizado por µ-CT, se puede asignar el SPO a los correspondientes agregados de cristales de olivino, lo que confirma los resultados de la comparación estadística. Este trabajo demuestra que las limitaciones de ambos métodos (es decir, no se pueden obtener datos de orientación del cristal por µ-CT y no hay información espacial en EBSD) pueden ser superadas y la orientación 3-D de los ejes cristalográficos de olivinos de diferentes grupos pueden ser correlacionados con éxito con las formas cristalinas de los granos de olivino representativos. A través de este enfoque, se puede establecer el vínculo entre las estructuras geológicas, la macroestructura, la

fábrica de la roca y la relación SPO-CPO tridimensional a la escala de la muestra de mano incluso en materiales geológicos complejos de grano grueso.

El Capítulo 5 de la tesis aplica la nueva técnica combinada de µ-CT y EBSD en un estudio detallado de muestras debidas a la deshidratación de Atg-serpentinita. Se investiga la evolución textural durante la deshidratación de esta roca a una Chl-harzburgita y su relación con la orientación de los esfuerzos y la cinemática de la placa que subdujo. La Atg-serpentinita que aflora por encima de la isograda "Atg-out" muestra una foliación milonítica prograda y una débil orientación SPO de los agregados de óxidos que definen una lineación de estiramiento con orientación N-S. La CPO de la antigorita se caracteriza por $[001]_{Atg}$ perpendicular a la foliación y una distribución de los polos $(100)_{Atg}$ y $(010)_{Atg}$ que sitúa a $[100]_{Atg}$ casi paralela a la lineación de estiramiento. La microestructura y CPO de la antigorita son consistentes con una deformación por "dislocation creep", maclado y "creep" debido a disolución-precipitación. Estas texturas registran la deformación por cizalla a largo plazo cerca de la interfaz de la placa, donde la orientación del esfuerzo de compresión principal, σ1, formaba un ángulo de c. 30°±15° con respecto a la foliación.

Por debajo de la isograda, la Chl-harzburgita, producto de la deshidratación de Atg-serpentinita, presenta tamaño de grano grueso, ausencia de foliación y texturas "granofélsica" o "spinifex", distribuidas en lentes alternantes de dimensiones decamétricas. La cristalización con estas texturas registra, respectivamente, una secuencia de eventos en la que se alternaban el drenaje lento y rápido del fluido durante la deshidratación de serpentinita bajo la misma orientación de los esfuerzos principales que dieron lugar a la deformación por cizalla de la Atg-serpentinita. Ambos tipos de texturas exhiben tamaño de grano grueso con CPO y SPO sistemáticas de los minerales y microestructuras sin evidencia de deformación dúctil importante. La textura de la Chl-harzburgita "granofélsica" se formó por una reacción de deshidratación topotáctica de la Atg-serpentinita acoplada a la compactación que condujo a la formación de un bandeado de olivino subparalelo a la foliación de la Atg-serpentinita. Los olivinos "granofélsicos" son redondeados y muestran una CPO débil que puede explicarse por la reacción topotáctica $<100>_{Atg}||<100>_{Ol}$ y $(001)_{Atg}||(010)_{Ol}$ a partir de la Atg-serpentinita. De manera similar, el ortopiroxeno muestra una CPO bien marcada y consistente con la reacción topotáctica $(100)_{Opx}||(001)_{Atg}$ y $[001]_{Opx}||[100]_{Atg}$.

La Chl-harzburgita “spinifex” muestra SPO y CPO sistemáticas de los minerales. Los olivinos “spinifex” son tabulares en $(100)_{Ol}$, alargados paralelamente a $[001]_{Ol}$ (c> b >> a), y definen una lineación con orientación ESE-WNW. La textura promedio se caracteriza por $[001]_{Ol,Opx}$ subparalelos a una fuerte lineación ESE-WNW definida por los agregados de óxidos y por la orientación de $[100]_{Ol,Opx}$ y $[001]_{Ol,Opx}$ dentro de un plano de orientación similar al de la foliación de la Atg-serpentinita.

Las SPOs y CPOs de la Chl-harzburgita “spinifex” están compuestas por hasta cuatro poblaciones de olivinos tabulares con diferente orientación, aunque una de ellas es volumétricamente dominante en todas las muestras estudiadas. En la población principal, la CPO del olivino muestra una distribución agrupada de los máximos de $[100]_{Ol}$ y $[010]_{Ol}$ rotados en ángulos sistemáticos alrededor de $[001]_{Ol}$. Estas CPOs y SPOs agrupadas muestran una notable correlación con la orientación de los principales paleo-esfuerzos. La población de orientación preponderante de olivinos tabulares se encuentra en el plano de compresión máxima (plano $\sigma2 - \sigma3$) y tiene $[010]_{Ol}$ y sus caras tabulares $(100)_{Ol}$ casi perpendiculares a la foliación de la Atg-serpentinita. Esta población puede explicarse por el crecimiento orientado de cristales tabulares perpendiculares a $\sigma1$. Las otras poblaciones se encuentran en el plano perpendicular al menor esfuerzo de compresión ($\sigma3$) y en los planos de máxima cizalla. La fuerza motriz y las causas de la cristalización orientada del olivino tabular en estos planos es incierta, pero su correlación con los paleo-esfuerzos sugiere una relación causa-efecto entre ambos.

Tanto la Chl-harzburgita “spinifex” como la “granofélsica” muestran una lineación bien definida, marcada agregados de óxidos con orientación ESE-WNW, que difiere de la orientación de la lineación de la Atg-serpentinita y es aproximadamente paralela al esfuerzo de compresión intermedio ($\sigma2$). Estas lineaciones, así como los cristales tabulares de olivino “spinifex” pueden deberse a un flujo de fluido a lo largo y por debajo de la barrera de permeabilidad que constituyó la formación de la isograda de deshidratación “Atg-out”. El estudio discutido en el Capítulo 5, por lo tanto, muestra que la cinemática de la placa, los paleo-esfuerzos y el flujo de fluidos ejercen un control dinámico sobre las texturas de Atg-serpentinita que se está deshidratando a peridotita en las placas que están subduciendo.

En el sexto y último capítulo, esta tesis presenta un registro excepcional de la transición morfológica del olivino formado durante el metamorfismo de subducción y la

deshidratación a alta presión de Atg-serpentinita a Chl-harzburgita. Las muestras poco comunes de Chl-harzburgita con una textura mixta entre la "granofélsica" y la "spinifex" revelan la existencia de porfiroblastos de olivino formados por núcleos redondeados cubiertos por coronas de granos tabulares "spinifex". Los granos de olivino individuales con una morfología tabular también aparecen en la matriz. El estudio correlativo con μ-CT y EBSD de dos muestras de roca muestra que el olivino tabular en las coronas es tabular en $(100)_{Ol}$ con c> b >> a, y creció con prácticamente la misma orientación cristalográfica que los núcleos de olivino redondeados. Estos olivinos tabulares difieren fuertemente de los olivinos tabulares ígneos y metamórficos descritos por otros autores y que son tabulares en $(010)_{Ol}$ con a> c >> b o bien a ≈ c >> b. Los olivinos tabulares sobrecrecidos en olivinos redondeados son más probablemente debidos a un cambio del crecimiento de olivinos isotrópicos a anisotrópicos causado por un crecimiento inhibido en la cara (100) y, en menor medida, la (010).

El análisis cuantitativo de la textura y el balance de masa de la reacción apuntan a un proceso de nucleación y crecimiento en dos etapas del olivino durante el progreso de la reacción de deshidratación de Atg-serpentinita a Chl-harzburgita. La primera etapa se produjo con una baja afinidad y velocidad de la reacción y dio lugar a una baja velocidad de nucleación integrada en el tiempo y al crecimiento isotrópico de los porfiroflastos de olivino redondeados. Esta etapa fue seguida por un aumento repentino en la afinidad y la velocidad de reacción, lo que resultó en una tasa de nucleación de olivino integrada en el tiempo relativamente más alta y en el cambio de un crecimiento isotrópico del olivino a uno anisotrópico con un hábito tabular. Los olivinos redondeados y tabulares muestran diferentes composiciones de elementos traza que probablemente se deben a la llegada de fluidos externos durante la etapa de crecimiento tabular de olivino. Cualquiera que sea la causa del aumento en la afinidad y la velocidad de reacción, los factores cinéticos (mayor velocidad de nucleación y de los mecanismos de crecimiento) no pueden explicar por sí solos la morfología inusual del olivino, que es tabular en la cara (100). Los trabajos teóricos en fluidos altamente polimerizados predicen el crecimiento inhibido en las interfaces de olivino (100) y (010) debido a la adsorción molecular y disociativa de las monocapas de agua en estas interfaces. Es probable que la transición morfológica del olivino registre la llegada al sistema abierto de fluidos acuosos altamente polimerizados y ricos en Ti durante la deshidratación de la Atg-serpentina. Además de la afinidad y la

velocidad de reacción, las moléculas tensioactivas podrían jugar un papel importante en la configuración de la morfología de los cristales en crecimiento durante la cristalización metamórfica.

***Palabras clave**: Zonas de subducción; serpentinita con antigorita; harzburgita con clorita; macizo del Almirez; deshidratación de antigorita; liberación episódica de fluidos; expulsión impulsada por la compactación; Tomografía Computerizada de rayos X (μ-CT); Difracción de Electrones Retrodispersados (EBSD); microestructura 3-D; de Forma (SPO); Orientación Cristalográfica Preferente(CPO); esfuerzos; flujo de fluidos; olivino redondeado; olivino tabular; transición morfológica; surfactante; crecimiento inhibido.*

Acknowledgments

I cannot express the deepest gratitude I am feeling after finishing this thesis. Words will not be enough to mirror these past five years with the help and guidance of so many kind and warmhearted people. Without you, I would not have had this courage, laughs, space and freedom, that helped me grow through this PhD journey.

My foremost gratitude goes to my supervisor, **Carlos J. Garrido**, to his critical view and deep caring. I have learned many values on the way —not just science—, gained precious new insights and perspectives, and have great respect for what commitment you showed me one is capable of having. I thank you for all this tremendous amount of time in guidance, creative and critical thinking, shaping of endless manuscripts, and of course, for the hardcore earth scientist with valuable ideas and discussions.

As for my co-supervisor, **Vicente López Sánchez-Vizcaíno**, I cannot tell you how grateful I am for your guiding support on the field, conferences and project trips, for the pen you gave me for making my first notes in the field and taking my first steps into this thesis. Your guidance, combined with critical thinking and advice, did not stop ever since.

Dear **Karoly**, it is not fare not to include you as a co-advisor, with all the dedications, time and utter patience you had for me. You are indeed a collaborating, guiding, vivid spirit through analyses and processing towards helping in shaping manuscripts. I am most grateful for your continuous support, understanding and caring kindness. This thesis deserves a big recognition to you too.

A special thanks for the worthy contribution to the research and thesis content I give to **Antonio Sánchez-Jabaloy** (Universidad de Granada), **Wolf-Achim Kahl** (Universität Bremen), **José Alberto Padrón-Navarta** (Université de Montpellier), **Manuel J. Román Alpiste** (IACT-CSIC) and **Taras Gerya** (ETH Zürich). I am very grateful and honored to have you as co-authors on my publications.

I would like to express my gratitude to the members of the tribunal, **Dr. José Miguel Azañon** (UGR), **Dr. Antonio Sánchez-Jabaloy** (UGR), **Dr. Andrea Tommasi** (Univ. Montpellier), **Dr. Philippe Agard** (UPMC), **Dr. Sergio Llana Fúnez** (Univ. Oviedo), for their time and interest in this work. Special appreciation goes to **Philippe Agard**, for the huge effort of coordinating the ITN-ZIP and all related training activities for the network.

During this Ph.D., I traveled to so many places and had the pleasure and outstanding opportunity to meet **Taras Gerya** for my secondment at ETH Zürich. I was stunned by his care of teaching, dedicated patience and understanding for students that are new to geodynamic numerical modeling. Being a source full of modeling ideas, motivation and endless positivity, he got me inevitably hooked to modeling geodynamic settings. My stay in Zürich was even more priceless by meeting many wonderful and talented people of the department: thank you so much, **Casper, Iris, Diogo, Luca, Robert, CJ, Claudio, Timm, Long, Tessa, Usman, Cédéric**.

Alpi, **Chari**, **Inma, Juani, Carolina, Ana,** no sé expresar bien cómo agradecer todo el apoyo y entendimiento que habéis tenido hacia mí y mis preguntas y solicitudes interminables durante mi estancia en el IACT. Siempre me habéis ayudado con cariño y una sonrisa en la cara, ¡Sois el sol del instituto! Llevo vuestra amabilidad en mi corazón.

To my other dear colleagues at the IACT, I cannot imagine it without you. All these laughs, solidarity, assisting hands and listening ears, during work, lunch and tapas, and evenings. To **Marievi,** my dear caring and sharing office mate, in love, kindness and Greek food. To **Manolis,** the other Greek half with love and affection that became part of the office. To **Amel, Mari, Kamar, Yassamina,** with whom I shared so many precious encouraging and warmhearted moments in the same office. Thank you so much for your enriched culture too! To those in the office in front of ours (the coffee room!), **Laura, Claudia, Bob, Carmina,** with your humor and listening ears. To **Manu, Adrián, Claudio, Mayte, Leonardo, Muhammad, Ari, Marga** (¡qué masajes terapéuticos!), **Annika, Ruben, Gan, Electra**, thank you for keeping me above the water! And Earth conscious ;).

A mis compañeros de baile de swing porque cada martes era un incremento de energía y un verdadero momento "funky" de felicidad. ¡Gracias a todos vosotros: **Julia, Aitana, Fernanda, Eva, Lea, Miguel, Leo y Manu**! Y no olvidemos los momentos de tapas y noches de baile "fuera". Julia, espero que te vaya bien encontrando nueva compañera de natación!

A mis compis de piso: **Eva** (Ich vermisse unsere Gespräche auf Deutsch y en español), **Sara**, **Toñi**, **Abder**, **Kahina**, de Cervantes y a mi querida **María** del centro de Graná (¡qué Granaína la María!). Gracias por los momentos juntos y apoyo en el piso y por haber podido compartir esta gran experiencia con vosotros.

I also wish to thank my traveling companions, on adventurous hikes through the mountains. Dear **Manu, Gan, Laura, Ari, Ruben, Leonardo, Angel, Mauri, Casper,** thank you for your accompaniment towards challenging, but so rewarding summits.

Also **Manu**, da ich dich ja schon dreimal erwähnt habe, danke um so ein toller, spaßiger und loyaler Kamerad zu sein und vielen Dank damit ich mein Deutsch ein bisschen üben konnte ☺.

To whom I shared my Ph.D. traveling the most with, my dear fellow Zippies! **Marija, Casper, Gianina, Mattia, Sarah, Michele, Léa, Slaven, Gian, Io, Daniel, Jonas, Liang**. I found such valuable friendship in you (and exciting destinations to visit ;)), I hope we will continue such warm contact through work and in spare time! Thank you for sharing the ZIP-experience with me!

Liefste ouders, het is niet altijd even gemakkelijk als het enigste kind toch maar even beslist van land te veranderen. Ik kan niet uitdrukken hoe dankbaar ik ben voor jullie vertrouwen in mij en mijn ambitieuze doelen, voor jullie eindeloos geduld (is die thesis nu nog niet af? Jawel, nu wel!), jullie aanmoedigingen, maar vooral uit grond van mijn hart voor jullie eindeloze liefde, begrip en ondersteuning. Al mijn verwezenlijkingen vloeien voort uit jullie tijd en toewijding gedurende mijn studiejaren voorheen en is zeker niet te onderschatten in deze thesis. Bedankt om mij zo vaak te komen bezoeken in het verre Granada (en Zürich) en te laten weten wat familie betekent.

Liefste **mémé**, **pépé**, liebe **Oma**, lieber **Opa**. Ook jullie hebben mij zoveel moed en een groot hart onder de riem gestoken. Liefste mémé en pépé, Ik koester alle momenten die we samen mogen delen, jullie steun en toeverlaat en oneindige liefde. Auch bedanke ich gerne das Deutsche Haus, wo ich da oben im Zimmerchen ab und zu meine Arbeit leisten durfte und wo ich so lieb versorgt wurde. Danke Oma und Opa für eure Geduld, Verständnis und liebevolle Herzen. Auch danke **Detlef** und **Doris**, für eure Besuche in Granada, die mich sehr unterstützt haben. Ihr seid Herz und Seele für mich, danke dafür. Ook **Martina** en **Mark**, bedankt mij niet te vergeten in het verre Granada :).

Joris, hoe kan ik jou bedanken, voor al het geduld die je had voor mij de afgelopen 5 jaar, voor mij geen enkel moment te verwijten dat ik zomaar ben vertrokken, dat je mij deze enorme vrijheid hebt geschonken om deze uitdaging aan te gaan, om daarbovenop ook nog zo veel steun te geven. En hier op het einde van de rit, ben je er nog. Bedankt om het met mij vol te houden :). We gaan verder naar het volgende avontuur!

To **all** I might have missed to thank, I hope I will be able to do so through words when we meet, Namasté!

Yours Sincerely,

Nicole

Contents

PART I – INTRODUCTION, AIMS, THESIS STRUCTURE AND METHODOLOGY

Part I

INTRODUCTION, AIMS AND THESIS OUTLINE, AND METHODOLOGY

1 Introduction

1.1 Our Earth, a unique place

The dynamic behavior of plate tectonics on Earth is a unique occurrence with respect to other planets (Schubert et al., 2001). With convecting cells in the mantle, new crust is continuously created at mid-ocean ridges and destroyed again into the Earth's mantle at subduction sites (Fig. 1.1) (Stern, 2002; Turcotte and Schubert, 2014; van Keken et al., 2018). Two types of crust are distinguished: oceanic (c. 7 km thick) and continental crust (c. 40 km thick). The oceanic crust is mainly composed of sediments and dense lithologies, such as basalt, gabbros and peridotites (Rudnick and Gao, 2003). The continental crust formed as the mantle started differentiating during early Earth and is thus less dense than the oceanic plate (Brown, 2013; Hans Wedepohl, 1995). Slabs in subduction at convergent plate margins therefore are the older ends of the heavier oceanic plates and drag down ocean floor with huge amounts of water into Earth's interior (Rüpke et al., 2004; van Keken et al., 2018).

The prerequisite for a plate tectonic regime to exist —i.e. whether the viscous stress during deformation exceeds the lithospheric stress— depends not only on temperature and applied stresses, but also on the water content (O'Neill et al., 2007). Without the versatile feedback between water and dynamics, plate tectonics would not even have been able to initiate. Numerical modeling by Dymkova and Gerya (2013) shows that subduction initiation fails under fluid-absent conditions, but starts naturally when fluids are present in the oceanic crust along the plate boundaries. Presence of water indeed can lower the friction coefficient of rocks drastically (0.15 instead of 0.6-0.85 in dry rock; O'Neill et al., 2007 and references therein). Even small amounts of water can have significant effect on the viscosity and melt productivity and therefore may influence directly convection and plate tectonics (e.g. Inoue, 1994; Jung and Karato, 2001; Mei et al., 2002; van Keken et al., 2011). Hence, water carries one of the main fingerprints of Earth tectonics, with important implications in subduction zones.

Many questions remain concerning the evolution of subduction zones and their role in Earth dynamics. The movement of downgoing slab expresses itself at the surface in the

form of seismic and volcanic activity and is much more dominating than at divergent (i.e. mid-ocean ridges) or transform plate boundaries (Fig 1.2; e.g. Bird, 2003; Poli and Schmidt, 2002). This has a major impact on human society worldwide due to the dense populations living at these boundaries. The nature, structure and properties of plate margins are insufficiently known to improve hazard assessments and to understand stress and energy releases. Material and energy are mainly transferred via fluids and melts (e.g. Bebout and Penniston-Dorland, 2016; Brown, 2013 and references therein), which makes it critical to understand fluid-mediated transport (Poli and Schmidt, 2002).

This PhD thesis aims for new insights into the dynamics and mechanisms of fluid release mechanisms during metamorphic dehydration under high pressure at intermediate subduction depth. I present a field, textural, petrological and microstructural study of a unique exhumed paleo-subduction terrane, the Almirez ultramafic massif, which preserves compelling evidence of one of the most important high-pressure dehydration reactions in subduction zones, i.e. the antigorite serpentinite breakdown into chlorite harzburgite. The study presented aims at unveiling the physical mechanism behind the serpentinite dehydration reaction, at investigating its relationship between its dynamics and deformation and stresses and at unveiling the role of its kinetics and fluid dynamics.

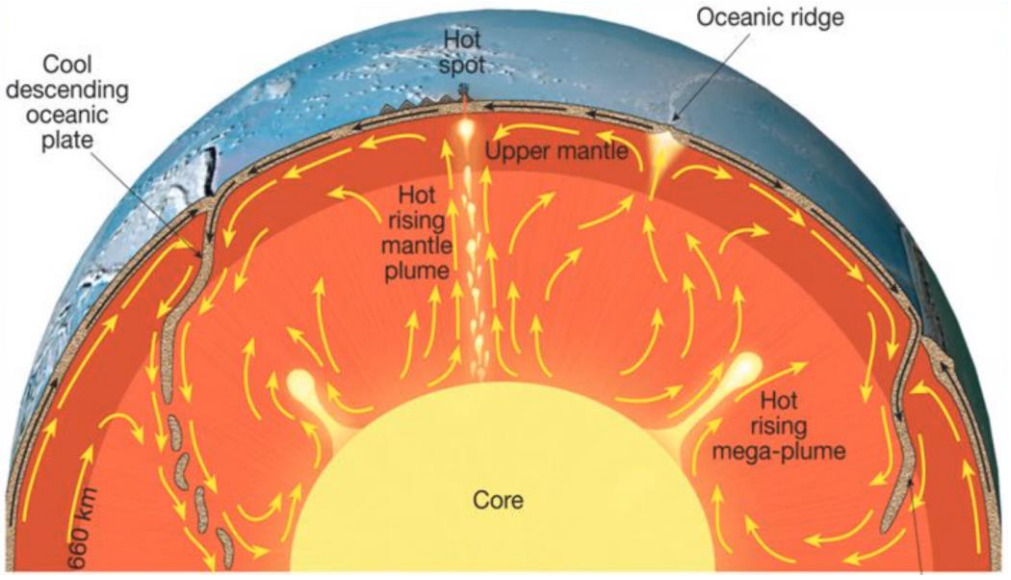

Figure 1.1. *General sketch on the Earth's mantle convection and plate tectonics. Convection currents in the mantle (yellow arrows) create new oceanic plates at ocean ridges in upwelling and recycle the cooled oceanic plate at downwelling. (Oregon State Univ. ,2017, The Earth's Layers Lesson. Oregon State University: Dept. of Geosciences. Available at http://volcano.oregonstate.edu/earths-layers-lesson-1)*

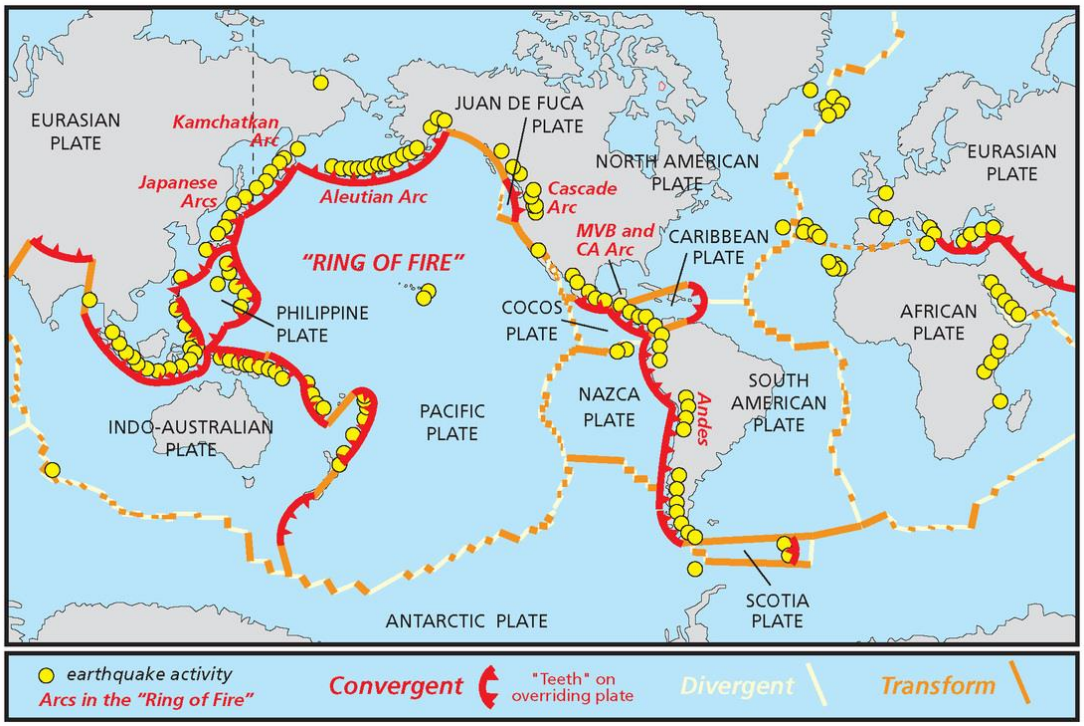

Figure 1.2. *Map illustrating the tectonic plates on Earth. Convergent plate boundaries (red lines) is where plates collide to form mountains and main volcanism and earthquakes (yellow dots) occur. At divergent boundaries (light yellow) new oceanic crust is created as plates are drifting apart. Around these regions main transform faults (orange lines) occur. (https://www.nps.gov/subjects/geology/plate-tectonics.htm; Modified after Lillie, 2005)*

1.2 Subduction

The unique behavior of plate tectonics provides the equivalent to say that only Earth has subduction zones (Stern, 2002, 2004). Subduction zones are known to be the main recycling places on Earth as they drag thousands of square kilometers of spreading ocean floors back down into its interior, including volatiles such as water (Frohlich, 1989; Furukawa, 1993; Hacker et al., 2003a,b; Nur and Walder, 1992; Peacock, 2001; Rüpke et al., 2004; Stern, 2002; Ulmer and Trommsdorff, 1995). Slab pull is one of the key forces, which maintains motion of plates as the slab sinks into the mantle and pulls the rest of the plate behind it (Davies and Richards, 1992; Forsyth, 1975; Hager and O'Connell, 1981; Spence, 1987; Wilson, 1993). There is even a consensus dictating that the unstable sinking lithosphere that drives the plates also indirectly causes mantle to well up underneath mid-ocean ridges (Conrad and Lithgow-Bertelloni, 2002; Stern, 2004). In this sense, subduction zones are the driving forces of plate tectonics.

1.2.1 Settings

The dimensions of subduction zones are defined by deep trenches, volcano arcs parallel to these trenches, as well as parallel occurring arrays of deep earthquakes (known as the double seismic zone or 'Wadati-Benioff Zone') (Fig. 1.2). Subduction zones comprise two plate ends, i.e. the subducting plate with incoming and downgoing part, and the overriding plate that contains the mantle wedge and magmatic arc (Fig. 1.3; Stern, 2002).

The *incoming part* of the subducting plate consists of mantle lithosphere, crust and sediments, which form the 'slab'. The *downgoing part* of the slab is the part of the subduction zone where the most significant processes happen and its behavior depends significantly on the features on the incoming part (e.g. old vs young plates; Fig. 1.4). Slab penetration can be very shallow (<200 km) or subduct down to 660 km depth to the mantle transition zone, depending for instance on its age. Old lithosphere is more dense and will sink deeper and steeper when entering a subduction setting (e.g. Mariana type), whereas a younger lithosphere is more buoyant and will have a shallower subduction dip (e.g. Chile type) (Fig. 1.4; Jarrard, 1986; Stern, 2002). This results in different behavior of

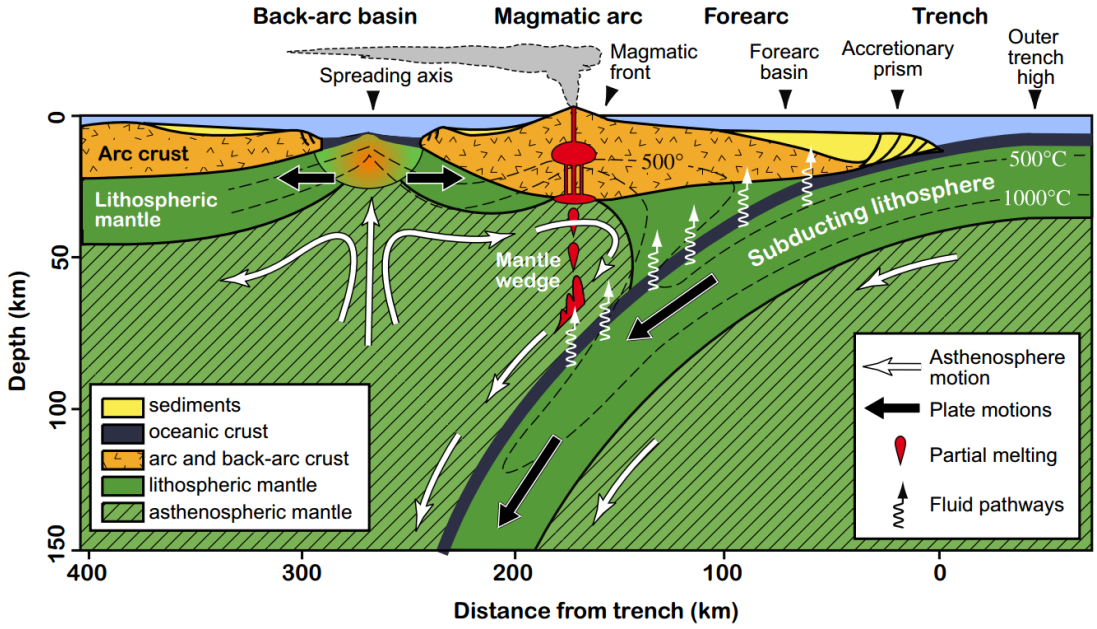

Figure 1.3. *Sketch of a section through the upper part of a subduction zone setting, with the downgoing subducting plate underneath the overriding plate with magmatic arc and back-arc basin. Due to fluid release (white arrows) from the subducting plate, partial melting occurs in the mantle wedge below the overriding plate, giving rise to igneous activity in the arc. (Modified by Padrón Navarta (2010) from Stern (2002)).*

subduction settings with rifting in back arc basins at old plate subduction or folding and thrusting behind the arc at younger plate subduction.

Unfortunately, the *downgoing part* of the slab is less known due to its great depth and we have to rely on geophysics of active systems, on experimental studies and on petrological and geochemical studies of exhumed paleo-subduction terranes. Fast subduction of younger plates leads to stronger coupling and larger amounts of shallow earthquakes (<50 km) than slow subduction of older plates, which leads to weak coupling and lower amount of shallow earthquakes (Stern, 2002). Deep earthquakes are a reflection of the thermal state of the subducting slab (Jarrard, 1986; Molnar et al., 1979; Peacock, 2003; Wei et al., 2017): the deeper the earthquakes, the cooler the subducting slab is maintained, i.e. the longer it needed to heat before no ruptures occurred anymore. Therefore, older and colder slabs tend to have deeper earthquakes than younger and warmer slabs (Houston, 2015; Kirby et al., 1991; Peacock and Wang, 1999; Syracuse et al., 2010; Wei et al., 2017).

The *mantle wedge* is the part of the mantle that lies between the upper part of the subducting slab and the lower part of the overriding plate (Fig. 1.3) (Deschamps et al., 2013; Schmidt and Poli, 2014; Stern, 2002). Here, input from the slab mixes to generate magmas, fluids and continental crust (John et al., 2012; Stern, 2002; Walowski et al., 2015). Magmas generated here —by the fluxing effect of aqueous fluids from the dehydrating slab— are fundamentally different than the magmas generated by upwelling hot asthenosphere at mid ocean ridges. Continental crust is thus underplated by melt that is emplaced by not only dry melting, but also by fluid-induced melting through lowering

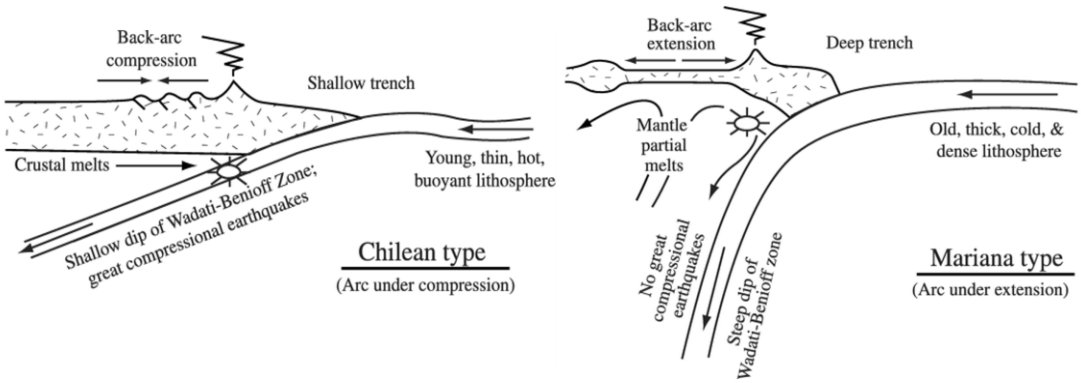

Figure 1.4. *Example of typical young (Chilean type) and old (Mariana type) subducting plates, giving rise to differing subduction zone settings. (modified after Uyeda and Kanamori (1979) by Stern (2002)).*

of the melt solidus (i.e. melting in presence of fluids occurs at 600-700°C, whereas dry melting occurs at temperature far beyond 700 °C, i.e. even above 1000 °C) (Sawyer et al., 2011; Weinberg and Hasalová, 2015; Whitney, 1988). Water is hence essential in generating large volumes of continental crust, whereas other water-induced melts can rise vertically to erupt at arc volcanoes (Fig. 1.3), sites where igneous activity forms abundant ore deposits (Grove et al., 2012; Hacker, 2008; Rüpke et al., 2004; Stern, 2002). The interaction between sinking slab, rising fluids and mantle convection, therefore, defines the fluid/rock recycling and dynamics of a subduction zone. What is not recycled in the upper 100 km of a subduction zone sinks in a form of residual slab towards the core-mantle boundary (e.g. Fig. 1.1), where it remains until it can revive again as a mantle plume (Hofmann, 1997).

1.2.2 Volatile recycling

A general picture of the key volatile bearing phases occurring in a subduction zone is given in Figure 1.5. Devolatilization —of mainly H_2O and CO_2— of the subducted lithosphere occurs over more than 300 km of the slab-mantle interface (e.g. Poli and Schmidt, 2002; Rüpke et al., 2004). The evolution of a subduction system is intimately related to fluid releasing metamorphic reactions, which control buoyancy forces, drive slab pull, and account for volatile transport and release (Poli and Schmidt, 2002). Mass transfer to the mantle wedge yields a series of fluids or melts, linked to convection and rising of melts into the overriding plate for development of arc magmas and continental crust (Grove et al., 2012; John et al., 2012; Rüpke et al., 2004; Schmidt and Poli, 2014; Stern, 2002; Walowski et al., 2015).

Fluids that get subducted are present as either pore fluids in oceanic sediments or incorporated in hydrous minerals in sediments (e.g. micas), altered basalt and gabbro (e.g. amphibole, biotite) and hydrated ultramafic upper mantle peridotite (e.g. antigorite, chlorite) (Hermann et al., 2006; Poli and Schmidt, 2002; Rüpke et al., 2004; Stern, 2002; Ulmer and Trommsdorff, 1999; van Keken et al., 2011). Pore fluids and fluids produced by diagenetic and low-grade metamorphism are released at shallower depths by mainly compaction (< 50 km; Peacock, 1990; Rüpke et al., 2004; Stern, 2002 and references therein), whereas water carried to deeper subduction depth (up to > 100 km) is released

from breakdown of hydrous minerals during higher grade metamorphism (Hacker, 2008; Rüpke et al., 2004; van Keken et al., 2011).

Major volatile-carrying phases in subduction zones are (Fig. 1.5): phengite (phe; 4.3 wt% H_2O), phlogopite (phl; 4.1 wt% H_2O) and chlorite (chl; 12.5 wt% H_2O) in metasediments (> 20 vol% phe, 5-20 vol% phl and 5-20 vol% chl); amphiboles (amp; 2.2 wt% H_2O), chlorite and lawsonite (law; 11.2 wt% H_2O) in basalts and gabbros (> 40 vol% amp, > 20 vol% chl, 5-20 vol% law); antigorite (atg; 12.3 wt% H_2O), chlorite, phase A (ph-A; 11.8 wt% H_2O) and 10 Å phase (10 Å ph; 8-14 wt% H_2O) in peridotites (> 20 vol% atg, < 5 vol% chl) (Schmidt and Poli, 2014). Besides H_2O, smaller amounts of CO_2 (< 5 vol%) are carried into the subduction zone by carbonate phases as calcite (cc), dolomite (dol) and magnesite (mag) in metasediments, basalts/gabbros or peridotites.

Phase A and 10 Å phase develop in colder subduction zones in which antigorite breakdown almost does not release water —due to cooler temperature at high pressure— but reacts directly to these phases (Figs. 1.5 and 1.6; Schmidt and Poli, 2014; van Keken et al., 2011; Wunder and Schreyer, 1997). In hot subducting slabs, antigorite breaks down

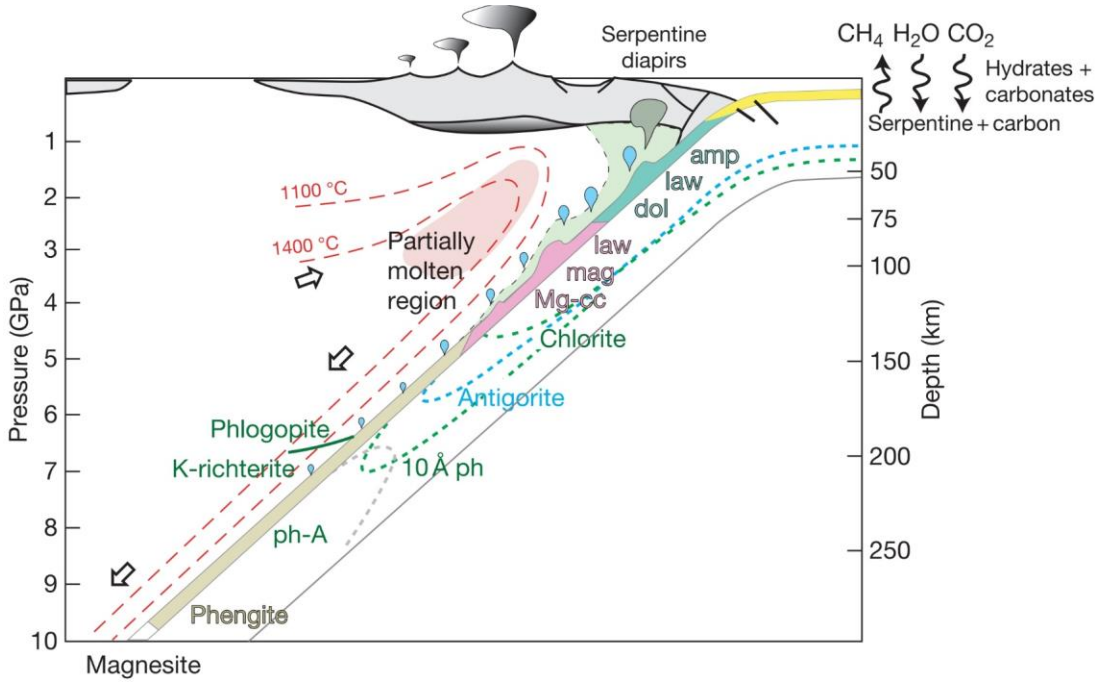

Figure 1.5. *Sketch of devolatilization events, showing the stability field of volatile-bearing phases in subduction zones. Stability of these phases within oceanic crust is marked by yellow to pink colors. The stability field of hydrous peridotite is demarcated with green to blue colors. The green area in the mantle wedge marks the stability of serpentine. Modified from Poli and Schmidt (2002). Abbreviations used in this figure are mentioned in the text.*

before phase A can form and all water is released (Fig. 1.6; Rüpke et al., 2004). Likewise, the transformation of phlogopite to K-richterite can be responsible for further H_2O fixation in the solid (Fig. 1.5; Konzett and Ulmer, 1999; Schmidt and Poli, 2014). Values for water budgets are thus highly dependent on the thermal structure of the subduction zone (Rüpke et al., 2004; van Keken et al., 2011). Mineralogically bound water can thus pass to higher depths in colder subduction zones than in hot ones. Therefore, the degree and depth of dehydration of deeper subducted slab and mantle wedge is diverse, depending on composition (i.e. gabbro or peridotite), age, subduction rate and pressure-temperature conditions.

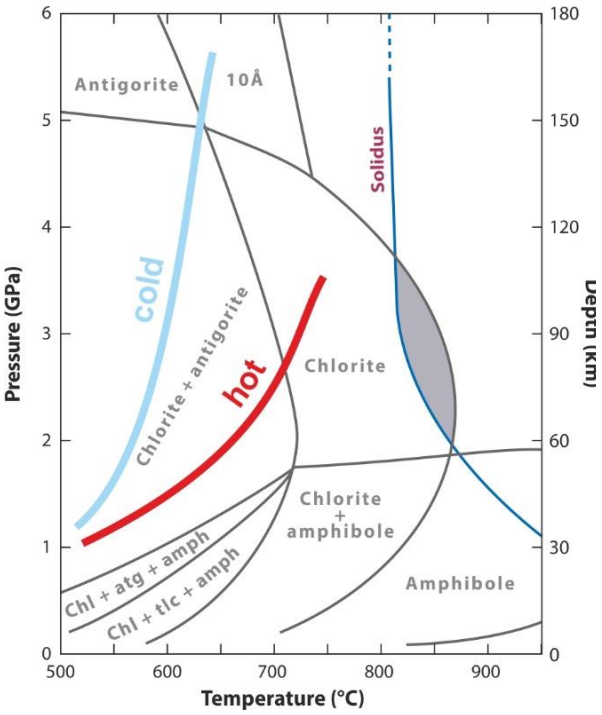

Figure 1.6. *Phase diagram for H_2O-saturated peridotite, showing hydrated minerals, after Grove et al. (2012). Abbreviations: amph, amphibole; atg, antigorite; Chl, chlorite; tlc, talc. Illustrative cold (blue thick line) and hot (red thick line) subduction are indicated, giving differing —still– – water-bearing products for dehydrating antigorite (10* Å phase *and chlorite, respectively).*

Hydrous peridotite is considered to deliver the largest amounts of water to postarc depth —40 to 60 % of its initial water (Rüpke et al., 2004; Schmidt and Poli, 1998)—, whereas hydrous basalts and gabbros, and sediments only deliver c. 28 % and c. 5 %, respectively (Hacker, 2008). Serpentine minerals —main components of hydrous peridotite— are the critical volatile-bearing phases in the subducting slab up to pressures of 5 GPa (Poli and Schmidt, 2002) or even 8 GPa (Ulmer and Trommsdorff, 1995). As their breakdown in the hydrated mantle releases an order of magnitude more water than the dehydration of the oceanic crust (Ulmer and Trommsdorff, 1995), serpentinite minerals play a fundamental role in subduction zones as the major water source (Padrón-Navarta et al., 2011; Scambelluri et al., 2004).

1.2.3 Fluid flow

Fluids from various slab sources (i.e. from shallow sediments to deep dehydration events) are transported through the interface between subducting oceanic lithosphere and the hanging wall, and through the mantle wedge (Fig. 1.7). The complex interplay of deformation and fluid flow makes the interface a major channelway for fluid transport, often creating complex veining networks and metasomatic features by chemical diffusion (Bachmann et al., 2009; Bebout and Penniston-Dorland, 2016; Zack and John, 2007). Fluids, and possibly melt, migrate up-dip towards the seafloor or emanate from the interface and enter the mantle wedge. At shallower depth, these fluids in the interface can induce pseudotachylites formation (Fig. 1.7), rock deformation in zones of unstable slip that record evidence of seismic events (Bebout and Penniston-Dorland, 2016 and references therein).

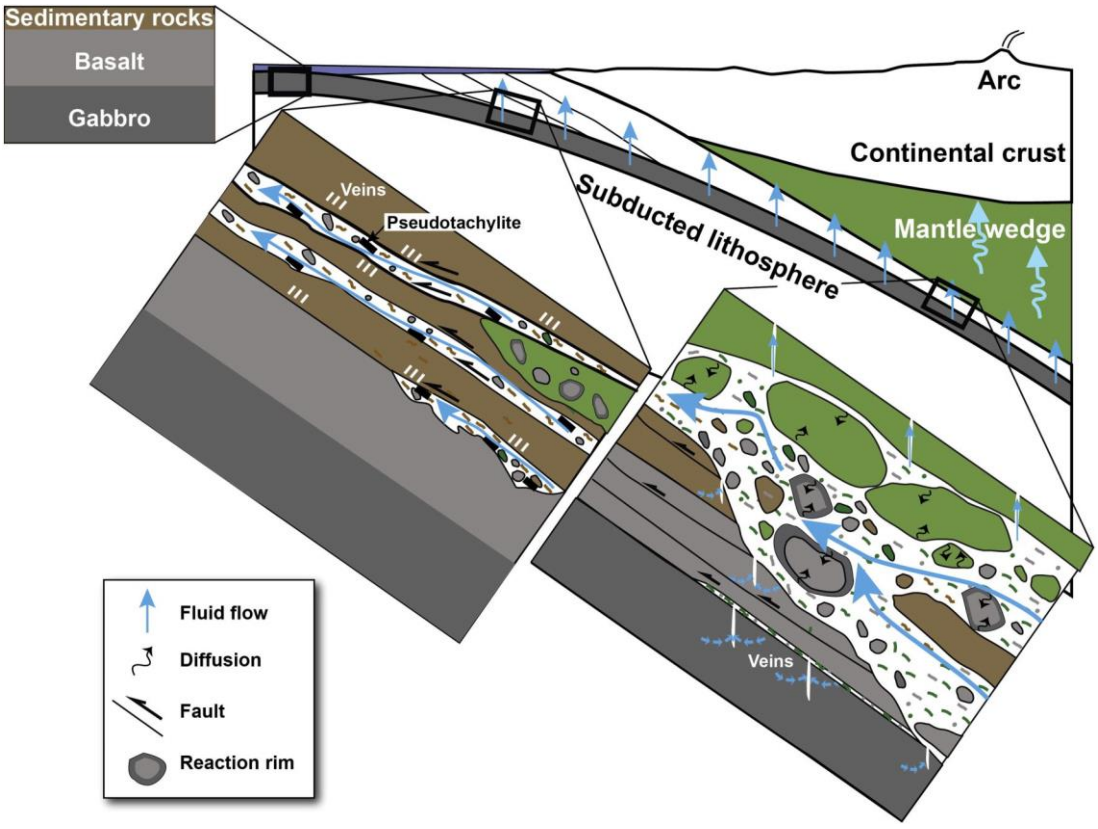

Figure 1.7. *Sketch of an oceanic plate (sediment + basalt + gabbro) subducting underneath a continental plate in a subduction zone. Key fluid flow pathways are shown at the plate interface and in mantle wedge. At shallow (upper box) and deep (lower box) levels key structural elements and likely fluid flow are schematically represented. Modified after Bebout and Penniston-Dorland (2016). Diagram is not to scale.*

At higher depth, it is critical to know how fluids escape from the subducting slab for understanding how the overlying mantle melts (Stern, 2002). Orientation of dehydration reactions is often perpendicular to typical subduction geotherms (Fig. 1.5), providing different effects for discontinuous and continuous devolatilization reactions (Schmidt and Poli, 2014). Discontinuous devolatilization involves abrupt mineral changes, whereas for continuous reactions only the relative proportion of phases is changed. This has important implications on the related fluid flow, as continuous reactions can release water over several tens of kilometers depth and discontinuous reactions release a large amount over a restricted depth range of only a few kilometers (Schmidt and Poli, 2014).

Besides fluid generation, understanding the path and flow mechanisms is fundamental to decipher the role of fluids in the dynamics of subduction zones. Several aspects can influence and change the way of fluid transport. During dehydration, fluid pressure will change independently from confining pressure (e.g. Hacker, 1997) as it is controlled by the fluid migration and, thus, by the rock rheology (Connolly, 1997, 2010; Connolly and Podladchikov, 1998; Miller et al., 2003). Fluctuation of fluid pressure can also produce fluctuations of the reaction rate and thus affect the expulsion rate of water, which again provides feedback to fluid pressure fluctuations and fluid migration (Connolly, 1997). The mode of fluid percolation thus depends on several different factors, such as dehydration rate and compaction rate, rock permeability and porosity, rock viscosity, elasticity and yielding strength (Connolly, 1997, 2010; Connolly and Podladchikov, 1998; Faccenda, 2014). Three mechanisms have been proposed to explain how fluids, produced mainly by serpentinite dehydration, migrate into the anhydrous mantle wedge (Stern, 2002): (1) porous flow, (2) channelized flow and (3) diapiric ascent.

Compaction-driven fluid flow is a *porous flow*, depending on the visco-elasticity of the rock (Connolly and Podladchikov, 1998), whereas when dehydration rate would exceed the expulsion rate —due to low surrounding permeability and relatively lower compaction rate— and deviatoric stresses are present, large-scale and rapid fluid flow associated with hydrofracturing might occur (e.g. Faccenda, 2014; Padrón-Navarta et al., 2011), giving rise to *channelized flow*. Porous flow is slow and maximizes interaction of fluids with the rock close to the dehydration site. Channelized flow is much more rapid due to the hydrofracturing or faulting (Davies, 2001), thus minimizing the fluid-rock

interaction at the dehydration source and carrying massive amounts of fluids over large distances in subduction zones (Faccenda, 2014; Zack and John, 2007). Water released from the slab will percolate upward and react with the mantle peridotite to form hydrous serpentine minerals when its temperature is lower than 700 °C (Deschamps et al., 2013 and references therein). This creates a buoyancy effect due to the strong contrast in density and viscosity between newly formed serpentinites (2.6 g/cm^3) and anhydrous peridotites (3.2 g/cm^3). This could give rise to the third mentioned mechanism, for which cold *diapirs* rise from the slab surface into the mantle wedge (e.g. Fig. 1.5) by compositional buoyancy (Gerya and Yuen, 2003). Feedback between solid rock and fluid expulsion mechanisms is therefore critical to understand fluid flow processes.

Large amounts of fluid transport definitely lead to extensive mass transfer in subduction zones with a complex interplay between deformation and fluid flow (Bebout and Penniston-Dorland, 2016). Besides arc volcanism, the double seismic zone (Fig. 1.8) has been linked in several studies to metamorphic dehydration fluid production and subsequent flow (Brown et al., 2005; Faccenda, 2014; Hacker et al., 2003b; Kirby, 1995; Komabayashi, 2006; Peacock, 2001). High-resolution images of the position of earthquakes in the slab support the predicted location of main dehydration reactions (Abers et al., 2006; Kita et al., 2006). Dehydration alone, however, is not sufficient to induce earthquakes, but could nevertheless be the controlling trigger. Fluid pressure and/or stress transfer namely can strongly influence the mechanical behavior of the rock as they undergo sudden weakening and embrittlement (Brantut et al., 2017; Ferrand et

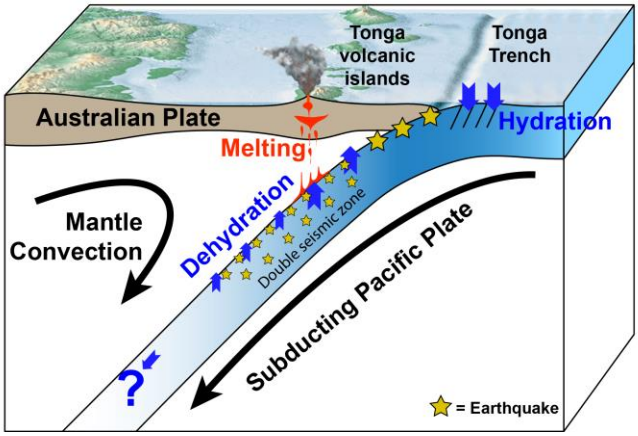

Figure 1.8. *Sketch on the subduction of the Pacific plate underneath the Australian plate at the Tonga Trench. Dehydration water release might trigger intermediate-depth earthquakes and create the double seismic zone (two rows of stars). Some portion of hydrous minerals might survive to greater depths (indicated by '?'). Illustration: S. Shawn Wei from Washington University in St. Louis (https://source.wustl.edu/2017/01/release-water-shakes-pacific-plate-depth/)*

al., 2017; Hacker et al., 2003b; Ko et al., 1997; O'Neill et al., 2007; Raleigh and Paterson, 1965; Rutter and Brodie, 1988).

Modeling of the fluid-rock interaction, based on elemental and isotopic diffusivity, unveils short time scales —100 kyr or less— in which fluids traveled from slab through mantle rock to volcanic arc (John et al., 2012; Pogge von Strandmann et al., 2015). This relatively short duration of fluid flows suggests an episodic nature of fluid release mechanism during subduction metamorphism in cycles of short pulses or bursts (Bebout and Penniston-Dorland, 2016). Studying these cyclic events can gain an insight into the periodicity of flow and its relationship to seismicity. Our understanding of fluid generation and transfer in a subducting slab can be linked to our understanding of metamorphic dehydration reactions involving hydrous minerals (Padrón-Navarta et al., 2011). Serpentinite dehydration is the focus within this thesis, as this is one of the most important dehydration reactions in subduction zones.

1.3 Serpentinite formation and dehydration

The serpentinite dehydration reaction is that has been invoked as the main dehydration reaction explaining the lower seismic zone (of the double seismic zone) of subduction zones (Furukawa, 1993; Komabayashi, 2006; Peacock, 2001; Seno and Yamanaka, 1996), as well as the linked island arc magmatism (e.g. Furukawa, 1993; Grove et al., 2012; Hattori and Guillot, 2003; Ulmer and Trommsdorff, 1995). Serpentinite is the dominant water carrier in hydrated mantle rocks (Rüpke et al., 2004) and is stable to high pressure and temperature, which could even reach up to 720°C (at 2 GPa; Schmidt and Poli, 1998) or 8 GPa (at c. 500 °C; Ulmer and Trommsdorff, 1995). This provides an effective way to transport water to great depth (Fig. 1.9a). To understand the massif amount of water transported in serpentinites, first the uptake of water is discussed, followed by a description of its journey into the deep mantle with interrelated hydration and dehydration reactions.

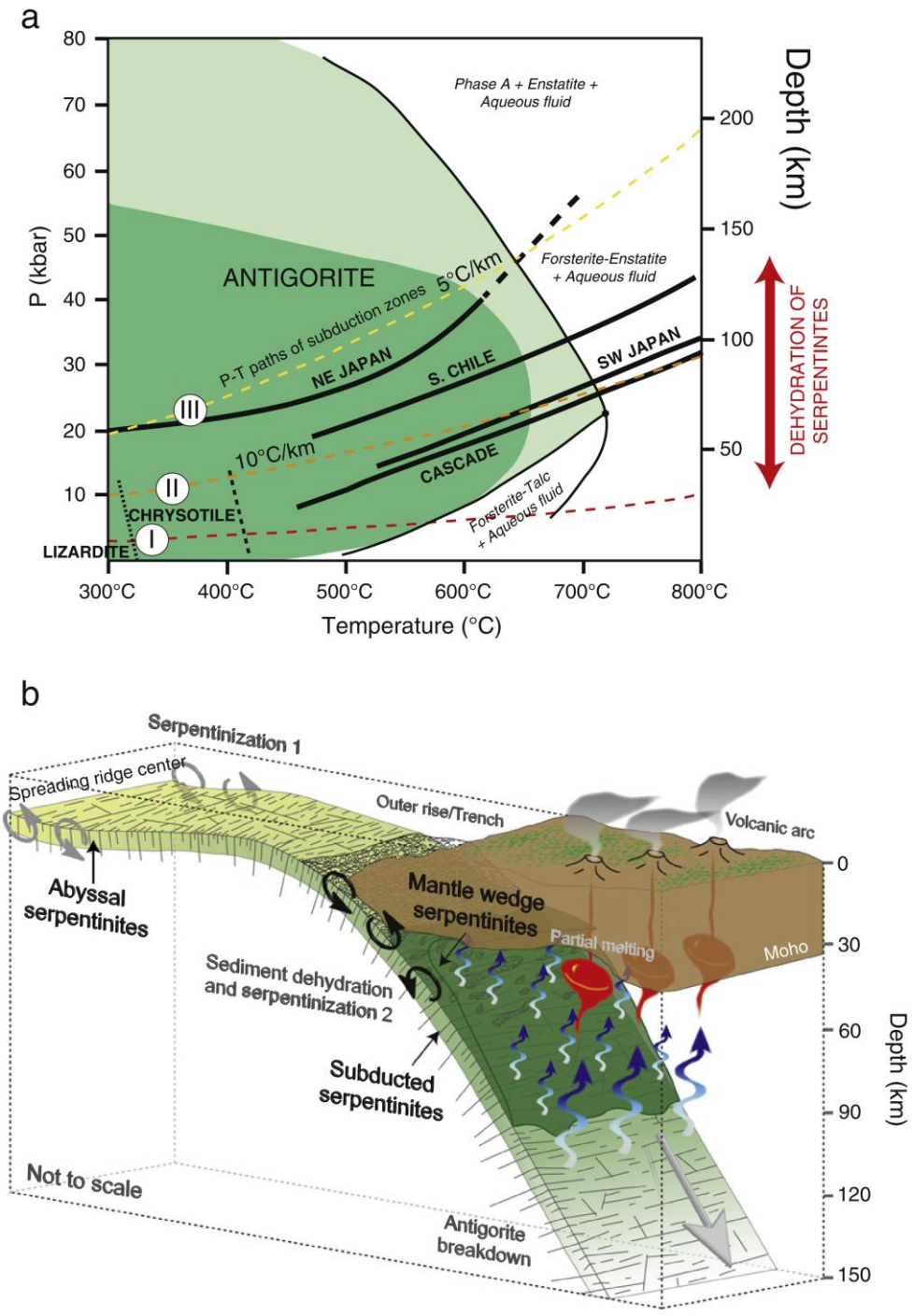

Figure 1.9. *a) P-T diagram of serpentine minerals, their stability field and their breakdown reaction products at higher P-T conditions. Dark green and light green area represent, respectively, the stability fields of antigorite determined by the studies of Wunder and Schreyer (1997) and Bromiley and Pawley (2003) and by the study of Ulmer and Trommsdorff (1995). Dashed lines (I, II and III) represent theoretical P-T paths of subduction zones in differing age, i.e. young to old or hot to cold, respectively (Peacock, 1990). Solid black lines represent existing P-T paths of current subduction zones (data sources are from Fukao et al., 1983; Furukawa, 1993; Peacock and Wang, 1999). Theoretical antigorite breakdown depth is indicated with a red arrow to the left. Modified after Hattori and Guillot (2003).* ***b)*** *3-D sketch of a typical subduction zone setting with formation stages of serpentinite and breakdown of antigorite in subduction. Image from Deschamps et al. (2013).*

1.3.1 The serpentine mineral group

Serpentinites are hydrated ultramafic rocks (with H_2O content up to 15–16 wt%, average of 13 wt%) which form through the alteration of peridotite protoliths (Deschamps et al., 2013; Faccenda, 2014; Mével, 2003; Ulmer and Trommsdorff, 1995; Wunder and Schreyer, 1997). Serpentine minerals —generalized formula $Mg_3Si_2O_5(OH)_4$— have a 1:1 octahedral-tetrahedral layer structure (Bromiley and Pawley, 2003; Mével, 2003; Wicks and O'Hanley, 1988), forming the three basic phyllosilicates chrysotile, lizardite and antigorite (Fig. 1.9a; Bromiley and Pawley, 2003; Ulmer and Trommsdorff, 1995; Wunder and Schreyer, 1997). Lizardite consists of planar layers, whereas chrysotile consists of scrolled layers that tend to form cylinders and antigorite has periodically reversed layers that result in the loss of octahedral sites (Mével, 2003). Due to this lack, antigorite has less Mg and $(OH)_4$ with respect to Si (on octahedral and tetrahedral sites, respectively) and is therefore systematically enriched in Si (e.g. Mével, 2003 and references therein).

The periodically reversed layering of antigorite is displayed as alternating sinusoidal octahedral and tetrahedral layers (Kunze, 1956, 1958; Zussman, 1954). The composition of individual antigorites can be expressed by the formula $M_{3m-3}T_{2m}O_{5m}(OH)_{4m-6}$ (Kunze, 1961), where m is the number of tetrahedra in a single chain defined by the sinusoidal wavelength, M = octahedral cations (Mg, Fe^{2+} Ni, Mn^{2+}, Al), and T = tetrahedral cations (Si, Al). The value m often varies between 14 and 23. The most representative value for antigorite is m=17 (Ulmer and Trommsdorff, 1995; Wunder and Schreyer, 1997) with the corresponding structural formula and composition of $Mg_{48}Si_{34}O_{85}(OH)_{62}$ (Mellini et al., 1987).

Chrysotile and lizardite are stable at temperatures lower (< c. 350 °C) than antigorite (< c. 650-700 °C) (Deschamps et al., 2013; Hyndman and Peacock, 2003; Mével, 2003). Therefore, the predominance of a certain serpentine mineral depends on the conditions during formation and subsequent evolution of the serpentinite. Lizardite mainly occurs as a dominant phase in serpentinites from seafloor, whereas chrysotile is the major phase occuring in veins (Mével, 2003). Antigorite typically is the high-P serpentine group mineral that forms and remains stable until deeper depths at higher pressure and

temperature than the other two serpentine minerals (Rüpke et al., 2004; Schmidt and Poli, 2014; Wunder and Schreyer, 1997).

1.3.2 Water delivery to deep mantle

Due to their high water content, serpentine minerals have a predominant role in the water budget of subduction zones and lead to profound changes in the properties of ultramafic rocks (Faccenda, 2014). In a subduction zone setting, the presence of three main serpentinite types may be distinguished, being abyssal, mantle wedge and subduction zone serpentinites (Fig. 1.9b; Deschamps et al., 2013; Hilairet et al., 2007). *Abyssal serpentinites* represent hydration of oceanic peridotites by seafloor hydrothermal activity/seawater alteration (e.g. Bach et al., 2004; Mével, 2003; Schroeder et al., 2002). *Mantle wedge serpentinites* are hydrated mantle peridotites by fluids released from the subducted slabs (e.g. Hilairet et al., 2007). *Subduction-related* serpentinites are the ones that got subducted to higher depth, undergoing transformation, and can be of abyssal

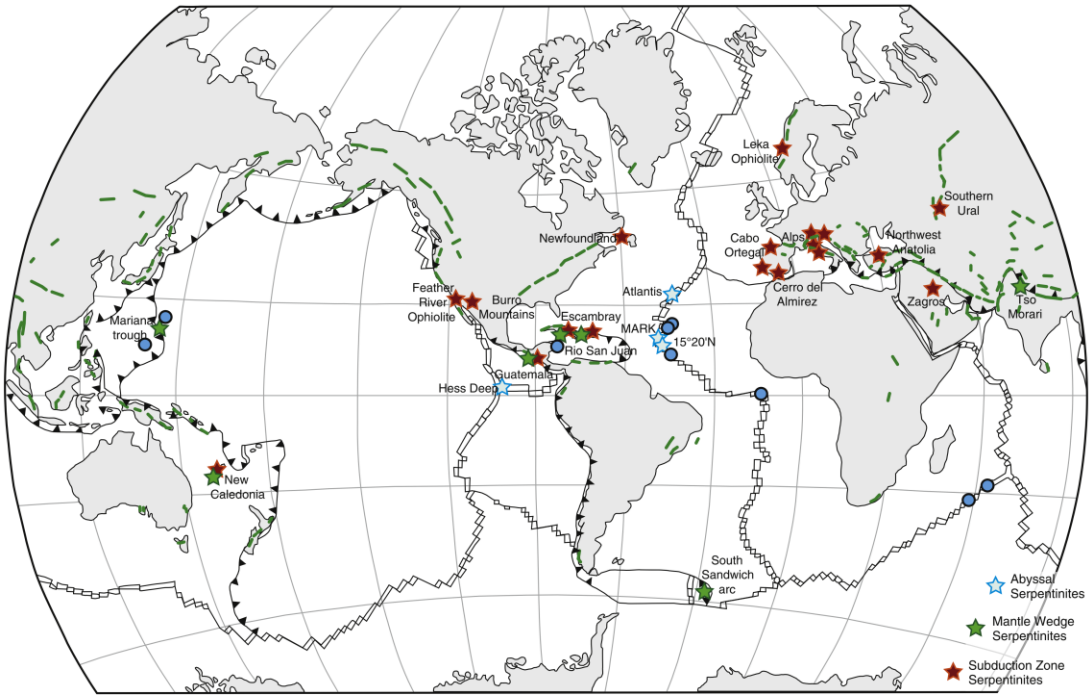

Figure 1.10. *Map representation of locations of serpentinite outcrops and massifs, showing three distinctions: abyssal (blue star), subducted (red star) and mantle wedge origin (green star); major occurrences of serpentinites on continents (green lines) and major seafloor sites where serpentinites were recognized (blue circles) are indicated as well. See Deschamps et al. (2013) for more detailed literature on the locations. Note the Almirez paleo-subduction setting in the SE of Spain, referred to as 'Cerro del Almirez'.*

and/or mantle protolith (Deschamps et al., 2013). Worldwide, some locations provide the opportunity to study these serpentinites, either in situ (abyssal) or in exhumed metamorphic terranes (mantle wedge, subduction) (Fig. 1.10) (e.g. Deschamps et al., 2013; Lamadrid et al., 2017; Mével, 2003).

1.3.2.1 Abyssal serpentinites: the uptake of water

Ocean floor or abyssal serpentinites (e.g. Alt et al., 2013; Früh-Green et al., 2004; Iyer et al., 2008a) are predominantly formed by lizardite and minor chrysotile (Mével, 2003). Serpentinization of the slab lithospheric mantle takes place in a first stage (Serpentinization 1; Fig. 1.9b) during hydrothermal alteration of peridotite at ridge axes and along sea floor fault systems and, in a second stage (Serpentinization 2; Fig. 1.9b), along bend faults outboard and within the subduction trench (Bach et al., 2004, 2006; Faccenda, 2014; Fryer, 2002; Hatakeyama et al., 2017; Peacock, 2003; Ranero et al., 2003). Oxygen and hydrogen isotopes show that seawater is the main fluid responsible for serpentinization of abyssal peridotites (Deschamps et al., 2013).

The uptake of water within dense peridotite decreases density by increasing volume (around 40%) to form serpentinites (e.g. Iyer et al., 2008a; Mével, 2003; Schroeder et al., 2002). This reaction-assisted positive volume change does not occur simultaneously, which causes local compressional stresses that can cause fracturing deformation in surrounding rocks with pervasive fluid infiltration (Faccenda, 2014; Iyer et al., 2008b). Besides fracturing, volume expansion also seals fluid pathways that limit the percentage of rock serpentinized and, thus, for complete serpentinization tectonic activity is required (Schroeder et al., 2002). Serpentinization therefore mainly occurs within fracturing and major faulting structures at unroofing of peridotite protolith, tips of propagating rifts or other extensional deep faults of tens of kilometers that permitted seawater to penetrate to deep crust and upper mantle to form serpentinite masses (Deschamps et al., 2013; Faccenda, 2014; Fryer, 2002; Iyer et al., 2012; Mével, 2003; Peacock, 2001; Rüpke et al., 2004; Schroeder et al., 2002).

The first stage of serpentinization (Serpentinization 1; Fig. 1.9b) occurs during progressing hydration as the newly formed peridotite at ridges is cooling into the serpentinite field (Fig. 1.6; Mével, 2003; Schroeder et al., 2002). The amount of hydration within oceanic crust depends on whether it forms at slow or fast spreading ridges

(Deschamps et al., 2011; Mével, 2003; Paulatto et al., 2017). It namely incorporates more water to form serpentinized peridotite at surface and along detachment faults when it spreads slower instead of producing basalt, diabase and gabbro with minimal hydration confined to upper crustal levels at fast spreading ones (Faccenda, 2014; Fryer, 2002; Karson, 1998). Besides the spreading rate, also the salinity of the reacting fluid seems to play a role in the amount of serpentinization as the serpentinization rate decreases with increasing salinity (Lamadrid et al., 2017). Slow spreading ridges in low salinity oceans therefore probably provide more volatiles into the subduction recycling factory.

The second stage of ocean floor serpentinization (Serpentinization 2: Fig 1.9b) is without doubt the most important in water uptake before and during subduction. At the outer-rise and early subduction, newly formed or reactivated faults due to slab bending create deep pathways (even > 15 km) for fluid penetration and hydration deep into the mantle (Deschamps et al., 2011, 2013; Grevemeyer et al., 2018; Hatakeyama et al., 2017; Iyer et al., 2012; Naliboff et al., 2013; Ranero et al., 2003). This significantly increases the proportion of serpentine in the lithosphere and the amount of water carried down into the subduction zone (Peacock, 2001; Ranero et al., 2003; Rüpke et al., 2004). Lithospheric serpentinites are therefore considered as a big source of water during sub-arc slab dewatering (Schmidt and Poli, 1998; Ulmer and Trommsdorff, 1995), a key process in the global water cycle (Grevemeyer et al., 2018; Paulatto et al., 2017).

Another consideration is the relative weakness of serpentinite that significantly affects geodynamic processes along the lithospheric strike-slip faults (Hirth and Guillot, 2013). Serpentinite viscosity is sufficiently low for subduction initiation along the serpentinized faults (Hilairet et al., 2007). Serpentinization (Fig. 1.9b) at relatively shallow depth (< 20 km) in subduction, where lizardite remains the dominating serpentine mineral (Deschamps et al., 2013), is therefore an important key for maintaining the subduction factory.

1.3.2.2 Mantle wedge serpentinites

A wide range of geological and geophysical data point out that mantle wedge serpentinites (Fig. 1.9b) are produced by fluids released from subducting slab lithologies such as sediments, altered basalts and gabbros, and serpentinites (Deschamps et al., 2012, 2013; Doo et al., 2016; Faccenda, 2014; Hyndman and Peacock, 2003). Recent

geophysical data suggest that mantle serpentinization at subduction trenches is globally occurring above oceanic plates of >10-15 Myrs (Grevemeyer et al., 2018), i.e. they have to be old enough and most likely come from slower spreading ridges. Dewatering mainly occurs due to compaction in between 300 – 600 °C and < 1.5 GPa (Rüpke et al., 2004). Water percolates upwards by buoyancy and hydrates the dry peridotite as long as temperatures are below 700 °C (Deschamps et al., 2013; Ulmer and Trommsdorff, 1995; Wunder and Schreyer, 1997).

Serpentinite minerals in mantle wedges are either lizardite/chrysotile or antigorite, depending on the depth and stability of serpentine mineral (Fig. 1.9a). With increasing P-T conditions, around 400°C the antigorite serpentine mineral becomes stable (Evans, 1976) and the low-grade serpentines lizardite and chrysotile transform into antigorite (Deschamps et al., 2011, 2012; Lafay et al., 2013).

1.3.2.3 Subduction zone serpentinite

Serpentinite in subduction undergoes changes in its chemistry. The geochemistry of serpentinites namely depends, besides on the nature of hydrating fluids, also on temperature and pressure during formation. This implies an important control of the geological and geodynamic setting. Exhumed mantle serpentinites, for instance, can be distinguished from abyssal serpentinites by their higher oxygen fugacity (Deschamps et al., 2013 and references therein). The more deeply subducted serpentinites, however, occur mainly highly deformed within suture zones and associated with HP–LT metamorphic rocks (Hattori and Guillot, 2007) and are therefore a heterogeneous mix of different serpentinite origins. This poses the challenge to determine whether they originated from abyssal peridotite, oceanic-continent transition zone (OCT) or mantle wedge (Deschamps et al., 2013). Towards higher pressure and temperature all lizardite progressively rebuilds its serpentine structure into antigorite (Fig. 1.9a) (Deschamps et al., 2011, 2012; Lafay et al., 2013).

At subduction depth beyond 20 km, antigorite can stay stable until depth up to 180 km, depending on whether it occurs in cold (deeper) or hot (less deep) subduction zones (e.g. Rüpke et al., 2004; Ulmer and Trommsdorff, 1995). Antigorite, therefore, is the principal high-P serpentine group mineral that carries water to the intermediate depths of subducting slabs (Rüpke et al., 2004; Schmidt and Poli, 2014; Wunder and Schreyer,

1997). Exhumation and preservation of these deeply subducted antigorite-serpentinites should have occurred relatively fast, in order to "freeze" antigorite (without retrograde transformation into the low-grade serpentine minerals) through e.g. metamorphic core complexes, accretionary complexes or suture zones (e.g. Deschamps et al., 2013; Jabaloy-Sánchez et al., 2015; and references therein). In spite of their low abundance (Fig. 1.10), these outcrops provide a unique opportunity to study the deep subduction water release processes linked to antigorite breakdown.

1.3.3 Water release at great depths: the antigorite breakdown reaction

The antigorite breakdown (up to 600–700 °C; Fig. 1.9a; Deschamps et al., 2013) is the main prograde metamorphic dehydration reaction taking place under high P-T conditions in subduction zones. Results of high-pressure experiments by Ulmer and Trommsdorff (1995) on samples of hydrated mantle rocks show that the serpentine mineral antigorite could be stable to approximately 720 °C at 2 GPa, to approximately 690 °C at 3 GPa, and to approximately 620 °C at 5 GPa. The breakdown reaction products vary with P-T conditions (cf. Fig. 1.9a) and are with increasing pressure (Bromiley and Pawley, 2003; Ulmer and Trommsdorff, 1995; Wunder and Schreyer, 1997):

$$antigorite = talc + forsterite + water \quad (1)$$

$$antigorite = forsterite + enstatite + water \quad (2)$$

$$antigorite = enstatite + phase\,A + water \quad (3)$$

In reaction (1) and especially in reaction (3), water is still retained in the breakdown-products of antigorite (i.e. talc and phase A, respectively), whereas in reaction (2) antigorite fully breaks down into anhydrous mineral phases. Reaction (2) thus releases the highest amount of water with respect to reaction (1) and (3).

Whether reaction (1), (2) or (3) happens during antigorite dehydration, does not simply depend on subduction depth. Subducting slabs of different geological ages and rates — the older and faster, the colder the slab at a certain depth— have different depths and thus P-T conditions of dehydration (see yellow, orange and red dashed lines in Fig. 1.9a; Peacock, 1990. Total dehydration efficiency decreases with increasing incoming plate age (Rüpke et al., 2004). The serpentinized peridotite layer of relatively colder oceanic lithosphere will not produce any significant fluid to pressures of 3–6 GPa (Schmidt and

Poli, 2014; van Keken et al., 2011). Cold subduction settings may not even reach 650 °C, even at 130 km depth, as in NE Japan (Hattori and Guillot, 2003; Peacock, 2001). Above the invariant point between reaction (2) and (3) (Path III in Fig. 1.9a) dehydration will not be complete, as some of the water incorporated into antigorite will be incorporated at these high pressures in the hydrous phase A (Peacock, 1990; Rüpke et al., 2004; Wunder and Schreyer, 1997). In more common hotter portions of subduction zones (path II in Fig. 1.9a) breakdown happens at lower pressures and higher temperatures and will not retain H_2O as antigorite dehydrates into forsterite + enstatite + water. This would correspond to depths of 90-110 km, such as in subduction zones in Cascadia, SW Japan and S Chile (Hattori and Guillot, 2003; van Keken et al., 2011). For very young slabs and slow subduction (Path I in Fig. 1.9a), dehydration of antigorite will again be incomplete due to the reaction forming the solid assemblage talc + forsterite which retains about 1.8 wt% H_2O (below the invariant point between reaction (1) and (2); Wunder and Schreyer, 1997). To gain more insights into the antigorite dehydration reaction in subduction zones, more constraints on the P-T conditions of these key breakdown reactions —especially of reaction (2)— are necessary.

Several experiments focused on the phase stability fields and confined variable invariant points that distinguish these reactions (Fig. 1.9a). The invariant point dividing reaction (2) and (3) is located at c. 580°C and 4.5 GPa by Wunder and Schreyer (1997) and at c. 550°C and 5 GPa by Hilairet et al. (2006) and Komabayashi et al. (2005). Reaction (1) and (2) are divided by the invariant point determined as 650 °C and 1.5 GPa by Wunder and Schreyer (1997) or as 720 °C and 2 GPa by Ulmer and Trommsdorff (1995). Padrón-Navarta et al. (2010a) retrieved preferred experimentally-based values of approximately 670 °C and 1.6 GPa. Differences in these experiments are due to the complex antigorite composition that can vary significantly in subduction zones and influence P-T conditions of its breakdown (Padrón-Navarta et al., 2010a; Wunder and Schreyer, 1997). The addition of iron and Al increases the variance of antigorite reactions (Padrón-Navarta et al., 2010a). Iron seems to displace the reactions slightly towards lower temperature (Bromiley and Pawley, 2003; Padrón-Navarta et al., 2010a; Worden et al., 1991), whereas Al would shift values considerably towards higher P-T conditions (Bromiley and Pawley, 2003). For iron substitution, no new phases would occur in the reactions (1) to (3) as it can replace Mg in all silicates, whereas incorporating Al is more

complex and chlorite will appear as a new product phase (Bromiley and Pawley, 2003; Padrón-Navarta et al., 2010a; Worden et al., 1991). Al and —to a lesser extent— other minor trivalent cations such as Fe^{3+} and Cr^{3+} could shift the antigorite breakdown to c. 60-70 °C higher temperatures at 1.8 GPa (Padrón-Navarta et al., 2010a). Bromiley and Pawley (2003) similarly reported a shift of 50 °C with Al-incorporation below 2.5 GPa.

Taking into account Al considerably affects the water budget of reaction (2), as not all hydroxyl groups break down and are instead partially transferred to chlorite-bearing assemblages. This certainly discloses a wider range over which water is tied up in hydrous phases relative to Al-free systems (Bromiley and Pawley, 2003). Involving chlorite into reaction (2), the following intermediate reactions (occurring entirely within the stability field of olivine) can be reconstructed with increasing temperatures: Chl-in (2a), Opx-in (2b) and Atg-out (2c) isograd (Padrón-Navarta et al., 2011; Padrón-Navarta et al., 2013):

$$antigorite = antigorite + chlorite + water \quad (2a)$$

$$= antigorite + chlorite + enstatite + forsterite + water \quad (2b)$$

$$= enstatite + forsterite + chlorite + water \quad (2c)$$

Besides its composition, also the extent of polysomatic ordering can have a great influence on the stability of antigorite (Bromiley and Pawley, 2003; Padrón-Navarta et al., 2010a; Wunder et al., 2001). The highly ordered antigorite (m=17; Padrón-Navarta et al., 2008b) with high Al- and Cr-content from Almirez (Spain) provides herewith the high-end temperature conditions of antigorite breakdown found in natural systems in subduction environment with the maximum stability of antigorite at 680 °C at 1.9 GPa (Padrón-Navarta et al., 2010a). The disappearance of antigorite at the Atg-out isograd at Almirez marks the full antigorite breakdown into chlorite-harzburgite with 9 wt% water released (Padrón-Navarta et al., 2011 and references therein).

1.3.4 The signature of deserpentinization fluids

Geochemical signatures of deserpentinized fluids have been investigated thoroughly. Hattori and Guillot (2003) have proposed a relation between location of active arc volcanoes on the surface, and the depth of slab below the volcanic front, which is generally between 80 and 140 km depth (Fig. 1.9). This depth interval corresponds to the maximum pressure of the stability field of antigorite (Schmidt and Poli, 2014; Ulmer and

Trommsdorff, 1995; Wunder and Schreyer, 1997). Volcanic arcs are enriched with fluid soluble elements (e.g. As, Sb, Pb, B and Sr, Cs, Rb, Ba, U), the same that are incorporated within antigorite (e.g. Deschamps et al., 2013; Hattori and Guillot, 2003; Leeman, 1996; Marchesi et al., 2013; Noll et al., 1996; Ryan et al., 1995; Scambelluri et al., 2001; Scambelluri et al., 2014; Tenthorey and Hermann, 2004), and depleted in high-field-strength trace elements (HFSE) relative to mid-ocean ridge basalts (MORB) (Garrido et al., 2005; Kovalenko et al., 2010; Scambelluri et al., 2004). This is the most distinctive geochemical fingerprint of subduction magmatism. When antigorite is destabilized, the great amount of aqueous fluids released are enriched in the fluid soluble elements as they leach the overlying crust and sediments while they migrate upward into the mantle wedge (Garrido et al., 2005). They lead to partial melting in the anhydrous mantle and thus account for the observed enrichment of these elements in arc magmas (Fig. 1.9b) (Deschamps et al., 2013 and references therein). Alt et al. (2012, 2013) furthermore reveal that volatiles released from antigorite breakdown are consistent with the observed enrichments of the isotopes ^{18}O, D, and ^{34}S in arc magmas and oxidation of the sub-arc mantle wedge that resulted from metasomatism by fluids from the subducting slab. Harvey et al. (2014) link the enrichment of $\delta^{11}B$ signature in island arc magma to the antigorite breakdown in downgoing slabs. Serpentinite dehydration thus releases highly oxidizing fluids in subduction zones that contribute to the oxidation and melting of the sub-arc mantle wedge (Debret et al., 2015) and the release of oxidized volatiles through lava eruptions back into the atmosphere (Debret and Sverjensky, 2017).

The role of these volatiles on rock dynamics, their time scale and fluxes, however, are still barely understood and even precise global mass balance computations of volatile cycling in subduction zones remains difficult due to incomplete data (van Keken et al., 2011). A unique opportunity to study the Atg-breakdown reaction in subduction zones is provided by the Almirez ultramafic massif in the SE of Spain (Fig. 1.10). This natural laboratory shows the Atg-out isograd with antigorite serpentinite in contact with its dehydration product preserved.

1.4 The Almirez ultramafic massif: a key outcrop on subduction dehydration

We still lack a profound understanding of the mechanisms and kinetics of fluid expulsion during serpentinite breakdown, due, among other reasons, to the scarcity of geological records of this process. Metamorphic terrains that record this main dehydration reaction can be used as an invaluable tool to decipher the mechanism for fluid expulsion. The Cerro del Almirez ultramafic massif (hereafter Almirez massif), with its unique preservation of reactant and product of the antigorite dehydration reaction, provides us this opportunity. This outcrop is situated in the Betic Cordillera in the south-east of Spain (Fig. 1.10, 1.11).

1.4.1 Geological background

1.4.1.1 The Betic Cordillera

Together with the Rif Mountains in northern Morocco, the Betic Cordillera forms an arcuate belt —the Betic-Rif belt— that surrounds the Alborán Sea, and represents

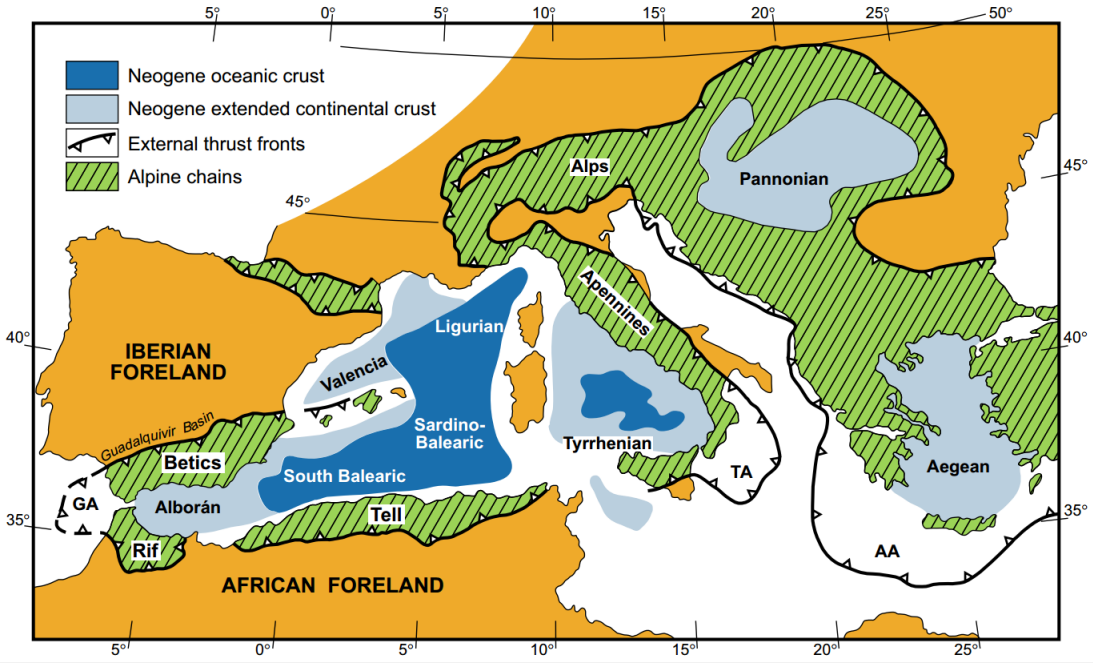

Figure 1.11. *Sketch of the tectonic setting around the Mediterranean Sea during the Neogeen, with extensional basins and external front of surrounding Alpine thrust belts. AA = Aegean Arc; GA = Gibraltar Arc; TA = Tyrrhenian Arc (Comas et al., 1999).*

herewith the westernmost segment of the Mediterranean Alpine orogeny (Fig. 1.11; Torne et al., 2000). The Betic-Rif belt is bound to the north and south by the Iberian and African forelands, respectively, and to the west and east by the Gibraltar arc and the Balearic Sea, respectively.

The Betic Cordillera is divided into three main domains being the External zones, the Flysch Trough units and the Internal Zones (Booth-Rea et al., 2007 and references therein; Platt et al., 2013), which expand in the south-east of Spain. The External Zones are composed of non-metamorphic Triassic to Miocene sedimentary rocks, deposited on the south Iberian paleomargin (Lonergan and White, 1997; Platt et al., 2013), close to the Iberian and African foreland (Fig. 1.12). The Flysch Trough units comprise Cretaceous to Miocene siliclastic and calcareous turbidites (Crespo-Blanc et al., 2012; Guerrera et al., 2005; Luján et al., 2006). Traditionally, the Internal Zones —being stacked as three metamorphic nappes: Maláguide, Alpujárride and Nevado-Filábride complexes (Tubía et al., 1992)— have been included in the allochthonous Alborán domain (Balanyá et al., 1997; Hidas et al., 2013; Platt et al., 2013). The Nevado-Filábride complex, however, was later on identified as being part of the Iberian paleomargin that subducted to high pressures beneath the Alborán domain and was later exhumed and overthrusted on the Alpujárride complex (Fig. 1.12) (Booth-Rea et al., 2005, 2015; de Lis Mancilla et al., 2015; Gómez-Pugnaire et al., 2012; Jabaloy-Sánchez et al., 2015).

1.4.1.2 The Nevado-Filábride Complex[1]

The Nevado-Filábride Complex (NFC) is a subduction complex exposed in the core of the E-W elongated, antiformal dome structures in the Internal Zones of the central and eastern Betics (SE Spain) to form the mountain ranges of the Sierra Nevada to the west and Sierra de los Filabres to the east (Fig. 1.12a). Recent contributions have reviewed the tectono-metamorphic and geochronological evolution of the NFC, and present different views of its geodynamic evolution (Booth-Rea et al., 2015; Gómez-Pugnaire et al., 2012; Jabaloy-Sánchez et al., 2015, 2018; Kirchner et al., 2016; López Sánchez-Vizcaíno and

[1] This section has been published within the Geological setting of Dilissen, N., Hidas, K., Garrido, C.J., Kahl, W.-A., López Sánchez-Vizcaíno, V., Padrón-Navarta, J.A., 2018. Textural evolution during high-pressure dehydration of serpentinite to peridotite and its relation to stress orientations and kinematics of subducting slabs: Insights from the Almirez ultramafic massif. Lithos 320-321, 470-489.

Gómez-Pugnaire, in press; Platt et al., 2013; Puga et al., 2009; Puga et al., 2011). Here, we provide a summary of the geodynamic evolution of the NFC that is of relevance for the Almirez ultramafic massif.

The lithological sequence of the NFC is composed of metapelites, marbles, and orthogneisses —derived from the continental margin that developed on the Paleozoic

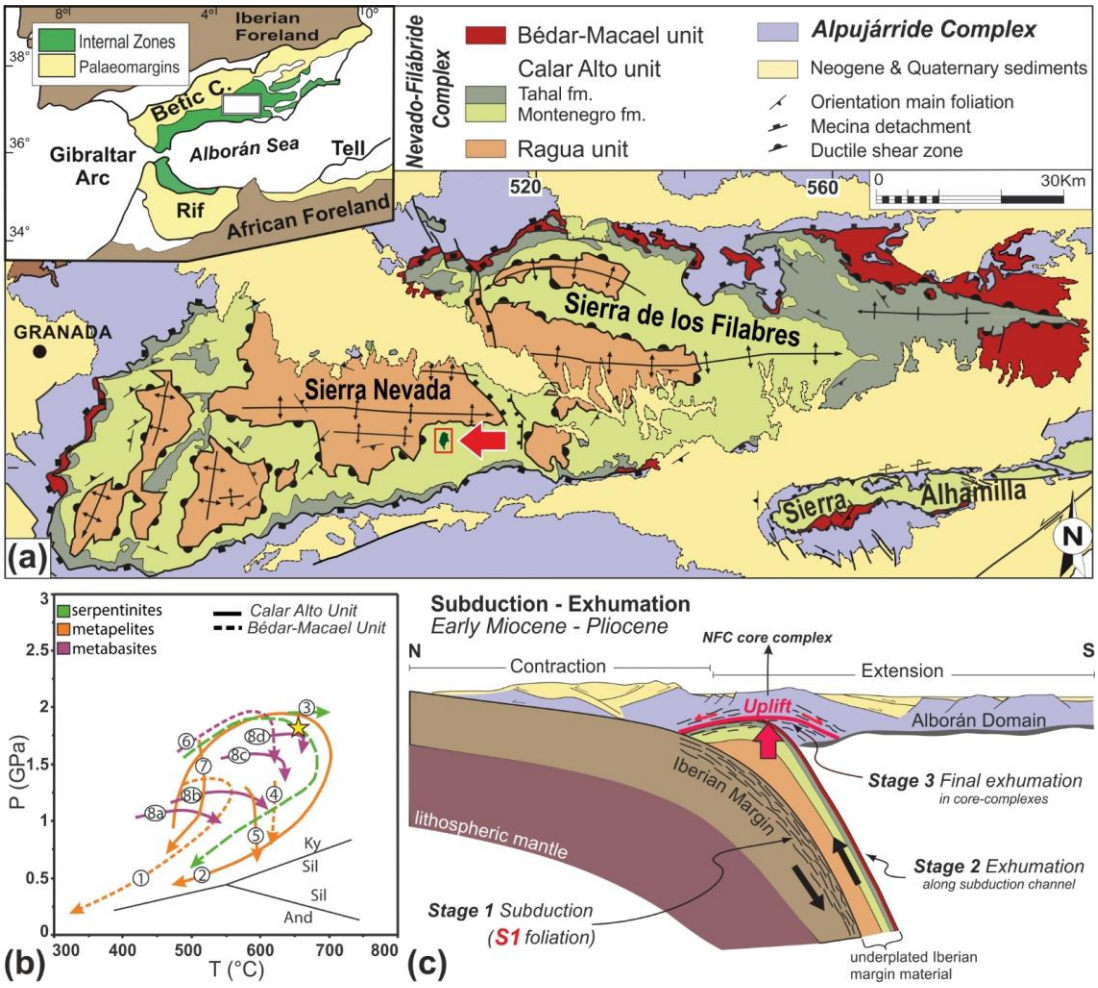

Figure 1.12. *(a) Geological map of the Nevado-Filábride complex (NFC) E–W domes (Sierra Nevada, Sierra de los Filabres and Sierra Alhamilla) in the central Betics (modified after Martínez-Martínez et al., 2002). The arrow shows the location of the Almirez massif. Upper left inset: main tectonic domains of the peri-Alborán orogenic system; the white square indicates the location of the NFC map shown in Fig. 1a; (b) Compilation of representative P-T metamorphic paths of different lithologies in the NFC grouped by units (modified from López Sánchez-Vizcaíno and Gómez-Pugnaire, in press): (1) Behr and Platt (2012, 2013); (2) Gómez-Pugnaire et al. (1994); (3) López Sánchez-Vizcaíno et al. (2009) and Padrón Navarta et al. (2010a); (4-6) Augier et al. 2005; (7) Jabaloy-Sánchez et al. (2015); (8 a–d) P-T-t paths of four eclogites from Platt et al. (2006). Also shown is the P-T-t path of the Almirez massif (dashed green line) and the peak metamorphic conditions (yellow star) of the dehydration of Atg-serpentinite in this massif (after Jabaloy-Sánchez et al., 2015). (c) Tectonic model for the Alpine evolution of the NFC (after Behr and Platt, 2012). See text for further details.*

(Variscan) basement of the continental crust— and, to a minor extent, of metaserpentinites and metabasites (Gómez-Pugnaire et al., 2012 and references therein; Puga et al., 2011). From top to bottom, the NFC is structured in three main units: the Bédar-Macael, the Calar-Alto, and the Ragua units. The Almirez ultramafic massif (Figs. 1.13-14; Padrón-Navarta et al., 2010b; Trommsdorff et al., 1998) is the largest (c. 2.3 km^2) of several bodies of metaserpentinites and metabasites that occur in shear zones in the uppermost two units of this complex. The stable isotope and trace element signatures of Almirez metaserpentinite, along with metarodingite boudins preserving seafloor metamorphic mineral parageneses, attest for a stage of seafloor serpentinization (Alt et al., 2012; Laborda-López et al., 2018; Marchesi et al., 2013; Puga et al., 1999, 2011). SHRIMP U-Pb ages of igneous zircon in metabasites and metaserpentinite-hosted metarodingites yield crystallization ages of c. 185 ± 3 Ma (Puga et al., 1999, 2011). These ages marked the Pangea break-up and earliest opening of the western branch of the Alpine Tethys Ocean (Puga et al., 2011). Whether the NFC metabasites and metaserpentinites were portions of a slow-oceanic spreading ridge or an ocean-continent transition with a narrow oceanic basin is uncertain and matter of some debate (Gómez-Pugnaire et al., 2000, 2012; Puga et al., 1999, 2011). The Iberian provenance of continental lithologies and the E-MORB signature of the metabasites (Gómez-Pugnaire et al., 2004, 2012) indicate that these rocks likely constituted the Jurassic magma-starved, hyperextended continental margin of S–SE Iberia with portions of exhumed mantle (Booth-Rea et al., 2015; Jabaloy-Sánchez et al., 2018). A narrow ocean basin likely separated the S–SE Iberia hyperextended continental margin from the easterly meso-Mediterranean terranes of the Alborán domain, which are currently exposed in the Alpujárride and Maláguide complexes of the Betics (Booth-Rea et al., 2007 and references therein).

Rocks of the NFC record high-P metamorphism with peak P–T conditions in the range of 1.5 ± 0.4 GPa and 550–650 ºC (Augier et al., 2005; Booth-Rea et al., 2005, 2015; Jabaloy-Sánchez et al., 2015; Puga et al., 1999). The structures and mineral assemblages of the NFC metaserpentinites and metabasites preserve a unique record of the prograde subduction stage, which was strongly overprinted in the NFC metasedimentary rocks during the exhumation stages (Fig. 1.12b). In the Almirez massif, the prograde peak subduction metamorphic conditions attained c. 1.6–1.9 GPa and 680–710 °C (Fig. 1.12b) leading to the dehydration of Atg-serpentinite into prograde metaperidotite (López

Sánchez-Vizcaíno et al., 2005; Padrón-Navarta et al., 2010a; Trommsdorff et al., 1998). SHRIMP U-Pb ages of zircon overgrowths, Lu-Hf garnet, and Rb-Sr multi-grain isochron ages yield early mid-Miocene (15–18 Ma) for the high-P metamorphism in the NFC (Gómez-Pugnaire et al., 2012; Kirchner et al., 2016; López Sánchez-Vizcaíno et al., 2001; Platt et al., 2006). In the Almirez massif, zircons with antigorite inclusions in a metapyroxenite layer unambiguously constrain the mid-Miocene age (15 ± 0.6 Ma) of the high-P Atg-serpentinite dehydration reaction to prograde Chl-harzburgite (López Sánchez-Vizcaíno et al., 2001).

There is a high amount of geochronological evidence that the high-P metamorphism of the NFC records the mid-Miocene subduction of the SE Iberian margin beneath the extended Alborán domain, during the westward rollback of the east-directed Alpine Tethys slab (Fig. 1.12c; Stage 1) (Behr and Platt, 2012, 2013; Booth-Rea et al., 2005, 2007, 2015; Gómez-Pugnaire et al., 2012). The petrological and geochemical evidence of oceanic seafloor alteration of Jurassic, hypabyssal metabasites and rodingites, and their E-MORB geochemical signature, unequivocally indicate the lower plate provenance of the NFC metaserpentinites and metabasites from the subducted Iberian ocean-continent transition. The upper plate mantle rocks of the Alborán domain —now exposed in Ronda peridotites in the western Alpujárride units of the Betics— show a radically different pre-Miocene tectono-metamorphic evolution with evidence of a Jurassic ultrahigh pressure subcontinental mantle provenance (e.g., Garrido et al., 2011; Hidas et al., 2013; Hidas et al., 2015; Lenoir et al., 2001; Précigout et al., 2013).

The exhumation of the NFC was synorogenic and occurred from the mid-Miocene to the Pliocene. The lower plate units of the NFC are now exhumed along E-W domal core complexes that are separated by detachment faults from the upper plate Alpujárride Complex (Fig. 1.12a) (Booth-Rea et al., 2005, 2015; Martínez-Martínez et al., 2002, 2006; Platt et al., 2013; and references therein). To account for the fast cooling and exhumation derived from zircon fission track data, Behr and Platt (2013) proposed a two-stage exhumation process for the NFC (Stages 2 and 3; Fig. 1.12c). A first stage (Stage 2; Fig. 1.12c) of fast exhumation from peak subduction conditions to mid-crustal levels occurred along a subduction channel in the top of the NFC subducting slab (Behr and Platt, 2013). A later stage (Stage 3; Fig. 1.12c) of slower exhumation and cooling took

place along low-angle detachment faults —rooted at the brittle-ductile transition— that formed the NFC core complexes (Behr and Platt, 2013; Platt et al., 2015).

1.4.2 The Almirez ultramafic massif

The ultramafic rocks of the Almirez appear on the top of the metasedimentary sequence of the Calar Alto Unit (Figs. 1.12-14). They crop out in a main body of ~2.3 km^2 at the Almirez peak (i.e. the *Almirez massif*) and in several smaller, discontinuous ultramafic bodies scattered west of the main outcrop (Fig. 1.13; Jabaloy-Sánchez et al., 2015 and references therein). They are overthrusted onto the schists of the Montenegro and Tahal Fms and occur with discontinuous, often brecciated, pale yellow to white marble bodies (Fig. 1.13), metarodingite boudins (i.e. metamorphosed mafic dykes; e.g. Laborda-López et al., 2018), clinopyroxenite layers, and dunitic pods (López Sánchez-Vizcaíno et al., 2001; Puga et al., 1999; Trommsdorff et al., 1998).

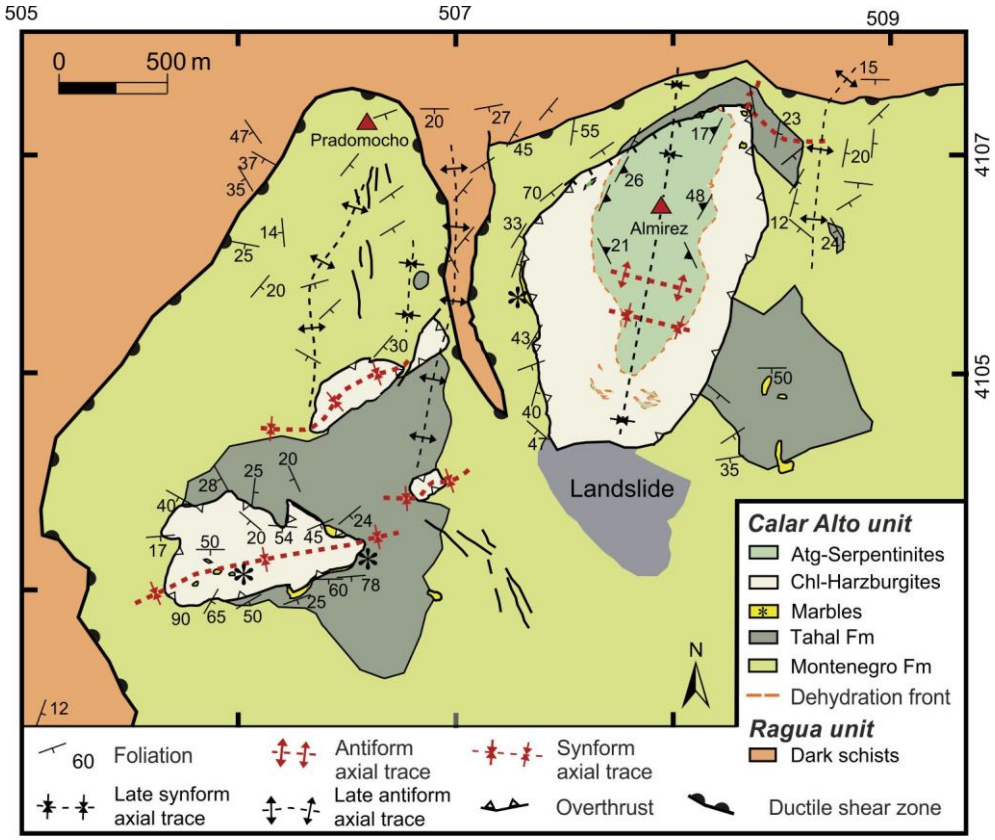

Figure 1.13. *The Almirez ultramafic massif with smaller ultramafic outcrops and other lithologies nearby. Structural elements and map modified after Jabaloy-Sánchez et al. (2015).*

Two main ultramafic lithologies occur at the Almirez massif: antigorite serpentinite (hereafter Atg-serpentinite) and chlorite harzburgite (hereafter Chl-harzburgite) separated by a meter-scale zone of transitional lithologies (Fig. 1.14b; Padrón-Navarta et al., 2011). This contact shows no evidence of a tectonic discontinuity (Trommsdorff et al., 1998) and has been interpreted as the arrested dehydration front of Atg-serpentinite producing Chl-harzburgite, that is, the Atg-out isograd (Padrón-Navarta et al., 2011). This unique front preservation has not yet been observed elsewhere, providing thus an exceptional natural laboratory for scientific research.

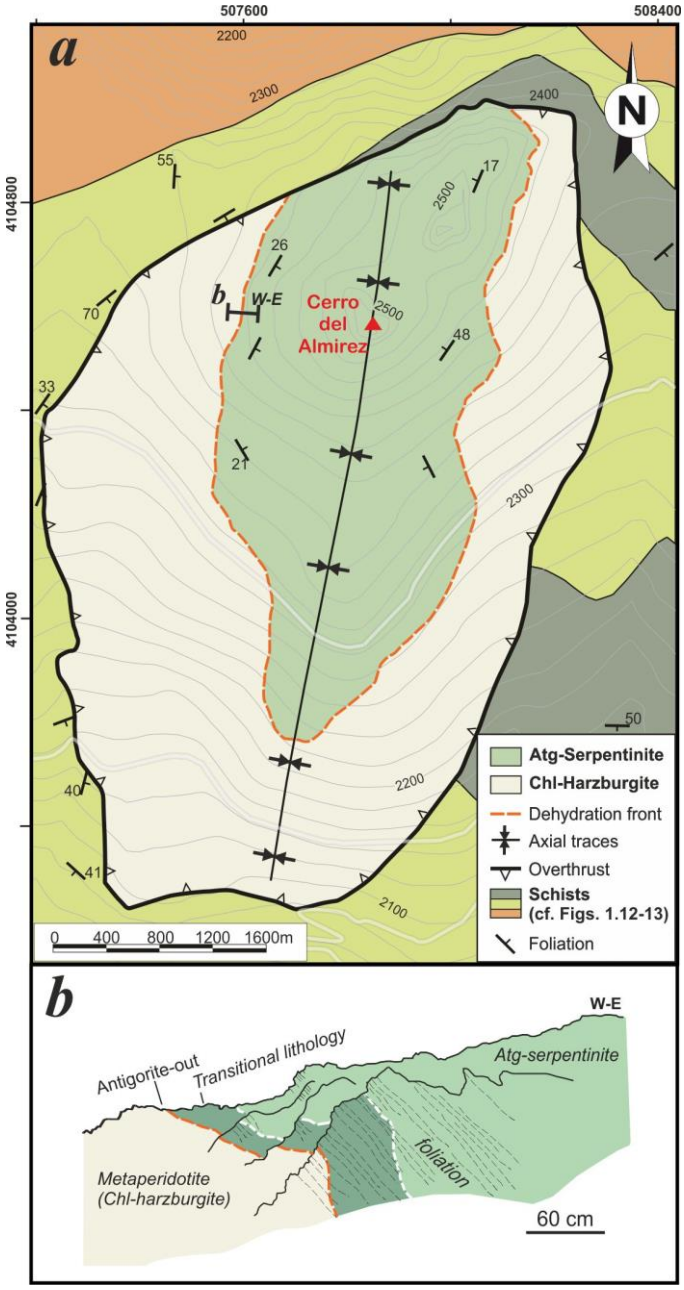

Figure 1.14. *(a) Zoom onto the geological map of the studied area in Fig. 1.12a, the Almirez massif (Nevado–Filábride Complex, Betic Cordillera, Spain), with the lithological description. (b) Cross section of outcrop to the west of the massif showing a transition from antigorite serpentinite into transitional lithologies into chlorite-harzburgite, modified from Padrón-Navarta et al. (2015). The antigorite-out isograd can be observed in this outcrop.*

1.4.2.1 Petrology

Atg-serpentinite (samples linked to green area in Fig. 1.15; *antigorite + olivine + chlorite + magnetite + ilmenite ± diopside ± tremolite ± titanian clinohumite*) appears in the upper part of the contact (Fig. 1.14a) as a strongly foliated sequence (c. 100 m thick) preserving a subduction-linked,

high-pressure, planar-linear fabric as well as evidences of several dehydration reactions during prograde metamorphism (Jabaloy-Sánchez et al., 2015; López Sánchez-Vizcaíno et al., 2005, 2009; Padrón-Navarta et al., 2008b, 2010a; Trommsdorff et al., 1998). The narrow band of transitional lithologies (Fig. 1.14b; samples linked to yellow area in Fig. 1.15) is oblique to the serpentinite foliation and changes down section from *chlorite-serpentinite* (Al10-09; Fig. 1.15) to an *antigorite-chlorite-orthopyroxene-olivine rock* (Al10-10; Fig. 1.15), and, finally to prograde Chl-harzburgite (samples linked to blue area in Fig. 1.15; *forsterite + enstatite + chlorite + magnetite + ilmenite ± tremolite ± titanian clinohumite*) according to the global reaction (Padrón-Navarta et al., 2011):

$$antigorite \rightarrow enstatite + olivine + chlorite + H_2O$$

This reaction matches with reaction (2a-c) in section *1.3.3* and would thus correspond to the main water releasing antigorite dehydration reaction (e.g. Bromiley and Pawley, 2003; Peacock, 1990; Ulmer and Trommsdorff, 1995; Wunder and Schreyer, 1997) in a relatively warm to hot subduction zone (profile II; Fig. 1.9a) (e.g. Hattori and Guillot, 2003).

Chl-harzburgite (c. 70-100 m thick) crops out in the lower part of the ultramafic body (Fig. 1.14a) (Padrón-Navarta et al., 2010b, 2011), in which two contrasting textures can be differentiated. Just beneath the reaction front, Chl-harzburgite shows everywhere a

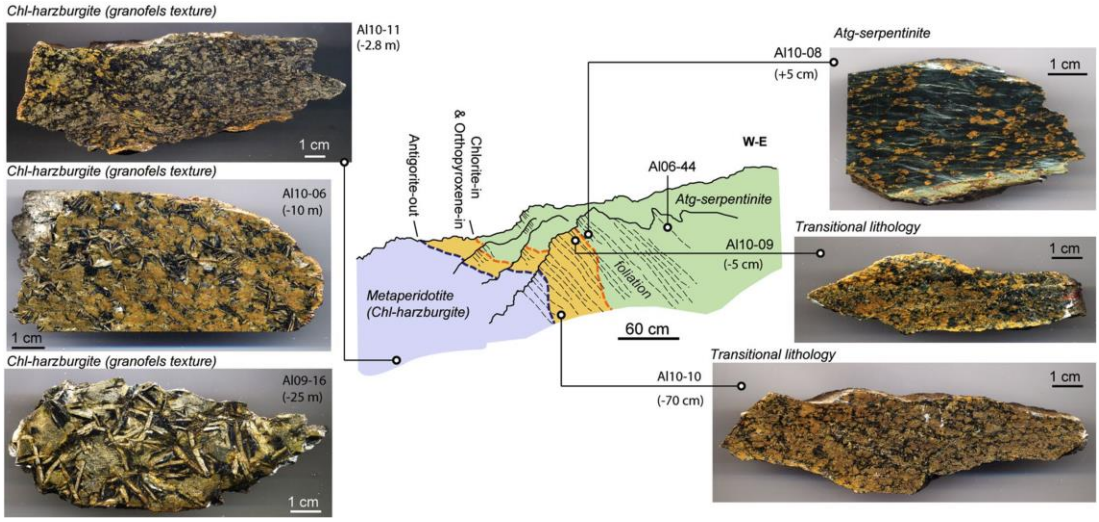

Figure 1.15. *Sketch of the Atg-out isograd as in Fig. 1.14b. Scans of hand samples are linked to their sampling location on this particular outcrop, except for samples Al10-06 and Al09-16, which were collected at c. 10 and 25 m from the isograd (after Padrón-Navarta et al. (2015)).*

granofelsic texture (Fig. 1.15); however, down section, it is interspersed in decameter-sized domains with spinifex-like Chl-harzburgite (Fig. 1.16a). The first textural name was used by Padrón-Navarta et al. (2011) according to the granofels definition of (Goldsmith, 1959), whereas the classification name spinifex-like (only spinifex in the following for the sake of simplicity) applies to the jackstraw cm-size elongated, radiating olivine and orthopyroxene, similar to those of spinifex textures in komatiites (Dickey, 1972; Trommsdorff et al., 1998). Both textural types of Chl-harzburgite are crosscut by grain size reduction zones (GSRZ), which can be a few mm to several m thick (Fig. 1.16b-c). The crack-seal infillings of the GSRZ with high P-T minerals —dominantly olivine, lower amounts of orthopyroxene (Padrón-Navarta et al., 2010b)— shows they must have formed during the peak metamorphic conditions of Chl-harzburgite formation.

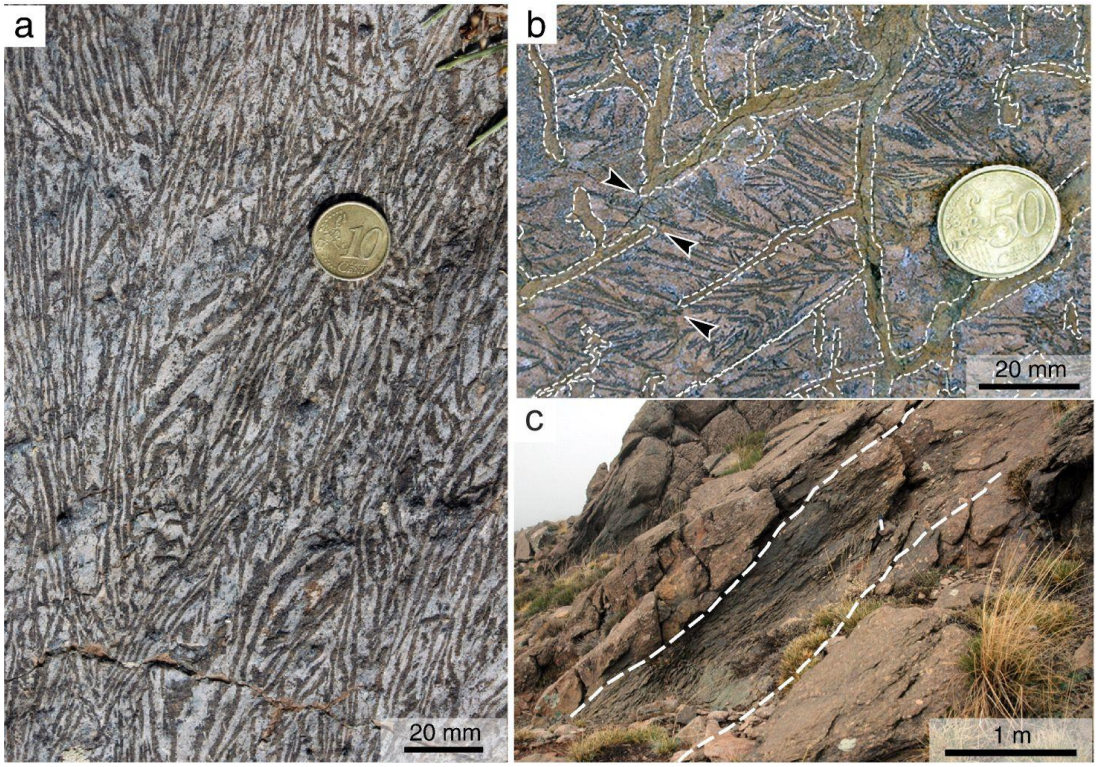

Figure 1.16. (a) *Field image of spinifex Chl–harzburgite with centimeter-size brown olivine (dark areas) in orthopyroxene-chlorite-talc matrix (light areas);* ***(b)*** *spinifex Chl-harzburgite crosscut by grain size reduction zones (GSRZ)(contoured by dashed white lines).* ***(c)*** *Sketch of main orientations of GSRZ planes and orientation of the elongation direction of spinifex olivine grains.* ***(d)*** *Large scale GSRZ (meter size) on an outcrop. (After Padrón-Navarta et al. (2010b)).*

1.4.2.2 Sequence of subduction-related structures and constraints on the geometry of the slab[2]

Ultramafic rocks from the Nevado-Filábride Complex preserve structures and assemblages of the oceanic stage and prograde metamorphic evolution during the mid-Miocene subduction of the Iberian margin (Fig. 1.12b; Jabaloy-Sánchez et al., 2015; Laborda-López et al., 2018; López Sánchez-Vizcaíno and Gómez-Pugnaire, in press; Puga et al., 2009, 2011). Previous works have thoroughly documented the subduction-related structures in the Almirez ultramafic massif (Jabaloy-Sánchez et al., 2015; Padrón-Navarta et al., 2010a, 2011, 2015; Trommsdorff et al., 1998). The pseudosection in Figure 1.17 shows the P-T-t path and the relative timing of mineral parageneses and structures formed during the prograde subduction path of the Almirez serpentinites up to peak metamorphic conditions (c. 1.6–1.9 GPa and 680–710 °C). A block diagram with the present-day orientation of the lithological sequence and these structures is shown in Figure 1.18. The upper part shows the foliated Atg-serpentinite (c. 100 m) overlaying the coarse-grained, unfoliated Chl-harzburgite (c. 70–100 m) (Fig. 1.14a). The transition from Atg-serpentinite to Chl-harzburgite is marked as the Atg-out isograd by the progressive disappearance of antigorite (Figs. 1.14b, 1.17 and 1.18) (Padrón-Navarta et al., 2011; Trommsdorff et al., 1998). Previous studies in the Almirez massif have inferred the following sequence of structures, assemblages, and fluid-release events during the subduction metamorphism of Atg-serpentinite and its dehydration to Chl-harzburgite:

(i) The earliest subduction structure preserved in the massif is the S1 foliation of Atg-serpentinite that formed along the prograde P-T-t path (Fig. 1.17; S1 path). This path is similar to that predicted by thermo-mechanical models in the mantle section of hot subducting zones (HSZ in Fig. 1.17). The S1 foliation is crosscut by en echelon veins of olivine and Ti-clinohumite formed at c. 1.3 GPa and c. 475 °C during the prograde dehydration of brucite (point I in Fig. 1.17) (López Sánchez-Vizcaíno et al., 2005; 2009). Similar veins and structural relationships with the prograde Atg-

[2] This section has been published within the Discussion of Dilissen, N., Hidas, K., Garrido, C.J., Kahl, W.-A., López Sánchez-Vizcaíno, V., Padrón-Navarta, J.A., 2018. Textural evolution during high-pressure dehydration of serpentinite to peridotite and its relation to stress orientations and kinematics of subducting slabs: Insights from the Almirez ultramafic massif. Lithos 320-321, 470-489.

serpentinite foliation are documented in subducted serpentinites from exhumed metamorphic terranes elsewhere (Hermann et al., 2000; Scambelluri et al., 1991). Further down section, near the Atg-out isograd (Fig. 1.18), large antigorite ± chlorite porphyroblasts —formed by fluid-assisted dissolution-precipitation of fine-grained oriented antigorite (Padrón-Navarta et al., 2008b)— overgrew the Atg-serpentinite S1 foliation (path II in Fig. 1.17). The high-Al content of antigorite conditions and pervasive evidence of dissolution-precipitation indicates a fluid-rich environment near the Atg-out isograd (Padrón-Navarta et al., 2008b; 2010b; 2013).

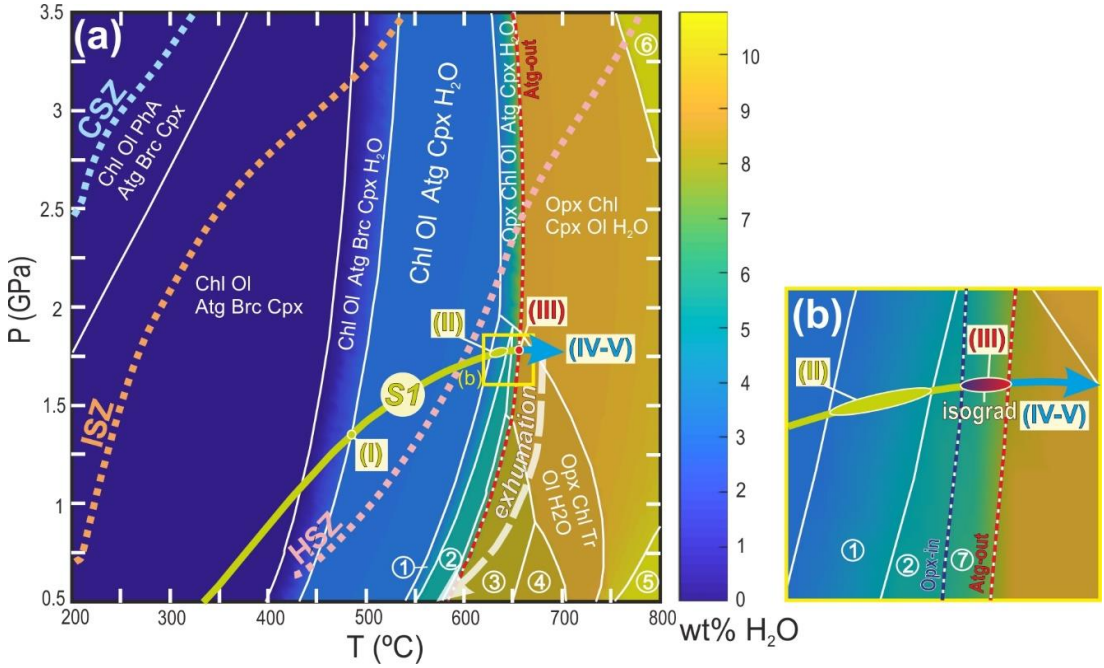

Figure 1.17. *(a) Phase diagram pseudosection showing prograde metamorphic reactions in a typical serpentinite from the Almirez massif. Colored contours are variations in H_2O content (wt%). Thick dotted lines are the P-T paths of a slab in cold (dotted light blue; CSZ), intermediate (light orange; ISZ) and hot (light rose; HSZ) subduction zones (after van Keken et al., 2011). The red and white dotted line marks the Atg-breakdown (Atg-out) reaction. Also shown in the figure the P-T-t path during the prograde subduction metamorphism (S1: light green and thick blue arrow) and exhumation (white dashed thick arrow) of the Almirez massif (after Laborda-López et al., 2018). The Roman numerals are the prograde reactions documented in the Almirez massif: (I) Brc breakdown; (II) overgrowth of Atg and Tr; (III) formation of Atg-Chl-Opx-Ol transitional lithologies; and Atg-breakdown; and (IV-V) formation of granofels and spinifex Chl-harzburgite and grain-size reduction zones (GSRZ). Phase assemblages in numbered pseudo-invariant fields are (1) Chl-Tr-Ol-Atg-Cpx-H_2O; (2) ChlTr-Ol-Atg-H_2O; (3) Chl-Tlc-Tr-Ol-H_2O; (4) Chl-Ath-Tr-Ol-H_2O; (5) Sap-Opx-Ol-H_2O; (6) Opx-Ol-Grt-H_2O; (7) Chl-Tr-Ol-Atg-Opx-H_2O. Mineral name abbreviations after Whitney and Evans (2010). Calculations were made using the Perple_X software (Connolly, 2009). (b) Enlarged section of the pseudosection shown in (a)(the enlarged area corresponds to the yellow rectangle) showing the P-T-t path of the Almirez massif near the Atg-out reaction with Opx-in and Atg-out over the full range of the isograd.*

(ii) At the Atg-out isograd (Figs. 1.14b and 1.18), the Atg-serpentinite S1 foliation is overprinted by the narrow band of weakly foliated Chl-serpentinite and unfoliated Atg-Chl-Opx-Ol rocks, which mark the first appearance of orthopyroxene (Opx-in, path III in Fig. 1.17b). These transitional lithologies formed by the series of continuous metamorphic reactions (cf. reaction (2a-c) in section 1.3.3) that resulted in the dehydration of Atg-serpentinite to prograde Chl-harzburgite at c. 1.6–1.9 GPa and c. 650 ºC (path III to IV-V in Fig. 1.17) (Padrón-Navarta et al., 2011). Path III in Figure 1.17b shows the onset of high-P dehydration of Atg-serpentinite, which ends at the Atg-out conditions with the Atg-out isograd. This isograd cuts at low angle the Atg-serpentinite S1 foliation that vanishes down section grading to coarse-grained, granofels Chl-harzburgite (Figs. 1.14b and 1.18). The dehydration of Atg-serpentinite to Chl-harzburgite released up to 9 wt% of water (Fig. 1.17).

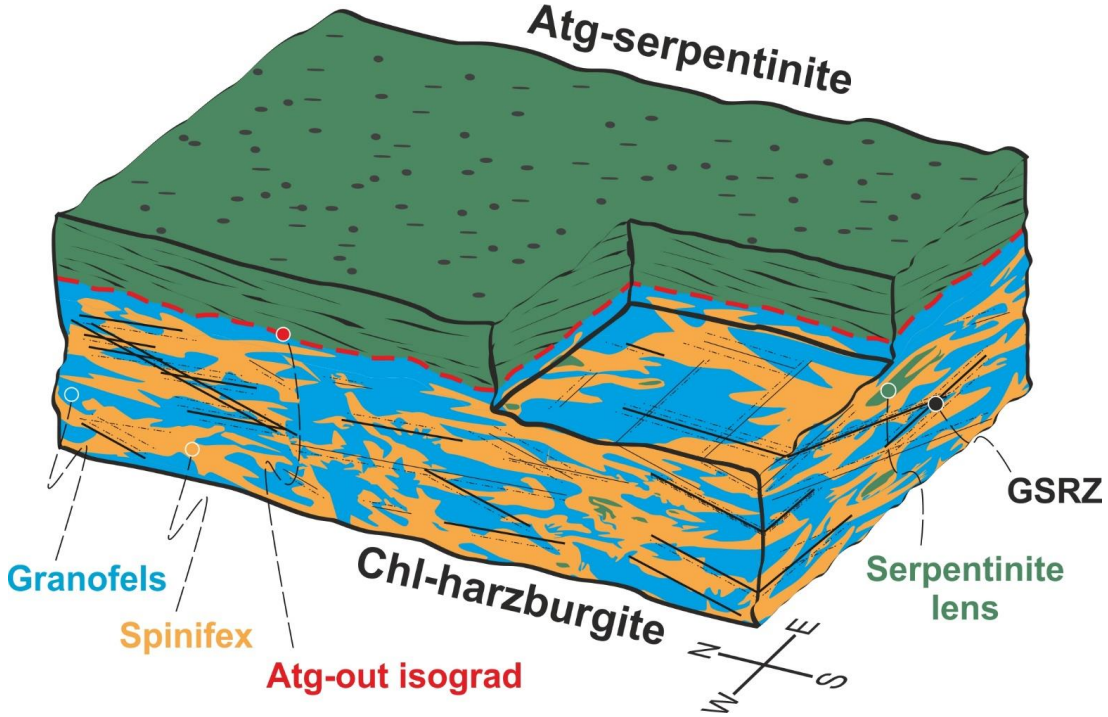

Figure 1.18. *3-D sketch summarizing the main structures of the Atg-serpentinite (upper part) and Chl-harzburgite (lower part) sequences in the Almirez massif in present-day geographical orientation. The dashed red line is the Atg-out isograd. Atg-serpentinite: elongated solid lines are the trace of Atg-serpentinite foliation; rounded and elongated patches show the oxide microstructure and the oxide aggregates elongation lineation. Chl-harzburgite: different colors show lenses of granofels (blue) and spinifex (orange) Chl-harzburgite. Solid and dashed black lines indicate the two main sets of grain size reduction zones (GSRZ) that crosscut the Chl-harzburgite sequence.*

(iii) Further below the Atg-out isograd, granofels Chl-harzburgite is interspersed in decametric lenses with spinifex Chl-harzburgite (Fig. 1.18). Occasionally, intercalated lenses of metastable foliated serpentinites also occur in the Chl-harzburgite section. Chl-harzburgites formed at peak metamorphic conditions (path IV-V in Fig. 1.17). Padrón-Navarta et al. (2011) ascribed the differing textures of Chl-harzburgite to shifts in the nucleation and growth rate of the Atg-serpentinite dehydration products. They interpreted these events as due to spatial fluctuations in the affinity of the antigorite-breakdown reaction driven by cyclic variations of the pore-fluid pressure. The granofels and spinifex textures were formed, respectively, during events of slow and fast draining of fluids produced by the dehydration of Atg-serpentinite (Padrón-Navarta et al., 2011).

(iv) The grain-size reduction zones (GSRZ) —few mm to meters wide— that locally crosscut granofels and spinifex Chl-harzburgites occur as planar conjugate planes and vanish at the Atg-out isograd (Fig. 1.18) (Jabaloy-Sánchez et al., 2015; Padrón-Navarta et al., 2010b). Phase diagram and mineral composition —mainly olivine and minor orthopyroxene and chlorite— constraints indicate they formed at peak P–T similar to those of surrounding Chl-harzburgite (point V in Fig. 1.17) (Padrón-Navarta et al., 2010b). Field and microstructural observations exclude any relative displacement across GSRZ (Fig. 1.16b). Their olivine microstructure reveals they formed by micro-cracking induced by rock hydrofracturing under high pore-fluid pressures (Padrón-Navarta et al., 2010b, 2011). GSRZ are interpreted as high-permeability fluid flow pathways of Atg-dehydration fluids through the brittle prograde Chl-harzburgites (Padrón-Navarta et al., 2010b).

Due to the polyphase exhumation of the Almirez massif (Fig. 1.12c), the original orientation and kinematics of the Almirez prograde structures in the subducting NFC slab are unknown. Some inferences, however, can be made assuming that the S1 prograde foliation of the Almirez Atg-serpentinite was nearly parallel to the slab interface shear zone, as concluded in other subduction-related serpentinites and supported by experimental work (e.g., Amiguet et al., 2014; Auzende et al., 2015; Hermann et al., 2000; and references therein). Thermo-mechanical models of subduction predict that near the upper slab interface the Atg-out isograd is approximately subparallel to the movement of

the slab, while elsewhere it cuts the direction of slab motion at a high angle (Hacker et al., 2003; Peacock, 2001). In Almirez, the low angle between the Atg-serpentinite foliation and the Atg-out isograd indicates that the S1 was likely subparallel to the paleo-slab surface. The lower plate provenance of the Almirez serpentinites from the subducting NFC indicates that S1 formed by the slab-induced shear flow, and reflects the local kinematics of the subducting slab; the strong and penetrative mylonitic foliation of the Almirez Atg-serpentine is consistent with a position close to the subduction shear zone interface.

Another significant uncertainty in the interpretation of the Almirez subduction structures is the relative position of the Chl-harzburgites in the subducting slab. In particular, whether they were located downward or upward the Atg-out dehydration front. To account for the hot P-T-t path of NFC rocks (Fig. 1.12b), Behr and Platt (2013) suggested that the NFC slab was mostly heated from above beneath the extended Alborán Domain, and cooled from below by continuing subduction (Fig. 1.12c). If so, it would be expected that enhanced heat flow came from the upper plate, and the Chl-harzburgite formed upwards the Atg-out isograd facing the Alborán domain upper plate. This geometry is the inverse of the present-day structure of the massif, where the Atg-serpentinite is on top of Chl-harzburgite (Fig. 1.18).

2 Aims and Thesis Outline

2.1 Motivation

My Ph.D. is part of the European Commission FP-7 Marie-Curie Initial Training Network (ITN) 'Zoom In between Plates' (ITN–ZIP). The motivation behind the ITN-ZIP is to investigate the nature of the plate interface in subduction zones through (i) determining the plate interface dimensions, geometry, and physical properties, (ii) modelling the time-integrated material fluxes, and (iii) constraining how rock rheology controls seismicity, mega-earthquake nucleation, and rupture propagation.

My Ph.D. Thesis research project is framed within the investigation of the time-integrated material fluxes and the relationships between dehydration metamorphic reactions, stress, and fluid flow to better understand fluxes of volatiles through the subduction interface by combining field, microstructural and geochemical data. In the framework of ITN-ZIP, my Ph.D. Thesis tackles the study of the mechanisms of serpentinite dehydration in subduction zones using field, microstructural, and petrological observations from the Almirez exhumed metamorphic terrane (Betic Cordillera, SE Spain). As outlined in Ch. 1, dehydration of Atg-serpentinite constitutes one of the main metamorphic dehydration reactions involved in the deep budget and transfer of volatiles in subduction zones. Exhumed metamorphic terranes in paleo-subduction zones offer a unique opportunity to investigate the dynamics of metamorphic dehydration reactions in rocks from well-exposed outcrops. Because it preserves the frozen Atg-out reaction at P–T conditions relevant for hot subduction zones, the Almirez ultramafic massif (cf. Ch. 1) is a unique outcrop worldwide to investigate the high-P dehydration of Atg-serpentinite.

2.2 Aims of the thesis

Previous studies in the Almirez massif (cf. Ch. 1) have investigated different aspects of Atg-serpentinite encompassing, among others, the deformation mechanisms of antigorite serpentinite processes involved in the metamorphic crystallization of granofels Chl-harzburgite, the P-T conditions of deformation and geochemical mass balances. Building upon previous field, petrological and geochemical studies of the Almirez massif

(cf. Ch. 1), the present Ph.D. Thesis is aiming to provide new insights into the dynamics and mechanisms of Atg-serpentinite dehydration as recorded in this massif. To attain this goal, in this Ph.D. Thesis I will:

i. constrain the episodic nature of fluid release during high-P Atg-serpentinite dehydration, and unveil the physical mechanism behind this process.
ii. investigate the dynamics of Atg-serpentinite dehydration and its relation to the orientation of stresses and the kinematics of the subducting slabs.
iii. unveil the role of kinetic and fluid dynamics in the dehydration of Atg-serpentinite.

To accomplish these goals, I have combined field, textural, petrological and geochemical studies at different length scales in the Almirez massif:

i. To address the first goal, I have carried out a detailed field study at the massif scale to characterize the length-scale and spatial distribution of the two main textural types of Chl-harzburgite reaction products. I will show how different parameters can be used to unveil the episodic nature and physical mechanism during Atg-serpentinite dehydration and the associated time scale and water fluxes.

ii. To investigate the dynamics of Atg-serpentinite dehydration and its relation to the orientation of stresses and the kinematics of the subducting slabs, I present a correlative X-ray and micro-computed tomography (μ-CT) and Electron Backscatter Diffraction (EBSD) study of geographically oriented samples across the Atg-serpentinite dehydration isograd in the western section of this massif. These data provide, in a common geographical reference frame, a detailed account of the evolution of the Shape Preferred Orientation (SPO) of oxides and olivine, and the Crystal Preferred Orientation (CPO) of antigorite, olivine, and orthopyroxene during high-P dehydration of Atg-serpentinite to peridotite. These data are combined with structural observations to investigate the textural evolution during prograde Atg-serpentinite dehydration to peridotite and its links with the orientation of the paleo-stresses and the kinematics in the subducting slab.

iii. To address the third and final goal, I have investigated a unique textural record of morphological transition in Almirez Chl-harzburgite olivine porphyroblasts formed during prograde high-pressure dehydration of Atg-serpentinite. Previous studies in this massif have reported Chl-harzburgite with granofels and spinifex textures displaying, respectively, anhedral rounded and subhedral tabular olivine morphologies (Padrón-Navarta et al., 2011). These different textural types were ascribed to metamorphic olivine growth at different affinity of the dehydration of Atg-serpentinite to Chl-harzburgite reaction (Padrón-Navarta et al., 2011). I report a new textural variety of Chl-harzburgite in this massif (hereafter, referred to as transitional Chl-harzburgite) containing varied-textured olivines and composite olivine porphyroblasts displaying morphologies transitional between those of the granofels and spinifex textural types. Based on a detailed chemical —EPMA and LA-ICP-MS— and microstructural characterization —combining correlative μ-CT and EBSD-SEM microscopy— of the transitional Chl-harzburgite olivine, I discuss the different factors that induced this unusual morphological transition during olivine growth, and I relate them to possible variations of physicochemical environmental conditions in subduction zones.

An ancillary goal of my thesis has been developing a new methodology to reconstruct the 3-D microstructure of centimeter-sized olivine crystals in rocks from the Almirez ultramafic massif by using combined μ-CT and EBSD. The semi-destructive sample treatment involves geographically oriented drill pressing of rocks and preparation of oriented thin sections from cores previously scanned by μ-CT. I demonstrate that the limitations of both methods (i.e., no crystal orientation data in μ-CT and no spatial information in EBSD) can be overcome by this new approach, and the 3-D orientation of the crystallographic axes of olivines from different orientation groups can be successfully correlated with the crystal shapes of olivine grains. I will use this innovative technique to establish the link among geological structures and 3-D SPO-CPO rock fabric, which are fundamental to address the aims (ii) and (iii) of the thesis.

2.3 Structure of the thesis

The thesis is divided into three main parts. **Part I** includes the introduction to the subject (**Ch. 1**), and the motivation, aims and structure of the thesis (**Ch. 2**). In **Chapter 3**, I describe the novel methodology we have developed to integrate μ-CT and EBSD data for the 3-D characterization of the microstructure of prograde peridotites. This technique has been published in *Journal of Microscopy*[1], a journal indexed in the Journal of Citation Report (JCR). For consistency, other routine and specific methodological aspects of the thesis are presented together with the main results of the thesis in Part II.

Part II presents the results of the thesis. **Chapter 4** discusses the first aim of the thesis; it presents the results of a detailed field study aimed at understanding the mechanisms of fluid expulsion during high-pressure Atg-serpentinite dehydration. **Chapter 5** investigates the mechanisms of metamorphic crystallization of prograde Chl-harzburgite and its relation to the dynamics and the orientation of stresses in subducting slabs, as recorded in the microstructure (SPO and CPO) of Atg-serpentinite and Chl-harzburgite in the Almirez massif. The results of this study have been published in the JCR journal *Lithos*[2]. **Chapter 6** addresses the third aim of the thesis by investigating the morphological transition during prograde olivine growth during Atg-serpentinite dehydration. Through correlative X-ray μ-CT and EBSD, and mineral geochemistry in a varied-textured Chl-harzburgite, I examine the role of reaction affinity, stress, and surfactants in shaping the morphology of growing crystals during dehydration of Atg-serpentinite to Chl-harzburgite. This chapter is currently under revision in the JCR journal *Lithos*[3]. Finally, **Chapter 7** presents the main conclusions of my thesis. The references cited throughout the thesis are given in **Part III**.

[1] Kahl, W.A., **Dilissen, N.**, Hidas, K., Garrido, C.J., López Sánchez-Vizcaíno, V., Román-Alpiste, M.J., 2017. 3-D microstructure of olivine in complex geological materials reconstructed by correlative X-ray μ-CT and EBSD analyses. *Journal of Microscopy* 268, 193-207.

[2] **Dilissen, N.**, Hidas, K., Garrido, C.J., Kahl, W.-A., López Sánchez-Vizcaíno, V., Padrón-Navarta, J.A., 2018. Textural evolution during high-pressure dehydration of serpentinite to peridotite and its relation to stress orientations and kinematics of subducting slabs: Insights from the Almirez ultramafic massif. *Lithos* 320-321, 470-489.

[3] **Dilissen, N.**, Hidas, K., Garrido, C.J., López Sánchez-Vizcaíno, V., Kahl, W.-A. (submitted). Morphological transition during prograde olivine growth formed by high-pressure dehydration of antigorite-serpentinite to chlorite-harzburgite in a subduction setting. Lithos.

In addition to the above-cited papers, the results of this thesis have been presented in several international conferences and meetings, including several European Geoscience Union General Assemblies (2014–2018) (Vienna, Austria); the American Geoscience Union Fall 2015 meeting (San Francisco, USA), a talk at the SIP conference on Subduction Interface Processes in 2017 (Barcelona, Spain); 3 minute thesis (3MT) presentation at the Abyss Meeting in 2017 (Granada, Spain); COST-Flows Meeting in 2017 (Granada, Spain); and at the seminars of the GFD (Geophysical Fluid Dynamics) group at the ETH in 2016 (Zürich, Switzerland).

Part II

RESULTS

3 Methodology: 3-D Microstructure of Olivine in Complex Geological Materials reconstructed by Correlative X–ray µ–CT and EBSD Analyses[1]

3.1 Introduction

The quantification of rock microstructure in terms of growth relations, volumetric abundance, grain size, crystallographic and shape orientation of minerals is of paramount importance in geosciences for the better understanding of petrological, geochemical and tectonic processes. Traditional microstructural analyses in geological materials are based on data obtained from 2-D thin sections. However, due to the lack of information in the third dimension, the quantification of rock microstructure by extrapolation from thin sections is limited and must remain inferior to a true 3-D characterization (e.g., Baker et al., 2012; Berger et al., 2011; Exner, 2011; Jerram and Higgins, 2007 for a review).

For direct visualization of the internal structure of rocks in 3-D, the use of µ-CT has become increasingly popular in Earth sciences and fueled research in many fields (see review papers of Carlson, 2006; Cnudde and Boone, 2013; Ketcham and Carlson, 2001; Noiriel, 2015 and references therein). Both synchrotron- and laboratory-based µ-CT have been successfully used in the quantitative 3-D analyses of minerals and pores investigating the diagenesis of reservoir sandstone (e.g., Long et al., 2009; Louis et al., 2009; Noiriel et al., 2005; Remeysen and Swennen, 2008; Van Marcke et al., 2010), connectivity of porosity (e.g., Appoloni et al., 2002; Peng et al., 2012; Schmitt et al., 2016) and microfractures (e.g., Renard, 2012), in petrophysical studies (Dautriat et al., 2009; Louis et al., 2007), to establish the effects of the microfabric on mechanical and seismic properties (e.g., Kahl et al., 2013) and also on rock micro-cores from percolation experiments to parameterize coupled transport-reaction models (e.g., Flukiger and Bernard, 2009; Noiriel et al., 2009). Furthermore, µ-CT has been applied to study 3-D

[1] This chapter has been published in: Kahl, W.A., Dilissen, N., Hidas, K., Garrido, C.J., López Sánchez-Vizcaíno, V., Román-Alpiste, M.J., 2017. 3-D microstructure of olivine in complex geological materials reconstructed by correlative X-ray µ-CT and EBSD analyses. Journal of Microscopy 268, 193-207

crystal size distribution of olivine populations in kimberlites (Jerram et al., 2009), magma mixing enhanced by bubble segregation (Wiesmaier et al., 2015), as well as fabric analysis in metamorphic rocks (Sayab et al., 2015) and meteorites (Uesugi et al., 2010). The ability to characterize the true 3-D spatial arrangement of fabric compounds in the rock enables µ-CT to deliver directional data, such as orientation of grains or grain contacts (Ketcham, 2005), shape preferred orientation (SPO) of crystals and vesicles in volcanic rocks (e.g., Voltolini et al., 2011; Vonlanthen et al., 2015), or SPO of ore-minerals in orogenic gold deposits (Sayab et al., 2016). The success of these applications, however, highly depends on the ability to separate the features of interest from the rock matrix due to the nature of physical processes responsible for X-ray absorption (e.g., Ketcham and Carlson, 2001; Van Grieken and Markowicz, 2001). Challenges may arise in high-density geomaterials hosting coarse-grained minerals with similar attenuating coefficients, which limits the sample size for a meaningful µ-CT analysis. Moreover, the major drawback of µ-CT in microstructural studies is the lack of information on the crystallographic orientation of the crystalline phases.

Quantitative information on the crystal preferred orientation (CPO) of the constituent mineral phases can be obtained by electron backscatter diffraction (EBSD) in the scanning electron microscope (SEM). This technique adequately characterizes the phases and the microstructure in 2-D even in complicated minerals such as antigorite (e.g., Padrón-Navarta et al., 2012; Van de Moortèle et al., 2010), gypsum (e.g., Hildyard et al., 2009), or ice (e.g., Chauve et al., 2017; Hidas et al., 2017; Piazolo et al., 2008; Prior et al., 2015). Nevertheless, grain size, shape and SPO determined in thin sections require stereological methods to translate 2-D information into 3-D (e.g., Higgins, 2006 and references therein). These stereological conversions are, however, only applicable to known, regular crystal shapes (e.g., Jerram and Higgins, 2007), hence they are impeded in anisotropic textures.

Advances in automated destructive serial-sectioning techniques, including robot-assisted grinding and polishing (Spowart, 2006; Uchic et al., 2012), femtosecond laser ablation (Echlin et al., 2014) or tomography in dual-beam focused ion beam (FIB) microscope (e.g., Saowadee et al., 2013; West and Thomson, 2009; Zaefferer et al., 2008) aim at overcoming these issues for certain applications in materials sciences. In fact, the FIB-assisted 3-D EBSD is a powerful tool in the characterization of strain, morphology

and crystallographic relationships between phases or inclusions, within grains and at grain boundaries (e.g., Bastos et al., 2008; Calcagnotto et al., 2010). However, routine 3-D FIB-EBSD is difficult to apply on low-conductive Earth materials, and the maximum observable volume is currently up to about 10^6 µm^3 (Burnett et al., 2016 and references therein), which is at least six orders of magnitude smaller than that required for the characterization of the microstructure of natural rocks composed of cm- to mm-sized crystals. To acquire mineral CPO with information on the 3-D SPO in larger samples, high-energy synchrotron X-rays and neutron diffraction were applied in shale and schist (Wenk et al., 2010), as well as in fragments of mylonitized metagranites (Zucali et al., 2014) up to *ca.* 0.25 cm^3 in size. Although this sample volume is representative for the very fine-grained rocks subject of those studies, it is still not adequate for plutonic or metamorphic rocks with coarser grain sizes. Moreover, in these techniques the spatial control is limited, and synchrotron light source and neutron diffraction are barely available for routine analytical work.

In contrast, combined µ-CT and SEM-EBSD has been successfully applied to investigate growth mechanisms and mineral replacement microstructures in 3-D (e.g., Plümper et al., 2012; Robyr et al., 2007), demonstrating the potential of this technique in Earth sciences applications. This methodology section presents a semi-destructive approach to combine laboratory-based µ-CT and SEM-EBSD and provides representative 3-D microstructural data for a challenging set of high-density (*c.* 3.3 g/cm^3) rocks which are composed of up to centimeter-scale crystals with similar mass densities. These rocks are rich in olivine, a mineral with orthorhombic symmetry that is the main component of the Earth's upper mantle (e.g., McDonough, 2001). This phase is present in the studied samples with two distinctly different crystal morphologies (Fig. 3.1), which in either case have been formed by the same dehydration reaction of serpentinites but under different physico-chemical conditions (e.g., Padrón-Navarta et al., 2011 and references therein). The main goal is to (1) filter large olivine crystals as grains and grain aggregates from the rock matrix in the µ-CT volume, (2) distinguish the two olivine varieties from each other for assigning SPO to both, and (3) render CPO data to the SPO for the volumetrically more dominant, highly anisotropic olivine textural variety in order to reconstruct its 3-D microstructure at the hand specimen scale (Fig. 3.2). This data is crucial for the better understanding of the formation of dehydration reaction products with

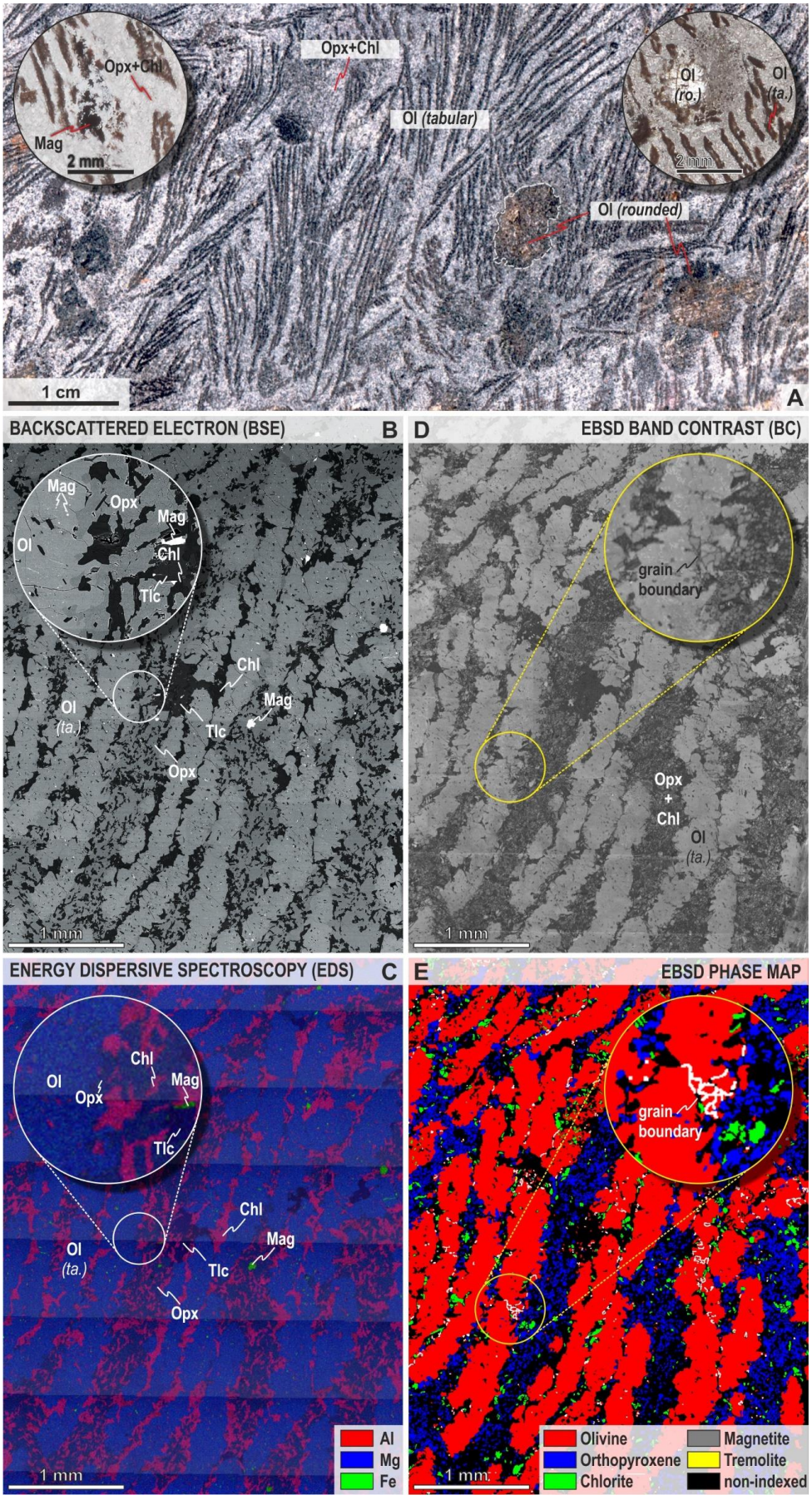
Opx+Chl
Mag
2 mm
Opx+Chl
Ol (tabular)
Ol (ro.)
Ol (ta.)
2 mm
Ol (rounded)
1 cm
A
BACKSCATTERED ELECTRON (BSE)
B
Mag
Opx
Mag
Ol
Chl
Tlc
Chl
Mag
Ol (ta.)
Tlc
Opx
1 mm
D
EBSD BAND CONTRAST (BC)
grain boundary
Opx + Chl
Ol (ta.)
1 mm
ENERGY DISPERSIVE SPECTROSCOPY (EDS)
C
Chl
Ol
Opx
Mag
Tlc
Chl
Mag
Ol (ta.)
Tlc
Opx
Al
Mg
Fe
1 mm
E
EBSD PHASE MAP
grain boundary
Olivine
Orthopyroxene
Chlorite
Magnetite
Tremolite
non-indexed
1 mm

respect to far-field stresses in subduction zones (Dilissen et al., 2018), but the presented methodology may be applicable to future studies addressing the 3-D microstructure of anisotropic minerals in any polyphase rock including, for example, flow processes in lavas, layered intrusions and reaction interfaces in 3-D.

3.2 Overview of methods

3.2.1 Sample preparation

Samples are geographically oriented and stem from the Chl-harzburgite domain of the Almirez ultramafic massif (e.g., López Sánchez-Vizcaíno et al., 2005; Padrón-Navarta et al., 2010, 2011; Trommsdorff et al., 1998). Figure 3.1 summarizes the coarse-grained (mm- to cm-sized) olivine-rich spinifex Chl-harzburgite as an example and shows the olivine (Ol; *ca.* 40 vol%) + orthopyroxene (Opx; *ca.* 40 vol%) + chlorite (Chl; <20 vol%) + magnetite (Mag; <5 vol%) ± ilmenite (Ilm; <5 vol%) ± tremolite (Tr; <1 vol%) ± Ti-clinohumite (Ti-Chu; <0.5 vol%) ± talc (Tlc; <0.5 vol%) minerals (Fig. 3.1a-e). spinifex Chl-harzburgite can be characterized by two strikingly different shaped olivines, which occur either as transparent, isometric crystals (hereafter referred to as *rounded*), or as brown, elongated grains materializing the spinifex-like microstructure (hereafter referred to as *tabular*) (Padrón-Navarta et al., 2011; Trommsdorff et al., 1998). The rounded olivines show major element chemical composition identical to the tabular ones and therefore a similar mass density (Padrón Navarta, 2010). The texture of the rocks selected for a detailed study is essentially dominated by tabular olivine crystals but it also contains

Figure 3.1. *(a) Spinifex texture of a Chl-harzburgite rock from the Almirez ultramafic massif; scanned images of a cut surface (sample AL14-11). Note the presence of granular olivine dispersed in the rock (one grain outlined with white dashed line). Insets show representative plane polarized light photomicrographs of highly attenuating opaque magnetite (Mag) with fine-grained orthopyroxene (Opx) and chlorite (Chl) on the left, and transparent granular olivine (Ol gr.) surrounded by brown spinifex olivine (Ol sp.) crystals on the right (thin section AL14-11V). Brown pleochroism in spinifex olivine is produced by oriented, submicroscopic inclusions of Fe-Cr-Ti-oxides (Ruiz Cruz et al., 1999) and by the products of destabilization of lamellar intergrowths of titanian clinohumite (López Sánchez-Vizcaíno et al., 2005); also see part b of the figure. (b-e) SEM backscattered electron image (b), SEM-EBSD energy dispersive spectroscopy image (c), SEM-EBSD band contrast image, and (d) SEM-EBSD phase map (e) showing the mineral composition and phase distribution in the thin section AL14-11V. Insets in (b-c) and (d-e) show the same area, respectively. Note that talc is a retrograde phase in the rocks. In (e) grain boundaries and non-indexed phases are black, except for olivine, where grain boundaries are highlighted in white. Phase boundaries and subgrain boundaries are not shown.*

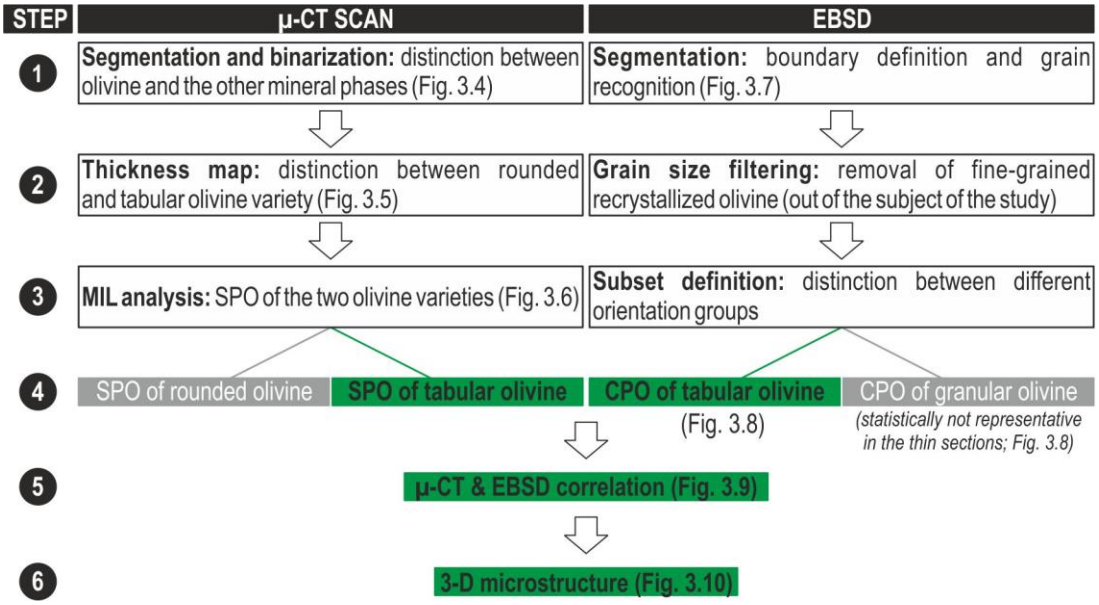

Figure 3.2. *Summary of the applied methodology. The main goals of this study are highlighted in green. Step 4 provides statistical analysis of SPO and CPO, whereas the exact 3-D microstructure can only be reconstructed in step 6, after the correlation of µ-CT and EBSD data.*

rounded olivine grains in variable amounts (Fig. 3.1a).

From the samples collected in the field oriented cylindrical cores were drill-pressed ca. 28 or 33 mm in diameter and ca. 30 mm in height (Fig. 3.3). The size of the cores was found as a compromise between the transmissivity of the core for low energy X-rays and the representativity of the sampled rock volume. Low energy X-rays are more distinctively absorbed by the rock's constituent minerals (which is favorable in terms of the contrast width of the reconstructed gray levels; e.g., Fig. 4 in Ketcham and Carlson, 2001), but they cannot pass large rock volumes. On the contrary, smaller volumes are not representative for the coarse-grained microstructure of the rocks (Fig. 3.1a-e). Beneficial for drill core sampling, the rotational-symmetric cylindrical shape of the micro cores is most suited for µ-CT investigations.

3.2.2 X-ray micro-computed tomography (µ-CT)

The X-ray µ-CT scans were performed using the ProCon CT-ALPHA system of the Petrology of the Ocean Crust research group at the University of Bremen, Germany. The cylindrical cores were mounted oriented with the top up and north towards the X-ray source and they were scanned with a beam energy of 130 kV, an energy flux of 350 µA,

and using a thin copper filter in 360° rotation scans conducted with a step size of 0.3° at a detector resolution of 16.26 µm per pixel. After an acquisition time between 4 and 5 hours, for each sample an image volume of 2000 × 2000 × 2000 voxels (or larger) was available. Correction of ring artifacts and reconstruction of the spatial information on the linear attenuation coefficient in the samples was done with the Fraunhofer software VOLEX, using a GPU-hosted modified Feldkamp algorithm based on filtered backprojection (Feldkamp et al., 1984). Subsequent filtering of the raw data, volume reconstruction, segmentation, and rendering were done using Avizo 9.2 (FEI). The software CTAn from Skyscan (now Bruker µ-CT) was used to perform analyses of mean intercept length on the segmentations of the different olivine growth types. Avizo was employed to measure SPO of magnetite and olivine single grains.

3.2.3 Thin section preparation

Following the µ-CT scanning, a thin section pair was prepared from each rock core (Fig. 3.3). The first thin section was prepared along a horizontal plane (looking downward) at least 8 mm from the top of the cylinder (hereafter referred to as horizontal section; sample label 'H'). The second thin section was prepared in the center of the core along a N-S vertical plane looking to the W (hereafter referred to as vertical section; sample label 'V') (Fig. 3.3). The position of the horizontal and vertical sections with respect to the edges of the cylinders was controlled by digital Vernier caliper measurements (estimated error <1 mm) and the volume loss due to cutting and grinding is <2 mm. After grinding the rock slices to a 100 µm thickness, the thin sections were polished using 3 µm and 1 µm Buehler diamond paste. Final surface for the EBSD analyses was achieved after 45 minutes chemical and mechanical polishing using Buehler colloidal silica suspension.

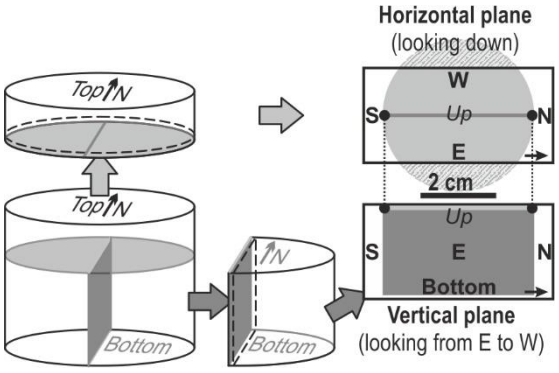

Figure 3.3. *Illustration of the preparation of oriented thin section pairs from the rock micro cores. The N-S centerline in the horizontal thin section and the upper edge of the vertical thin section contain the same grains (shown by black circles). The gap between the horizontal and vertical thin sections due to the material loss during cutting (<2 mm) is negligible with respect to the olivine grain size (cm-scale).*

3.2.4 Electron backscatter diffraction (EBSD)

The uncoated thin sections were mounted with conductive carbon tape to reduce charging, and analyses were carried out at high vacuum (in the range of 10-5 mbar) using a Zeiss EVO MA-15 SEM equipped with an Oxford Instruments Nordlys Nano EBSD detector at IACT (Armilla, Granada, Spain). Instrumental settings were 17 kV acceleration voltage, 24 mm working distance, and probe current of 0.5-1.0 nA. Acquisition conditions in the EBSD software (AZtec v3.1, Oxford Instruments) were 4×4 binning and low (0) gain with grid steps between 17 and 35 µm, covering most of the sample surface. All major constituent minerals of the rocks were included in the phase list and the percentage of indexed points in the raw maps always exceeded 75%. Due to polishing problems, chlorite had systematically low indexing rate in certain orientations, thus it could not be evaluated for CPO (Fig. 3.1d-e). Post-acquisition data treatment to clean raw maps by filling non-indexed pixels based on neighboring pixel orientation, as well as the removal of wild-spikes were carried out using the built-in functions of the Oxford/HKL Channel 5 software package following the method of Soustelle et al. (2010). Hereafter only the EBSD data is discussed of olivine using the cleaned datasets.

3.2.5 Plotting orientation data

For plotting CPO, the horizontal and vertical thin sections were rotated into a common geographic reference frame where north, east, south and west are at 0°, 90°, 180° and 270°, respectively. The SPO from µ-CT and the CPO from EBSD are plotted as lower hemisphere equal-area projection in the geographically referenced pole figures using in-software functions for µ-CT and the careware software package by David Mainprice for EBSD (http://www.gm.univ-montp2.fr/PERSO/mainprice/W_data/CareWare_Unicef_Programs/).

3.3 Results

3.3.1 Phase segmentation in µ-CT

In the reconstructed volume data, areas of highly attenuating phases (e.g., magnetite, olivine) are encoded in light gray values, whereas areas of low X-ray absorption are color-coded in dark gray (e.g., chlorite) or black (e.g., voids, cracks) (Fig. 3.4a). The

distribution of low density phases at the boundaries of olivine is critical for the success of segmentation (Fig. 3.1b-c). To reduce noise and enhance segmentability, a

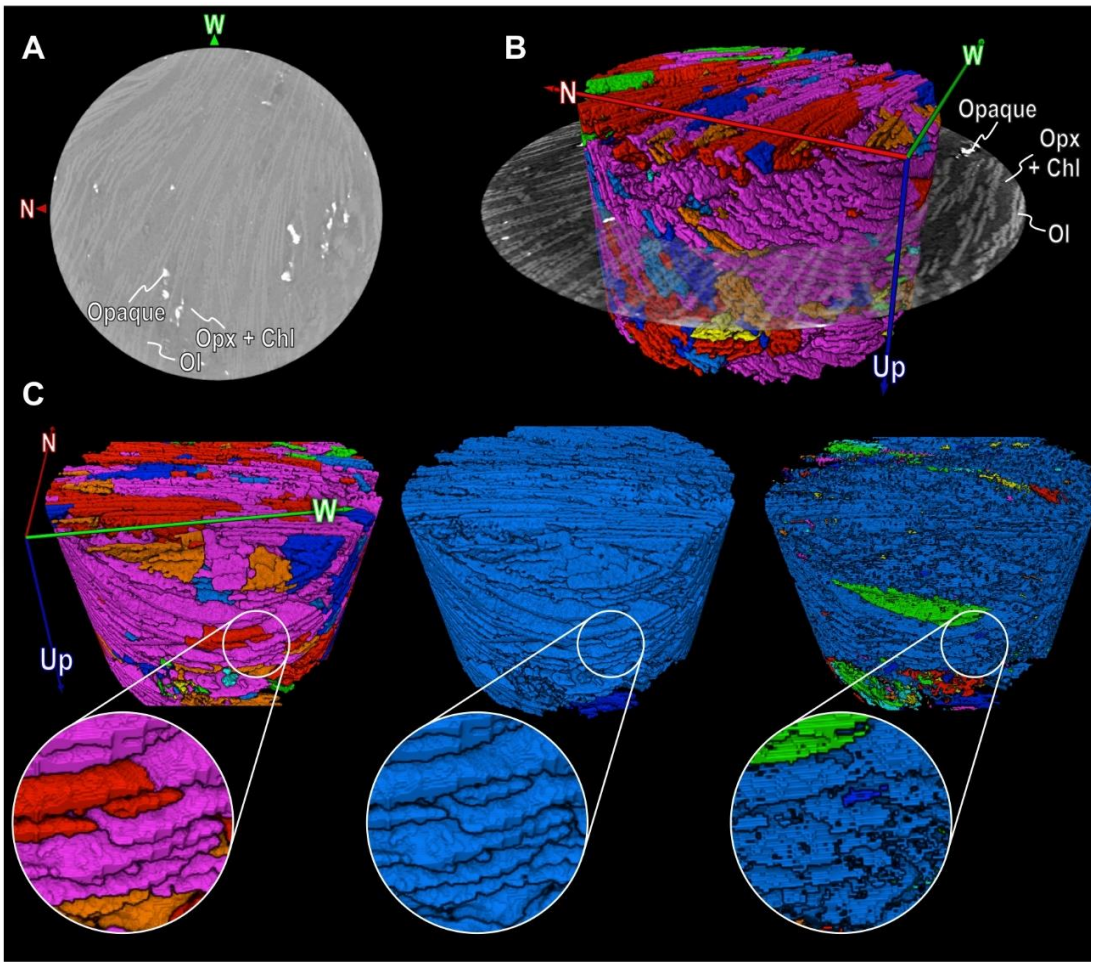

Figure 3.4. *Optimization of segmentation and feature extraction in the reconstructed µ-CT data volume in the sample AL14-11. Note that for the sake of better visibility the core is presented upside down, the volume is shrunk proportionally in (c) and has been rotated between the different subparts of the figure. The total width of the core is 33.4 mm. (a) Reconstructed image of the Chl-harzburgite exhibiting the tabular olivine fabric-type. Segmentability was enhanced by application of a composite filtering procedure (see text for details). Ol: olivine (light gray); Opx+Chl: fine-grained orthopyroxene- and chlorite-rich matrix (cf. Fig. 3.1b) with low X-ray absorption (dark gray); Opaque: highly attenuating phases, mostly magnetite and ilmenite (white). (b) Visualization of the outcome of an automated separation procedure applied to the binarized 3-D model of the segmented tabular grain framework to distinguish individual olivine crystals. Proper grain separation is impeded by the sub-parallel orientations of the bladed olivine grains. Also shown is a reconstructed slice (from the same level as in part a) modified by histogram normalization, which favors the segmentability of intermediate attenuating phases. Labeled phases are explained in (a). (c) Failed attempts to separate individual grains from the spinifex olivine network. Note that both automated, watershed-based procedure (left) and extensive morphological thinning operations (right) are unable to recognize individual grains in the initial segmentation of the tabular grain network (center). Insets show the close-up view of inseparable grain aggregates.*

combination of three digital image filters was applied to the reconstructed raw data (Fig. 3.4a). This filter composition technique consists of the arithmetic blending based on the local image gradient of an edge-preserving filter, and a strong uniform filter. Therefore, three different digital image filters were applied in each case to a separate instance of the reconstructed raw data: (i) a gradient image was computed using a Canny-Deriche 3-D type algorithm, (ii) limited edge smoothing was performed using an edge-preserving Bilateral filter (in 3-D-mode with a voxel window of 5), and (iii) a Gaussian filter (in 3-D-mode with a voxel window of 3 Px and deviation of 3.57 sigma) for strong smoothing, respectively. Subsequently, both the (ii) Bilateral and (iii) Gaussian-filtered data volumes were blended linearly using the normalized (i) gradient image (as float with a range from 0 to 1) following: (ii) × (i) + (iii) × [1.0 - (i)]. Thus, the resulting data volume generated by this filtering procedure comprises enhanced segmentability due to both preserved edges at the grain boundaries and, simultaneously, very homogenous grain centers due to strong smoothing of these uniform but former noisy areas. Eventually, a slight beam hardening was removed using the *Correct Background and Flat-Field* module to facilitate the segmentation of the rock's constituent fabric compounds by gray level thresholding.

Since each image consists of isometric voxels (volumetric pixels) and has a certain thickness depending on the detector resolution, a stack of images contains true volumetric information. Therefore, the segmentation of voxels into the different fabric components by assigning gray levels (which correspond to their different densities and elemental composition) is a crucial step to derive meaningful information on the rock fabric compounds. After filtering, the segmentation of both high (e.g., magnetite) and low (e.g., chlorite) attenuating phases is straightforward (Fig. 3.4a). After histogram normalization in favor of intermediate attenuating phases (Fig. 3.4b), olivine and orthopyroxene yielded distinctive gray values which correspond to their slightly differing attenuation (e.g., FeO^{ol}: *c.* 11 wt.% vs. FeO^{opx}: *c.* 7 wt.%; Padrón-Navarta, 2010a) (Fig. 3.4b-c). Therefore, olivine as a mineral became segmentable (Fig. 3.4b-c).

3.3.2 Feature extraction in µ-CT: separation of olivine fabric types

The automatic separation of individual olivine grains in the studied ultramafic rocks is hampered by two reasons: (1) olivine is present in two different fabric types (tabular and rounded, see sample Fig. 3.1); (2) due to the subparallel growth of the tabular grains, their

contact surface extends to almost half the length of adjacent grains, which then become inseparable (Fig. 3.4b-c). Neither morphological voxel operations (erosion or opening) nor common automated separation methods (e.g., watershed; Fig. 3.4c, to the left) succeed in individual grain separation in the samples due to the challenging determination of a "central axis" when thinning a tabular grain aggregate. From the binarized 3-D models of tabular olivine grain network (Fig. 3.4c, in the middle) even the extreme morphological thinning operations fail to recognize individual grains, yet destroy true spatial information (Fig. 3.4c, to the right). For an eventual manual refinement of olivine grains, the blow-tool was used of the Avizo Segmentation Editor parameterized with tolerance of 15.

In contrast to grain separation, the semi-automated distinction of tabular and rounded olivine types is possible using 3-D measurements of the local thickness of the olivine grain phase (module *Thickness-Map* in Avizo) (Fig. 3.5a). The local thickness at a given point in a structure is defined as the diameter of the largest sphere (sphere fitting, Hildebrand and Rüegsegger, 1997) which includes the point and which can be fitted completely inside the structure (*i.e.*, it would address the thickness of a pencil regardless of its length). The result of this method as color-coded representation of the structural thickness has been successfully thresholded to yield the distinct olivine fabric of tabular and rounded growth types (Fig. 3.5b-c).

3.3.3 Characterization olivine grain framework by mean intercept length analysis

Although the sub-parallel orientation of the tabular olivine impedes proper assignment of grain boundaries and, therefore, excludes assessment of SPO for individual crystals via inertia tensors, the SPO of the aggregate in its entirety can be determined by analysis of the mean intercept length (MIL) of the grain framework. This analysis measures the isotropy of a structure (Harrigan and Mann, 1984), and the reader is referred to consult Odgaard (1997) for a description and the Figure 4 of Kahl et al. (2013) for a conceptual sketch of the method. An ellipsoid fitted to the MIL data describes the 3-D shape of the MIL distribution. Considering that in the studied rocks rounded and tabular olivine are separable, this analysis provides the SPO of both grain frameworks based on the values and orientation of the shortest, intermediate and longest axis of the MIL fitted ellipsoid

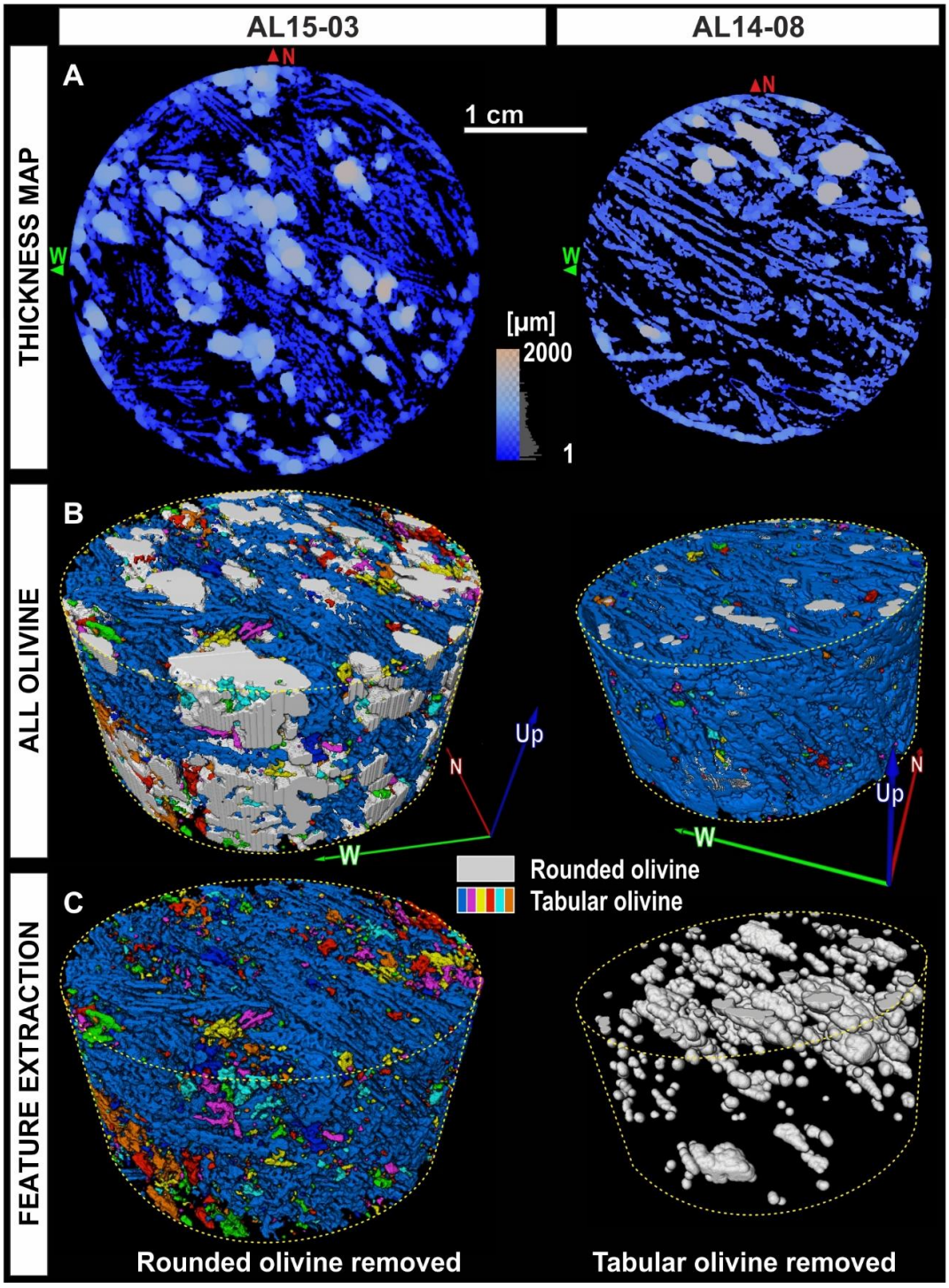

Figure 3.5. *Distinction of tabular and rounded fabric types by application of local thickness methods on the segmented olivine grain framework (samples AL15-03 and AL14-08). The same scale applies to the figure (scalebar is shown in a) but due to the perspective view it is correct only for the top of the core in b-c. (a) Local thickness map (i.e., a color-coded representation of the structural thickness) of one slice of the data volume. Units are in micron. (b) 3-D models of rounded (rendered white) and tabular olivine. Color-coding of the tabular olivine grains indicates separated crystal aggregates as a result of a conservative morphological thinning operation on the 3-D model of the grain framework. (C) Visualization of feature extraction by removing either the rounded (left) or the tabular (right) olivine crystals from the volumes reconstructed in b.*

(Fig. 3.6). To evaluate the quality and feasibility of olivine MIL data, in Figure 3.6 olivine SPO is compared to that of the highly attenuating magnetite in each sample. This mineral phase can unequivocally be segmented in the µ-CT data (Fig. 3.4a) and it is considered to denote a strong lineation in the Almirez ultramafic massif (e.g., Padrón-Navarta et al., 2015). The segmented highly attenuating phases were sent to a sieve analysis, where particles larger than 10^7 µm^3 with an aspect ratio of at least 5 were isolated in order to eliminate misleading effects of boudinaged or isometric grains. Selected grains that passed through the sieve fraction were plotted along the longest axis and SPO data were contoured in Figure 3.6.

The SPO of the rounded olivines closely aligns with that of the highly attenuating phases despite the different geographic directions (i.e., subhorizontal E-SE) recorded in the rock samples (Fig. 3.6). Comparison of the tabular and rounded olivine SPO reveals an approximate but not complete conformity of their largest MIL values (Fig. 3.6).

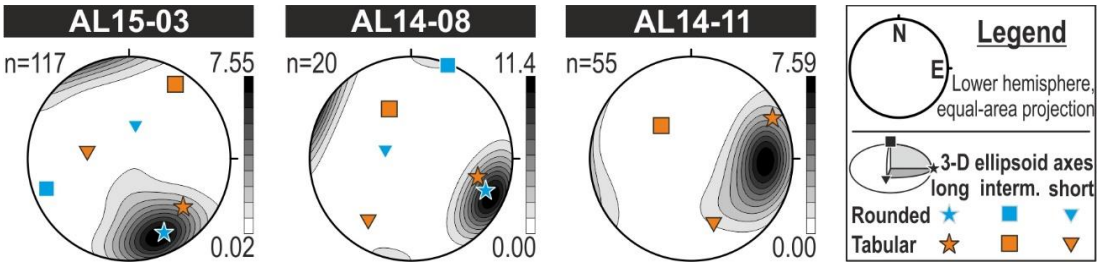

Figure 3.6. *Characterization of the olivine grain framework by analysis of the mean intercept length (MIL; shown as blue and orange symbols). The sample volumes are shown in Figs. 3.4-3.5. In the sample AL14-11 there was not enough rounded olivine for its MIL analysis. Pole figures are lower hemisphere equal area projections in a geographic reference frame (see legend on the right). Gray-shaded contouring in the background of each pole figure contains the SPO of highly attenuating magnetite from the corresponding sample. Contouring was calculated as cosine sums with a cosine exponent of 15 using the free version of Stereo32 v.1.0.1 software by Klaus Röller and Claudia Trepmann (Ruhr University Bochum, Germany).*

3.3.4 EBSD: optimization of segmentation and CPO

For segmentation of the cleaned EBSD datasets the *'calcGrains'* built-in function of the MTEX 4.4.alpha.2 Matlab toolbox (https://mtex-toolbox.github.io; Bachmann et al., 2010; Hielscher and Schaeben, 2008) was used. To reconstruct microstructures from EBSD data, in the geological literature grain boundaries are typically defined at minimum misorientation between neighboring pixels (segmentation angle) in the range of 12-15°. However, deviation from this range of segmentation angles sometimes becomes

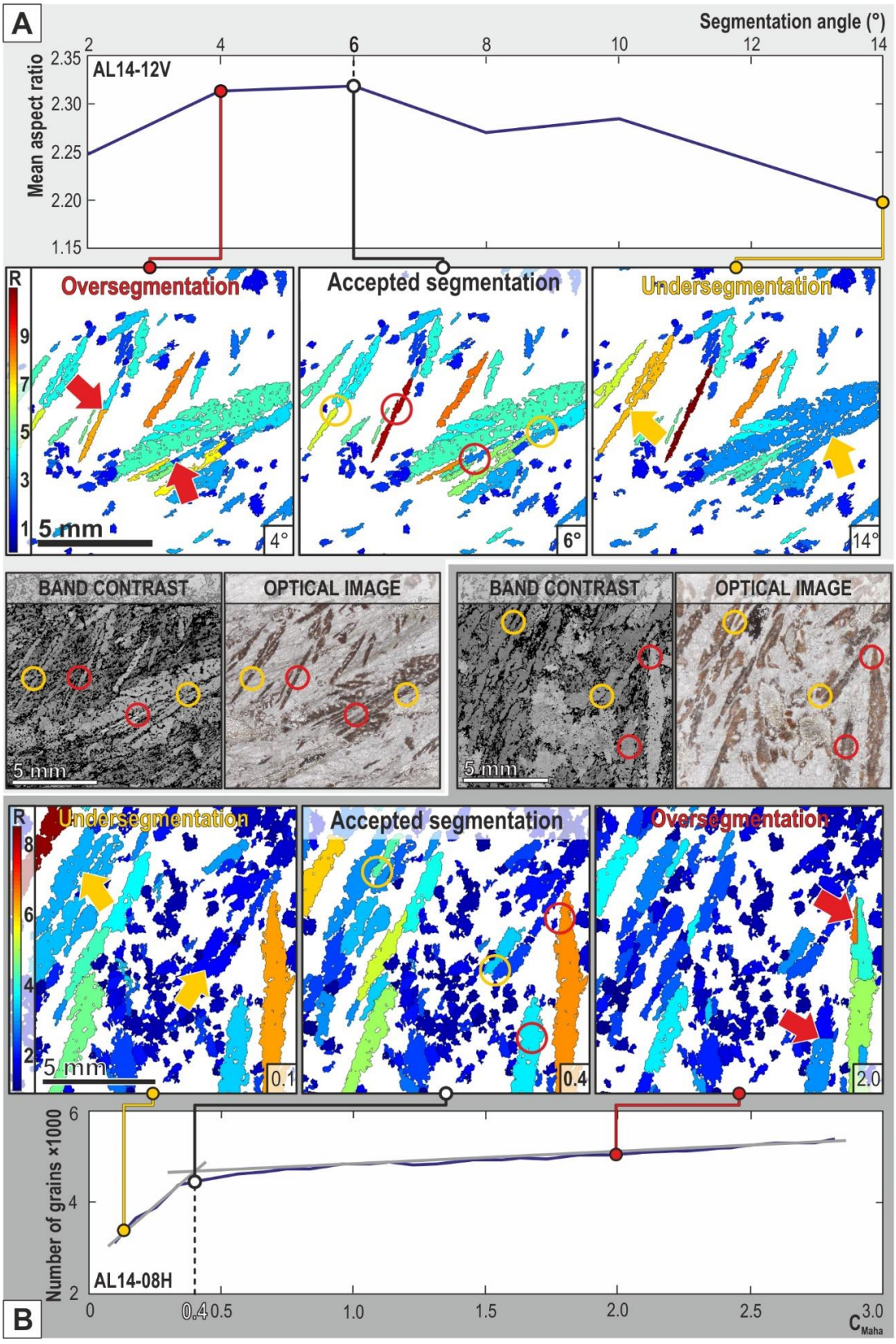
A
Segmentation angle (°)
2
4
6
8
10
12
14
Mean aspect ratio
2.35
2.30
2.25
2.20
1.15
AL14-12V
R
9
7
5
3
1
Oversegmentation
Accepted segmentation
Undersegmentation
5 mm
4°
6°
14°
BAND CONTRAST
OPTICAL IMAGE
BAND CONTRAST
OPTICAL IMAGE
5 mm
5 mm
R
8
6
4
2
Undersegmentation
Accepted segmentation
Oversegmentation
5 mm
0.1
0.4
2.0
Number of grains ×1000
6
4
2
AL14-08H
B
0
0.4
0.5
1.0
1.5
2.0
2.5
3.0
C Maha

necessary as demonstrated, for example, in the work of Chauve et al. (2017), where a value of 7° was applied to segment ice EBSD data. Grain recognition using the typical segmentation values undersegments the tabular olivines and produces erroneous laterally interlaced crystals in the texture (Fig. 3.7a to the right), because neighboring crystals are very closely oriented to each other. In contrast, a too low angle leads to oversegmentation and results in the subdivision of elongated single crystals into artificial crystal aggregates in the maps (Fig. 3.7a to the left). It is observed that both errors tend to lower the aspect ratio of spinifex olivine, hence typically the best solution is found within a range of ±2° to the segmentation value, which results in the highest mean aspect ratio of the analyzed surface (Fig. 3.7a). The accepted value of segmentation angle ranges from 2 to 10° in the different thin sections and reproduces the overall 2-D rock microstructure as close as possible. The only exceptions are the sample AL14-08 and the horizontal thin section of AL14-11, where the fast multiscale clustering (FMC) algorithm with a C_{Maha} value of 0.4-0.65 provided more reliable results than the classical segmentation method; where the C_{Maha} value is a constant scaling factor applied on Mahalanobis distance, which controls the segmentation sensitivity (McMahon et al., 2013). The value of the optimal C_{Maha} in each thin section was determined by applying the 'elbow' technique recommended by the authors (Fig. 3.7b). The quality of the grain recognition for every sample was checked against band contrast images and polarized light optical microscopy (Fig. 3.7).

Considering that the main aim of this study is the quantitative characterization of the 3-D microstructures of primary dehydration products (i.e., tabular and rounded olivine), a minimum equivalent grain diameter of 3100 μm was set up in order to remove as much

Figure 3.7. *Optimization of the segmentation of tabular olivine EBSD data. For the sake of better visibility, insets show only the close-up views of representative areas of the thin sections but the diagrams contain data of the total analyzed surface. Color coding of the inset base maps refers to the aspect ratio (R) of olivine. Arrows point at some particular errors of the given segmentation result (oversegmentation in red, undersegmentation in yellow) and the improvements of these areas in the accepted solution are encircled with the same color coding. The same scale applies to every image. (a) Effect of the segmentation angle on the mean aspect ratio of olivine in the vertical thin section of the sample AL14-12 using the normal segmentation method, which is based on neighboring pixel misorientation. See band contrast map and plane polarized light optical image for comparison; circles show the same areas as those highlighted in the accepted segmentation. (b) Application of the 'elbow'-technique (McMahon et al., 2013) to find the best CMaha value in those samples where normal segmentation method fails. See text for further details. See band contrast map and plane polarized light optical image for comparison; circles show the same areas as those highlighted in the accepted segmentation.*

as possible from the fine-grained, recrystallized, interstitial mineral matrix, which formed during later geological processes (e.g., grain size reduction zone, Padrón-Navarta et al., 2010b). This involves that grains smaller than this threshold value do not appear in the CPO data, nor in the EBSD maps (*cf.* Fig. 3.7 insets). The CPO of tabular olivine always show clustered distribution of the three main crystallographic axes with the [001]-axes (*i.e.*, crystal c-axes) oriented subhorizontal in E-NE to E-SE directions (Fig. 3.8a). Olivine [001]-axis has a maximum subparallel to the longest axis of the MIL ellipsoid of the corresponding tabular olivine crystal aggregate. Moreover, in the samples AL14-08 and AL14-11 the shortest axis of the spinifex MIL ellipsoid overlaps the maximum of olivine

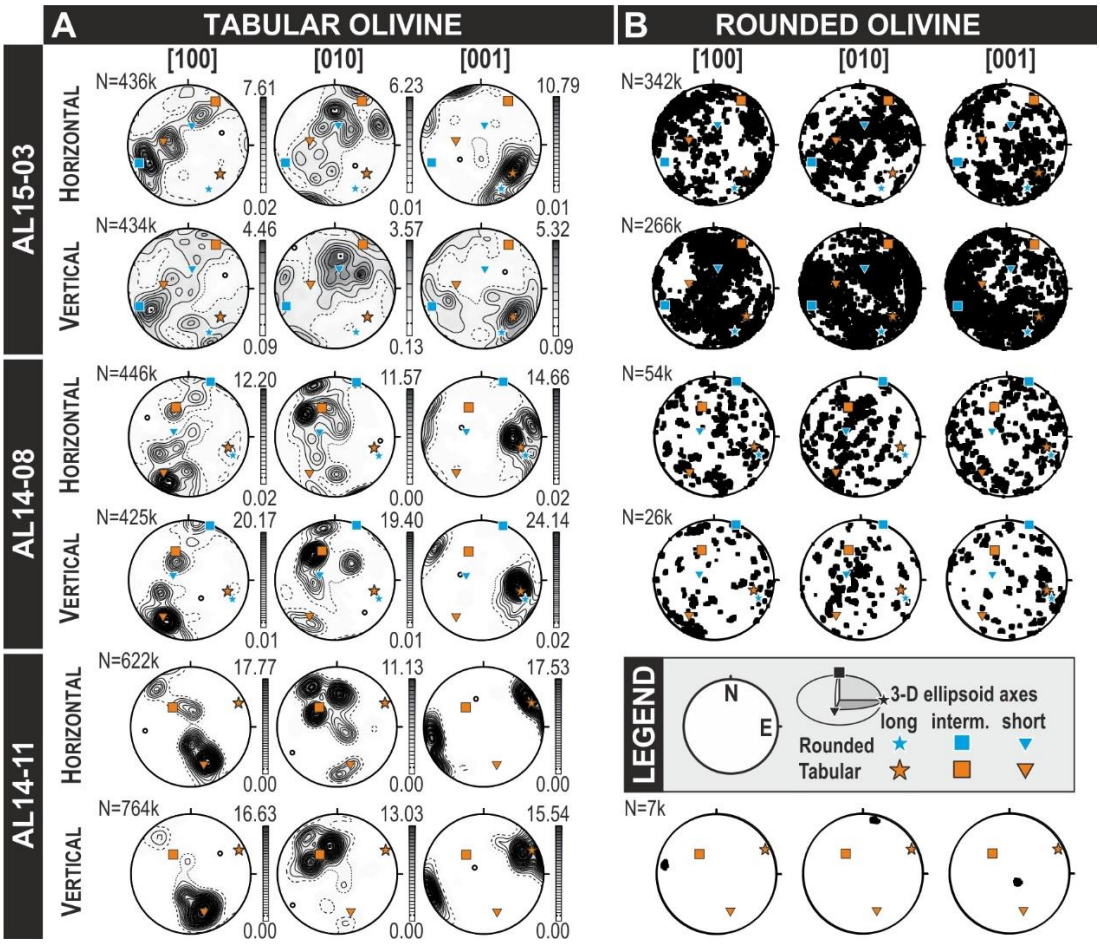

Figure 3.8. *Lower hemisphere, equal area stereographic plots of the crystal preferred orientation (CPO) of tabular (a) and rounded (b) olivine varieties in a geographic reference frame (see legend for orientation) from the horizontal and vertical thin section pairs of representative samples. All measured pixels are plotted if the corresponding grain size was above the minimum threshold (see text for details); N: number of measurement pixel. For the tabular olivine, contours are at 0.5 multiples of a uniform distribution and white circle denotes minimum density. Also shown are the results of MIL analysis for comparison of olivine SPO and CPO (MIL data from Fig. 3.6).*

[100]-axis and the intermediate axis of the tabular MIL ellipsoid is also aligned with the olivine [010]-axis (Fig. 3.8a). The CPO of tabular olivine in the horizontal and vertical thin section pairs is almost identical to each other (Fig. 3.8a), which is consistent with the strong crystallographic orientation and the volumetrically high abundance of this variety in the studied rocks (Fig. 3.5). In contrast, due to the overall poor exposure of rounded olivine in the thin section pairs, their CPO are statistically not representative. Nevertheless, in most of the cases rounded olivine CPO is roughly correlated to that of the tabular ones but the clusters are more dispersed and the distribution of the crystallographic axes in the horizontal and vertical thin sections is substantially different from each other (Fig. 3.8b), even in sample AL15-03, where the rounded olivine is relatively abundant (Fig. 3.5a). Considering that clear correlation between the axes of the MIL ellipsoid and the rounded olivine CPO cannot be established based on the studied samples, the CPO of rounded olivine is not discussed hereafter.

3.3.5 Correlation µ-CT and EBSD data

The careful documentation of core dimensions before and after thin section preparation is necessary to locate the thin section planes in the µ-CT volume reconstructions. Then, the fundamental requirement to correlate µ-CT and EBSD data is the alignment of coordinate systems because small errors are introduced during cutting the rock samples (Fig. 3.9). In order to have a real, visual control on the µ-CT volume selection, the thin section planes were designated as references for north direction, and conformity of geographic axes was achieved by rotation of the reconstructed µ-CT volume around the core axis. Considering that the angle of rotation is typically very minor (0.5-3.5°; e.g., Fig. 3.9) and has never exceeded 5.5°, our choice of reference frame has negligible effect on the CPO with respect to the true north direction yet it significantly increases the reliability of µ-CT volume selection. Thus, the CPO from EBSD analyses of the vertical and horizontal thin section planes can be correlated to the SPO provided from the quantitative 3-D image analysis of µ-CT volume data (Figs. 3.6, 3.8-3.10).

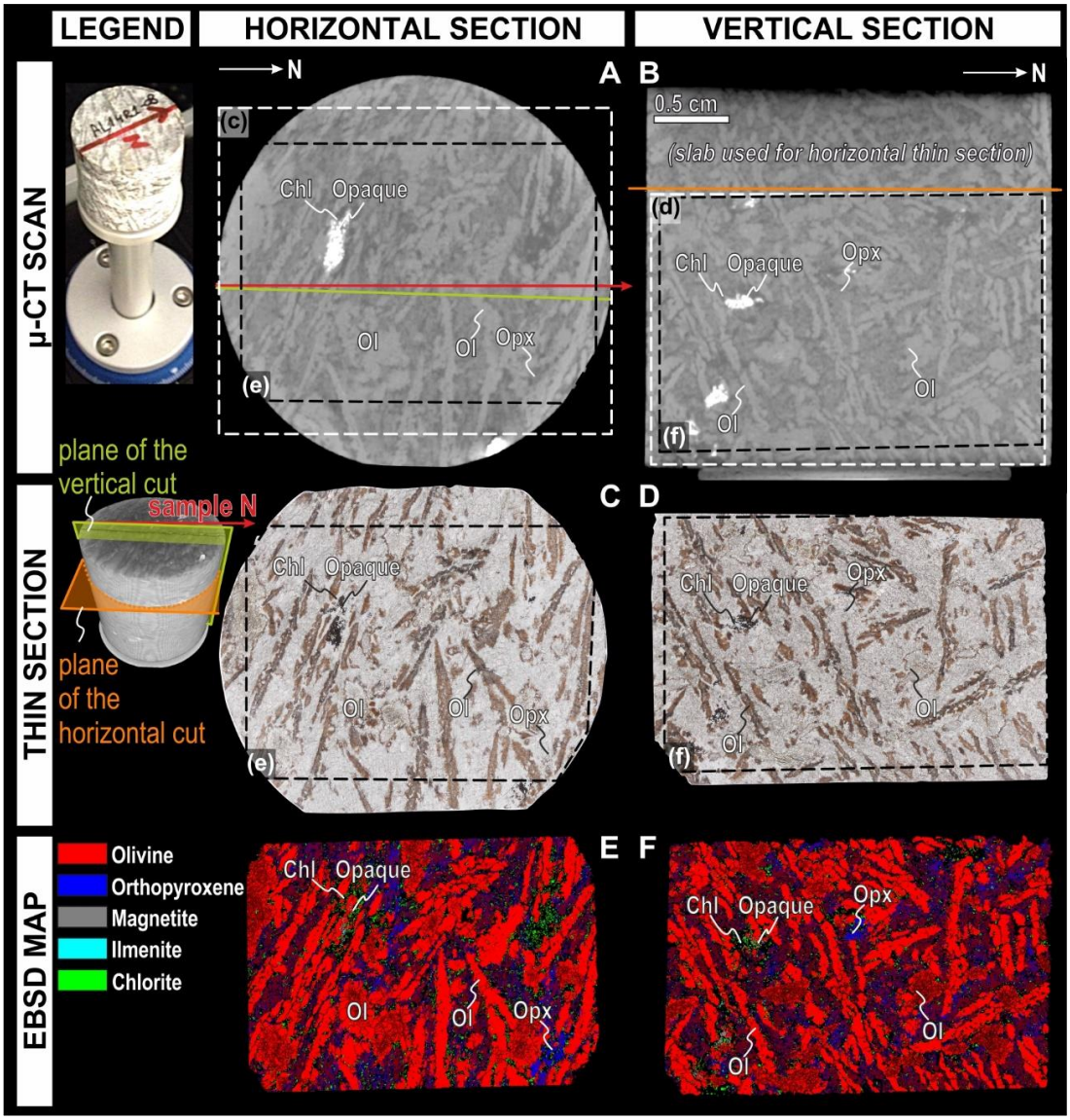

Figure 3.9. *Correlation of μ-CT and EBSD data to facilitate proper correlation of orientation information in the sample AL14-08. The same scale applies to each part of the figure; the scale bar is shown in (b). (a-b) Reconstruction of the μ-CT slice that corresponds to the position of the horizontal (a) and the vertical (b) thin sections shown in c-d (here denoted by white dashed lines). The area mapped by EBSD (shown in e-f) is also outlined by black dashed lines. The mismatch between sample North (red) and the trace of the North-South vertical plane (green), shown in (a), is 2°. (Cc-d) Transmitted light photomicrographs of the horizontal (c) and vertical (d) thin sections. Location of EBSD maps (shown in e-f) is outlined by black dashed lines. (e-f) EBSD phase maps. Chl: chlorite; Ol: olivine; Opx: orthopyroxene. Magnetite and ilmenite are opaque phases. Grain boundaries and non-indexed phases are black, phase boundaries are not shown. Maroon color denotes subgrain boundaries.*

3.4 Discussion

The combination of µ-CT —in cylindrical cores— and EBSD-SEM data —in thin section planes— overcomes the limitations of these two instrumental techniques to characterize the shape and crystallographic orientation of many coarse-grained rocks at representative millimetric to centimetric length scales. The proposed semi-destructive approach is successful in the reconstruction of the 3-D microstructure of complex geomaterials with phases of similar composition but different SPO and CPO. The method is particularly relevant for the characterization of phases with highly anisotropic shape —such as the tabular olivine in ultramafic rocks— that cannot be easily inferred from stereology of 2-D sections. The applicability of this method primarily depends on the density contrast within the components of the polyphase assemblage (cf. Fig. 3.4a) because low contrast may hinder successful segmentation and feature extraction from the µ-CT data (i.e., it cannot be applied to monomineralic rocks, or rocks with heterogeneously distributed constituent phases forming monophase layers), and also on the anisotropic microstructure to quantify directionality in the samples.

The potential of this technique for the quantitative analysis of the 3-D microstructure of coarse-grained geomaterials with highly anisotropic phases is illustrated by the statistical analysis of the correlation of SPO-CPO of tabular olivine (Fig. 3.8). Based on the clustered distribution of the crystallographic axes of tabular olivine obtained by EBSD, several CPO groups (cf. CPO in horizontal and vertical thin sections in Fig. 3.10) are distinguished. The different olivine grains and aggregates with differing CPO are then identified in the µ-CT volume. The separation of individual tabular olivine grains in the µ-CT volume is accomplished by user-interactive tracing of selected crystals and follow-up through the reconstructed volume (Fig. 3.10, right). This visualization shows that subordinate CPO groups of olivine crystals exist because, regardless their 3-D spatial orientation, tabular olivines have tablet-like shapes that are elongated parallel to the olivine [001]-axis in a plane perpendicular to the olivine [100]-axis (Fig. 3.10). The statistical analysis of the 3-D olivine microstructure based on the bulk MIL and CPO data supports this observation (Fig. 3.8). Although in the MIL data the SPO of the subordinate CPO groups are not visible (Figs. 3.6 and 3.8), the volumetrically dominant distribution of crystal a-, b- and c-axis directions correspond to the short, intermediate and long axis

of the MIL 3-D ellipsoid, respectively (cf. density maximum of [100]-, [010]- and [001]-axes vs. orange triangle, square and star in Fig. 3.8, respectively). The strong coupling of the CPO and SPO of tabular olivine crystals (cf. data for tabular olivine in Fig. 3.8) shows that the MIL analysis of this textural variety of olivine yields reliable data. The SPO directions revealed that rounded olivines are aligned with the highly attenuating phases along distinct microstructural lineation (Fig. 3.6; maximum contouring density vs. position of blue star). Therefore, it can be concluded that the small mismatch between the maximum elongation direction of the rounded and tabular olivine is statistically significant and it is not an artifact of the MIL analysis due to the anisotropic crystal shapes

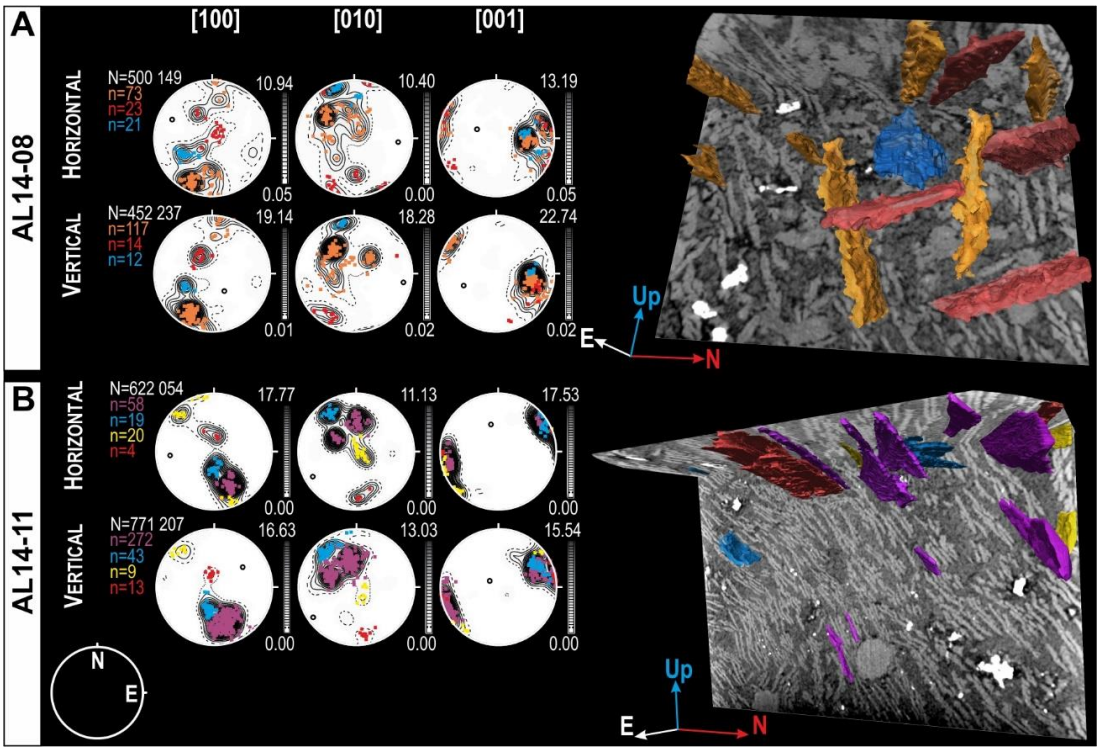

Figure 3.10. *Characterization of the microstructure of tabular olivine by combined shape and crystallographic orientation in samples AL14-08 (a) and AL14-11 (b). From the EBSD orientation data different CPO groups can be distinguished based on the horizontal and vertical thin sections (left) and the spatial arrangement of some representative crystals is visualized by volume rendering (right). Pole figures are lower hemisphere, equal area stereographic projections in a geographic reference frame (see legend in the bottom-left corner) showing the orientation of olivine [100], [010] and [001] crystallographic axes (a-, b- and c-axes, respectively). Contouring in the background contains all data (tabular and rouded olivine; cf. Fig. 3.8) with contours at 0.5 multiples of a uniform distribution; white circle: minimum density, N: number of measurement pixel. CPO groups are visualized as the average orientation of each grain ('one point per grain'; n: number of grains) and share the same color coding in the pole figures as in the µ-CT scans. The core diameters in the horizontal plane are 28.3 mm and 33.4 mm for the samples AL14-08 (a) and AL14-11 (b), respectively.*

of tabular olivines (Fig. 3.6; position of blue and orange stars). Considering that the Atg-serpentinite in the Almirez massif —which is the protolith of Chl-harzburgite prior to dehydration (e.g., Padrón-Navarta et al., 2011 and references therein)— is strongly foliated with stretching lineation denoted by the highly attenuating phases, the parallelism of highly attenuating phases in Chl-harzburgites with the elongation direction of the rounded olivine reaction products indicates that dehydration progressed strongly controlled by pre-existing rock structures. Comparison of SPO and CPO of the tabular olivines in the Almirez Chl-harzburgites reveals that the highly anisotropic crystals have a strong correlation between shape and crystallographic orientation (Fig. 3.8), and the tablet-like olivines grow in the b-c plane (i.e., in a plane perpendicular to the [100]-axis) elongated along the c-axis (Fig. 3.10). The dominantly subparallel elongation of the anisotropic olivine to the SPO, denoted by the rounded olivines and the highly attenuating phases (Fig. 3.6), suggests that the growth of the anisotropic spinifex olivine variety also occurred with a well-defined orientation at a different stage of the dehydration process. Our data hence indicate that the statistical comparison of SPO data from µ-CT to the bulk CPO data from EBSD provides a basis for reliable 3-D microstructural interpretations of coarse-grained geomaterials.

3.5 Concluding remarks on correlation technique

In order to use both crystallographic and morphometric data to reconstruct the microstructure of complex geomaterials, EBSD and µ-CT-derived information have been combined for Chl-harzburgite. The semi-destructive approach presented here involves drill pressing oriented micro cores for µ-CT and preparation of oriented thin sections from the micro cores for EBSD analyses. This method depends on the segmentability of the µ-CT volume but enables the correlation of mineral SPO and CPO, and it is proven to provide reliable information for both the statistical analysis of SPO and CPO in the total volume of the samples, and for the detailed investigations addressing crystal shapes and growth directions. The limitations of both methods (i.e., no crystal orientation data in µ-CT and no spatial information in EBSD) have been overcome, which also allows for establishing the link between field work and rock fabric at the hand specimen scale in future 3-D microstructural studies.

4 Episodic Fluid release during High-pressure Dehydration of Antigorite-serpentinite in Subducting Slabs

4.1 Introduction

The mechanisms of release and subsequent flow of deserpentinization fluids in the overlying mantle wedge are poorly constrained. Theoretical work predicts a somewhat episodic character of fluid expulsion and flow during metamorphic devolatilization reactions (Bebout and Penniston-Dorland, 2016; Connolly, 1997; Connolly and Podladchikov, 1998, 2013; Ferry and Gerdes, 1998; Nur and Walder, 1992; Whitney and Evans, 2010). Studies of exhumed paleo-subduction terranes show that fluids are released and transported in hydrofractures, shear zones and porous flow channels (Ague, 2007; Bebout and Penniston-Dorland, 2016; John et al., 2012; Padrón-Navarta et al., 2010; Plümper et al., 2017; Zack and John, 2007). The duration and frequency of devolatilization fluid events at intermediate depth of subduction zones are, however, mostly unknown due to the lack of evidence in the geological record (Bebout and Penniston-Dorland, 2016; Connolly and Podladchikov, 2013; van Keken et al., 2011).

Here, we provide new constraints from the Almirez massif on the episodic nature of Atg-serpentinite dehydration fluid expulsion in subducting slabs. The Almirez paleo-subduction metamorphic terrane preserves a record of high-pressure Atg-serpentinite dehydration to prograde Chl-harzburgite (Padrón-Navarta et al., 2011; Trommsdorff et al., 1998) (Fig. 4.1) (cf. to Ch. 1 for the description of the geological setting of the Almirez massif). The detailed mapping of the two different textural types of Chl-harzburgite — produced through the dehydration of Atg-serpentinite— unveils that they are distributed in an intricate network of alternating lenses. This detailed field study at the massif scale is further used to constrain the length-scale and spatial distribution of the two main textural types of Chl-harzburgite reaction products. I will show how these length-scales can be used to investigate different parameters to unravel the nature of the physical instability that triggered the episodic nature of Atg-serpentinite dehydration in subducting slabs.

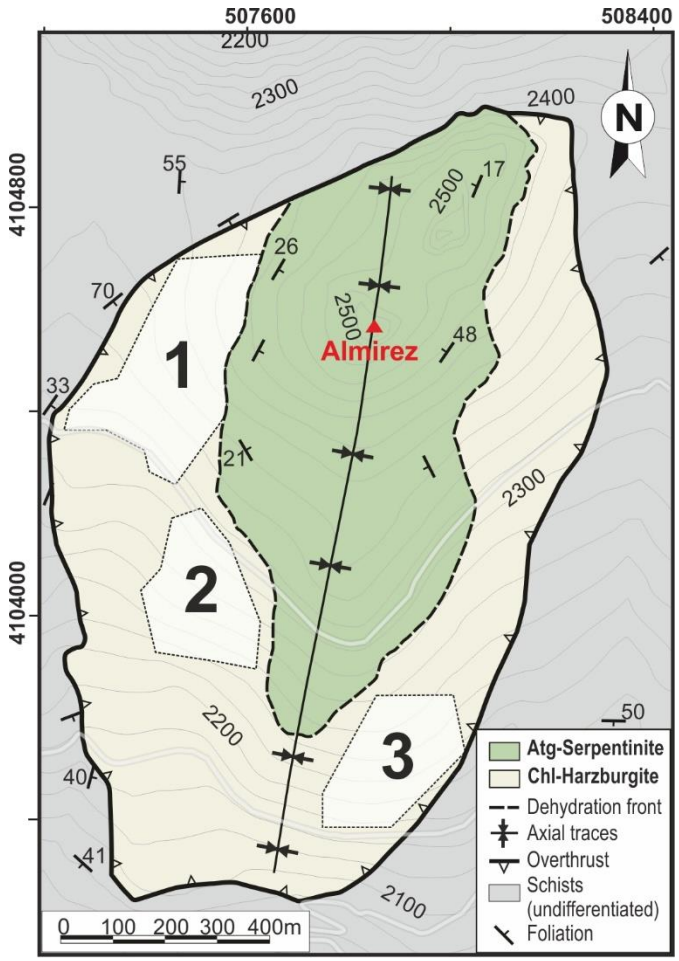

Figure 4.1. *Geological map of the Almirez massif showing the dehydration front between Atg-serpentinite and Chl-harzburgite. In the Chl-harzburgite, the dotted line areas show the three selected zones for detailed mapping of the Chl-harzburgite sequence (see Fig. 4.3).*

4.2 Methods

4.2.1 Mapping of the Chl-harzburgite textural domains

Detailed description of the Chl-harzburgite textures is provided in Ch. 5 and 6. Chl-harzburgite occurs as granofels and spinifex texture (Dilissen et al., 2018; Padrón-Navarta et al., 2011). Granofels Chl-harzburgite (Fig. 4.2a) is composed of clear, anhedral, rounded olivine crystals, prismatic orthopyroxene grains and chlorite ranging from flakes to granular aggregates, associated with oxides as magnetite and ilmenite (cf. Ch. 5). Spinifex Chl-harzburgite (Fig. 4.2b) contains brown, euhedral, tabular olivine crystals with high apparent axial ratios and occasionally —as in granofels Chl-harzburgite— rounded clear olivine grains. These olivines are surrounded by a fine-grained matrix of

orthopyroxene and chlorite; with occasionally, long radiated orthopyroxene aggregates and chlorite associated with oxides (cf. Ch. 5).

Field observations in the Chl-harzburgite sequence reveal that the transition between granofels and spinifex textures can be either sharp (Fig. 4.2c) or occur along a transitional zone —up to c. 50 *cm*— of varied-textured Chl-harzburgite (Ch. 5 and 6). Outcrop-scale mapping shows that both textural types crop out as interspersed metric domains separated by a straight or convoluted contact (Fig. 4.2d) and that the intercalation of their elongated bodies occurs parallel to the dehydration front (Figs 4.3 and 4.4). Projection of the textural mapping on the Almirez topography reveals the pseudo-three-dimensional (3-D) geometry of granofels and spinifex Chl-harzburgite bodies (Fig. 4.4a).

To characterize the spatial distribution of both textural types at scale of the massif, we focused in the western and southeastern hills of the massif where textures are better exposed (Fig. 4.1). The mapping area of c. 0.87 km^2 was subdivided into three sectors (hereafter referred to as sector 1, 2, and 3, respectively) (Figs 4.1 and 4.3). We carried out a detailed mapping of outcrop in areas with steepest slope and densest occurrence of well-

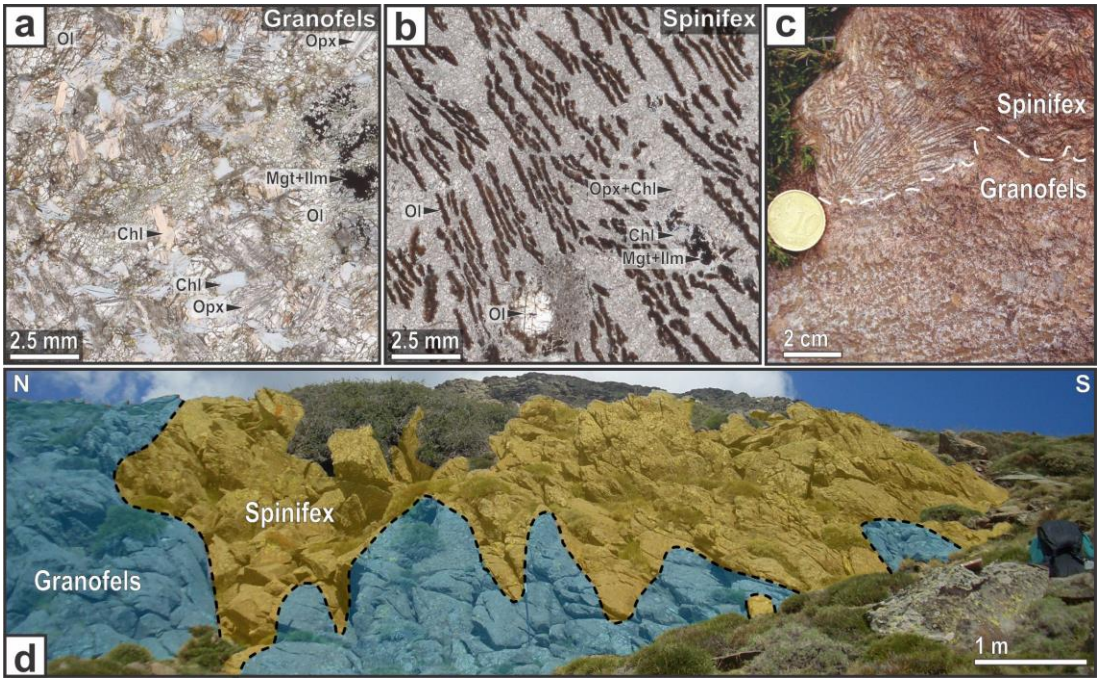

Figure 4.2. *Granofels and spinifex texture in the Chl-harzburgite sequence. (a-b) Optical images of representative granofels (a) and spinifex (b) textures in oriented thin sections with Ol=olivine, Opx=orthopyroxene, Chl=chlorite, Mgt=magnetite, Ilm=ilmenite. (c) Sharp contact between the spinifex and granofels texture. (d) Detailed mapping of the transition from the granofels to the spinifex texture in a ca. 15 m wide outcrop. Note the complex convolute character of the contact.*

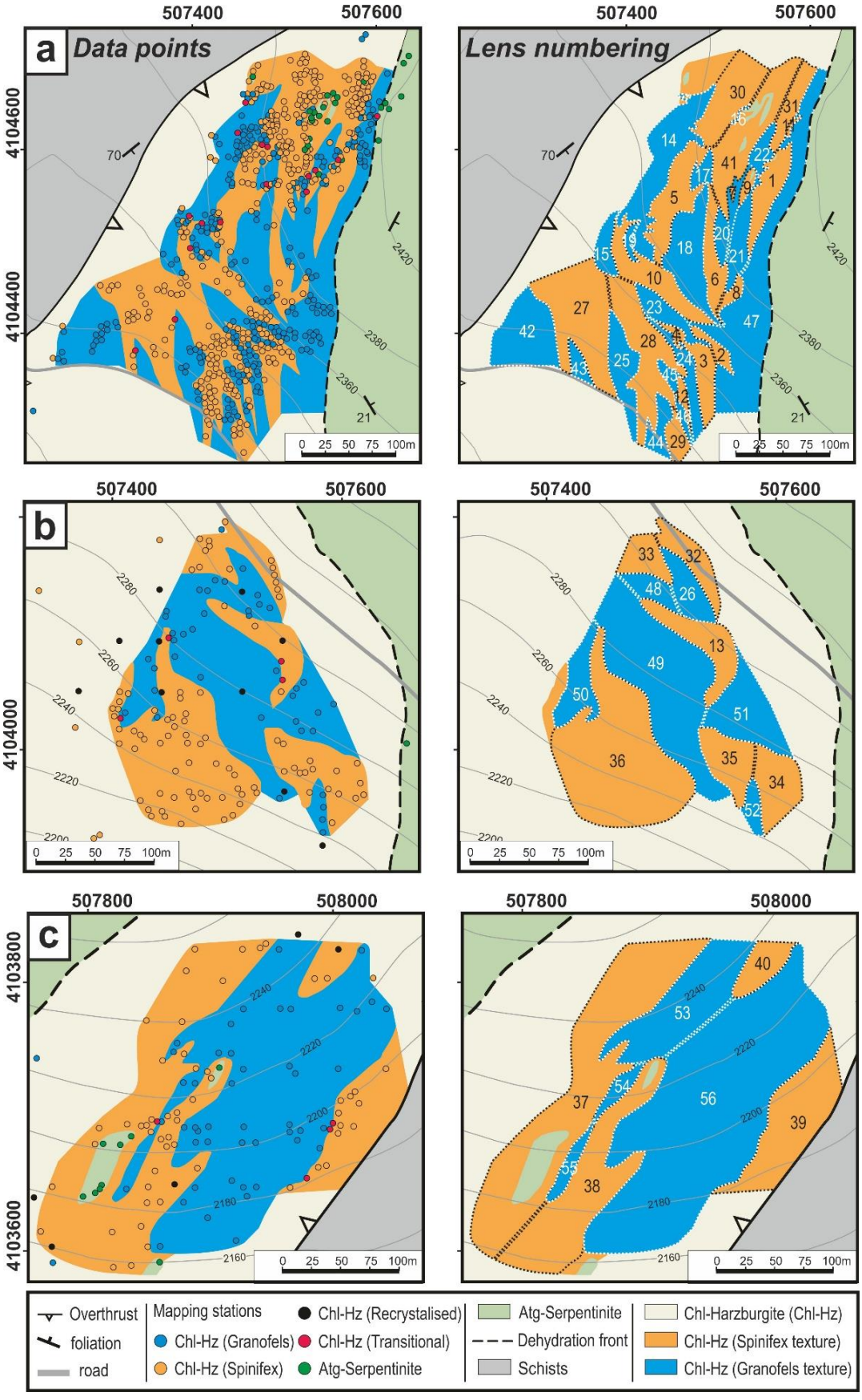
a
Data points
Lens numbering
b
c
507400
507600
507800
508000
4104600
4104400
4104000
4103800
4103600
0 25 50 75 100m
Overthrust
foliation
road
Mapping stations
Chl-Hz (Granofels)
Chl-Hz (Spinifex)
Chl-Hz (Recrystalised)
Chl-Hz (Transitional)
Atg-Serpentinite
Atg-Serpentinite
Dehydration front
Schists
Chl-Harzburgite (Chl-Hz)
Chl-Hz (Spinifex texture)
Chl-Hz (Granofels texture)

exposed outcrops (mostly Sector 1; Fig. 4.3a), and grid mapping using coarse (40 x 40 m) or fine (10x10 m) grid of 1738 GPS observation stations (mostly in sectors 2 and 3; Fig. 4.3b,c). Observation stations were classified into granofels or spinifex Chl-harzburgite, granofels-spinifex contacts, recrystallized Chl-harzburgite (cut by grain size reduction zones; GSRZ) and Atg-serpentinite. The map of textural variation (Fig. 4.3) was done in GIS software by delineating the boundaries of the textural domains mapped at the outcrop scale —sector 1— and defined by clouds of georeferenced station with same texture —mostly sector 2 and 3.

4.2.2 Reconstruction of distribution and shape of textural domains

The three-dimensional (3-D) geometry of the textural bodies (Fig. 4.4) was reconstructed by digitalization of their upper and lower boundaries into a Digital Elevation Model of the massif (LiDAR-PNOA of the Spanish Instituto Geográfico Nacional). For those bodies that crop out along slopes with variable orientations, we studied the spatial variability of the elevation (z) of the outcrop using the variogram function and the trend tendency of the surface fitting the data. As they come from outcrops with elevations varying from c. 2500 to 2000 m (Fig. 4.4), the surface trend is strong and was removed by the mean of a local second order polynomial interpolation. The theoretical elevation of the limiting surfaces was estimated beyond their outcrops by a cross-validation analysis using ordinary kriging on the detrended (residual) data. The identified textural bodies with their thickness, N-S length, E-W length, ratios, texture, and distance to the dehydration front, are listed in Table 4.A1.

Figure 4.4b shows the 3-D reconstruction of two well-exposed spinifex bodies in sector 1 (Fig. 4.4a; inset). They have 3-D lensoidal shapes roughly similar to tri-axial ellipsoids (Fig. 4.4b). Hence, the volume and surface area of each domain was calculated as those of a tri-axial ellipsoid with the longest (*L*) intermediate (*I*) semi-axes corresponding, respectively, to half of the longest N-S and E–W chords, and the shortest

Figure 4.3. *Detailed maps of textural variation within the Chl-harzburgite sequence below the dehydration front in the Almirez. To the left, GPS locations indicate textural observation with solid circles. To the right, individual granofels and spinifex textured Chl-harzburgite bodies are numbered and contoured with white and black dashed lines, respectively. (a) Zoom into the northwestern area of the Almirez massif, corresponding to sector 1 in Fig. 4.1b, (b) south-western area, corresponding to sector 2 in Fig. 4.1b and (c) south-eastern area, corresponding to sector 1 in Fig. 4.1b.*

(*S*) semi-axis as half of the maximum differential elevation (Δz) between the upper and lower boundary of the domain. Axial ratios were used to derive the missing volume of lenses that was eroded. The median of all N-S measurements is divided by the median of all E-W measurements for granofels and spinifex, respectively, to obtain the *L*/*I* ratio, respectively. The spread on the granofels and spinifex ratios, respectively, was calculated by excluding outliers on N-S and E-W measurements, respectively. This was done by calculating the difference between upper (Q3) and lower (Q1) quartile, i.e. the difference between the median of the upper half and the median of lower half of data points of N-S and E-W measurements, respectively. The spread is shown as $median \pm (Q3 - Q1)/2$ for granofels and spinifex, respectively. This general spread per texture is used to calculate the spread of the missing semi-axes L or I from $R = (Q3 - Q1)/2/median$, which is for spinifex lenses $R_{Ls} = 0.3$ and $R_{Is} = 0.5$ for L and I semi-axis, respectively, and for granofels lenses $R_{Lg} = 0.4$ and $R_{Ig} = 0.5$ for *L* and *I* semi-axis, respectively. The missing semi-axis is then calculated as $L = I \cdot ratio \pm L \cdot R_L$ or $I = \frac{L}{ratio} \pm I \cdot R_I$.

The bodies of granofels and spinifex texture distribution are herewith reconstructed as tri-axial ellipsoidal lenses with longest (*L*) semi-axis oriented N-S, intermediate (*I*) semi-axis oriented E-W and shortest (*S*) semi-axis subparallel to the topographic elevation z

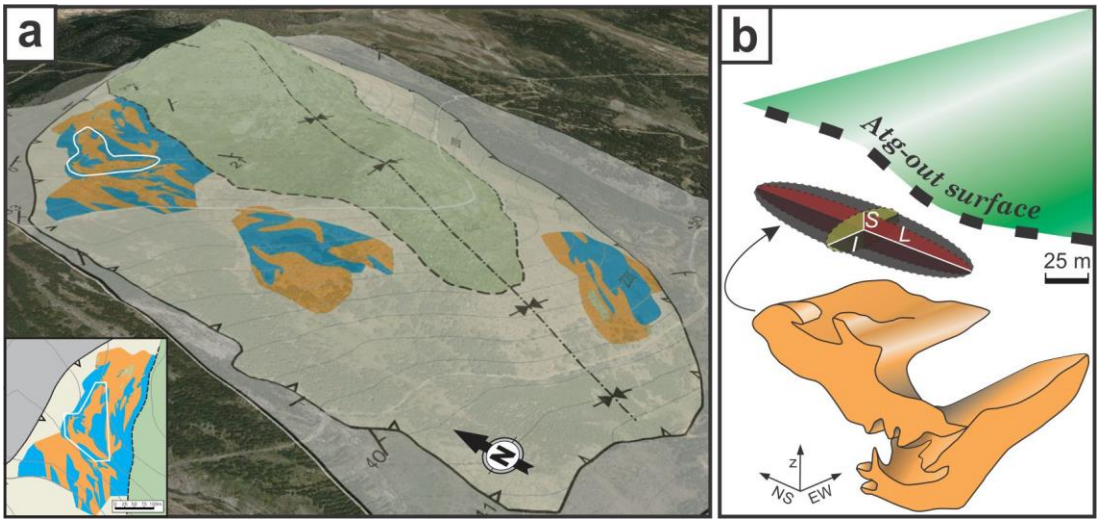

Figure 4.4. *(a) 3-D image overlay of the map with detailed petrological mapping of granofels (blue) and spinifex (orange) textures in Google Earth© to visualize outcrops. (b) 3-D representation of spinifex textured lenses (corresponding to lenses 5 and 10 in Fig. 4.3a), parallel to the dehydration front. Plain colored area corresponds to the piece of the spinifex network outcropping in (a) indicated with the white frame. Shaded areas are interpretation according to observations in the field, i.e. representing flat triaxial lenses, parallel to the dehydration front and tending to pinch out.*

(Fig. 4.4b). Rendering of the 3-D shape reveals that granofels and spinifex lenses are very similar in shape with *L*/*I* axial ratio equal to 3.5 (±2.1) and 3.8 (±2.1), respectively, and *L*:*I*:*S* axial ratio equal to 15:4:1 and 16:4:1, respectively. The lens thicknesses —parallel to the *S* axis— vary 2–20 m, and the longest length —parallel to *L* axis— ranges from 18 to 300 m. The *L*-*I* planes are nearly horizontal and broadly parallel to the Atg-out dehydration front (Fig. 4.4).

The volume (m^3) of a lens is computed as the volume of a triaxial ellipsoid according to the equation:

$$V = \frac{4}{3}\pi \cdot (L \cdot I \cdot S) \tag{4.1}$$

and its Surface Area (m^2) is approximated (< 1% error) according to the equation:

$$SA = 4\pi \cdot \left(\frac{L^p I^p + L^p S^p + I^p S^p}{3}\right)^{1/p} \tag{4.2}$$

where p = 1.6075 is a constant.

4.2.3 Volume of released water

From the volume of a Chl-harzburgite lens (eq. 4.1), we estimate the amount of released water by dehydration of Atg-serpentinite. The olivine fraction on Chl-harzburgite is estimated to be 45% (Dilissen et al., 2018; Padrón-Navarta et al., 2011), allowing to calculate the amount of olivine (m^3) as:

$$V_{Ol} = 0.45 \cdot V \tag{4.3}$$

Olivine density is 3.32 $g\ cm^{-3}$, and mass (kg) of olivine per lens is:

$$m_{Ol} = 3.32 \cdot 10^3 \cdot V_{Ol} \tag{4.4}$$

The amount of moles of olivine per lens, with olivine molar mass of 147 $g\ mol^{-1}$, is:

$$mol_{Ol} = \frac{10^3 \cdot m_{Ol}}{147} \tag{4.5}$$

The amount of moles of water can be derived through the model dehydration reaction of Atg-serpentinite to Chl-harzburgite:

$$1\ \mathrm{Atg} = 4\ \mathrm{Chl} + 6\ \mathrm{Ol} + 6\ \mathrm{Opx} + 15\ \mathrm{H_2O} \tag{4.6}$$

Through stoichiometry ratio of olivine and water, the amount of water moles per lens is:

$$mol_{H_2O} = 2.5 \cdot mol_{Ol} \quad (4.7)$$

Solid phases like antigorite are not very compressible (e.g. Brantut et al., 2017), unlike water, which density depends on P-T conditions. For 1.8 GPa (Atg-dehydration pressure of Almirez; Laborda-López et al., 2018; Padrón-Navarta et al., 2011) water density can be extrapolated until 650 $°C$ based on temperature (T; $°C$) – density (ρ; $kg\,m^{-3}$) correlation at 1.8 GPa as $\rho_f = 1000 \cdot (-0{,}0004T + 1{,}3409)$ from Table 2 of Abramson and Brown (2004). This gives 1080.9 $kg\,m^{-3}$ water density at 1.8 GPa and 650 $°C$. Mass (kg) and volume (m^3) of water per lens is then, respectively:

$$m_{H_2O} = \frac{18 \cdot mol_{H_2O}}{1000} \quad (4.8)$$

$$V_{H_2O} = \frac{m_{H_2O}}{1080.9} \quad (4.9)$$

4.3 Results

4.3.1 Dimensions of Chl-harzburgite lenses and fluid production

The thickness, the half-surface area and volume of granofels and spinifex lenses is shown in Figure 4.5 using blue and orange circles and as a function of their distance (i.e. middle of the lens) from the Atg-out dehydration front. The vertical distribution of the lenses shows an alternation of 28 granofels and 28 spinifex lenses interspersed throughout the c. 70 m thick Chl-harzburgite sequence. Grouping of the mid-distances of granofels and spinifex lenses of all three sectors reveals twelve intervals of granofels and spinifex textured Chl-harzburgite (indicated with roman numbering; Fig. 4.5). The thickness-weighted average mid-distance from the Atg-out dehydration front of the twelve granofels intervals are 2.0, 10.3, 14.3, 23.0, 26.6, 31.5, 33.2, 38.3, 42.2, 43.8, 51.8 and 64.1 m, and that of the spinifex intervals are 8.2, 11.3, 18.9, 24.6, 29.0, 32.0, 34.3, 38.9, 43.4, 47.3, 54.7 and 74.4 m.

Remarkably, the volume-weighted average thickness, half-surface area, and volume of granofels and spinifex lenses is, within error, undistinguishable (blue dashed and orange short-dashed vertical lines in Fig. 4.5a-c). The average thickness of the granofels and spinifex lenses is 12.1 and 11.5 m, respectively, and varies for granofels lenses between 2.0 and 17.7 m, and for spinifex between 2.0 and 19.7 m. The half-surface area

of the granofels and spinifex is also similar and equal to $15 \cdot 10^3$ and $11 \cdot 10^3$ m^2, respectively, and fall in the range from 125 to $22 \cdot 10^3$ m^2 for the granofels lenses and 77 to $24 \cdot 10^3$ m^2 for the spinifex lenses. The average volume of the granofels and spinifex lenses is $125 \cdot 10^3$ and $80 \cdot 10^3$ m^3, respectively, and ranges for granofels lenses between 79 and $244 \cdot 10^3$ m^3, and for spinifex between 86 and $155 \cdot 10^3$ m^3.

The formation of granofels and spinifex lenses of Chl-harzburgite after Atg-serpentinite generated about $321 \cdot 10^3$ m^3 and $389 \cdot 10^3$ m^3 of H_2O, respectively, totalizing c. $711 \cdot 10^3$ m^3 of H_2O. The volume-weighted average volume of H_2O for the granofels and spinifex lenses (blue dashed and orange short-dashed vertical lines in Fig. 4.5d) is

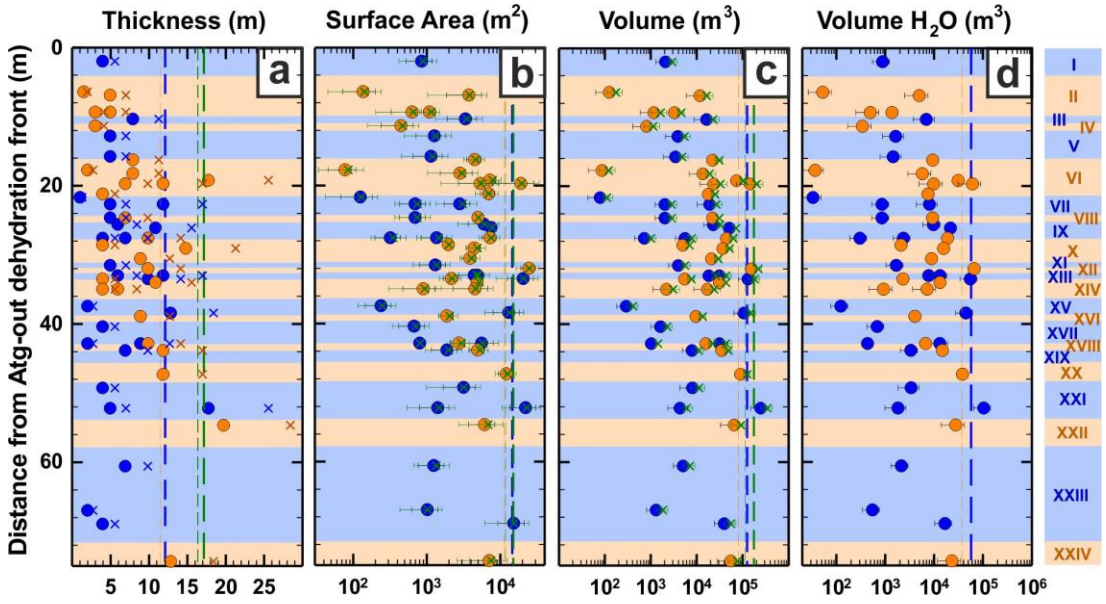

Figure 4.5. *Plots of the (a) thickness, (b) half-surface area, (c) volume and (d) initial water content of granofels (blue circles) and spinifex (orange circles) Chl-harzburgite lenses and corresponding precursor Atg-serpentinite lenses (blue and orange X's, respectively to granofels and spinifex in (a) and green X's in (b) and (c)) as a function of their distance to the Atg-out dehydration surface. The distance to Atg-out dehydration surface is the minimum vertical distance of the mid-point of the Chl-harzburgite lens to the Atg-out dehydration plane assuming a similar strike and dip of 10º for the L-I plane of lens and Atg-out plane. The thickness of a lens is parallel to the S-axis. The water content is the hypothetical volume of water (i.e., a pure hydrous fluid and its volume non-corrected for P-T conditions of Atg-out dehydration) produced by the Atg-breakdown reaction in the MASH system (MgO-Al_2O_3-SiO_2-H_2O): 1 Atg = 4 Chl + 6 Ol + 6 En + 15 H_2O (Padrón-Navarta et al., 2013; mineral abbreviation after Whitney and Evans, 2010). The blue dashed and orange short-dashed vertical lines are the volume-weighted averages for the granofels and spinifex lenses, respectively. The green thick dashed and thin short-dashed vertical lines represent the same for the precursor Atg-serpentinite lenses, recalculated from granofels and spinifex Chl-harzburgite, respectively. The light orange and blue areas mark the intervals where spinifex and granofels lenses occur, indicated with roman numbering to the right.*

$53 \cdot 10^3$ and $34 \cdot 10^3\, m^3$, respectively, and ranges from 33 to $103 \cdot 10^3\, m^3$ for the granofels lenses, and from 36 to $66 \cdot 10^3\, m^3$ for the spinifex lenses.

4.3.2 Volume, size and shape of precursor Atg-serpentinite domains

The current volume of the Chl-harzburgite lenses is different from the volume of their precursor Atg-serpentinite domains. In this section, we consider changes in volume that occurred during Atg-serpentinite dehydration to infer the volume, size and shape of the precursor Atg-serpentinite domains.

The pseudosection in Figure 4.6 (white and black contour areas; see figure caption for details on the calculations) shows the volume of H_2O (Fig. 4.6a), solids (Fig. 4.6b) and the total volume (solid + H_2O; Fig. 4.6c) for a serpentinite over the range of 0.5 – 2 GPa and 200 – 800 $°C$ (colored background Fig. 4.6). The total volume change (ΔV_t) of the Atg-serpentinite dehydration to Chl-harzburgite results in a net increase of the volume of fluids ($+\Delta V_f$; Fig. 4.6a) and a net decrease in the solid volume ($-\Delta V_s$; Fig. 4.6b) (Brantut et al., 2017; Padrón-Navarta et al., 2010, 2011). Atg-serpentinite dehydration at Almirez occured at 1.6-1.9 GPa and 650-680 $°C$ (López Sánchez-Vizcaíno et al., 2009; Padrón-Navarta et al., 2010, 2011). Within this temperature range and at increasing temperature, the volume of water increases (Fig. 4.7a) and that of solid decreases (Fig. 4.7b) along the Opx-in and the Atg-out isograd, respectively. The zone within these two events is marked by the transitional lithologies (Padrón-Navarta et al., 2011) of partially dehydrated Atg-serpentinite. The transitional lithologies mark a net decrease in total volume, i.e. $-\Delta V_t$, whereas at full dehydration at the Atg-out, a net increase in total volume, i.e. $+\Delta V_t$, occurs (Fig. 4.7c).

The total volume change considering the Opx-in and the Atg-out isograds is given in Table 4.1 in pressure steps of 0.1 GPa. The Atg-out results in a significant porosity production of $-\Delta V_s$ of c. -22.5 $vol.\%$, that is similar to those inferred in previous studies (-21.5–25 $vol\%$; Brantut et al., 2017; Padrón-Navarta et al. 2010b, 2011). From 1.5 to 2 GPa, after the Opx-in, the $-\Delta V_t$ changes from -0.1 to -0.5 $vol.\%$ (Table 4.1; Fig 4.6c). For full dehydration (i.e. after the Atg-out isograd), $+\Delta V_t$ decreases with increasing pressure from +1.0 $vol.\%$ to +0.04 $vol.\%$ (see also Brantut et al., 2017). At 1.8 GPa along the prograde dehydration path of the Almirez massif (Laborda-López et al., 2018),

the solid volume decreased by -22.4 $vol.\%$ for Atg-serpentinite dehydration, and the fluid volume increased +22.8 $vol.\%$ per unit volume (Fig. 4.7a-b). The dehydration of Atg-serpentinite into Chl-harzburgite in the Almirez massif resulted in a volume change of +0.4 $vol.\%$.

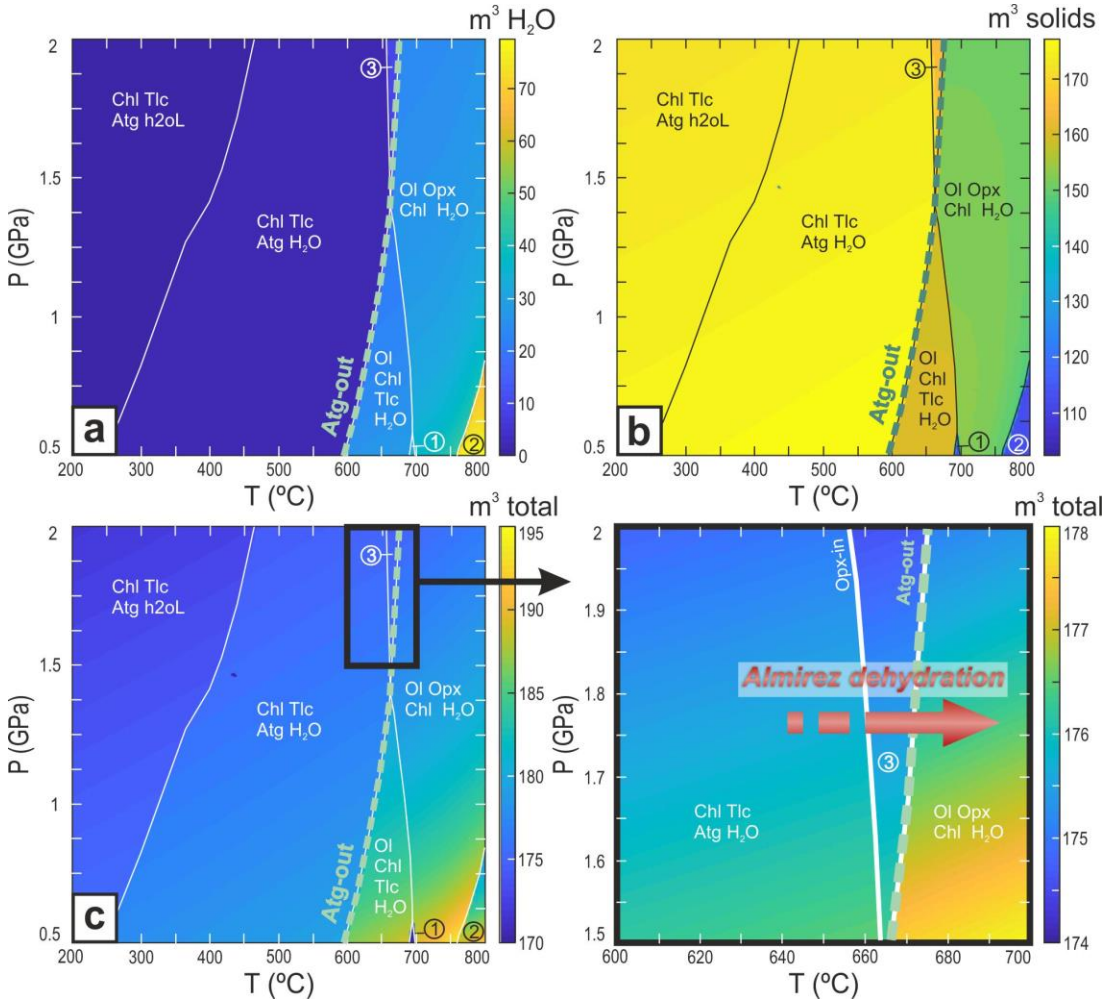

Figure 4.6. *Phase diagram pseudosection in the MASH system with solution models for Atg, Chl, Ol, Opx, Tlc (mineral abbreviations after Whitney and Evans, 2010) and H_2O, showing prograde metamorphic reactions of Atg-serpentinite into its dehydration products in pressure and temperature conditions of 0.5-2 GPa and 200-800 ºC. Phase assemblages in numbered pseudo-invariant fields are: (1) Ol-Chl-Ath-H_2O, (2) Ol-Opx-Sap-H_2O, (3) Opx-Chl-Atg-H_2O. Colored background indicates the total absolute volume (m^3) per unit of (a) H_2O, (b) the solid phases Atg+Chl+Ol+Opx+Tlc and (c) the total solid phases + H_2O, with in (c) including a close-up in the range of 1.5-2 GPa and 600-700 ºC. The disappearance of Atg is indicated with an Atg-out isograd (greenish dashed line) and the appearance of Opx with an Opx-in isograd, labeled in the zoom of (C). The prograde Almirez Atg-serpentinite dehydration reaction around 1.8 GPa is indicated with a red arrow in the zoom of (c). The computations are made with Perple_X (Connolly, 2005) and the dataset of Holland and Powell (1998), using the CORK fluid equation of state (Holland and Powell, 1991, 1998) with a initial composition of 44 MgO, 4 Al_2O_3, 32 SiO_2, 31 H_2O molar amounts and solution models for Opx, Chl, Ol, Tlc (Holland and Powell, 1998), and Atg (Padrón-Navarta et al., 2013).*

Taking into account a +0.4 $vol.\%$, we reconstruct the volume of precursor Atg-serpentinite by adding the volume of water (V_{H_2O}; eq. 4.9) to the volume of the Chl-harzburgite lens (V; eq. 4.1) and incorporating the factor 1.004 for the net total volume change. The volume (m^3) of the precursor Atg-serpentinite domains is calculated as:

$$V_{Atg} = \frac{V+V_{H_2O}}{1.004} \tag{4.10a}$$

Assuming that the precursor Atg-serpentinite lens was a triaxial ellipsoid, the volume can be represented by its semi-axes as (similar to eq. 4.1):

$$V_{Atg} = \frac{4}{3}\pi \cdot \left(L_{Atg} \cdot I_{Atg} \cdot S_{Atg}\right) \tag{4.10b}$$

where L_{Atg}, I_{Atg} and S_{Atg} are respectively longest, intermediate and shortest semi-axis (m) of this Atg-serpentinite lens. Due to compaction during dehydration, the longest and intermediate semi-axes are approximately unchanged ($L_{Atg} = L$ and $I_{Atg} = I$), while the shortest semi-axis S_{Atg} is shortened to S over a distance to account for the loss of water volume (i.e. V_{H_2O}). The former thickness (m) of the Atg-serpentinite lenses can be recalculated through S_{Atg} as:

$$2 \cdot S_{Atg} = 2 \cdot \frac{3}{4\pi LI} V_{Atg} \tag{4.11}$$

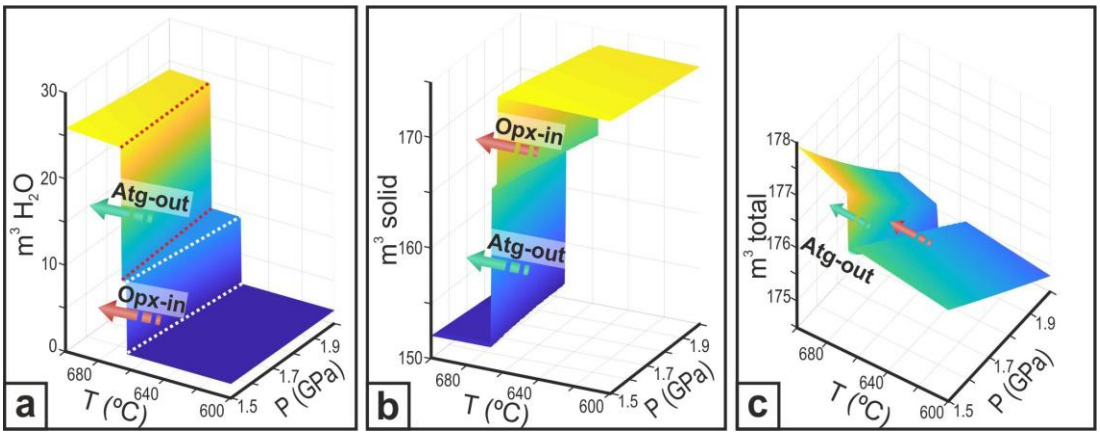

Figure 4.7. *3-D presentation of the absolute volumes (m^3) per unit of (a) H_2O, (b) solids and (c) total solid phases + H_2O. Solids are Atg, Chl, Ol, Opx and Tlc (mineral abbreviations after Whitney and Evans (2010); see Fig. 4.6 for details). Pressure and temperature range is 1.5-2 GPa and 600-700 ºC. the Opx-in isograd is indicated with a red arrow and the Atg-out isograd with a greenish arrow, both indicating jumps in water release (in a), accompanied with jumps in solid volume decrease (in b). Calculations were made using the Perple_X software (Connolly, 2005).*

and former Surface Area (m^2) as (similar to eq. 4.2):

$$(SA)_{Atg} = 4\pi \cdot \left(\frac{L^p I^p + L^p (S_{Atg})^p + I^p (S_{Atg})^p}{3}\right)^{1/p} \quad (4.12)$$

From these computations, we can calculate the volume of precursor Atg-serpentinite lenses, thickness and half-surface (Fig. 4.5a-c). The volume-weighted average volume of the Atg-serpentinite lenses was $177 \cdot 10^3$ and $114 \cdot 10^3$ m^3, with respect to their succeeding granofels and spinifex Chl-harzburgite lenses, respectively, which varied between 111 and $346 \cdot 10^3$ m^3 and between 122 and $220 \cdot 10^3$ m^3, respectively (green X symbols; Fig. 4.5c).

Due to compaction, the thickness of a Chl-harzburgite lens —i.e. lens shortest semi-axis— is significantly shorter than of its precursor Atg-serpentinite lens that were c. 41.8% thicker. For the Atg-serpentinite lenses that preceded the granofels and spinifex Chl-harzburgite lenses, respectively, the volume-weighted average thickness is 17.1 and 16.4 m, ranging between 2.8 and 25.1 m and between 2.8 and 27.9 m, respectively (blue and orange X symbols, respectively, in Fig. 4.5a), and the thickness of the entire precursor Atg-serpentinite section was approximately 100 m (~ $70 \cdot 1.418$ m). The half-surface areas of Atg-serpentinite lenses, on the other hand, are within error similar to the ones of the Chl-harzburgite lenses. The volume-weighted average is $15 \cdot 10^3$ and $12 \cdot 10^3$ m^2 for the Atg-serpentinite lenses precursor of the granofels and spinifex Chl-harzburgite lenses,

Table 4.1. *Volume changes in volume percentage (vol.%) of the Atg-serpentinite dehydration*

P (GPa)	T (°C)		H_2O (vol.%)		solid (vol.%)		total (vol.%)	
	Opx-in	Atg-out	Opx-in	Atg-out	Opx-in	Atg-out	Opx-in	**Atg-out**
1.5	663	666	+8.1	+23.7	-8.2	-22.7	-0.1	**+1.0**
1.6	662.5	669	+8.1	+23.4	-8.3	-22.6	-0.2	**+0.8**
1.7	661.5	670.5	+8.0	+23.1	-8.3	-22.6	-0.3	**+0.5**
1.8	660	672.5	+7.9	+22.8	-8.3	-22.4	-0.3	**+0.4**
1.9	685.5	674	+7.8	+22.5	-8.2	-22.3	-0.4	**+0.2**
2.0	656.5	675	+7.7	+22.2	-8.2	-22.2	-0.5	**+0.04**

Compute for the MASH system over a pressure (P) range of 1.5-2 GPa with increments of 0.1 GPa. Two isograds are crossed, being Opx-in and Atg-out, respectively. Per P-increment, the temperature (T) is given at which the two isograds are crossed. Likewise, volume changes (positive as '+' and negative as '-') are given for H_2O, solids and the total volume (being H_2O+solid), each time with respect to the precursor Atg-serpentinite volume (being field Chl+Tlc+Atg+H_2O in Figs. 4.6 and 4.7).

respectively, which range between 128 – $23 \cdot 10^3$ m^2 and between 85 – $25 \cdot 10^3$ m^2, respectively (green X symbols in Fig. 4.5b).

4.4 Discussion

4.4.1 Physical mechanism for episodic Atg-serpentinite dehydration in Almirez

The spatial alternation of granofels and spinifex Chl-harzburgite lenses in the Almirez massif below the dehydration front implies that crystallization of Chl-harzburgite occurred in an episodic sequence of Atg-serpentinite dehydration and fluid release events as predicted by theoretical models. The similar average length scale and volume of the lenses points out that the periodicity in fluid release was triggered by an instability with a characteristic length scale of ~10–30 m. This unique indication of the length scale associated with Atg-serpentinite dehydration in the natural record provides an unprecedented opportunity to test whether these length scales are consistent with those predicted by different theoretical models.

Theoretical models predict the episodic nature of fluid expulsion and flow in metamorphic devolatilization reactions (Connolly, 1997; Connolly and Podladchikov, 1998; Ferry and Gerdes, 1998; Nur and Walder, 1992). One potential mechanism for periodic fluid release in dehydrating systems is the *dehydration-driven compaction instability* (Connolly, 1997; Connolly and Podladchikov, 1998, 2013). For a viscous rock rheology and power law relating porosity and permeability, this two-phase flow instability is due to the coupling between mechanical compaction and pore fluid pressure build-up due to dehydration. This results in periodic fluid escape upward in so-called *"porosity waves"* (Connolly and Podladchikov, 2013; Connolly, 1997, 2010; Padrón-Navarta et al., 2011; Skarbek and Rempel, 2016). This instability occurs typically over characteristic length scales known as the viscous *"compaction length"* ($\delta_c; m$), which is the minimum length scale needed for compaction to squeeze out the fluids from the fluid-pressurized domains (Connolly, 1997; Connolly and Podladchikov, 1998, 2013; McKenzie, 1984). The compaction length increases with bulk rock strength —the bulk, shear viscosity ($\eta; Pa\ s$)— and with the ease that fluids can flow through the rock —the permeability ($k_\phi; m^2$) over fluid viscosity ($\mu; Pa\ s$)— (McKenzie, 1984):

$$\delta_c = \sqrt{\frac{\eta}{\mu} k_\phi} \tag{4.13}$$

At high pressure and temperature, the fluid viscosity can be considered constant: c. $1 \cdot 10^{-3}\ Pa\ s$ (Abramson, 2007). The compaction length becomes then a function of permeability and shear viscosity (η).

The permeability ($k_\phi;\ m^2$) of precursor Atg-serpentinite in Almirez can be estimated through the Kozemy-Carman equation (Okazaki et al., 2014; Turcotte and Schubert, 1982):

$$k_\phi = \frac{d^2 \phi^3}{180(1-\phi)^2} \tag{4.14}$$

where d is the antigorite grainsize ($d;\ m$) and ϕ is porosity. The range of d in Almirez Atg-serpentinite is $2 \cdot 10^{-5} - 2 \cdot 10^{-4}\ m$ (Padrón-Navarta et al., 2008; Padrón-Navarta et al., 2012; Padrón-Navarta et al., 2015). The ϕ of typical Atg- serpentinite ranges between $4 \cdot 10^{-4} - 4 \cdot 10^{-3}$ (Kawano et al., 2011) (see Table 4.2). Using these ranges of grain size and porosity, we estimated that the permeability of Almirez Atg-serpentinite ranges from $1.4 \cdot 10^{-22} - 1.4 \cdot 10^{-17}\ m^2$. This permeability range lies within the range of permeability of crystalline and metamorphic rocks (10^{-23}–$10^{-16}\ m^2$) (Ague et al., 1998; Brace, 1980; Manning and Ingebritsen, 1999; Turcotte and Schubert, 1982). Our estimates of k_ϕ for Almirez Atg-serpentinite are within the range of permeability evolution from $10^{-22}\ m^2$ to $10^{-18}\ m^2$ obtained in serpentinite dehydration experiments (at 600–700 $°C$; Tenthorey and Cox, 2003), and of $10^{-22}\ m^2$ to $10^{-19}\ m^2$ inferred, respectively, for k_ϕ perpendicular and parallel to Atg-serpentinite foliation (Kawano et al., 2011).

The shear viscosity ($\eta;\ Pa\ s$) of Atg-serpentinite can be estimated from the stress (σ ; Pa), and strain rate ($\dot{\varepsilon}$; s^{-1}) (Hilairet et al., 2007):

$$\eta = \frac{\sigma}{\dot{\varepsilon}} \tag{4.15}$$

or from the strain rate-dependent flow law of serpentine (Hilairet et al., 2007):

$$\eta = \left(\frac{2}{3}\right)^{\frac{1}{n}} A^{\frac{-1}{n}} \dot{\varepsilon}^{\frac{1-n}{n}} exp\left(\frac{E_a + PV^*}{nRT}\right) \tag{4.16}$$

with n the stress exponent, A a material parameter ($s^{-1}\ Pa^{-n}$), E_a the activation energy (J), P the pressure (Pa), V^* the activation volume ($m^3\ mol^{-1}$), R the gas constant

($J\ K^{-1}\ mol^{-1}$) and T the temperature (K) (Table 4.2). Based on the coexistence of orthopyroxene buckling and the inversion of enstatite to low clinoenstatite ($P2_1/c$) in the Almirez transitional lithologies generated during Atg-serpentinite dehydration and compaction, Padrón-Navarta et al. (2015) estimated lower bound for σ and $\dot{\varepsilon}$ in the order of 20–70 MPa and 10^{-13}–10^{-12} s^{-1}, respectively. Using these values and the parameters for serpentinite, we estimate η in the order of $2{\cdot}10^{19}$ – $7{\cdot}10^{20}$ $Pa\ s$ using eq. (4.15) and $7{\cdot}10^{18}$ – $3.8{\cdot}10^{19}$ $Pa\ s$ using eq. (4.16). These ranges of η correspond well to other values of $4{\cdot}10^{19}$ $Pa\ s$ (Hilairet et al., 2007) and other values in the literature ranging from 10^{18} –10^{21} $Pa\ s$ (Gerya et al., 2002; Horiuchi and Iwamori, 2016).

If the instability that triggered the episodic dehydration of Atg-serpentinite in Almirez was due to a viscous dehydration-driven compaction instability, the calculated length scale of the Atg-serpentinite domains precursor of the Chl-harzburgite lenses must

Table 4.2. *Parameters used in this study.*

Notation	Symbols	Units	Values	Reference
Fluid density	ρ_f	$kg\ m^{-3}$	1080.9	1
Fluid viscosity	μ	$Pa\ s$	$1x10^{-3}$	2
Grainsize antigorite	d	m	$2x10^{-5}$ – $2x10^{-4}$	3,4,5
Porosity	ϕ	-	$4x10^{-4}$ – $4x10^{-3}$	6
Stresses	σ	Pa	$2x10^{7}$ – $7x10^{7}$	5
Strain rate	$\dot{\varepsilon}$	s^{-1}	10^{-13} – 10^{-12}	5
Stress exponent	n	-	3.8	7
Material parameter	A	$s^{-1}\ Pa^{-n}$	$4.47\ x10^{-38}$	7
Activation energy	E_a	J	8900	7
Pressure	P	Pa	$1.8\ x10^{9}$	8
Activation volume	V^*	$m^3\ mol^{-1}$	$3.2\ x10^{-6}$	7
Gas constant	R	$J\ K^{-1}\ mol^{-1}$	8.31	
Temperature	T	K	923	8
Antigorite density	ρ_{Atg}	$kg\ m^{-3}$	3000	9
Earth gravity	g	$m\ s^{-2}$	9.80665	
Molar volume antigorite	V_m	$m^3\ mol_{Atg}^{-1}$	$1.73\ x10^{-3}$	10
Width antigorite-crystal	W	m	$5x10^{-5}$ – $2.5x10^{-4}$	3,4,5
Length antigorite-crystal	L	m	$1x10^{-5}$ – $6x10^{-5}$	3,4,5
Rate constant	κ'	$mol_{Atg}\ m^{-2}\ s^{-1}$	$9.2\ x10^{-11}$	11
Pore pressure at equilibrium	p_{eq}	Pa	$2\ x10^{9}$	
Net volume change per unit volume antigorite	c'	$m^3\ mol_{Atg}^{-1}$	$8.1\ x10^{-5}$	10

1) Abramson and Brown, 2004; 2) Abramson 2007; 3) Padrón-Navarta et al., 2008; 4) Padrón-Navarta et al., 2012; 5) Padrón-Navarta et al., 2015; 6) Kawano et al., 2011; 7) Hilairet et al., 2007; 8) Padrón-Navarta et al., 2010; 9) Hacker et al., 2003; 10) Brantut et al., 2017; 11) Eggler and Ehman, 2010.

be consistent with the theoretical viscous compaction length ($\delta_c; m$) for dehydrating serpentinite. Figure 4.8 shows the range of δ_c (eq. 4.14) as a function of k_ϕ and η estimated for Almirez Atg-serpentinite. The range of δ_c is strikingly similar to the range of thickness (3–30 m) of the Atg-serpentinite precursor of the Chl-harzburgite mapped in the Almirez massif (cf. Fig. 4.8b & Fig. 4.5a). The volume-weighted average thickness of the precursor Atg-serpentinite lenses (16.4 and 17.1 m, respectively) yields k_ϕ ~10^{-20} m^2 typical of serpentinite for the η of $2{\cdot}10^{19}$ – $4{\cdot}10^{19}$ $Pa\,s$ inferred for Almirez serpentinite. These results indicate that the intercalated network of Chl-harzburgite was very likely caused by the viscous dehydration-driven compaction of Atg-serpentinite as predicted in theoretical models. At Almirez, since the length scales of compaction length for typical permeability and viscosity values of Atg-serpentinite matches the length scales of Atg-serpentinite lenses precursor of Chl-harzburgite, porosity wave instabilities likely

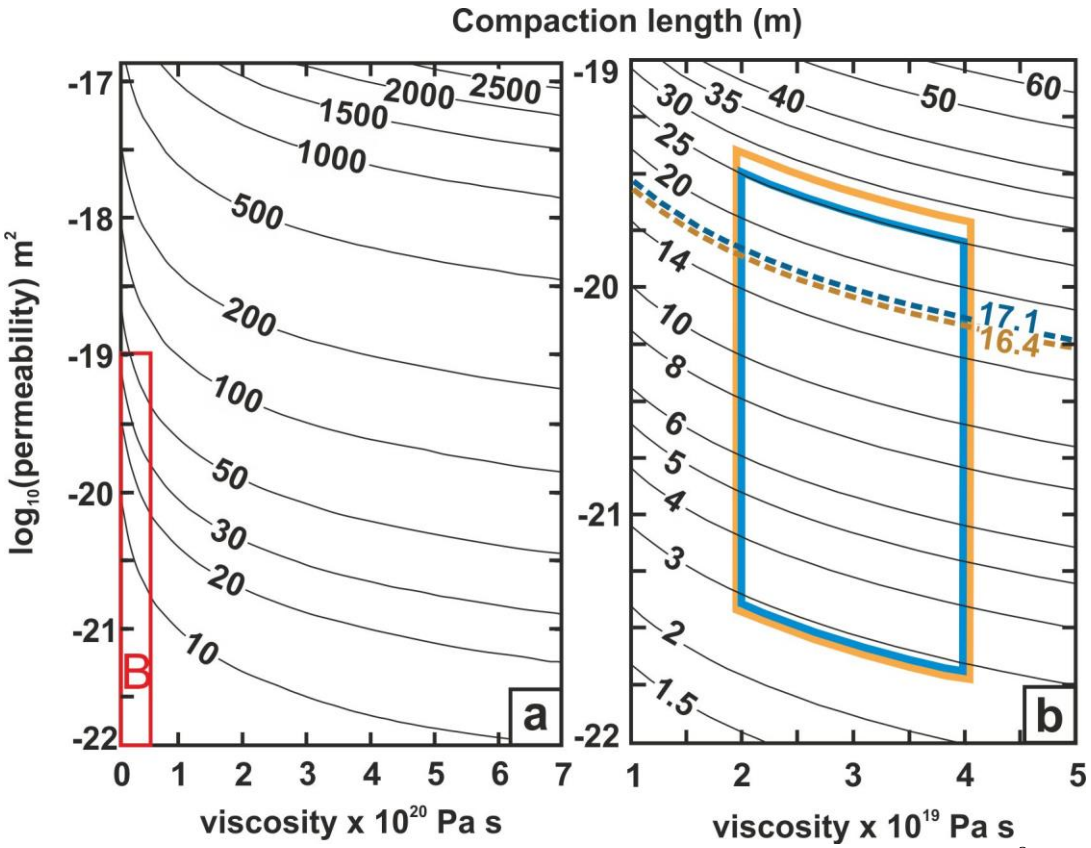

Figure 4.8. *The compaction length of serpentinite as a function of permeability (m^2) and viscosity (Pa s). (a) Viscosity and permeability range of serpentinite lithologies. (b) Viscosity range based on the viscosity law and stress and strain rate from the Almirez (Padrón-Navarta et al., 2015). Volume-weighted average thicknesses of precursor Atg-serpentinite lenses based on granofels (blue dashed line) and spinifex (orange dashed line) lenses are plotted with the compaction length. Full range of Atg-serpentinite lens thicknesses based on granofels lenses is 2.8 – 25.1 m (blue area) and on spinifex lenses is 2.8 – 27.9 m (orange area).*

drove episodic fluid release during near-equilibrium serpentinite dehydration. This would be the first natural record of the compaction length of these instabilities.

4.4.2 Origin of the sequence of textural domains

Padrón-Navarta et al. (2011, 2015) suggested that crystallization of granofels texture in Chl-harzburgite was driven by compaction and fluid draining by porosity waves, in good agreement with these results. Slow draining and compaction mechanism is also consistent with the shape and crystal preferred orientation (SPO and CPO) of olivine in granofels Chl-harzburgite (Ch. 5; Padrón-Navarta et al., 2011; Dilissen et al., 2018). To account for the different texture of the spinifex Chl-harzburgite, Padrón-Navarta et al. (2011) proposed that spinifex Chl-harzburgite crystallized at higher affinity of the Atg-serpentinite reaction from undrained domains of meta-stable serpentinite that were surrounded by rigid and impermeable granofels Chl-harzburgite that crystallized during draining by porosity waves. Our results show that the SPO and CPO of spinifex Chl-harzburgite (Ch. 5) display a remarkable orientation with the main paleo-stresses derived from the GSRZ, supporting that crystallization of spinifex happened by a mechanism other than compaction and somewhat mirroring the main stress in the subduction slab (Ch. 5; Dilissen et al., 2018). The study of transitional texture in Chl-harzburgite (Ch. 6; Dilissen et al., submitted) shows that crystallization of spinifex Chl-harzburgite occurred after that of granofels Chl-harzburgite and under higher time-integrated nucleation rates and the olivine's tabular texture is shown to be consistent with the arrival of open-system fluids. All these observations are in agreement with open-system and fast draining of meta-stable serpentinite at faster kinetic of the reaction producing spinifex texture, as proposed by Padrón-Navarta (2011). If so, the thickness of precursor Atg-serpentinite lenses would correspond to the sum of the drained domain that formed the granofels Chl-harzburgite, and the immediately below undrained domain that later formed the spinifex Chl-harzburgite. The sum of the volume-weighted average thickness of Atg-serpentinite —precursor to granofels and spinifex Chl-harzburgite— lenses is 35 m. This thickness is consistent with the viscous compaction length with permeability of ~10^{-19} m^2 in the viscosity range of $2{\cdot}10^{19}$ – $4{\cdot}10^{19}$ $Pa\,s$ inferred for the dehydrating Almirez Atg-serpentinite (Fig. 4.8b).

Draining and crystallization of the spinifex Chl-harzburgite has been linked to dehydration embrittlement by pore-fluid increase coupled to the decrease of effective stress (Padrón-Navarta et al., 2010b). An alternative is stress-transfer dehydration embrittlement (Brantut et al., 2017; Ferrand et al., 2017; Kita and Ferrand, 2018). In this mechanism, the stress relaxation in dehydrating, ductile serpentinite causes lateral transfer of stress load to surrounding rigid rocks —marked by granofels Chl-harzburgite— leading to rapid stress amplification that induces mechanical instability and brittle failure (Bloch et al., 2018; Brantut et al., 2017; Ferrand et al., 2017; Rutter et al., 2009). However, this instability only arises when there is a net negative volume change during devolatilization reaction. At Almirez, at completion of the dehydration reaction the total volume change is close to zero and positive (+0.4 $vol.\%$ at 1.8 GPa). The appearance of orthopyroxene on behalf of antigorite breakdown at the onset of dehydration is associated with a slight negative total volume change (-0.3 $vol.\%$ at 1.8 GPa). Thus, dehydration instabilities might have occurred at dehydration onset (Brantut et al., 2017), in which, at Almirez conditions (1.5–2 GPa), the Opx-in isograd is crossed, but not yet the Atg-out isograd (Fig. 4.7). This would provide the feasible development of fluid pressure instabilities, in the case the dehydration rate exceeded the viscous compaction rate. Such a dehydration-driven stress transfer mechanism could induce short-lived hydrocracking —likely recorded by the GSRZ— and open-system arrival of external fluids that would explain the structure, texture and crystallization of spinifex Chl-harzburgite (Ch. 5 and 6).

4.4.3 Timescales of episodic fluid expulsion

In the Almirez massif, the timescales of episodic fluid expulsion during viscous compaction can be estimated from the length scales inferred from the mapping of the Chl-harzburgite lenses. In absence of instabilities and over the compaction length the fluid flow velocity (v; $m\ yr^{-1}$) during near-confining pressure dehydration is approximately the same as the rate of compaction and is given by (Connolly and Podladchikov, 2013):

$$v \approx d_{avr}^2 \phi_{avr}^2 (\rho_{Atg} - \rho_f) g/\mu \qquad (4.17)$$

with d_{avr} and ϕ_{avr} an average grainsize and porosity ($7 \cdot 10^{-4}$; from eq. 4.14, for d_{avr} and $k_\phi = 10^{-20}\ m^2$) for antigorite, ρ_{Atg} the density of antigorite ($kg\ m^{-3}$) at ca. 2 GPa and 650

°C (Hacker et al., 2003), and g the gravitational acceleration ($m\ s^{-2}$) (see Table 4.2 for parameters). For an average grainsize of $7.25 \cdot 10^{-5}\ m$, characteristic of Almirez Atg-serpentinite, and a serpentinite porosity of $7 \cdot 10^{-4}$ (eq. 4.14) fluid flow velocity over the compaction length through an undisturbed dehydrating serpentinite is 1.5 $m\ yr^{-1}$.

If the compaction rate is similar to fluid production rate, the compaction timescale (τ_c; s) can be obtained from v ($m\ s^{-1}$) and the compaction length (Connolly and Podladchikov, 2013):

$$\tau_c = \frac{\delta_c}{v} \tag{4.18}$$

The timescale of compaction-driven fluid expulsion for the 15 to 35 m thickness in this study is thus estimated to be 10 – 23 yr (Connolly and Podladchikov, 2013; Connolly, 2010). These pulses from metamorphic events typically happen over a time span of thousands of years or less (Bebout and Penniston-Dorland, 2016; Eggler and Ehmann, 2010; John et al., 2012; Tian et al., 2018; Zack and John, 2007). If the fluid production rate is slower than viscous compaction rates, the timescale increases up to three orders of magnitude.

If spinifex Chl-harzburgite were drained via a stress-transfer mechanism, the timescale of these instabilities would be determined by reaction kinetics as $1/r_0$ (s) (Brantut et al., 2017):

$$r_0 = V_m A^0_{rlm} \kappa' \left| \frac{p_{eq} c'}{RT} \right|^{n_r} \tag{4.19}$$

with V_m ($m^3\ mol^{-1}_{Atg}$) the molar volume of antigorite, A^0_{rlm} ($m^2\ m^{-3}$) the initial specific surface area of the rate limiting mineral (antigorite; Brantut et al., 2017; Eggler and Ehmann, 2010), κ' ($mol_{Atg}\ m^{-2}\ s^{-1}$) the rate constant, p_{eq} (Pa) the pore pressure at equilibrium, c' the net volume change of the reaction per unit volume antigorite ($m^3\ mol^{-1}_{Atg}$), R ($J\ K^{-1}\ mol^{-1}$) the gas constant, T (K) the temperature of dehydration, and n_r the reaction exponent (see Table 4.2 for parameters). Experimental work indicates that $n_r\ is$ approximately 1 (i.e., linear) or 2 (Eggler and Ehmann, 2010; Perrillat et al., 2005; Weber and Greer, 1965). When approximated as a square prism, A^0_{rlm} depends on the width (W; m) and length (L; m) through the equation (Eggler and Ehmann, 2010):

$$A^0_{rlm} = \frac{2W^2 + 4LW}{LW^2} \tag{4.20}$$

In Almirez Atg-serpentinite, antigorite crystals have W and L in the order of $1{\cdot}10^{-5}$ – $6{\cdot}10^{-5}$ m and $5{\cdot}10^{-5}$ – $2.5{\cdot}10^{-4}$ m, respectively (Dilissen et al., 2018; Padrón-Navarta et al., 2008, 2012, 2015), yielding a A^0_{rlm} range of $4.9{\cdot}10^4$ – $2.8{\cdot}10^5$ $m^2\ m^{-3}$. For a p_{eq} of 2 GPa and near-equilibrium linear kinetics (n_r = 1) (Brantut et al., 2017; Eggler and Ehmann, 2010), r_0 (eq. 4.19) ranges between $1.7{\cdot}10^{-7}$ – $9.4{\cdot}10^{-7}$ s^{-1} that corresponds to a timescale ($1/r_0$) for these instabilities of 12 – 70 $days$. For nonlinear kinetic of order two (n_r = 2), r_0 ranges between $3.5{\cdot}10^{-6}$ – $2.0{\cdot}10^{-5}$ s^{-1} that corresponds to a timescale ($1/r_0$) of 14 h up to 3 days. This timescale suggests that, if spinifex Chl-harzburgite is formed by this instability, it can form in very short-lived events of hydrocracking.

4.4.4 Fluid fluxes during Atg-serpentinite dehydration

4.4.4.1 *Estimated fluid fluxes for Almirez Atg-serpentinite dehydration*

Metamorphic rocks record time-integrated fluid fluxes ($m^3\ m^{-2}$) (Ferry, 1994), which are difficult to estimate in nature due to uncertainties in constraining the size and shape over which the flux integrated (Bebout and Penniston-Dorland, 2016). Our 3-D mapping in the Almirez massif provides a good opportunity to estimate the fluxes associated with episodic events of Atg-serpentinite dehydration at intermediate-depth of subduction slab. The time-integrated flux ($m^3\ m^{-2}$) per half surface $(SA)_{Atg}$ of the Atg-serpentinite precursors of Chl-harzburgite lenses can be computed as:

$$F_{(SA)_{Atg}} = \frac{2{\cdot}V_{H_2O}}{(SA)_{Atg}} \tag{4.21}$$

with V_{H_2O} (eq. 4.9) and $(SA)_{Atg}$ (eq. 4.12). The estimated volume-weighted average time-integrated fluxes are 2.9 $m^3\ m^{-2}$ and 2.7 $m^3\ m^{-2}$ for the precursor Atg-serpentinite of the granofels and spinifex Chl-harzburgite domains (Fig. 4.9), which are similar to the $F_{(SA)_{Atg}}$ (2.8 $m^3\ m^{-2}$) if the flux is calculated using the total mapped surface instead of that of individual lenses (see Appendix Table 4.A2). These are similar to the theoretical time-integrated fluid fluxes of 7 $m^3\ m^{-2}$ estimated at the head of porosity waves (Tian et al., 2018; their fig. 9a).

If the fluid flux occurred focused along hydrofractures and cracks (F_{HC}) of thickness t_{HC}, the time-integrated flux (F_{HC}) can be estimated substituting $(SA)_{Atg}$ in eq. (4.21) by $t_{HC}(L+I)$ (m^2) that is the surface area of the cracks with longest, L, and

intermediate, I, dimensions of thickness t_{HC}. For a t_{HC} of 1 m (Fig. 4.9; Appendix Table 4.A3), the time-integrated F_{HC} varies between 12 – 341 $m^3\ m^{-2}$, with volume-weighted averages of 198 $m^3\ m^{-2}$ and 226 $m^3\ m^{-2}$ for the precursor of the spinifex- and granofels-textured domains. These F_{HC} fluxes increase by an order of magnitude in fluid extraction if they are focused in thinner cracks of t_{HC} = 0.1 m (Fig. 4.9). The time-integrated fluid fluxes F_{HC} considering all mapped areas and spaced 2 – 50 m ranges from 8–141 $m^3\ m^{-2}$ and 58–1388 $m^3\ m^{-2}$ for cracks of 1 and 0.1 m, respectively (see Table 4.A2).

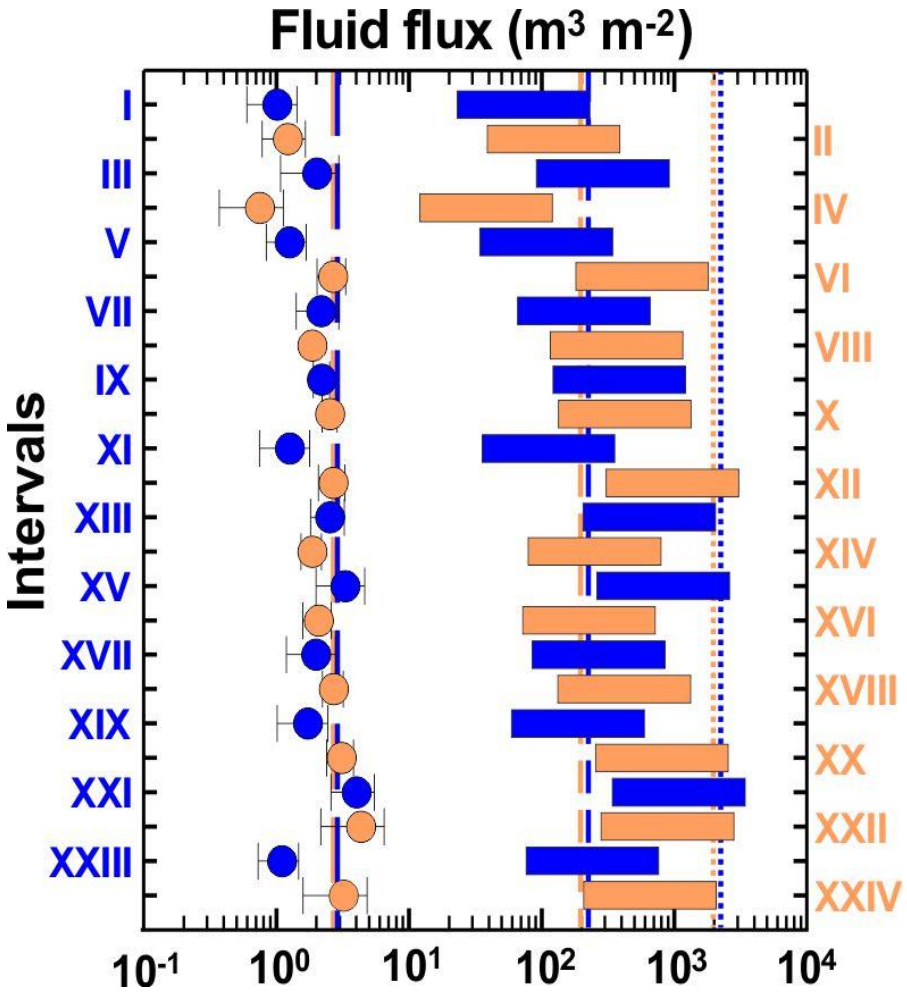

Figure 4.9. *Time-integrated fluxes (*$m^3\ m^{-2}$*) per textural interval (roman numbers, cf. Fig. 4.5; light orange is spinifex and blue is granofels Chl-harzburgite interval). Circles depict the flux per surface area of the lenses. Floating bars depict range of flux through hydrocracking with thickness ranging from 0.1 - 1 m (respectively, upper and lower end of the floating bar; see text).*

4.4.4.2 *Comparison with fluxes estimated from models and metamorphic terranes*

Figure 4.10 compares the fluid fluxes estimated for the Almirez massif with those derived from theoretical models and different observables and data in other exhumed metamorphic terranes. Estimated time-integrated fluid fluxes for fluids released from dehydration reactions at the top of the slab at subarc depth of 300 $m^3\ m^{-2}$ for a 7-10 km thick slab layer (Schmidt and Poli, 1998; Zack and John, 2007) reduces to c. 3 $m^3\ m^{-2}$ for a 70-100 m thick layer (i.e. dimensions of Almirez Chl-harzburgite) (long gray dashed line; Fig. 4.10). Based on numerical models, Rüpke et al. (2004) estimated time-integrated fluxes in young (20 Myr) and old (160 Myr) serpentinized mantle (83.3–425.6 $m^3\ m^{-2}$) associated with dehydration of a 10-km thick section that yields 0.8–4.3 $m^3\ m^{-2}$ for a 100 m cross section (Fig. 4.10). Both estimates are remarkably similar to the Almirez $F_{(SA)_{Atg}}$ of 2.8 $m^3\ m^{-2}$ (Table 4.A2). These Atg-dehydration fluxes are substantially higher than fluxes associated with dehydration of subducted oceanic crust derived from models (0.5 $m^3\ m^{-2}$; Ague, 2007) and exhumed Alpine metamorphic terranes in the Alps ($1.6{\cdot}10^{-2}\ m^3\ m^{-2}$; Philippot and Rumble, 2000).

Many metamorphic terranes exhibit veining networks indicating that fluid flow was focused along veins, thus resulting in several orders of magnitude increase in fluid fluxes compared to estimates based on non-focused fluid flow (Fig. 4.10) (Healy et al., 2009; Philippot and Rumble, 2000; Plümper et al., 2017; Spandler et al., 2011; Zack and John, 2007). Time-integrated fluid fluxes in veins of fluid derived from the dehydration at the top of a subducting slab (7-10 km) range $3{\cdot}10^3$–$3{\cdot}10^4\ m^3\ m^{-2}$ for a vein density of 10% and 1% (Zack and John, 2007), which in a vertical column of 70-100 m thick layer would be 30 $m^3\ m^{-2}$ (short gray dashed line; Fig. 4.10) to 300 $m^3\ m^{-2}$ (dotted gray line; Fig. 4.10), respectively. These results compare reasonably well with the Almirez values for time-integrated fluid fluxes of 30.5 – 280 $m^3\ m^{-2}$ if Atg-serpentinite fluids are focused in cracks (F_{HC}) spaced 10% and 1% (Table 4.A2), respectively. Similarly, F_{HC} fluxes estimated for the Almirez massif are in the range of those obtained in numerical models of the Cascadian hot subduction zone at 100 km depth (van Keken et al., 2011) that we estimate from the model parameters to be in the range of 58.6 $m^3\ m^{-2}$. The Cascadian estimated fluxes would be equivalent to Almirez-derived F_{HC} fluxes for 1 m thick veins spaced 20 m apart or to 0.1 m thick veins spaced 2 m apart (58.2 $m^3\ m^{-2}$; Table 4.A2).

Other estimated fluxes from deep crust terranes are in similar order ranges as discussed above. Modeling estimates prograde metamorphic dehydration of eclogite to be 5 – 50 $m^3\ m^{-2}$ (Fig. 4.10), if based on varying vein spacing of 10 – 100 m (Zack and John, 2007). Fracture flow in granulite terranes is estimated to maintain below 20 $m^3\ m^{-2}$ and eclogite veining within metamorphic terrane to reach up to 800 $m^3\ m^{-2}$ (Ferry and Gerdes,

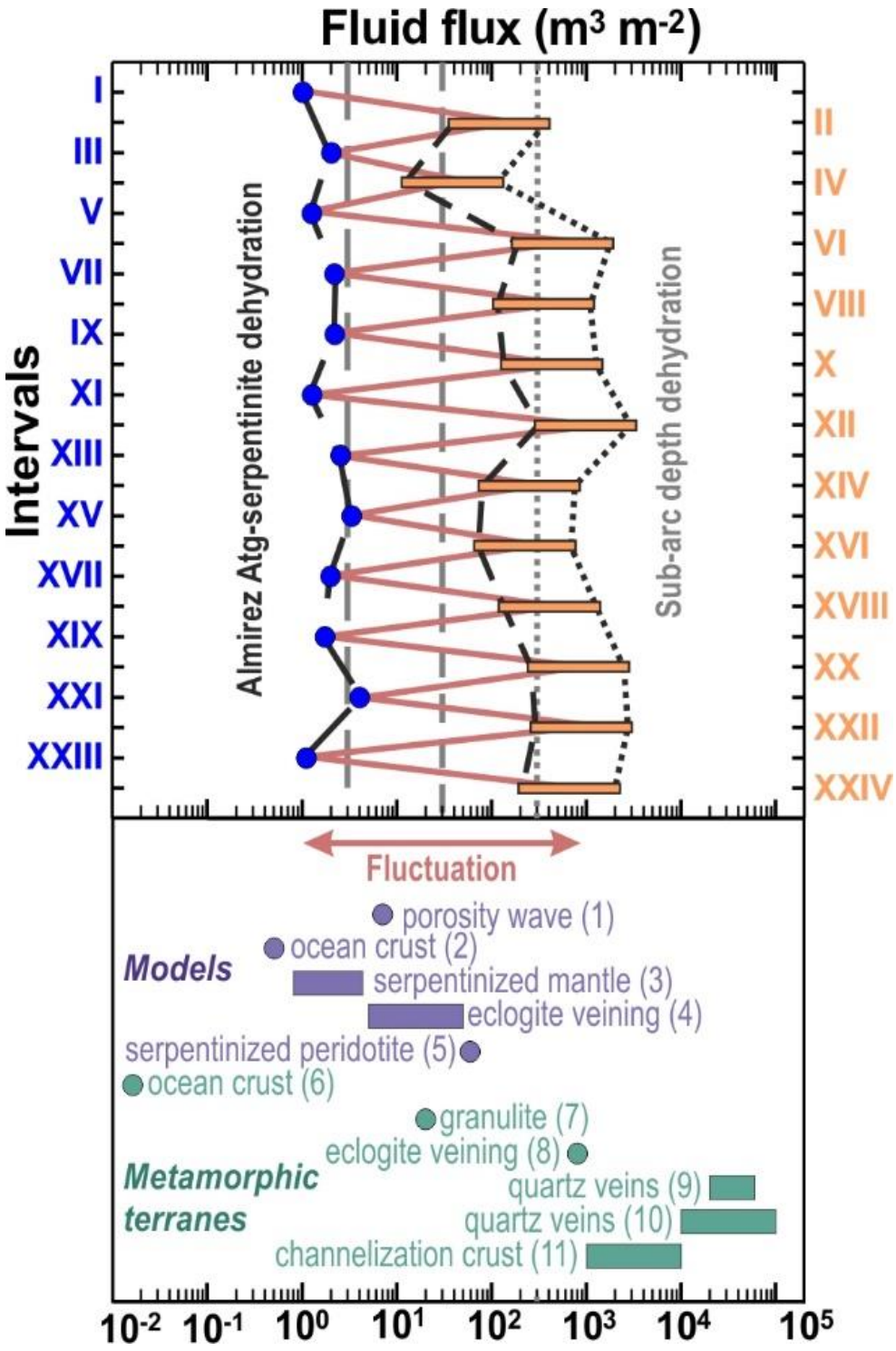

1998). At shallower levels, time-integrated fluid fluxes range e.g. from 2–6 $\cdot 10^4\ m^3\ m^{-2}$ in quartz veins of metapelites (Penniston-Dorland and Ferry, 2008), $10^4 - 10^5\ m^3\ m^{-2}$ for quartz veins in schists of an accretionary prism (Breeding and Ague, 2002) or $10^3 - 10^4\ m^3\ m^{-2}$ for general fracture fluid flow in upper and middle crust (Ferry and Gerdes, 1998; Zack and John, 2007) (Fig. 4.10).

Figure 4.10. *Time-integrated fluxes (*$m^3\ m^{-2}$*) per textural interval (roman numbers, cf. Fig. 4.5; light orange is spinifex and blue is granofels Chl-harzburgite interval). The long dashed black line with blue dots depicts flux per surface area of the granofels textured lenses. Short dashed and dotted black line, respectively, depict flux for hydrocracks with 1 m and 0.1 m thickness and are interspaced with orange bars. Pink solid line is the flux fluctuation between each successive textural interval. Vertical gray lines represent the time-integrated flux at the top of subducting slab, recalculated for a 70-100 m thickness layer (see text for details); long dashed being unfocused flow (3* $m^3\ m^{-2}$*); short dashed (30* $m^3\ m^{-2}$*) and dotted (300* $m^3\ m^{-2}$*) focused flow in veins with 10% and 1% spacing, respectively (Schmidt and Poli, 1998; Zack and John, 2007). Floating bars and dots in the lower panel represent time-integrated fluxes from models (purple) 1) porosity wave after metamorphic dehydration (7* $m^3\ m^{-2}$*) (Tian et al., 2018); 2) Complete dehydration oceanic crust (gabbro and basalt) (0.5* $m^3\ m^{-2}$*) (Ague, 2007); 3) young to old deserpentinizing mantle (0.8-4.3* $m^3\ m^{-2}$*) (Rüpke et al., 2004); 4) Eclogite prograde metamorphic dehydration with vein spacing 10-100 m (5-50* $m^3\ m^{-2}$ *)(Zack and John, 2007); 5) Dehydration serpentinized peridotite into chlorite-bearing peridotite at c. 100 km depth of the Cascadian subduction zone (58.6* $m^3\ m^{-2}$*) (van Keken et al., 2011); and metamorphic terranes (green) 6) Subducted oceanic crust in cold subduction zone environment (*$1.6 \cdot 10^{-2}\ m^3\ m^{-2}$*) (Philippot and Rumble, 2000); 7) granulite terranes (<20* $m^3\ m^{-2}$*) (Ferry and Gerdes, 1998); 8) eclogite veining (<800* $m^3\ m^{-2}$*) (Ferry and Gerdes, 1998); 9) quartz veins in metapelites (2-6* $\cdot 10^4\ m^3\ m^{-2}$ *) (Penniston-Dorland and Ferry, 2008); 10) quartz veins in accretionary prism, from slab fluids (*10^4*-*10^5 $m^3\ m^{-2}$*) (Breeding and Ague, 2002); 11) channelization in upper and middle crust (*10^3*-*10^4 $m^3\ m^{-2}$*) (Ferry and Gerdes, 1998).*

4.5 Appendices

Table 4.A1. *List of textural bodies of the Chl-harzburgite sequence at Almirez.*

Nº Body	z (m)	z* (m)	N-S length (m)	E-W length (m)	N-S/ z*	E-W/ z*	Texture	Distance (m)
1	5	4.9	133		27		Spinifex	7
2	4	3.9		47		11.9	Spinifex	22
3	10	9.8		47		4.8	Spinifex	28
4	4	3.9		26		6.6	Spinifex	34
5	6	5.9	146		24.7		Spinifex	36
6	7	6.9	158		22.9		Spinifex	20
7	2	2	18		9.1		Spinifex	18
8	3	3	54		18.3		Spinifex	10
9	3	3	45		15.2		Spinifex	12
10	10	9.8		88		8.9	Spinifex	33
11	1.5	1.5	25		16.9		Spinifex	7
12	4	3.9	64		16.2		Spinifex	36
13	7	6.9	98	62	14.2	9	Spinifex	25
14	9	8.9	152		17.1		Granofels	44
15	5	4.9	76		15.4		Granofels	53
16	1	1	23		23.4		Granofels	22
17	7	6.9		21		3	Granofels	28
18	11	10.8	152	59	14	5.4	Granofels	27
19	2	2	52	19	26.4	9.6	Granofels	44
20	5	4.9	68		13.8		Granofels	16
21	8	7.9	117		14.9		Granofels	11
22	5	4.9	72		14.6		Granofels	13
23	10	9.8		85		8.6	Granofels	34
24	6	5.9	152	39	25.7	6.6	Granofels	34
25	4	3.9	116		29.4		Granofels	50
26	6	5.9		46		7.8	Granofels	26
27	12	11.8		61		5.2	Spinifex	48
28	12	11.8		38		3.2	Spinifex	45
29	9	8.9		23		2.6	Spinifex	40
30	15	14.8		35		2.4	Spinifex	30
31	5	4.9		18		3.7	Spinifex	10
32	8	7.9	113		14.3		Spinifex	19
33	9	8.9		34		3.8	Spinifex	31
34	18	17.7		45		2.5	Spinifex	20
35	4	3.9	80	30	20.3	7.6	Spinifex	29
36	20	19.7	157		8		Spinifex	56

Table 4.A1. *Continued.*

Nº Body	z (m)	z* (m)	N-S length (m)	E-W length (m)	N-S/ z*	E-W/ z*	Texture	Distance (m)
37	12	11.8	300		25.4		Spinifex	20
38	11	10.8	171	32	15.8	3	Spinifex	35
39	13	12.8	178		13.9		Spinifex	76
40	10	9.8		28		2.8	Spinifex	44
41	8	7.9		37		4.7	Spinifex	17
42	4	3.9		74		18.8	Granofels	70
43	2	2		19		9.6	Granofels	68
44	7	6.9		25		3.6	Granofels	45
45	4	3.9		15		3.8	Granofels	41
46	2	2		9		4.6	Granofels	38
47	4	3.9		17		4.3	Granofels	2
48	5	4.9		21		4.3	Granofels	32
49	13	12.8		67		5.2	Granofels	39
50	7	6.9		20		2.9	Granofels	62
51	12	11.8	103		8.7		Granofels	23
52	5	4.9		15		3	Granofels	23
53	12	11.8		38		3.2	Granofels	34
54	5	4.9		15		3	Granofels	25
55	4	3.9		10		2.5	Granofels	28
56	18	17.7		87		4.9	Granofels	53
Median					**16**	**4.4**		
Spread					4.9	2		
Error					0.3	0.5		
Median spinifex					**16.2**	**4.3**		
Spread spinifex					4.3	2.1		
Error spinifex					0.3	0.5		
Median granofels					**15.4**	**4.4**		
Spread granofels					5.8	2		
Error granofels					0.4	0.5		

From left to right, number of corresponding body in Fig. 4.3; elevation z between upper and lower fitted surface of the body; corrected thickness of the lens z due to 10º tilting with respect to the horizontal; measured N-S length of a body when fully constrained in this direction; measured E-W length when fully constrained in this direction; the ratio of the N-S length over the corrected thickness z* of the body; the ratio of the E-W length over the corrected thickness z* of the body; texture of the Chl-harzburgite body; distance from the middle of the lens, to the dehydration front*

Table 4.A2. *Time-integrated flux per sector (Figs 4.1 and 4.3)*

Sector	SA (m^2)	SL (m)	V H_2O (m^3)	Flux SA (m^3/m^2)	Flux HC 1 m (m^3/m^2) spacing:				Flux HC 0.1 m (m^3/m^2) spacing:			
					2 m	10 m	20 m	50 m	2 m	10 m	20 m	50 m
1	127245	357	338350	2.7	8.0	29.2	55.8	135.6	55.8	268.6	534.5	1332.2
2	58641	242	151142	2.6	7.7	28.4	54.1	131.4	54.1	260.3	518.1	1291.3
3	70750	266	221259	3.1	9.4	34.4	65.7	159.5	65.7	315.9	628.6	1566.8
all	**256636**	**507**	**710751**	**2.8**	**8.3**	**30.5**	**58.2**	**141.2**	**58.2**	**279.7**	**556.7**	**1387.5**

Computations based on total volumes (m^3) of water (V H_2O) from all the lenses in the respective sector per surface area (SA) of the sector or through hydrofractures and cracks (HC) with varying thickness of 0.1 and 1 m, and spaced 2 – 10 – 20 – 50 m. Length of HC is estimated based on sector length (SL). See text for more details.

Table 4.A3. *Time-integrated fluxes per textural interval*

Interval	Texture	Flux SA (m^3/m^2)	Flux HC (m^3/m^2) 1m	Flux HC (m^3/m^2) 0.1 m
I	granofels	1 ± 0.4	23 ± 11	231 ± 111
III	granofels	2 ± 0.9	91 ± 43	914 ± 428
V	granofels	1.3 ± 0.4	34 ± 12	342 ± 123
VII	granofels	2.2 ± 0.8	66 ± 27	657 ± 269
IX	granofels	2.2 ± 0.3	122 ± 26	1218 ± 264
XI	granofels	1.3 ± 0.5	36 ± 17	356 ± 171
XIII	granofels	2.5 ± 0.7	204 ± 72	2043 ± 723
XV	granofels	3.3 ± 1.3	261 ± 131	2611 ± 1307
XVII	granofels	2 ± 0.8	85 ± 38	850 ± 383
XIX	granofels	1.7 ± 0.7	59 ± 28	593 ± 285
XXI	granofels	4 ± 1.5	341 ± 147	3411 ± 1468
XXIII	granofels	1.1 ± 0.4	76 ± 32	763 ± 319
II	spinifex	1.2 ± 0.4	39 ± 15	389 ± 148
IV	spinifex	0.7 ± 0.4	12 ± 6	121 ± 61
VI	spinifex	2.7 ± 0.6	181 ± 49	1809 ± 490
VIII	spinifex	1.9 ± 0.0	116 ± 0	1161 ± 0
X	spinifex	2.5 ± 0.3	134 ± 25	1338 ± 252
XII	spinifex	2.7 ± 0.6	306 ± 86	3057 ± 864
XIV	spinifex	1.9 ± 0.3	79 ± 15	793 ± 147
XVI	spinifex	2.1 ± 0.5	72 ± 20	719 ± 203
XVIII	spinifex	2.7 ± 0.5	132 ± 34	1325 ± 338
XX	spinifex	3.1 ± 0.7	254 ± 72	2543 ± 718
XXII	spinifex	4.3 ± 2.2	281 ± 141	2806 ± 1413
XXIV	spinifex	3.2 ± 1.6	207 ± 104	2068 ± 1041

Computation based on the total volume (m^3) of water per interval through either half the surface areas (m^2) of lenses per interval (Flux SA) or through hydrofractures and cracks (HC) of 0.1m to 1m. See text for further details.

5 Textural Evolution during High-Pressure Dehydration of Serpentinite to Peridotite and its Relation to Stress Orientations and Kinematics of Subducting Slabs: Insights from the Almirez Ultramafic Massif[1]

5.1 Introduction

Many studies have provided new insights into the rheology and microstructure of serpentinite and its dehydration to metaperidotite, and its bearing on the dynamics and physicochemical properties of subduction zones (Auzende et al., 2015; Hilairet et al., 2007; Plümper et al., 2017). Structural, petrological, and geochemical studies of exhumed paleo-subduction metamorphic terrains provide a unique opportunity to investigate the dehydration reaction of antigorite serpentinite at time and length scales complementary to those offered by experimental and geophysical studies (Bebout and Penniston-Dorland, 2016; Guillot et al., 2015; Hermann et al., 2000; John et al., 2012; Marchesi et al., 2013; Padrón-Navarta et al., 2011; Scambelluri et al., 2015; and references therein; Scambelluri and Philippot, 2001). Here, a correlative X-ray micro-computed tomography (µ-CT) and Electron Backscatter Diffraction (EBSD) study is presented of geographically oriented samples across the Atg-serpentinite dehydration isograd in the western section of the Almirez massif. These data provide, in a common geographical reference frame, a detailed account of the evolution of the Shape Preferred Orientation (SPO) of oxides and olivine, and the Crystal Preferred Orientation (CPO) of antigorite, olivine, and orthopyroxene during high-P dehydration of Atg-serpentinite to peridotite. These data are combined with structural observations to investigate the textural evolution during prograde Atg-serpentinite dehydration to peridotite and its possible links with the stress state, fluid flow, and the kinematics of the subducting slab.

[1] This chapter has been published: Dilissen, N., Hidas, K., Garrido, C.J., Kahl, W.-A., López Sánchez-Vizcaíno, V., Padrón-Navarta, J.A., 2018. Textural evolution during high-pressure dehydration of serpentinite to peridotite and its relation to stress orientations and kinematics of subducting slabs: Insights from the Almirez ultramafic massif. Lithos 320-321, 470-489.

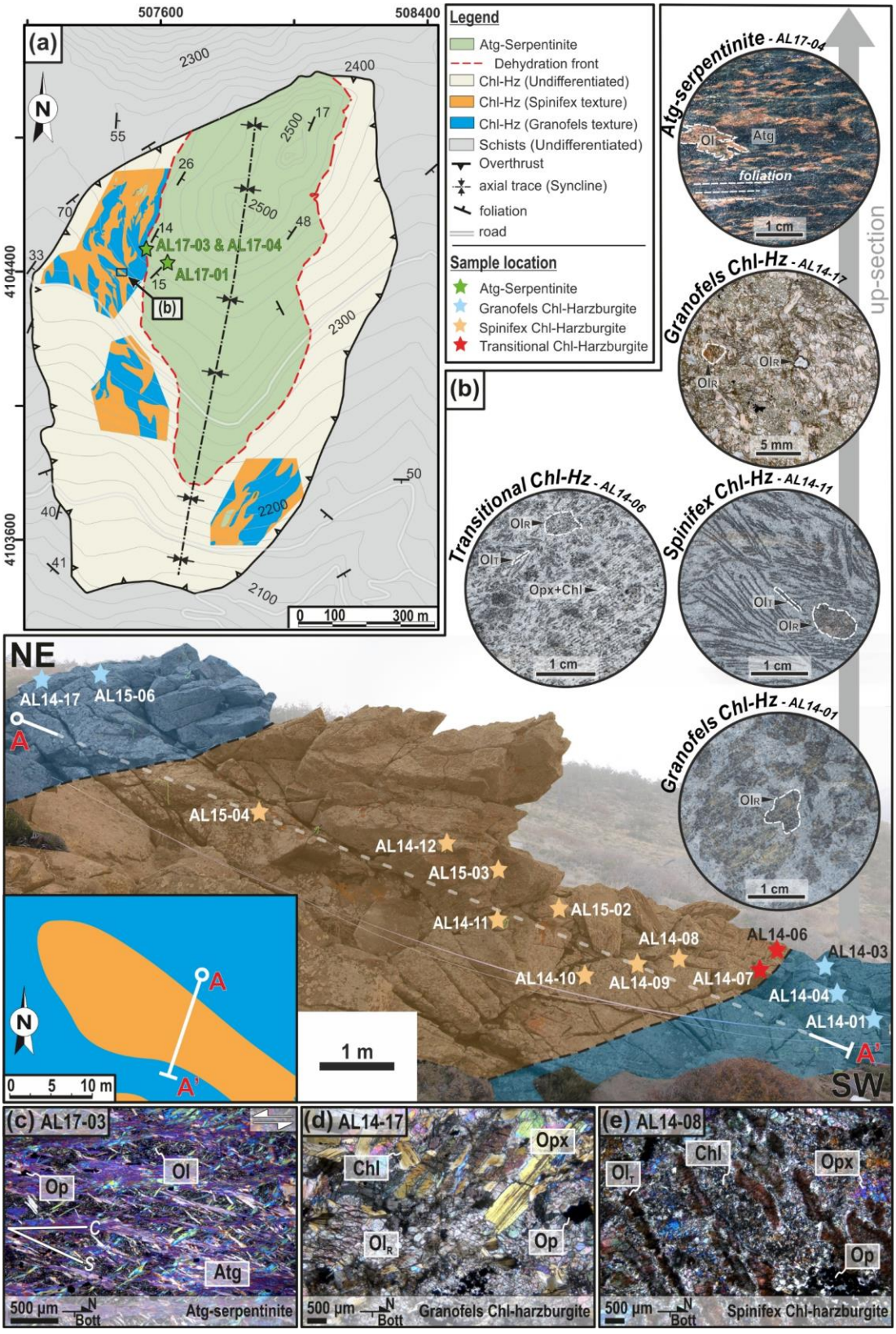
(a)
507600
508400
4104400
4103600
N
AL17-03 & AL17-04
AL17-01
(b)
0 100 300 m
Legend
Atg-Serpentinite
Dehydration front
Chl-Hz (Undifferentiated)
Chl-Hz (Spinifex texture)
Chl-Hz (Granofels texture)
Schists (Undifferentiated)
Overthrust
axial trace (Syncline)
foliation
road
Sample location
Atg-Serpentinite
Granofels Chl-Harzburgite
Spinifex Chl-Harzburgite
Transitional Chl-Harzburgite
(b)
Atg-serpentinite - AL17-04
Ol
Atg
foliation
1 cm
Granofels Chl-Hz - AL14-17
OlR
5 mm
up-section
Transitional Chl-Hz - AL14-06
OlT
Opx+Chl
Spinifex Chl-Hz - AL14-11
Granofels Chl-Hz - AL14-01
NE
SW
AL14-17
AL15-06
AL15-04
AL14-12
AL15-03
AL14-11
AL15-02
AL14-08
AL14-06
AL14-03
AL14-10
AL14-09
AL14-07
AL14-04
AL14-01
A
A'
1 m
0 5 10 m
(c) AL17-03
Op
Ol
C
S
Atg
500 µm
Bott
Atg-serpentinite
(d) AL14-17
Opx
Chl
Op
Granofels Chl-harzburgite
(e) AL14-08
Spinifex Chl-harzburgite

5.2 Study area and sampling

For the present study, foliated Atg-serpentinite and the underlying coarse-grained Chl-harzburgite was sampled in the NW hillside of the Almirez massif (Fig. 5.1a; cf. Ch. 1). This area was selected because it has good exposures of Atg-serpentinite and Chl-harzburgite across the Atg-serpentinite dehydration front, and the sampling sites lie in the same flank of the late gentle syncline folding of the massif (Fig. 5.1a) (Jabaloy-Sánchez et al., 2015; Padrón-Navarta et al., 2011). In the Atg-serpentinite sampling sites, the dip direction and dip of the foliation (135°/15° and 118°/14 in the two sample sites) are consistent with previously reported measurements nearby (115-170°/25–48°; Padrón-Navarta et al., 2010b), and the average foliation direction and dip in the western flank of the syncline (135°±20°/25°±15°; Jabaloy-Sánchez et al., 2015).

We collected geographically oriented samples of three Atg-serpentinites and twenty-three Chl-harzburgites. The Chl-harzburgites were sampled across a 14-meter wide section (A–A'; Fig. 5.1b) containing a spinifex lens (corresponding to lens "2" in Fig.

Figure 5.1. *(a) Simplified geological map of the Almirez ultramafic massif (modified after Jabaloy-Sánchez et al., 2015). Chl-harzburgite domain with granofels (blue) and spinifex (orange) textures are shown in three areas of the massif. Black square indicates the location of the studied cross-section shown in Figure 5.1b; green stars are the location of Atg-serpentinite samples. (b) Field view of the cross-section across a spinifex Chl-harzburgite lens (transparent orange shading) hosted in granofels Chl-harzburgite (transparent blue shading). The blue, orange and red stars indicate the sampling site of granofels, spinifex and transitional Chl-harzburgite, respectively. The bottom-left inset shows the enlarged view of the investigated lens showing the A–A' sampling cross-section. Circles in the top-right part of the figure show representative microstructures and micrographs of the different textural types of Chl-harzburgite along the A-A' cross-section (Chlorite harzburgites: Chl, chlorite; Ol_R, rounded olivine; Ol_T, tabular olivine; Opx, orthopyroxene), and that of an Atg-serpentinite sample (Ol: olivine; Atg: antigorite). (c–e) Photomicrographs comparing the microstructure of Atg-serpentinite, granofels, and spinifex Chl-harzburgite in the X-Z structural reference frame of the Atg-serpentinite (i.e., parallel to the oxide aggregate stretching lineation, and perpendicular to the tectonic foliation). Black arrows indicate the geographic orientation (N= North; Bott: bottom); (c) Cross-polarized light (with the 530 nm full wavelength retardation plate inserted) micrograph of the microstructure of Atg-serpentinite (sample AL17-03). The sheared matrix of fine-grained antigorite and coarser-grained antigorite crystals defines an anastomosing schistosity associated with an asymmetric S–C structure with a top-to-S kinematics (white-arrows in the top-right corner) (Atg= Antigorite; Ol= olivine; Op = opaque, mostly aggregates of oxide); (d) Cross-polarized light micrograph of the coarse-grained texture characteristic of granofels Chl-harzburgite (sample AL14-17) (Chl= Chlorite; OlR= rounded olivine; Op = opaque oxides; Opx = orthopyroxene); (e) Cross-polarized light micrograph of the texture of spinifex Chl-harzburgite (sample AL14-08) showing the elongated tabular brown olivine characteristic of this textural type (Chl= Chlorite; Ol_T = tabular olivine; Op = opaque oxides; Opx = orthopyroxene).*

4.2; Table 4.1) and its upper and lower granofels envelope (cf. Ch. 4). The spinifex Chl-harzburgite lens has a flat triaxial ellipsoid shape; it is located c. 75 m down section the Atg-out isograd and subparallel to it (Fig. 5.1a). The boundary between the granofels and the spinifex Chl-harzburgite textural types is sharp (Fig. 5.1a,b). The samples near the upper envelope of the lens were discarded from the study because their microstructure is strongly obliterated by recrystallization associated to grain-size reduction zones (Padrón-Navarta et al., 2010b).

For μ-CT imaging, we drilled cylindric cores (e.g., Fig. 5.2a) in the laboratory in three Atg-serpentinite samples (Fig. 5.1a) and fifteen samples of Chl-harzburgite (Fig. 5.1b). The sample cores were c. 30 mm in height and 25, 28 or 33 mm in diameter. They were geographically oriented, with their bases lying in the horizontal plane and their top base pointing upward the outcrop (e.g., Fig. 5.2a). Once scanned by μ-CT, we made two orthogonal petrographic thin sections that were cut, respectively, in the horizontal and the vertical N-S plane of the sample core. Because in the sampling area the Atg-serpentinite foliation is subhorizontal, the vertical and horizontal petrographic thin sections were, respectively, broadly normal and subparallel to the foliation (Fig. 5.2a).

5.3 Analytical methods

5.3.1 X-ray micro-computed tomography (μ-CT)

The scanner (cf. Ch. 3) was set up with a source voltage of 130 kV, a current of 350 μA, and a thin copper filter. The μ-CT data were acquired during 360° rotation of the sample core with a step size of 0.3° at detector resolutions ranging between 12.5 and 16.3 μm per pixel. From the three-dimensional (3-D) digital scans, we used data processing and analysis to discriminate the highly attenuating oxides —mostly magnetite and ilmenite— in Chl-harzburgite and Atg-serpentinite, and the different textural types of olivine in the Chl-harzburgite samples. Ch. 3 reports the segmentation and image analysis procedures for grain separation. Only features larger than 10^6 (Atg-serpentinite) and 10^7 μm^3 (Chl-harzburgite) in volume and with an Aspect Ratio (A.R.) of at least five were isolated to eliminate artifacts due to boudinaged or isometric grains (e.g., Fig. 5.2) (cf. Ch. 3). The 3-D shape of isolated features (i.e., oxides and rounded olivines) was quantified by fitting of ellipsoids. The length of the three semi-axes, the aspect ratio (i.e.,

the ratio of the shortest to longest semi-axes), and the 3-D orientation of the longest semi-axis of the ellipsoid fully characterize the size, shape, and orientation of the feature in 3-

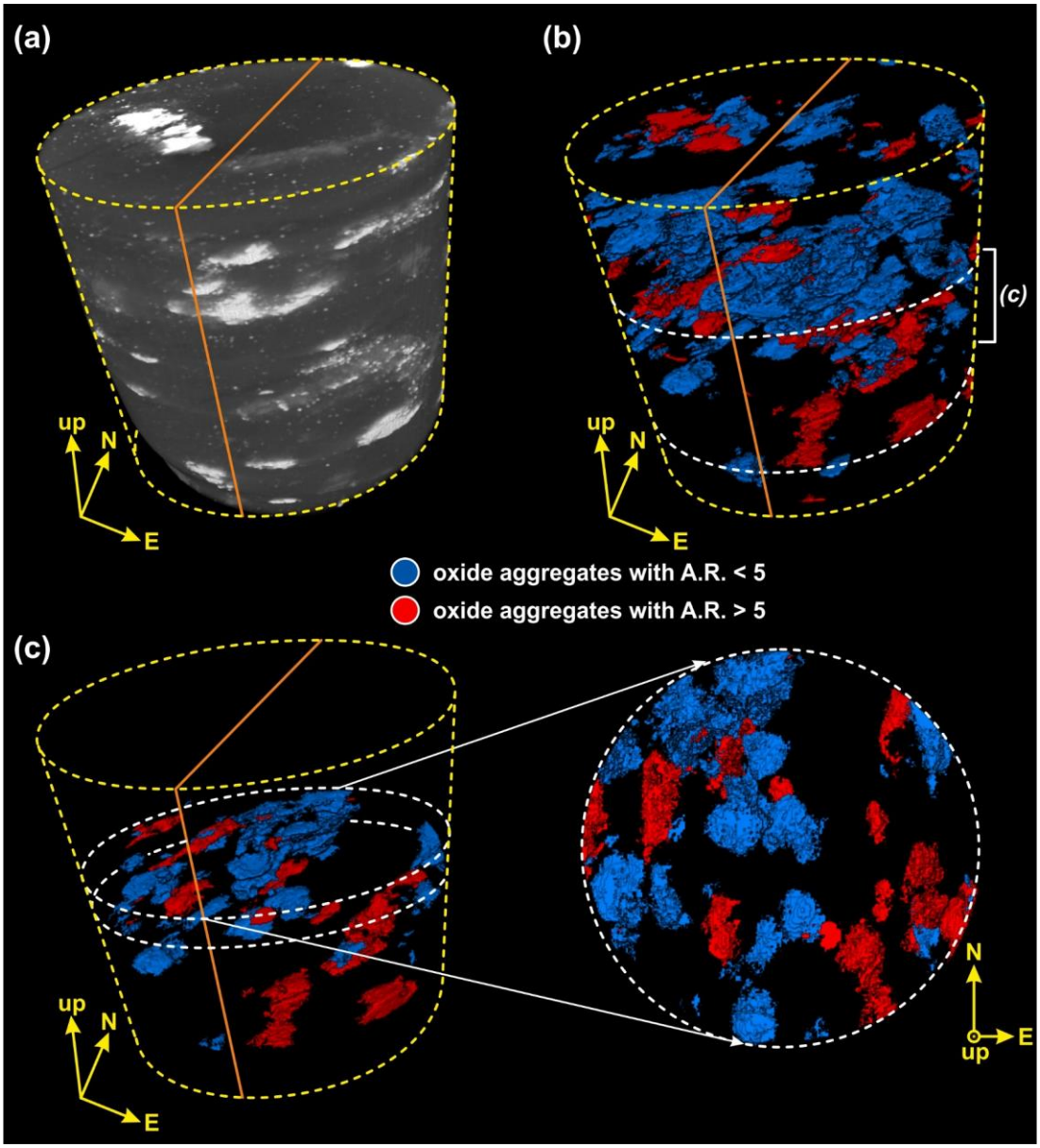

Figure 5.2. *µ-CT images of a geographically oriented drill core in a representative Atg-serpentinite (sample AL17-01; diameter: 25 mm, height: 26 mm). The yellow arrows indicate the geographical reference orientation; the bases of the cores are horizontal. (a) Grayscale µ-CT image of the drill core. The outline of the N–S vertical plane is shown in orange. Lighter gray levels correspond to highly attenuating oxide aggregates, and darker gray levels are relatively lower attenuation coefficient phases corresponding to silicates. (b) Results of the segmentation of the highly attenuating oxide aggregates classified into aggregates with aspect ratios (A.R.) < 5 (blue) and with A.R. > 5 (red). The CT volume between the dashed white lines is shown in (c). (c) Visualization of the oxide aggregate lineation. The close-up view on the right is looking along the vertical N-S plane from top to bottom, and it corresponds to the core section bordered by white dashed lines in the left panel. The Atg-serpentinite foliation in the close-up view is roughly parallel to the plane of the figure.*

D. Due to the interpenetrating nature of the olivine texture in spinifex Chl-harzburgite (cf. Ch. 3), its 3-D orientation was quantified using the mean intercept length (MIL) (Odgaard, 1997). In the MIL method, the 3-D SPO of a feature is characterized by the orientation and lengths of the short, intermediate and long axis of the ellipsoid calculated from the length and orientation of the intersections between a 3-D grid and the feature of interest (see Ch. 3).

5.3.2 Electron backscatter diffraction (EBSD)

For the EBSD analyses of antigorite in Atg-serpentinite, the SEM was operated in variable pressure mode at 10 (±1) Pa in a N_2 atmosphere to minimize sample charging, using a 20 kV acceleration voltage and 200 pA sample probe current, and at a 24 mm working distance and low magnification (c. 200×). We used a step size of 5 µm to map c. 100 mm^2 areas during up to 30 hours acquisition sessions. Automatic band recognition of the antigorite superstructure (Uehara, 1998) was accomplished using 45 reflectors at 4×4 binning and low (0) gain in refined accuracy mode for band centers of eight bands in the AZtec-HKL software. Indexing of the antigorite, as well as the fitting of the theoretical crystal structure to the Kikuchi bands, was better in horizontal than vertical thin sections. In the raw maps, the indexing was 64 – 67 % (of which 38–53 % Atg) in the horizontal and 50–55 % (of which 32–42 % Atg) in the vertical thin sections with the average of mean angular deviation (MAD) ranging 0.59° – 0.71°, and 0.60° – 0.69°, respectively. The maximum accepted angular deviation for measurements was 1.3°. This result is consistent with recent EBSD studies that show the preferential indexing of antigorite in thin sections parallel to the Atg-serpentinite foliation (Morales et al., 2018; Nagaya et al., 2017). We also found systematic indexing errors of antigorite due to its pseudo-symmetry that resulted in similar EBSD patterns for crystals rotated by 60° and 120° around the antigorite [001] axis (e.g., Padrón-Navarta et al., 2012). We corrected the pseudo-symmetry misindexing during data analysis using the built-in functions of the Aztec-HKL Channel5 software package.

For the EBSD analyses of Chl-harzburgite (cf. Ch. 3), we used a 17 kV acceleration voltage and c. 10^{-5} mbar chamber pressure. The acquisition conditions were 4×4 binning and low (0) gain and mapping using a variable grid step size between 17 and 35 µm. The indexation rate for olivine and orthopyroxene was excellent but inadequate for chlorite

likely due to mechanical deformation of chlorite surfaces during polishing. We use the usual grain segmentation procedure (i.e., grain identification by digital image analysis) for the detection of grains with segmentation angles in the range 2° – 10°, except for samples AL14-08 and AL14-11 where the fast multiscale clustering (FMC) technique performed better with C_{Maha} values in the range 0.4–0.64 (see Ch. 3 for details).

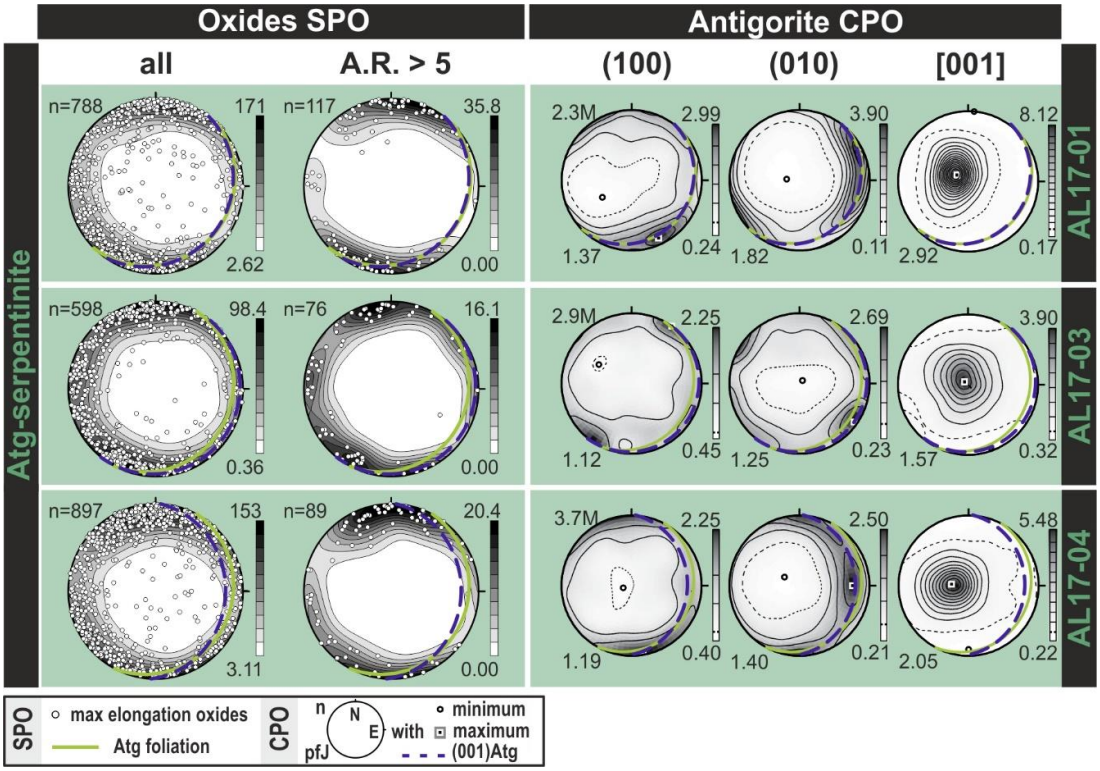

Figure 5.3. *Shape preferred orientation (SPO) of oxides from µ-CT (left panel), and crystal preferred orientation (CPO) of antigorite from EBSD (right panel) in Atg-serpentinite samples (see sample location in Fig. 5.1a). Pole figures are equal-area lower hemisphere projections, geographically oriented with N to the top and E to the right. Solid light green line denotes the trace of Atg-serpentinite foliation in individual sampling sites; dashed dark blue line is the (001)Atg plane calculated from EBSD data of each sample. Left panel (SPO oxides): white circles are the maximum elongation orientation of oxide aggregates with volume >106 µm3; gray-shaded contouring are contours at 0.5–1.0 multiples of uniform distribution; n= number of grains. The right column shows the orientation of all aggregates; the right column those with aspect ratio (A.R.) > 5. Right panel (Antigorite CPO): pole figures of the CPO of antigorite (one point per grain) from horizontal and the vertical thin section pairs for the same sample. The grain size threshold is 5 µm; n is the number of grains; contouring is at 0.5 multiples of uniform distribution. White circles and black squares are, respectively, the minimum and maximum value of the distribution. The bottom-left number in pole figures is the pfJ, a scalar measure of the strength of orientation of the axis.*

5.4 Atg-serpentinite texture and microstructure

5.4.1 Petrography

The textures of the Atg-serpentinite samples (Fig. 5.1c) are similar to those reported in previous studies of the Almirez massif (Padrón-Navarta et al., 2012). The Atg-serpentinites are composed of Atg, Ol, Chl, and magnetite. The alignment of platy blades of antigorite in closely spaced and evenly distributed, thin planar layers defines the penetrative schistose foliation of Atg-serpentinite (Fig. 5.1b). S–C structures show a top-to-South kinematics (Fig. 5.1c). In the plane of foliation, antigorite shows an interpenetrating texture (e.g., Boudier et al., 2010; Padrón-Navarta et al., 2012; and references therein) composed of blades of antigorite elongated along two conjugate directions at an angle of c. 60°.

5.4.2 SPO of oxide aggregates

The μ-CT images of the Atg-serpentinite sample cores show the presence of aggregates of highly attenuating iron oxides —magnetite and ilmeno-magnetite— (whitish spots in Fig. 5.2a) that have an oblate to prolate ellipsoidal shape (Fig. 5.2a–c). On the foliation plane, most oxide aggregates have an oblate spheroid shape with A.R. < 5 (blue aggregates in Fig. 5.2) and their shortest axis is perpendicular to the Atg-serpentinite foliation (Fig. 5.2c). A minor population has a prolate ellipsoidal shape (A.R. > 5; red aggregates in Fig. 5.2b-c) that defines an aggregate lineation ("aggregate lineation" as defined by Piazolo and Passchier, 2002). The 3-D orientation of oblate and prolate iron oxide aggregates is dispersed around a girdle in the N–S direction and flattened in the plane of foliation (Fig. 5.3; SPO of all oxides). The prolate ellipsoid population shows a N–S stretching lineation in the plane of foliation (Fig. 5.2c, Fig. 5.3: SPO of oxide aggregates with A.R. > 5). Our μ-CT study constrains the SPO and the orientation of the stretching lineation of oxides aggregates in Almirez Atg-serpentinite, which is challenging to measure unambiguously in the field (cf. Jabaloy-Sánchez et al., 2015).

5.4.3 CPO of antigorite

Despite the dependence of the indexing rate of antigorite on the orientation of the thin section relative to the foliation (see section 3.4.2.2 in Methodology), the EBSD analyses of two orthogonal petrographic thin sections from the same drill core show a strong antigorite CPO with a similar symmetry (Appendix 5.A). Figure 5.3 shows the average CPO obtained from merging the EBSD data of the two orthogonal petrographic thin sections. The antigorite shows a substantial alignment of the [001] normal to the foliation plane, and a weak girdle distribution of the poles to (100) and (010) in the foliation plane. The antigorite poles to (100) are subparallel or at < 20° to the oxide aggregate lineation (Fig. 5.3). The antigorite CPO symmetry is somewhat similar to that previously reported in Almirez Atg-serpentinites (Padrón-Navarta et al., 2012; Padrón-Navarta et al., 2015). In the present study, however, merging of the CPO from vertical and horizontal sections results in a more evenly distributed orientation of the antigorite [100] and [010] without a marked preferred orientation of any of the two axes.

5.5 Chl-harzburgite texture and microstructure

Based on their olivine microstructure, we classify Chl-harzburgite into granofels, spinifex, and transitional textures. The first two textural types are similar to those previously described in Almirez (Padrón-Navarta et al., 2011). The transitional Chl-harzburgite texture has not been previously reported in Almirez.

5.5.1 Granofels Chl-harzburgite

5.5.1.1 *Petrography*

In our sampling, this textural type occurs in the lower and upper envelope of the spinifex Chl-harzburgite lens (blue stars in Fig. 5.1b). The samples are composed of Ol (35–45 vol%), Opx (35–40 vol%), Chl (15–20 vol%), and minor oxides (1–5 vol%). The granofels Chl-harzburgite is made up of clear and inclusion-free, anhedral rounded olivine grains and olivine aggregates c. 2.5 mm in diameter (Fig. 5.1b), isolated prismatic orthopyroxene crystals, and 2–5 mm long flakes and granular decussate aggregates of chlorite (Fig. 5.1d). Chlorite is locally associated with magnetite and magneto-ilmenite. Near the contact with the spinifex Chl-harzburgite lens, granofels Chl-harzburgite samples contain a higher amount of anhedral brown olivine, and rounded olivine

porphyroblasts with clear cores and brown rims. The brown color of olivine is characteristic of the spinifex Chl-harzburgite olivines and due to nano-sized inclusions of magnetite, ilmenite, chromite, and talc (Ruiz Cruz et al., 1999).

5.5.1.2 *SPO of oxide aggregates and olivine*

Due to the lack of contrast in µ-CT images between the rounded olivines and surrounding silicate phases (Fig. 5.4a), only the highly attenuating oxide aggregates could be segmented (Fig. 5.4b). The 3-D distribution of elongated oxide aggregates (Fig. 5.4b) defines a patent subhorizontal NW–SE lineation (Fig. 5.5). In many of the studied samples, flattened to rounded olivine grains define a macroscopic olivine layering that dips 30–50° SSE (red solid planes in Fig. 5.5). The olivine layering is weakly penetrative at the drill core scale (Fig. 5.4a) but is locally penetrative at the hand-sample and outcrop scales.

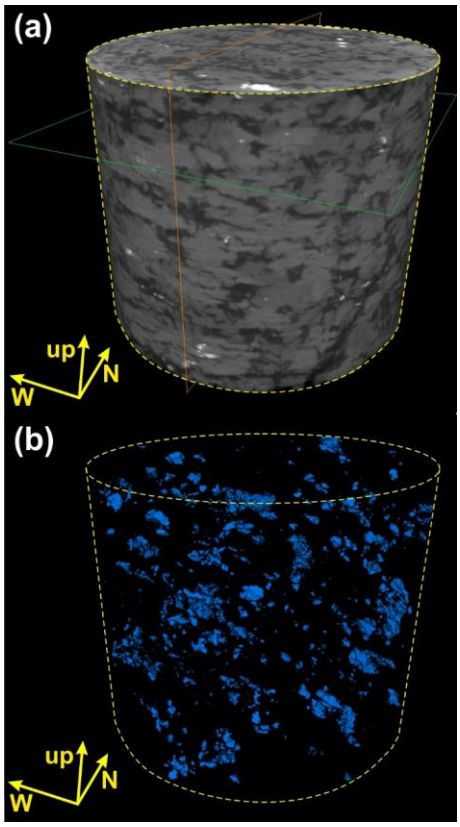

Figure 5.4. *µ-CT images of the geographically oriented drill core of a representative granofels Chl-harzburgite (sample AL14-17; diameter: 32 mm, height: 30 mm). (a) Grayscale µ-CT image of the core. Lighter gray levels are highly attenuating oxide phases, and darker gray levels are silicates (intermediate gray: olivine; dark gray: orthopyroxene and chlorite). The orange and green plane outlines show, respectively, the location of the vertical and horizontal thin sections used for the EBSD-SEM study. (b) Highly attenuating oxide aggregates (blue) obtained from the segmentation of the grayscale µ-CT image.*

5.5.1.3 *CPO of olivine and orthopyroxene*

Figure 5.5 shows the CPO of olivine and orthopyroxene in granofels Chl-harzburgite samples. The $[100]_{Ol}$ axes are dominantly subparallel to the NW–SE oxide aggregate lineation. The $[010]_{Ol}$ directions are comparatively more dispersed but are mainly subparallel to the poles of the olivine layering (red solid planes in Fig. 5.5). The $[001]_{Ol}$ directions are dispersed, and their maxima are usually distributed close to the plane of the olivine layering. The orthopyroxene also has a strong CPO with the $[001]_{Opx}$ axes distributed

subparallel to the $[100]_{Ol}$ axes and the SPO of the oxides (Fig. 5.5). The $[100]_{Opx}$ and $[010]_{Opx}$ axes show a girdle-like distribution along the NNE-SSW vertical plane at a high angle from the olivine layering (Fig. 5.5). In most of the samples, a single maximum of the $[100]_{Opx}$ axes is weakly correlated with that of the $[010]_{Ol}$, except for samples AL14-17 and AL15-06 where it is subparallel to the $[001]_{Ol}$ and $[100]_{Ol}$ axes, respectively (Fig. 5.5).

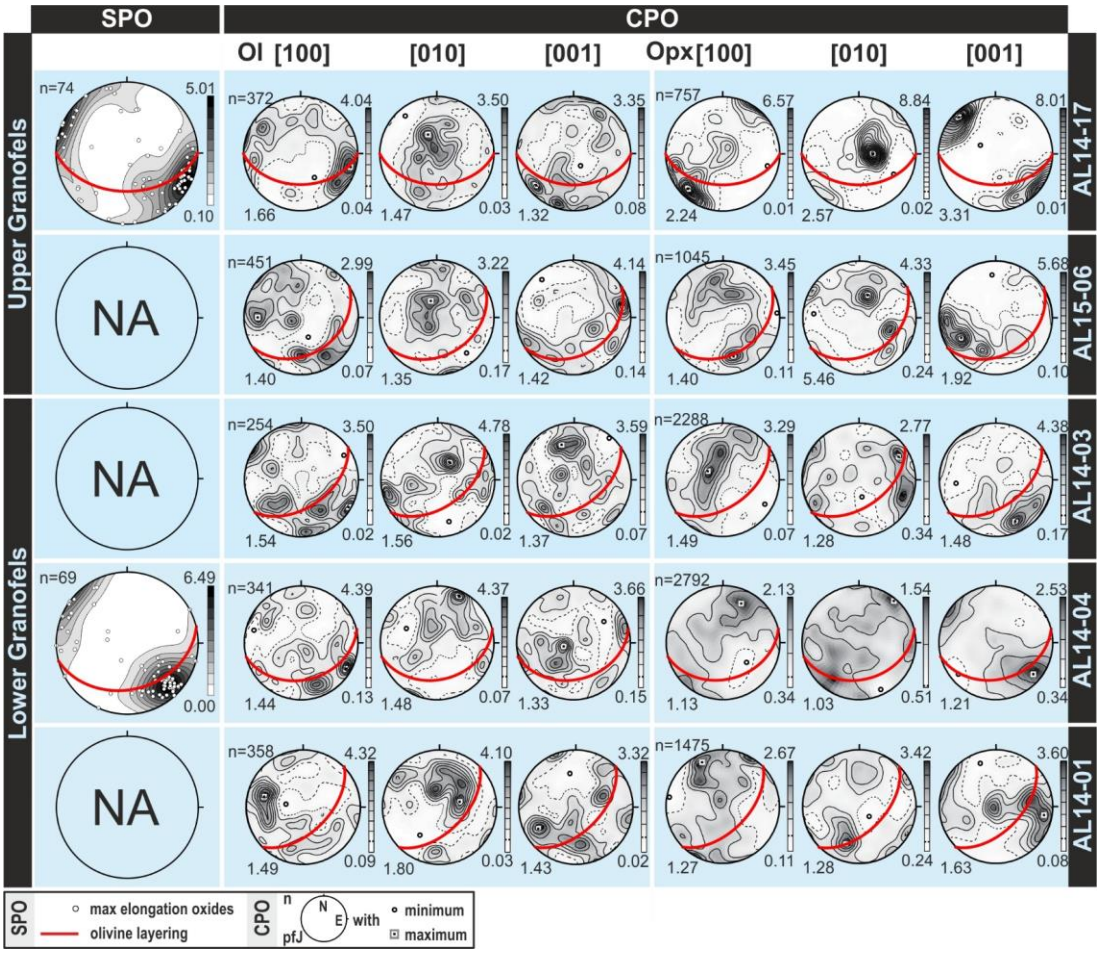

Figure 5.5. *Shape preferred orientation (SPO) of oxide aggregates (Left panel), and crystal preferred orientation (CPO) of olivine (Ol) and orthopyroxene (Opx) (Right panel) of granofels Chl-harzburgite samples. Pole figures are equal-area lower hemisphere projections, geographically oriented with N to the top and E to the right. Solid red lines are the olivine compositional layering at the hand specimen scale (see text for details). Left panel (SPO): white dots are the orientation of individual oxide aggregates with volume >107 µm3 and aspect ratio (A.R.) > 5; gray-shaded contouring are contours at 0.5–1.0 multiples of uniform distribution; n=number of grains. NA stands for not analyzed. Right panel (CPO): one point per grain orientation (n = number of grains) with contours at 0.5 multiples of uniform distribution. The shown CPOs are for the vertical thin sections. The white circle and the black squares are, respectively, the minimum and maximum of the distribution. The bottom-left numbers in pole figures is pfJ, a scalar measure of the strength of orientation of the axis.*

5.5.2 Spinifex Chl-harzburgite

5.5.2.1 *Petrography*

The samples of this textural type occur within the spinifex Chl-harzburgite lens (Fig. 5.1b) and show similar textures and mineral assemblages than those previously reported in the Almirez massif (Padrón-Navarta et al., 2011; Trommsdorff et al., 1998). The samples (orange stars in Fig. 5.1b) are composed of Ol (40–45 vol%), Opx (30–40 vol%), Chl (10–25 vol%), and oxides (1–3 vol%). They show a spinifex texture made up of cm-sized tabular brown olivine grains with high apparent axial ratios (Fig. 5.1b,e). Clear rounded olivine aggregates (e.g., AL14-11 in Fig. 5.1b; AL14-08 in Fig. 5.6c) —similar to those of the granofels texture— may also be found. Orthopyroxene appears as 50–100 µm wide radial aggregates (Fig. 5.1e) (commonly 0.5–2 mm, and up to 8 cm, in length). Chlorite occurs as 200–300 µm single crystals intergrown with orthopyroxene, as interstitial aggregates or associated with oxides in clots (Fig. 5.1e).

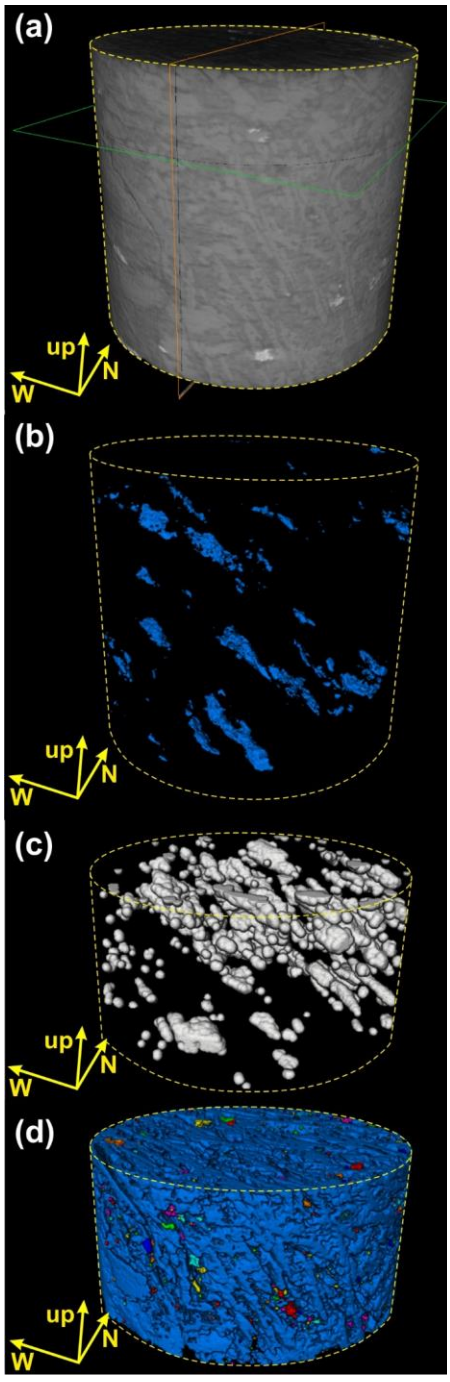

Figure 5.6. *µ-CT images of the geographically oriented drill core of a representative spinifex Chl-harzburgite (sample AL14-08; diameter: 28 mm, height: 26 mm). (a) Grayscale µ-CT image of the core. Lighter gray levels are highly attenuating oxide aggregates, and darker gray levels are silicates (medium gray: olivine; dark gray: orthopyroxene and chlorite). The orange and green outlines are, respectively, the position of the vertical and horizontal thin sections used for the EBSD-SEM study. (b–d) Images of different phases obtained from the segmentation of the µ-CT image: (b) highly attenuating oxide aggregates; (c) rounded olivine; (d) tabular olivines with different colors for aggregates of tabular olivines (see text, methodology (or Kahl et al., 2017) for further details). Figures (a) and (b) show images of the whole core. For the sake of legibility, only the bottom part of the core is shown in (c) and (d).*

5.5.2.2 *SPO of oxide aggregates and olivine*

The μ-CT images of spinifex Chl-harzburgite cores (Fig. 5.6) show aggregates of iron oxides with a predominantly oblate ellipsoidal shape with subhorizontal long and intermediate axes (Fig. 5.6b). The elongation of oxide aggregates defines an aggregate lineation with a SPO of variable strength and direction across the spinifex lens (Fig. 5.7). The oxide aggregate lineation is subhorizontal and, in most samples, trends NW–SE, but in some samples trends N–S to E–W (AL14-12 and AL15-04, respectively).

The analysis of μ-CT images reveals the presence of two types of 3-D olivine morphologies: prolate ellipsoidal shapes (Fig. 5.6c) and rectangular parallelepipeds with an interpenetrating tabular prism shape (Fig. 5.6d) (see also Kahl et al., 2017). These two textural types of olivine correspond, respectively, to the clear rounded olivines and the brown tabular olivines in petrographic thin sections (Fig. 5.1b,e). The tabular olivine is the dominant olivine shape and occurs as an interpenetrating network of tabular prisms with different orientations (Fig. 5.6d). The MIL analysis (cf. 3.4.3.6.3 in Methodology) shows that from the middle towards the lower edge of the spinifex Chl-harzburgite lens (Fig. 5.1b) the relative abundance of tabular olivine and their grain size decreases from several cm to 1–10 mm, and their semi-axis ratios from c. 20:10:1 to c. 6:3:1. Using Piazolo and Passchier (2002) their terminology of lineations, the longest axes —obtained from the MIL analysis— of the prolate ellipsoids define an olivine "grain lineation" (Fig. 5.6c), and those of the brown olivine tabular prisms define an olivine "platelet lineation" (Fig. 5.6d). The olivine platelet (Fig. 5.7; orange star) and olivine grain (Fig. 5.7; blue star) lineations have a strong SPO that is broadly subparallel to that of the oxide aggregate lineation (Fig. 5.7; SPO; and Fig. 5.6b). In detail, the olivine platelet lineation is 15–20° off relative to the maxima of the oxide aggregate and the olivine grain lineations (Fig. 5.7).

5.5.2.3 *CPO of olivine and orthopyroxene*

The olivines and orthopyroxenes of spinifex Chl-harzburgites show a remarkably strong CPO (Fig. 5.7). The olivine CPO is characterized by a maximum $[001]_{Ol}$ subparallel to the platelet lineation, and the oxide aggregate and olivine grain lineation. The $[100]_{Ol}$ and the $[010]_{Ol}$ typically corresponds, respectively, to the short and the intermediate MIL axes of the tabular olivine SPO (Fig. 5.7). An exception is sample

AL14-10. Besides the preeminent $[100]_{Ol}$ and $[010]_{Ol}$ maxima, the CPO also show minor clusters of $[100]_{Ol}$ and $[010]_{Ol}$ rotated around $[001]_{Ol}$ (e.g., AL14-08; Fig. 5.7). Orthopyroxene has a pronounced CPO characterized by $[100]_{Opx}$, $[010]_{Opx}$ and $[001]_{Opx}$ subparallel to $[100]_{Ol}$, $[010]_{Ol}$ and $[001]_{Ol}$, respectively, without submaxima in any axis (Fig. 5.7). Most $(010)_{Opx}$ are subhorizontal (Fig. 5.7). On average, the microstructure of spinifex Chl-harzburgite is characterized by $[001]_{Ol} \parallel [001]_{Opx} \parallel$ oxide aggregate lineation (Fig. 5.7). This relationship is different from that observed in granofels Chl-harzburgite.

5.5.2.4 *Relation between the SPO and CPO of tabular olivines*

To reconstruct the 3-D orientation of tabular olivines and to investigate the relationships between their CPOs and SPOs, we carried out a correlative 3-D µ-CT and EBSD-SEM study of two spinifex Chl-harzburgites showing clustered CPOs of olivine (AL14-08 and AL14-11; Fig. 5.8) (see details in Methodology or Kahl et al., 2017). We identified the olivine grain populations of each CPO cluster in EBSD orientation maps and used µ-CT images to correlate grain sections of a given group in the mutually perpendicular thin sections from the same core (see Appendix 5.B; different color-coded populations). Using the *principalComponents* function of the MTEX software, grain sections were fitted to equivalent area ellipses with their smallest axes equal to the minimum elongation of grain sections (Appendix 5.B). The angle of inclination of the ellipse largest axis —measured in anticlockwise direction from N in the reference frame of horizontal and vertical sections (Appendix 5.B)— defines the SPO of the grain section. For each SPO–CPO population, the dominant inclination angle in the relative area percentage histograms is taken as the strike —in the horizontal section— and the apparent dip —in the vertical section— of the tabular olivine population (Appendix 5.B). The average strike and actual dip of the olivine tabular interfaces of each SPO were reconstructed combining data from the vertical and horizontal thin sections.

Figure 5.8a shows the different SPO populations of tabular olivines identified in samples AL14-08 (three populations) and AL14-11 (four populations). The different populations are color-coded and plotted in the core geographical reference frame. In all populations, the olivines are tabular on $(100)_{Ol}$, elongated along $[001]_{Ol}$, and their lateral faces are $(010)_{Ol}$ and $(001)_{Ol}$ (see inset in Fig. 5.8a), commonly with c>b>>a. Figure 5.8b pole figures show the olivine CPOs of the different SPO populations of tabular grains in

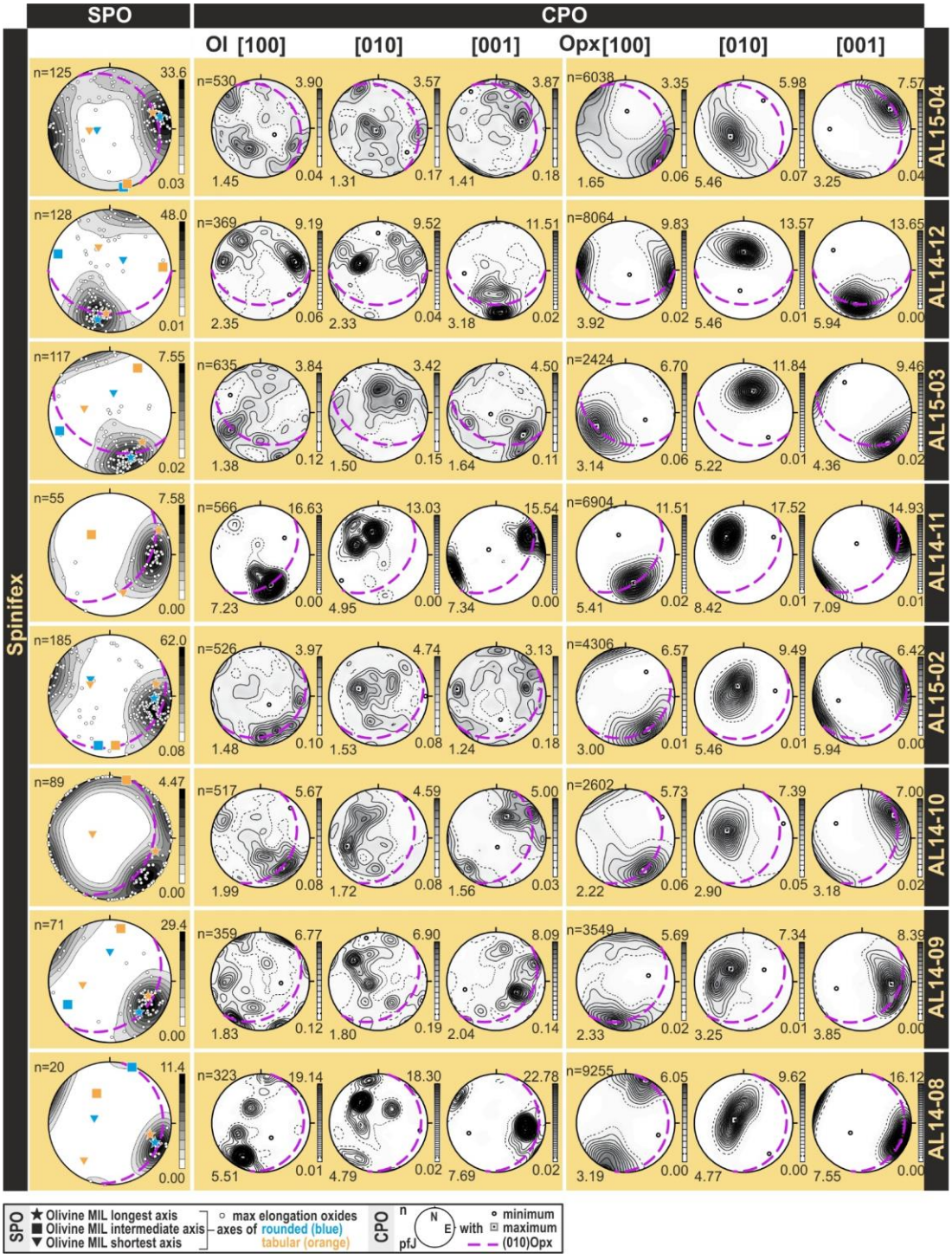

Figure 5.7. *Shape preferred orientation (SPO) of oxides from µ-CT (left panel), and crystal preferred orientation (CPO) of olivine (Ol) and orthopyroxene (Opx) from EBSD (right panel) in spinifex Chl-harzburgite (see sample location in Fig. 5.1b). Plotting convention and data selection are the same as in Fig. 5.5. Dashed purple lines indicate* $(010)_{Opx}$ *calculated from EBSD data (see text for details). In the left panel (SPO), the star, square and triangle symbols show the longest, intermediate and shortest axis of the mean intercept length (MIL) fitted ellipsoid, respectively, with orange and blue symbols indicating tabular and rounded olivine grain framework, respectively (see text and methodology (or Kahl et al., 2017) for details).*

the same orientation as they are displayed in Figure 5.8a. The figure illustrates the good correspondence between the planes normal to the $[100]_{Ol}$, $[010]_{Ol}$ and $[001]_{Ol}$ maxima of each CPO population (dashed curves in Fig. 5.8b pole figures) and the average orientation of the interfaces retrieved from horizontal and vertical thin sections (solid curves in Fig. 5.8b pole figures). The combined CPO–SPO data reveal that up to four populations of olivines tabular on $(100)_{Ol}$ —where the volumetrically dominant population is present in all samples (orange population in Fig. 5.8)— account for the CPOs and SPOs of spinifex Chl-harzburgite olivines. All populations share the same orientation of $[001]_{Ol}$, which plots at the intersection of the $(100)_{Ol}$ interfaces of the different populations (Fig. 5.8b). Relative to the tabular $(100)_{Ol}$ face of the dominant population (orange planes in Fig. 5.8b, pole figures), the SPO–CPO of spinifex Chl-harzburgites result from the rotation of three populations of the tabular olivines (red, blue and yellow planes, respectively, in Fig. 5.8b) by 84°±6°, 30°±7° and 53°±10° around their common $[001]_{Ol}$ direction.

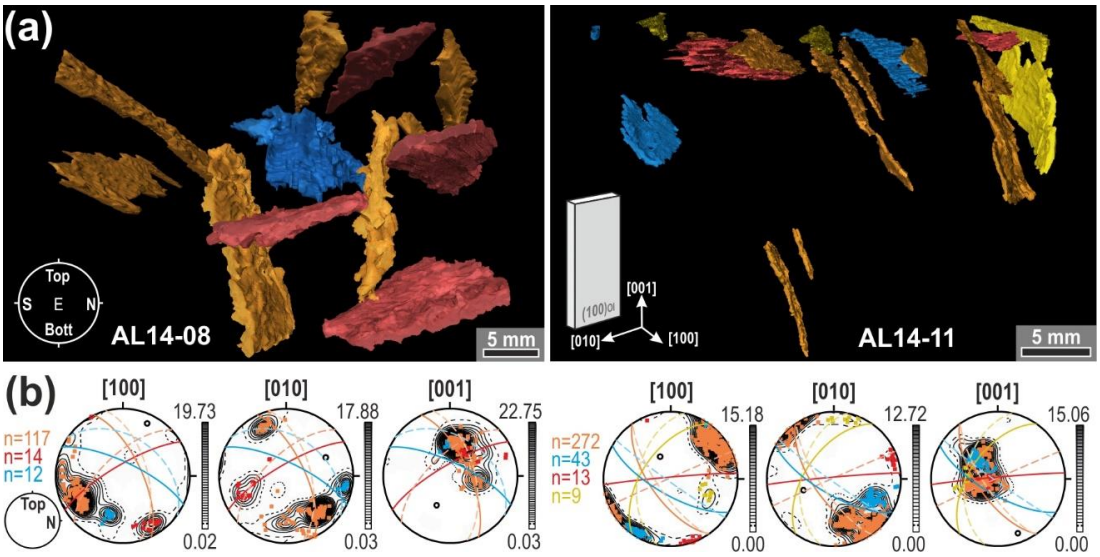

Figure 5.8. *Olivine shape preferred orientation (SPO; a) and crystal preferred orientation (CPO; b) of samples AL14-08 (left) and AL14-11 (right), showing different CPO populations of tabular olivines identified in the spinifex texture based on EBSD data. (a) 3-D volume reconstruction of tabular olivine grains, color-coded to identify the CPO populations shown in (b) (orange, red, blue and yellow, respectively). Inset is a reconstruction of tabular olivine grain with CPO matching SPO. View direction is from E to W. (b) Set of pole figures from AL14-08 and AL14-11 in Fig. 5.7 in a rotated geographic orientation frame, to match orientation in (a). Several CPO maxima —colored orange, red, blue and yellow— in the* $[100]_{Ol}$ *are identified, based on the average measurement per grain ('one point per grain' data); n: number of grains color-coded per population. The planes perpendicular to these maxima are shown by dashed lines. Only grains above the minimum threshold grain size of 3100 µm are shown. Solid lines indicate the orientation of the tabular olivine faces for a given population, calculated from the inclination angle of fitted ellipses of the elongated grains in horizontal and vertical thin section pairs. See Appendix 5.B and text for further details.*

5.5.3 Transitional Chl-harzburgite

5.5.3.1 *Petrography*

The sampled transitional Chl-harzburgite textural type occurs at the bottom of the spinifex Chl-harzburgite lens in the transition to the granofels Chl-harzburgite (red stars in Fig. 5.1b). This textural type has similar mineral assemblage and modal composition to the spinifex and granofels Chl-harzburgites. They are composed of Ol (c. 45 vol%), Opx (c. 45 vol%), Chl (c. 5–10 vol%), and oxides (1–3 vol%) and characterized by composite olivine porphyroblasts (<5 mm) made up of clear, rounded anhedral cores rimmed by coronas of brown, euhedral tabular olivines. The rims of tabular crystals are in optical continuity, and their longest apparent elongation is perpendicular to the interface of the rounded olivines (Fig. 5.1b, sample AL14-06). The textural relationships show that the spinifex textural type overgrew the rounded olivine, and somewhat records a shift in the growth habit of olivine. Orthopyroxene occurs mainly as euhedral crystals and, to a lesser extent, as radial fan-shaped aggregates (1–4 mm long).

5.5.3.2 *SPO and CPO*

Like granofels Chl-harzburgite, the transitional Chl-harzburgite samples also display alignment of prolate-to-oblate rounded olivines that develop a macroscopic compositional layering striking NE-SW and dipping 40–50° SE (Fig. 5.9; solid red plane

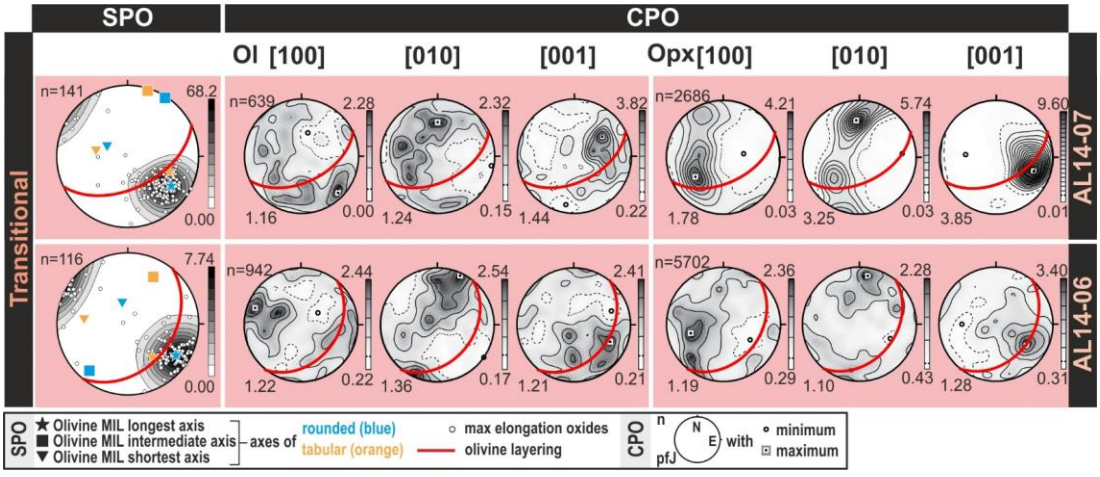

Figure 5.9. *Shape preferred orientation (SPO) of oxides from µ-CT (left panel), and crystal preferred orientation (CPO) of olivine (Ol) and orthopyroxene (Opx) from EBSD (right panel) in transitional Chl-harzburgite (see sample location in Fig. 5.1b). Symbols, plotting convention, and data selection are the same as in Fig. 5.7. Solid red lines indicate compositional layering measured on hand specimens. See text for further details.*

in pole figures). As in granofels and spinifex textures, the μ-CT images of transitional textures show that oxide aggregates with an oblate ellipsoid shape define an aggregate lineation with a strong NW–SE SPO (c. 135/30-40°; azimuth and dip directions) (Fig. 5.9; SPO white dots). The MIL analyses of the μ-CT volume show that in the varied-texture of transitional Chl-harzburgite, the rounded and the tabular olivine also define an olivine grain and platelet lineation (Fig. 5.9; blue and orange stars, respectively) that is parallel to the oxide aggregate lineation.

The olivine CPO is weak and characterized by $[100]_{Ol}$ axes distributed subparallel to the oxide aggregate lineation with a girdle-like $[010]_{Ol}$ distribution perpendicular to the $[100]_{Ol}$ maxima (Fig. 5.9). The SPO of the olivine grain and platelet lineations are close to the $[100]_{Ol}$ maxima (Fig. 5.9). The olivine CPO is, however, uncorrelated with the olivine compositional layering. The CPO of orthopyroxene is strong with the $[001]_{Opx}$ maxima subparallel to the oxide aggregate lineation in the plane of the olivine compositional layering (Fig. 5.9). The other two major crystallographic axes of orthopyroxene show a girdle-like distribution perpendicular to the $[001]_{Opx}$ maximum (Fig. 5.9).

5.6 Discussion

5.6.1 Structural and microstructural evolution during high-P Atg-serpentinite dehydration to Chl-harzburgite

5.6.1.1 *Constraints on the kinematics of the subducting slab from the microstructure of Atg-serpentinite*

The average SPO and CPO of Atg-serpentinites from the present study are shown in Figure 5.10 (upper panel). Under premise that the foliation of Atg-serpentinite is due to intense shear deformation subparallel to the slab interface (cf. Ch. 1, section *1.4.2.2*), the bulk flow plane and flow direction of the slab were, respectively, nearly parallel to the Atg-serpentinite foliation and the oxide aggregate stretching lineation (Fig. 5.10). The Atg-serpentinite structures then provide a common present-day spatial reference framework to investigate the textural evolution during the prograde dehydration of Atg-serpentinite to Chl-harzburgite in the subducting slab.

The average antigorite CPO from our study is similar to those previously reported in the Almirez Atg-serpentinite (Padrón-Navarta et al., 2012). The antigorite CPO can be accounted for by dislocation creep with dominant glide on the antigorite (001)[hk0] slip system, twinning and dissolution-precipitation creep (Padrón-Navarta et al., 2012). The girdle-like CPO symmetry of the $(100)_{Atg}$ and $(010)_{Atg}$ does not constrain the slip direction. The poles to the $(100)_{Atg}$ are the closest to the N–S oxide stretching lineation and, hence, to the shear flow imposed by the local kinematics of the subducting slab (Fig. 5.10). The Almirez Atg-serpentinite structure and CPOs are consistent with those inferred for serpentinite at intermediate depths of subducting slabs (Bezacier et al., 2010; Jung, 2011; Katayama et al., 2009; Morales et al., 2018).

5.6.1.2 *Microstructure of granofels Chl-harzburgite: near-equilibrium growth of olivine during Atg-serpentinite dehydration topotactic reactions*

Crystallization of the granofels Chl-harzburgite has been ascribed to near-equilibrium Atg-serpentinite dehydration associated with slow fluid draining events (Padrón-Navarta et al., 2011). Experimental work shows that topotactic crystallization reaction after Atg-serpentinite and compaction might account for the olivine and orthopyroxene CPOs of granofels Chl-harzburgite (Padrón-Navarta et al., 2015). The olivine CPO of granofels Chl-harzburgite (Fig. 5.10) is consistent with topotactic growth of olivine after antigorite following the topotactic relationships $<100>_{Atg}||<100>_{Ol}$ and $(001)_{Atg}||(010)_{Ol}$ (the topotactic replacement TR2 of Boudier et al., 2010; Padrón-Navarta et al., 2015; and references therein). Similarly, the orthopyroxene CPO can be explained by the topotactic relationships $(100)_{Opx}||(001)_{Atg}$ and $[001]_{Opx}||[100]_{Atg}$ from the CPO of the precursor Atg-serpentinite (Fig. 5.10). As a result of these topotactic crystallization reactions, the $[010]_{Ol}$ and $[100]_{Opx}$ maxima of granofels Chl-harzburgite coincide with the $[001]_{Atg}$ of the precursor Atg-serpentinite (green stars in Fig. 5.10).

The olivine and orthopyroxene CPOs of granofels Chl-harzburgite in our study (Fig. 5.5) are comparable to those reported by Padrón-Navarta et al. (2015) but differ by showing a more pronounced correlation of $[100]_{Ol}||[001]_{Opx}$ and a wider dispersion of $[010]_{Ol}$ and $[100]_{Opx}$ (cf. Fig. 6 with Fig. 8 of Padrón-Navarta et al., 2015). These differences could be due to a higher extent of compaction and coeval fluid migration in our samples. Compaction and topotactic reaction would also explain why the occasional

olivine layering of granofels Chl-harzburgite (red planes in Fig. 5.10) is broadly parallel to the Atg-serpentinite foliation.

The above results show that the CPO of Atg-serpentinite —ultimately governed by shear flow at the slab interface— shaped the CPO of the prograde granofels Chl-harzburgite via a topotactic oriented crystallization reaction. The orientation of the marked SE–NW oxide aggregate lineation of granofels Chl-harzburgite, which is broadly parallel to $[100]_{Ol}$ and $[001]_{Opx}$ differs, however, from the N–S stretching lineation in the overlying Atg-serpentinite (Fig. 5.10). The similar orientation of the oxide aggregate

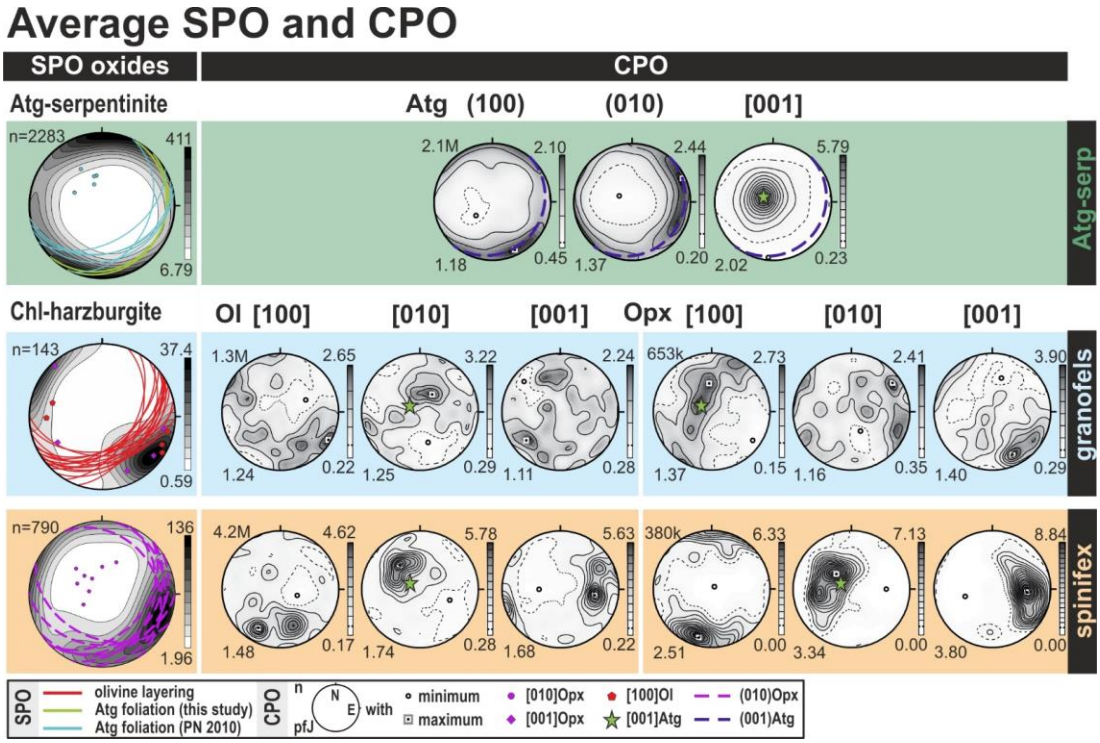

Figure 5.10. *Comparison of the orientation of the average structure and microstructure of Almirez Atg-serpentinite, and granofels and spinifex Chl-harzburgite (merged from Figs. 5.3, 5.5 and 5.7, respectively). The SPO of oxides and the CPO's of Antigorite (Atg), olivine (Ol) and orthopyroxene (Opx) are the bulk data integrating the measurements of all samples for a given rock-type. In case of Atg, pole figure contains a random selection of 2.1 million pixels from the three Atg-serpentinite samples. In the SPO pole figures of oxides, the main structures observed in each rock type are also plotted: the planes of the Atg-serpentinite foliation (light green solid lines, from this study; light blue solid lines from Padrón-Navarta et al., 2010b); the olivine layering of granofels Chl-harzburgite (solid red line). The purple dashed lines in the pole figure of the SPO of oxides in the spinifex Chl-harzburgite correspond to the calculated* $(010)_{Opx}$ *planes from the CPO of Opx in this rock type (cf. Fig. 5.7). The dark blue dashed plane in the Atg pole figures is the average* $(001)_{Atg}$ *plane. The green star indicates comparison with the maximum of* $[001]_{Atg}$*. Pole figures are equal area lower hemisphere projections. See text for further details.*

lineation in spinifex and granofels Chl-harzburgites points to a common origin unrelated to the slab-induced shear flow.

5.6.1.3 *Origin of the CPO and SPO of the spinifex Chl-harzburgite*

The crystallization of spinifex Chl-harzburgite has been ascribed to high overstepping of the Atg-serpentinite dehydration reaction associated with fast fluid draining events (Padrón-Navarta et al., 2011). Our correlative μ–CT and EBSD study unveils that texture of spinifex Chl-harzburgite displays systematic SPOs and CPOs (Fig. 5.10 lower panel). The SPO of oxide aggregates is dispersed on a plane with a similar orientation (145°±10/20°±5; Fig. 5.10) to the Atg-serpentinite foliation, the granofels Chl-harzburgite olivine layering and the $(010)_{Opx}$ (Fig. 5.10). As its granofels counterpart, the spinifex Chl-harzburgite also displays a strong ESE–WNW oxide aggregate lineation different in orientation to that of Atg-serpentinite (Fig. 5.10).

The average spinifex Chl-harzburgite CPOs of olivine and orthopyroxene are remarkably strong (Fig. 5.10). As granofels textures, the absence of ductile microstructures indicates that the CPO of Chl-harzburgite minerals is due to oriented metamorphic crystallization. However, topotactic crystallization reactions after Atg-serpentinite cannot account for the olivine and orthopyroxene CPOs and the different olivine orientation populations of spinifex Chl-harzburgite (Fig. 5.8). Unlike granofels Chl-harzburgite, the $[010]_{Ol}$ and $(100)_{Ol}$ of the volumetrically dominant population of tabular olivines is nearly perpendicular to the Atg-serpentinite foliation and, therefore, to the paleo-slab flow plane and slab flow direction (Fig. 5.10). The other three populations of tabular olivines show orientations that can hardly be due to topotactic reactions from the CPO of a common Atg-serpentinite precursor. Another unique feature of the spinifex Chl-harzburgites is the symmetries with $[100]_{Ol}||[100]_{Opx}$, $[010]_{Ol}||[010]_{Opx}$ and $[001]_{Ol}||[001]_{Opx}$. Hidas et al. (2016) reported similar symmetries in mantle peridotites that they ascribed to oriented crystallization of orthopyroxene after olivine dissolution and orthopyroxene precipitation reactions assisted by silica-rich fluids.

5.6.2 Role of far-field stresses and fluid flow in the development of the SPO and CPO of Chl-harzburgites

Figure 5.11 shows a sketch of the different lithologies and structures of Almirez massif. Also shown are estimates of the orientation of the principal stresses prevalent during dehydration of Atg-serpentinite inferred from different structural and microstructural observations (Clément et al., 2018; Jabaloy-Sánchez et al., 2015; Padrón-Navarta et al., 2010b). All data are shown in the present-day geographical orientation of the massif. As discussed in Ch. 1, the Chl-harzburgite was likely facing upward the hot, extending upper plate (Fig. 1.11c), so the present-day structure of the massif is likely inverted relative to its pristine position in the slab.

At the highly accumulated finite strain of the subduction-interface shear zone, the mylonitic foliation and the stretching lineation should be nearly parallel to the shear flow plane and kinematics of the slab motion near the interface, respectively, and the maximum compressive stress, σ_1, at an angle of 30º±15º to the flow plane (e.g. Sibson, 2017). At the present-day orientation of the Almirez massif, σ_1 should then be at an angle of 30°±15° relative to the foliation of Atg-serpentinite, and within a N–S subvertical plane containing the oxide stretching lineation (Fig. 5.11b). Shear sense indicators further constrain a top-to-South sense of shear (Figs. 5.1c and 5.11a). From the analysis of the orientation of orthoenstatite in Almirez Chl-harzburgite and transitional lithologies, Clément et al. (2018) have estimated the orientation of the σ_1 prevalent during dehydration of Atg-serpentinite (Fig. 5.11b-d, σ_1 red circle in pole figures). Their estimate of σ_1 is at an angle of 45° relative to the average Atg-serpentinite foliation, which is consistent with the theoretical consideration from our study (Fig. 5.11b-d). Based on the structural analysis of GSRZ –interpreted as high-permeability fluid flow pathways of Atg-dehydration fluids (cf. Ch. 1)– Jabaloy-Sánchez et al. (2015) provided another independent estimate of the orientation of the main paleostress axes, σ_1 (188°/30°), σ_2 (091°/32°) and σ_3 (314°/70°), right afterward the crystallization of Chl-harzburgite (Fig. 5.11c-d). Considering the significant uncertainties involved in the estimation of the paleo-stress field from different observables, there is an excellent match between the orientation of σ_1 estimated from independent observations in Atg-serpentinite and Chl-harzburgite. The combination of different observations allows us to determine the approximate

orientation of the three principal compressive stresses in the present-day orientation of the massif (Fig. 5.11a–d). The inferred paleo-stresses likely record the stresses near the slab interface during the high-P dehydration of Atg-serpentinite to prograde peridotite at the intermediate depth of the subducting NFC slab.

The excellent correspondence between the paleo-stress orientation estimates from Atg-serpentinite and Chl-harzburgite indicates that their textures were coevally formed under the same orientation of the principal stresses. While the tectonic texture of Atg-serpentinite records the long-term shear deformation at the slab interface, the coarse-grained texture of their prograde Chl-harzburgite product records the metamorphic crystallization likely at shorter timescales in an overpressured fluid environment.

The granofels and spinifex Chl-harzburgite textures record, respectively, metamorphic crystallization after serpentinite during slow and fast fluid draining events (Padrón-Navarta et al., 2011). The olivine and orthopyroxene CPOs of granofels Chl-harzburgite were formed during slow draining of fluids at near equilibrium conditions by topotactic Atg-serpentinite dehydration reaction and compaction (Padrón-Navarta et al., 2015; this thesis). The σ_1 component normal to the slab interface likely contributed to compaction during formation of granofels Chl-harzburgite. The texture of the transitional Chl-harzburgite from our study likely records the switch between slow and fast draining events that resulted in the crystallization of spinifex Chl-harzburgite. The SPO and CPO of spinifex Chl-harzburgite tabular olivines show a remarkable spatial correlation with the estimated orientation of paleo-stresses (inset in Fig. 5.11d). The $(100)_{Ol}$ tabular face of the volumetrically dominant population of tabular olivines lies on the plane of maximum compression (σ_2–σ_3; Fig. 5.11d, orange dashed plane in pole figure and orange rectangle in inset). The crystallization of this population is consistent with oriented growth of platy crystals perpendicular to the maximum stress direction, σ_1 (e.g., Means and Paterson, 1966; Vaughan et al., 1984) (Fig. 5.11d). The other orientation populations of tabular olivines lie on the plane perpendicular to the least compressive stress axis, σ_3 (Fig. 5.11d, red rectangle in inset), and the conjugate planes of maximum shear stress (Fig. 5.11d, yellow and blue rectangles in inset). In all cases, the $(100)_{Ol}$ tabular face populations are rotated around their $[001]_{Ol}$ and parallel to the intermediate compressive stress, σ_2 (Fig. 5.11d). The ultimate cause for the oriented crystallization of tabular olivines in directions other than the main compressive stress is uncertain. The correlation

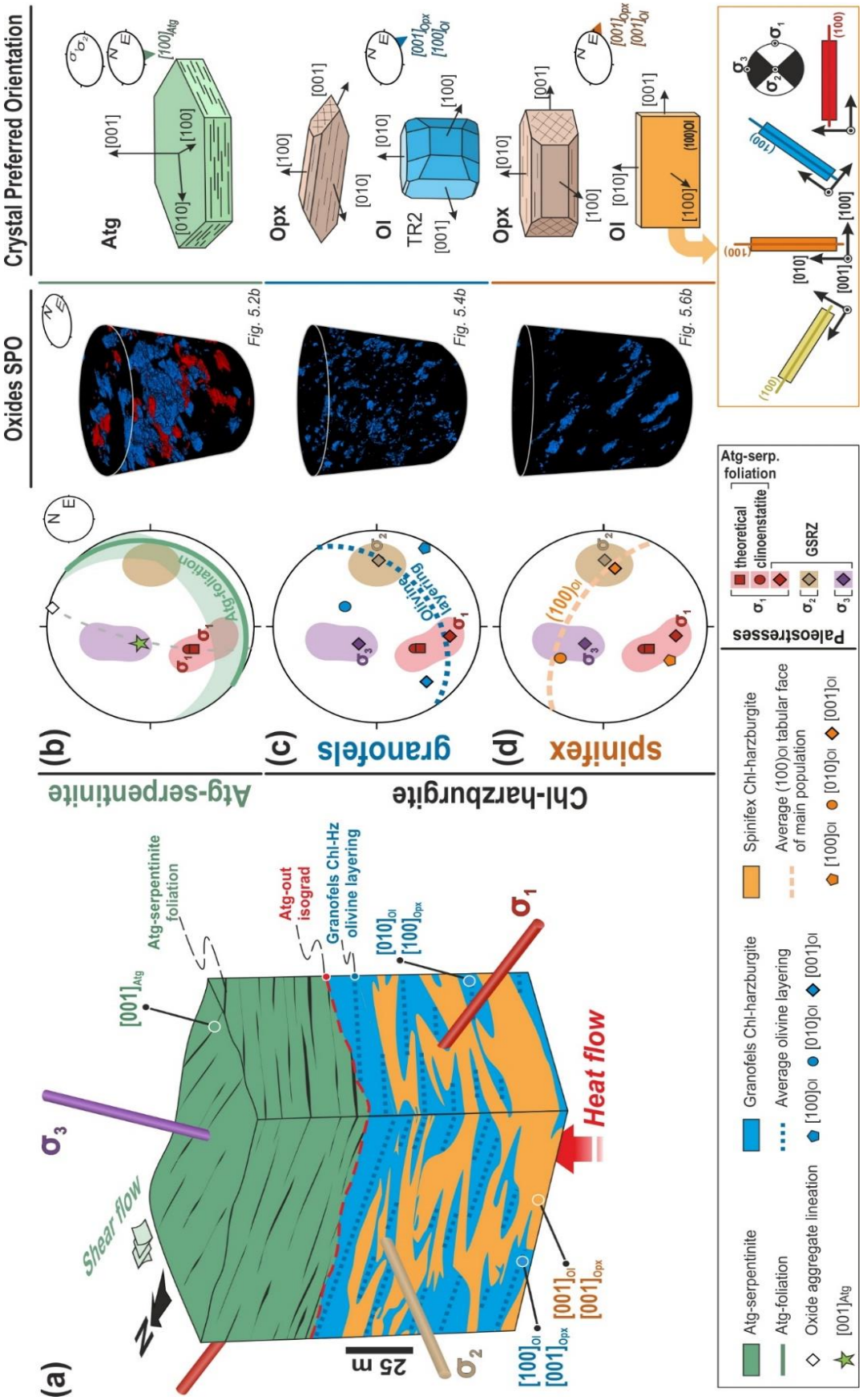
Crystal Preferred Orientation
Oxides SPO
Atg-serpentinite
Chl-harzburgite
(a)
(b)
(c)
(d)
granofels
spinifex
Atg
Opx
Ol
TR2
Fig. 5.2b
Fig. 5.4b
Fig. 5.6b
Atg-foliation
Olivine layering
(100)Ol
σ1
σ2
σ3
Shear flow
Heat flow
25 m
N
Atg-serpentinite foliation
Atg-out isograd
Granofels Chl-Hz olivine layering
[001]Atg
[010]Ol
[100]Opx
[100]Ol
[001]Ol
[001]Opx
Atg-serpentinite
Atg-foliation
Oxide aggregate lineation
[001]Atg
Granofels Chl-harzburgite
Average olivine layering
[100]Ol [010]Ol [001]Ol
Spinifex Chl-harzburgite
Average (100)Ol tabular face of main population
[100]Ol [010]Ol [001]Ol
Atg-serp. foliation
Paleostresses
theoretical
clinoenstatite
GSRZ

of the tabular olivine CPOs and SPOs with the orientation of principal paleo-stresses points that stress somehow exerted a control in the orientated crystallization of spinifex Chl-harzburgite olivines.

The strong ESE–WNW oxide aggregate lineations of spinifex and granofels Chl-harzburgites are markedly different in orientation from the N–S tectonic stretching lineation of the Atg-serpentinite (Fig. 5.10). The spatial correlations of the oxide aggregate lineations with the olivine and orthopyroxene CPOs in Chl-harzburgites indicate that these lineations were formed during metamorphic crystallization (Fig. 5.10). Previous studies have shown that dehydration of Atg-serpentinite to Chl-harzburgite resulted in bulk-rock iron reduction and consumption of oxides (Debret et al., 2015). Although the exact cause is uncertain, a possibility is that the aggregate lineations of oxides in Chl-harzburgite and the platelet lineation of spinifex olivines may be due to paleo-fluid flow and fluid-enhanced dissolution-precipitation along σ_2. Mesh structures may lead to structural permeability and lateral fluid flow along σ_2 (Sibson, 1996). In such structures, overpressured fluids may be deflected from vertical flow by stress-controlled lateral permeability along the σ_2 direction (Sibson, 1996). We speculate that similar structures may develop in overpressured fluid domains formed during dehydration of serpentinite below the permeability barrier constituted by the Atg-out isograd.

Figure 5.11. *(a) 3-D block diagram summarizing the main structural and microstructural data of the Almirez massif Atg-serpentinite and Chl-harzburgite, and the orientation of the principal paleo-stress axes (red: σ1, light brown: σ2 and purple: σ3) in present-day orientation. Solid black lines with dotted arrowheads indicate the approximate direction of the maxima of the corresponding crystallographic axes in olivine (Ol), orthopyroxene (Opx) or antigorite (Atg). See legend and text for further details. (b–d) Comparison of the orientation of the main structures and paleo-stresses (pole figures), μ-CT oxide aggregate SPO (from Figs. 5.2b, 5.4b, and 5.6b), and the mineral CPO in Almirez Atg-serpentinite, granofels and spinifex Chl-harzburgite. Gray dashed line in (b) indicates the trace of the plane perpendicular to Atg-serpentinite foliation and parallel to oxide aggregate lineation. See text for discussion.*

5.7 Appendices

5.A Crystal preferred orientation (CPO) of antigorite

Crystal preferred orientation (CPO) of antigorite in horizontal and vertical thin sections (TS) of Atg-serpentinite samples shown in Fig. 5.3. See caption of Fig. 5.3 for further details.

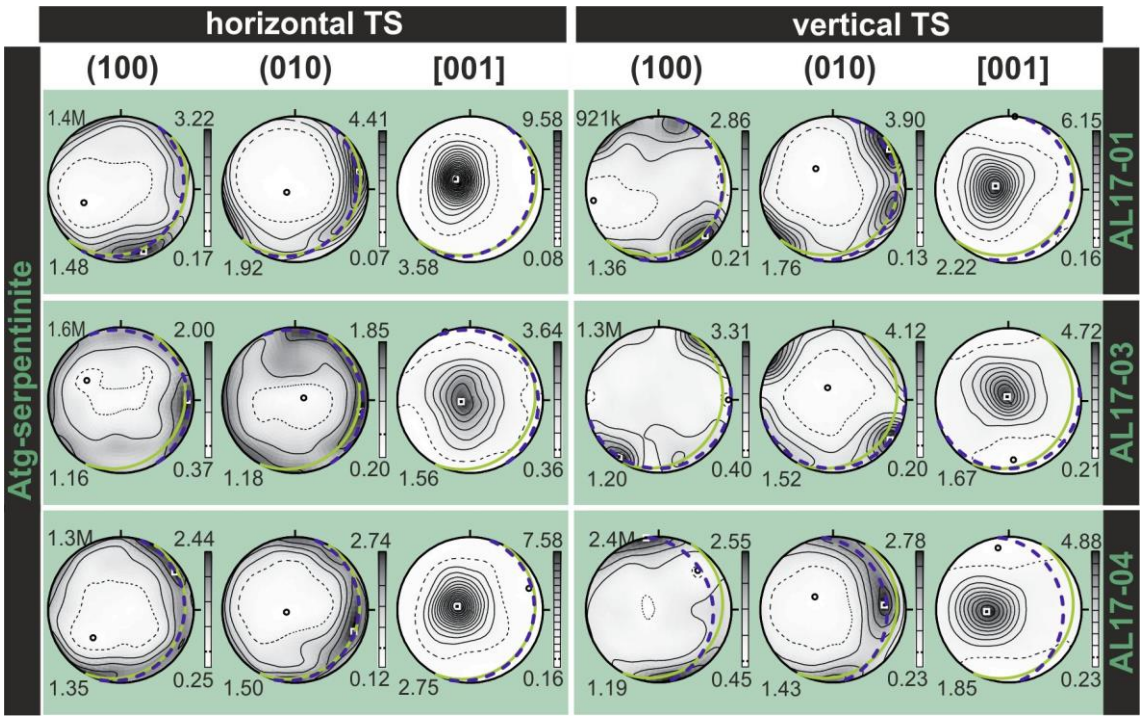

5.B SPO and CPO populations of tabular olivine

SPO and CPO populations of tabular olivine in spinifex Chl-harzburgite samples AL14-08 and AL14-11. Left: EBSD orientation maps of olivine grain sections in vertical and horizontal thin sections; groups of grains with the same CPO are color-coded into orange, red, blue and yellow; grains shown in gray are unclassified. Also shown are the cumulative histograms of the relative area% of grains from different groups versus their inclination angle — 5–180°; binned in 5° intervals; see inset— relative to N–S direction. Dashed square in horizontal thin section of sample AL14-08 indicates the area enlarged in the right panel. The solid gray lines in the horizontal section are the approximate trace of the vertical thin sections. Right: pole figures of the olivine CPO of each orientation group color-coded in the thin sections (see Fig. 5.8b). Dashed lines are the $(100)_{Ol}$ planes of each orientation group of tabular olivines. Solid lines are the calculated tabular faces

per group obtained from the combination of the apparent orientation of groups in the horizontal and vertical thin sections. See text for further details.

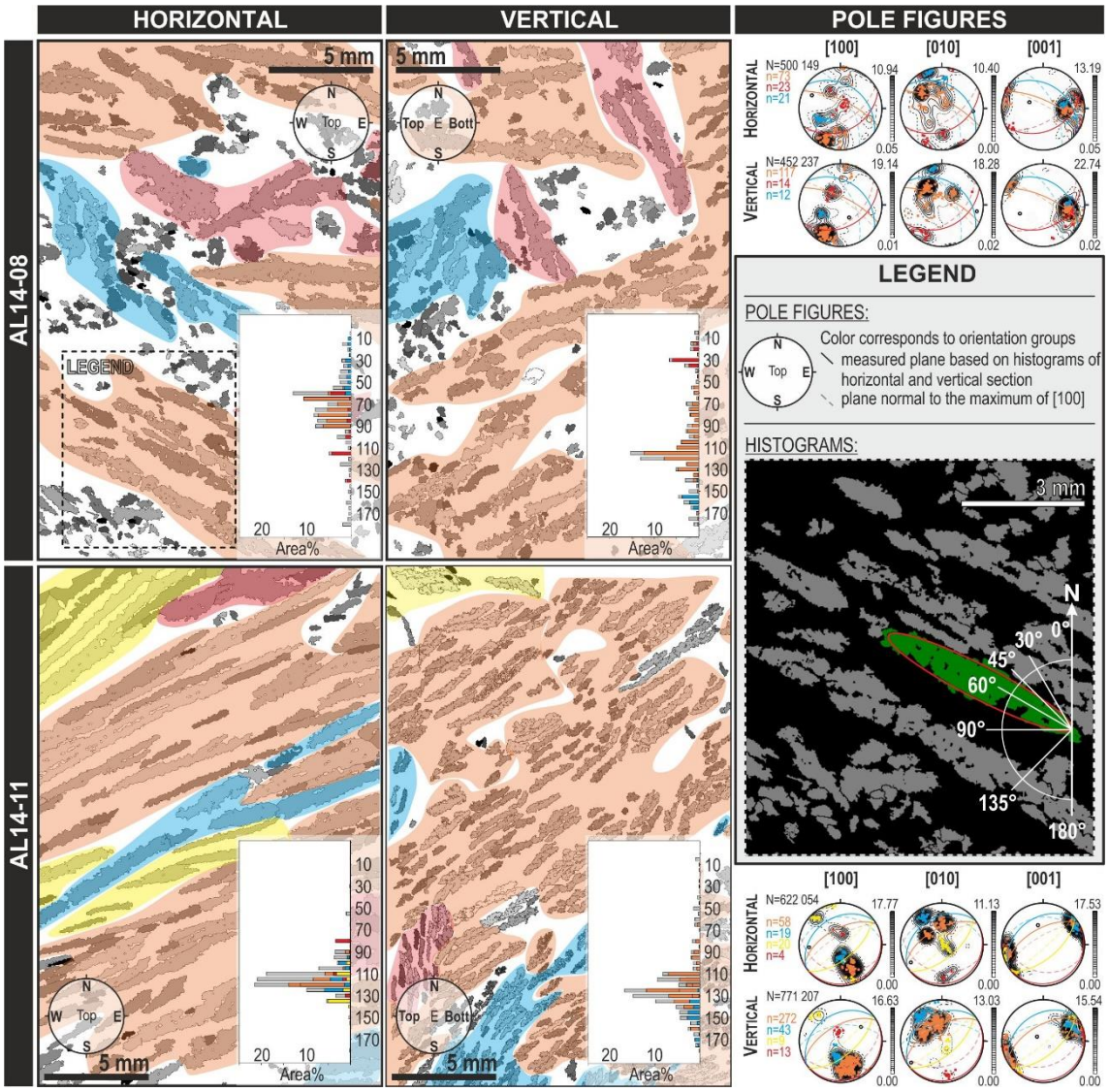

6 Morphological Transition during Prograde Olivine Growth formed by High-Pressure Dehydration of Antigorite-serpentinite to Chlorite-harzburgite in a Subduction Setting[1]

6.1 Introduction

The pressure (P) and temperature (T) history of metamorphic rocks is recorded in the chemical composition of coexisting minerals and their textures (e.g., Yardley, 1989). While the application of thermodynamics to the quantitative determination of equilibrium P and T in metamorphic petrology is highly advanced, our understanding of the kinetics of metamorphic processes recorded in metamorphic microstructures has lagged behind (e.g., Carlson et al., 2015). Rock microstructures —e.g., shape and crystal preferred orientations, crystal size and number, and the crystal size distribution— are the result of variable rates and mechanisms of nucleation and growth during metamorphic reactions (e.g., Carlson et al., 2015; Pattison et al., 2011; Ridley and Thompson, 1986). The rate of heterogeneous nucleation and growth mechanism strongly depends on the reaction affinity, which is the thermodynamic driving force for the reaction and can be defined as the difference of the Gibbs free energy between the thermodynamically stable reaction products and the metastable reactants (e.g., Pattison et al., 2011, and references therein). Kinetic barriers to nucleation and growth imposed a certain affinity for the reaction to proceed —commonly known as the overstepping of the reaction — delaying the onset of prograde metamorphic reactions (Carlson et al., 2015; Pattison et al., 2011; Ridley and Thompson, 1986; and references therein).

Crystal morphology during metamorphic crystallization is thought to depend mostly on the growth rate mechanism (interface- versus diffusion-controlled), which is

[1] This chapter is in review in the **Lithos** Special Volume on the Subduction Interface: Dilissen, N., Hidas, K., Garrido, C.J., López Sánchez-Vizcaíno, V., Kahl, W.-A., Morphological transition during prograde olivine growth formed by high-pressure dehydration of antigorite-serpentinite to chlorite-harzburgite in a subduction setting.

controlled by the affinity of the reaction (Ridley and Thompson, 1986). At near-equilibrium conditions, the slow growing crystal faces with the lowest Miller indices control the morphology and the equilibrium form has a minimum total surface free energy per unit volume (Mullin, 2001). Far from equilibrium, the crystal morphology in metamorphic crystallization is thought to reflect changes in the growth rate mechanisms of different faces set by the affinity of the reaction, mostly in response to changes in the rate of heat and fluid supply (Ridley and Thompson, 1986 and references therein). Rapid changes on the morphology during metamorphic growth —i.e., morphological instabilities— are rare but may occur due to rapid changes in the physicochemical environment of the growing crystals at high affinity of the reaction during metamorphic crystallization (e.g., Jamtveit and Andersen, 1992; Padron-Navarta et al., 2008).

We report a new rare textural variety of Chl-harzburgite in the Almirez massif (hereafter, referred to as transitional Chl-harzburgite) containing varied-textured olivines and composite olivine porphyroblasts displaying morphologies transitional between those of the granofels and spinifex textural types (cf. Ch. 5). Based on a detailed chemical —EPMA and LA-ICP-MS— and microstructural characterization —using correlative μ-CT and EBSD-SEM microscopy— of the transitional Chl-harzburgite olivine, we discuss the different factors that induced this unusual morphological transition during olivine growth, and we relate them to possible variations of physicochemical environmental conditions in subduction zones.

6.2 Sampling

Granofels and spinifex textural types in Chl-harzburgite differ in the morphology of olivine that occur as anhedral and rounded olivine porphyroblasts in the granofels Chl-harzburgite, and as subhedral, elongated tabular crystals in the spinifex Chl-harzburgite (Fig. 6.1a; Trommsdorff et al., 1998; Padrón-Navarta et al., 2011; Kahl et al., 2017; Dilissen et al., 2018). Both textural types have essentially the same mineralogy (ca. 45 vol.% Ol, 45 vol.% Opx, 5–10 vol.% Chl, 1–3 vol.% oxides; Padrón-Navarta et al., 2011) and bulk rock composition (Garrido et al., 2005; Marchesi et al., 2013). In the spinifex Chl-harzburgite, the usually brown appearance of tabular olivines is due to irregular and lamellar, planar intergrowths of F-OH, titanian clinohumite (Garrido et al., 2005; López

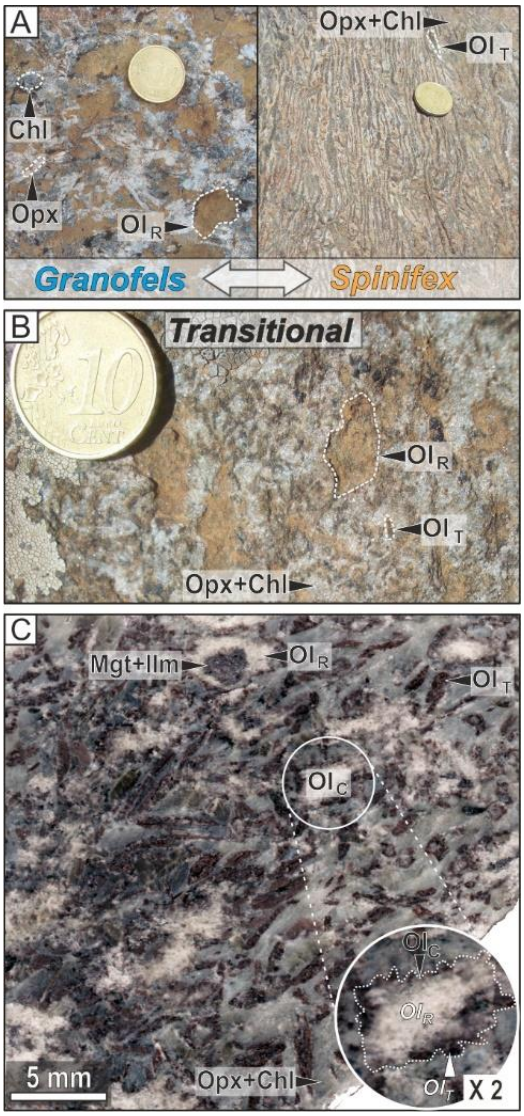

Figure 6.1. *(a) Field images of typical granofels (left) and spinifex (right) textured Chl-harzburgite with rounded (Ol_R) and tabular olivine (Ol_T), respectively, orthopyroxene (Opx) and chlorite (Chl). (b) Field image of transitional Chl-harzburgite with coexistent rounded (Ol_R) and tabular (Ol_T) olivine grains. (c) Transitional Chl-harzburgite (sample AL14-06, used in this study) after polishing and bleaching by diluted HCl (treatment after Nicolas and Poirier, 1976). Inset shows a composite olivine grain (Ol_C) composed of rounded olivine core (Ol_R) and tabular olivine corona (Ol_T). Note that after bleaching rounded and tabular olivines are white and dark brown, respectively, and the orthopyroxene (Opx) and chlorite (Chl) matrix became light green. Mgt: magnetite, Ilm: ilmenite.*

Sánchez-Vizcaíno et al., 2005), as well as magnetite, Cr-bearing spinel and ilmenite inclusions (Ruiz Cruz et al., 1999).

The transitional Chl-harzburgite was sampled —geographically oriented (cf. Ch. 5)— along the contact (red stars; Fig. 5.1b) of the spinifex lens (Fig. 5.1b; lens "2" in Fig. 4.2a) with its lower granofels envelope. The transitional Chl-harzburgite has a similar mineral modal composition to granofels and spinifex Chl-harzburgites (Fig. 6.1a) (ca. 45 vol%; Ol, 45 vol%; Opx, 5–10 vol%; Chl, 1–3 vol% oxides) and occurs in the field with both clear rounded and brown tabular olivine grains (Fig. 6.1b), in many cases in the form of composite porphyroblasts (Ol_C, Fig. 6.1c).

6.3 Analytical techniques

6.3.1 Sample preparation

Oriented cylindrical cores were prepared according to Ch. 3 to reconstruct the 3-D microstructure of olivine using correlative μ-CT and EBSD-SEM microscopy. After μ-CT imaging of cores, two mutually perpendicular thin sections were cut from the same cores following the methodology of Ch. 3. The petrographic thin sections were polished using 3 μm and 1 μm Buehler diamond paste for petrographic observation and geochemical analyses by EPMA and

LA-ICP-MS. Afterward, thin sections were polished with Buehler colloidal silica suspension for further EBSD-SEM analysis.

6.3.2 X-Ray micro-computed tomography (µ-CT)

The cylindrical cores were mounted oriented with the top up and north towards the X-ray source and they were scanned with a beam energy of 130 kV, an energy flux of 350 µA, and using a thin copper filter in 360° rotation scans conducted with a step size of 0.3° at a detector resolution of 16.26 µm per pixel. After an acquisition time between 4 and 5 hours, for each sample an image volume of 2000 × 2000 × 2000 voxels (or larger) was available. Further details on data processing of µ-CT are given in Ch. 3.

6.3.3 Electron backscatter diffraction (EBSD)

Instrumental settings of the SEM were 17 kV acceleration voltage, 24 mm working distance, and probe current of 0.5-1.0 nA. Acquisition conditions in the EBSD software (AZtec v3.1, Oxford Instruments) were 4×4 binning and low (0) gain with grid steps between 18 and 22 µm, covering most of the sample surface (cf. Ch. 3). Detailed EBSD mapping was carried out with a step size of 3 µm. All major constituent minerals of the rocks were included in the phase list, and the percentage of indexed points in the raw maps always exceeded 75%. Post-acquisition data treatment to clean raw maps by filling non-indexed pixels based on neighboring pixel orientation and the removal of wild-spikes were carried out using the built-in functions of the Oxford/HKL Channel 5 software package, and grain segmentation was accomplished using the 'calcGrains' built-in function of MTEX v.4.5.2 Matlab toolbox (https://mtex-toolbox.github.io/; Bachmann et al., 2010, 2011; Hielscher and Schaeben, 2008) following the method presented in Ch. 3.

6.3.4 Electron probe microanalysis (EPMA)

EPMA was performed at the Centre for Scientific Instrumentation (CIC, University of Granada, Spain) using a CAMECA SX100 equipped with five spectrometers. Analyses were carried out using 20 kV accelerating voltage, 20 nA beam current, 5 µm beam diameter, 38 µm raster length and counting times of 20-70 s. Natural and synthetic silicate and oxide standards were used for calibration, and ZAF correction were applied.

6.3.5 Laser ablation inductively coupled plasma mass spectrometry (LA-ICP-MS)

LA-ICP-MS analyses of trace elements in olivine were carried out in petrographic thin sections, previously cleaned with nitric acid. Analyses of olivine were carried out at the Andalchron facilities (IACT, Granada, Spain) using an Analyte G2 193 nm excimer Ar–F laser ablation (LA) system equipped with a HelEx II 2-volume ablation cell hyphenated to an Agilent 8800 ICP-MS/MS. Optimal ablation conditions were tuned using SRM NIST612 for maximum sensitivity, low background attaining oxide formation to a minimum. LA spot analyses were performed with a spot size of 110 µm in static spot mode, an energy fluence of 8 J/cm^2, a total laser energy of 7 mJ, and repetition rate of 20 Hz. A stream of He with a total flow of 1.2 l/min (1 l/min main flow, and 0.2 l/min auxiliary gas flow) was used as the carrier of the ablated material to the ICP-MS/MS torch. Time resolved analyses consisted of 30 s of gas blank and 45 s of sample. Every four unknowns, NIST612 glass and USGS basaltic synthetic glass BIR1-G were analyzed as calibration standard and reference material for quality assurance, respectively. Trace element mapping of Ol_C porphyroblast was performed using a laser fluence of 6.4 J/cm^2, and a total He flow of 0.8 l/min. A square-shaped laser aperture ensured evenly ablated lines from overlapping square with a side length of 24 µm and a 1µm overlap. For technique optimization the laser beam size was set to 24 µm and 12 µm, scan speed varied from 1, 2 to 5 µm/s and repetition rate from 10 to 5 Hz, with a 30 s washout between lines.

Data acquisition was done with Masshunter software (Agilent Technologies) in a single continuous experiment of 3 hours. Dwell time was 50 ms for Ca and Si and 100 ms for all other analytes, with 5 s washout time. Data reduction and production of trace element spot results and distribution map was carried out with Iolite v3.24 software (http://www.iolite.org.au; Paton et al., 2011; Woodhead et al., 2008), using Si concentration measured by EPMA as internal standard.

6.4 Results

6.4.1 Petrography of transitional Chl-harzburgite

Orthopyroxene occurs mainly as euhedral crystals and, to a lesser extent, as radial fan-shaped aggregates (1-4 mm long). Chlorite occurs as disseminated flakes (200 µm long) or aggregates associated with oxides. Olivine occurs as rounded (Ol_R) and tabular (Ol_T) grains (Fig. 6.2a). These two olivine morphologies are reminiscent of those observed in the granofels (Ol_R) and spinifex (Ol_T) Chl-harzburgites elsewhere in the Almirez Chl-harzburgite section (Padrón-Navarta et al., 2011). The presence of composite (Ol_C) olivine porphyroblasts (<5 mm) composed of large cores of Ol_R lined by coronas of Ol_T grains, is the most prominent textural characteristic of the transitional Chl-harzburgite (Fig. 6.1c and 6.2b-c). The Ol_T display their highest apparent elongation perpendicular to the Ol_R interface at regular directions and are in quasi-optical continuity with the Ol_R

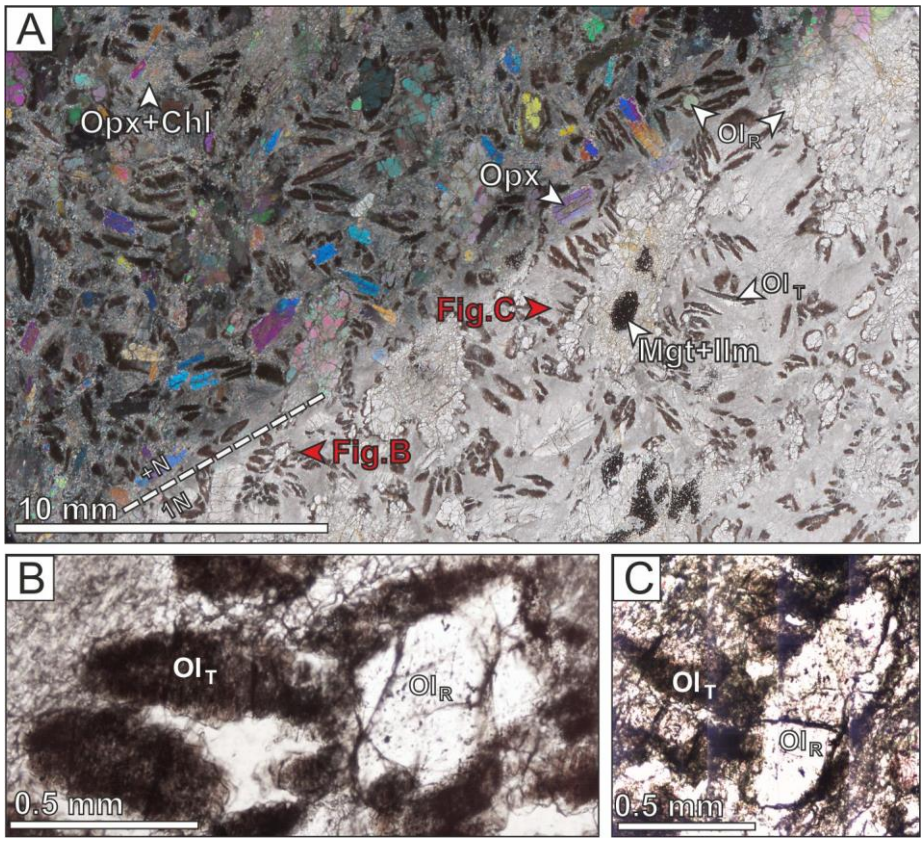

Figure 6.2. *(a) Optical microscope view of transitional Chl-harzburgite showing the varied-textured of olivine (Ol_R: rounded olivine; Ol_T: tabular olivine; Opx: orthopyroxene; Chl: chlorite; Ox: oxides). Plane polarized light (1N) photomicrograph (bottom-right corner) is overlaid by crossed polarized light (+N) photomicrograph (upper-left corner). (b-c) Close-up view of composite olivine porphyroblasts (Ol_R + Ol_T) shown in (a).*

cores (Fig. 6.2b-c). These Ol_C porphyroblasts provide a snapshot of the morphological transition from Ol_R to Ol_T. Short tabular (aspect ratio of 1:2 – 1:5) grains of brown Ol_T (<2 mm), and clear Ol_R (<5 mm) with brown rims also occur as isolated grains in the matrix (Fig. 6.2a).

6.4.2 Major and trace element composition of olivine

The major element analyses of tabular and rounded olivines in composite grains from two transitional Chl-harzburgite samples (AL14-06 and AL14-07; cf. Fig. 5.1) are illustrated in Figure 6.3, and average analyses are listed in Table 6.1. Within the detection limits of EPMA analyses, the core and rim composition of the two olivine crystal morphologies do not reveal significant intragranular variations in Fe and Mg (Appendix 6.A). The olivine forsterite content ranges between 0.895–0.901 in Ol_R (blue dots in Fig. 6.3) and 0.890–0.899 in Ol_T (orange triangles in Fig. 6.3). Ol_T grains show slightly higher NiO and Cr_2O_3 concentration than Ol_R grains (0.41±0.02 wt% vs. 0.37 ± 0.06 wt% and 0.16±0.1 wt% vs. 0.05±0.06 wt%, respectively; Table 6.1) and they have an identical concentration in MnO (0.13±0.01 wt% vs. 0.13±0.02 wt%; Table 6.1). The major element compositions of Ol_R and Ol_T in the transitional Chl-harzburgite overlap the compositional range of olivines in both granofels and spinifex Chl-harzburgites (e.g., Bretscher et al., 2018; Padrón-Navarta et al., 2011), except for some Ol_T grains that are slightly richer in FeO than tabular olivines in spinifex Chl-harzburgite (Fig. 6.3). These analyses also display anomalously high Cr and Ti contents (Appendix 6.A).

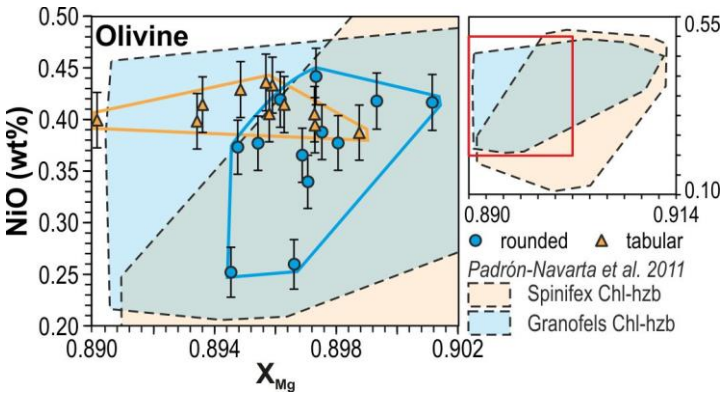

Figure 6.3. *NiO (wt%) vs XMg (=Mg/(Mg+Fe) in a.p.f.u.) composition of rounded olivine (blue dots) and tabular olivine (orange triangles) in Almirez transitional Chl-harzburgite based on electron microprobe analyses (EPMA). Fields in the background are the ranges of rounded olivines in granofels Chl-harzburgite (light blue field) and tabular olivines in spinifex Chl-harzburgite (light orange field) from Padrón-Navarta et al. (2011). The full range of literature data is shown in the inset in the top-right of the figure. NiO detection limit is 0.03 wt% and the standard deviation during EPMA analysis was 0.025 wt% (added to the analytical points as vertical bars).*

Trace element analyses of olivine in transitional Chl-harzburgite AL14-06 are

Table 6.1. *Average major and trace element composition of rounded and tabular olivine crystals in Almirez transitional Chl-harzburgite.*

Morphology	Rounded *Avg(n=12) ±1σ*		Tabular *Avg(n=11) ±1σ*	
SiO_2 (wt%)	40.3	± 0.1	40.1	± 0.2
TiO_2	0.01	± 0.006	0.06	± 0.04
Cr_2O_3	0.05	± 0.06	0.16	± 0.1
FeO*	10.1	± 0.2	10.2	± 0.2
MnO	0.13	± 0.02	0.13	± 0.01
NiO	0.37	± 0.06	0.41	± 0.02
MgO	49.1	± 0.2	49.0	± 0.2
CaO	0.01	± 0.001	0.01	± 0.004
Na_2O	0.01	± 0.001	0.01	± 0.002
Total	100.1	± 0.2	100.2	± 0.2
X_{Mg}	0.897	± 0.002	0.895	± 0.002
	Avg(n=7) ±1σ		*Avg(n=5) ±1σ*	
Cs (ppm)	0.009	± *0.0002*	0.02	± *0.007*
Rb	0.03	± *0.01*	0.09	± *0.08*
Ba	0.42	± *0.27*	1.92	± *1.03*
Th	0.007	± *0.004*	0.06	± *0.02*
U	0.01	± *0.008*	0.19	± *0.03*
Nb	0.24	± *0.07*	1.22	± *0.17*
Ta	0.008	± *0.003*	0.04	± *0.009*
La	0.01	± *0.006*	0.07	± *0.02*
Ce	0.03	± *0.01*	0.15	± *0.05*
Pb	0.06	± *0.04*	0.27	± *0.15*
Pr	0.003	± *0.001*	0.02	± *0.006*
Sr	1.41	± *1.03*	4.1	± *4.6*
Nd	0.01	± *0.005*	0.07	± *0.02*
Zr	0.05	± *0.02*	0.72	± *0.20*
Hf	0.004	± *0.002*	0.06	± *0.01*
Sm	0.005	± *0.003*	0.03	± *0.01*
Eu	0.002	± *0.0007*	0.004	± *0.002*
Gd	0.005	± *0.003*	0.04	± *0.01*
Ti	41.9	± *12.3*	360.0	± *119.7*
Tb	0.001	± *0.0004*	0.009	± *0.002*
Dy	0.01	± *0.007*	0.11	± *0.01*
Y	0.13	± *0.06*	0.90	± *0.04*
Ho	0.005	± *0.002*	0.04	± *0.002*
Er	0.02	± *0.01*	0.19	± *0.006*
Tm	0.005	± *0.001*	0.04	± *0.003*
Yb	0.06	± *0.01*	0.36	± *0.02*
Lu	0.02	± *0.002*	0.08	± *0.008*

Average values with standard deviations are calculated from data presented in Supplementary Tables in Appendix 6.A and Appendix 6.B, respectively. FeO: all iron reported as Fe2+; XMg=Mg/(Mg+Fe) expressed in cation numbers per formula units.*

listed in Table 6.1, and their Primitive Upper Mantle (PUM after Sun and McDonough, 1989) trace element pattern is shown in Figure 6.4a. The extended dataset is provided in Appendix 6.B. Due to the large spot size of LA-ICP-MS analyses, detailed spot analyses of olivine cores and rims were unfeasible. The PUM normalized trace element patterns of transitional Chl-harzburgite Ol_R are similar to those of olivines from the granofels Chl-harzburgite and Atg-serpentinite (Fig 6.4a) (Marchesi et al., 2013). On the other hand, Ol_T overlap with the field of those reported in spinifex Chl-harzburgite (yellow shaded area, Fig. 6.4a; Marchesi et al., 2013).

The trace element concentration of Ol_T is typically a factor of 5–7 greater than in Ol_R from the same sample. Fluid-mobile, Large-Ion Lithophile Elements (LILE), particularly Cs, Rb, Ba, Pb, Sr, show up to 3 times greater concentrations than in Ol_R (Fig. 6.4b). Among the enriched elements, no significant fractionation is observed in High Field-Strength Elements (HFSE; e.g., Nb, Ta, Zr, Hf and Ti) and most REE (rare earth elements) (cf. rather flat trace element pattern in Fig. 6.4b), but some HFSE (particularly U, Zr, Hf and Ti) are present with anomalously high concentrations, up to 20 times the composition of Ol_R (Fig. 6.4b; Appendix 6.B).

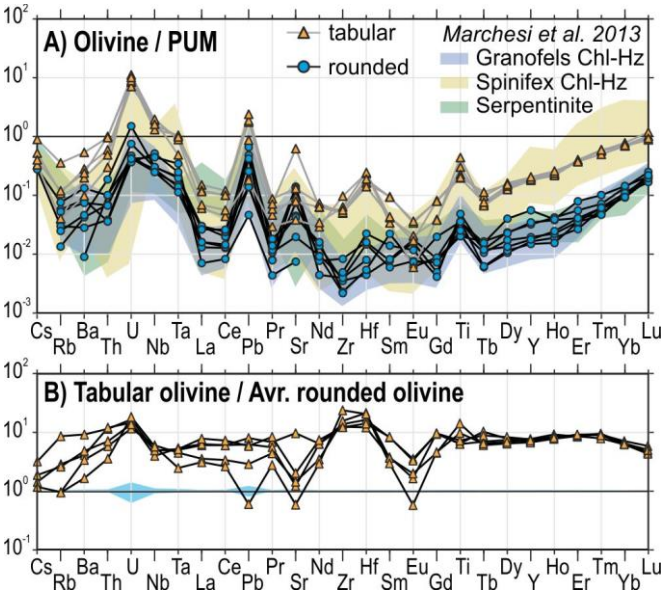

Figure 6.4. *(a) Primitive upper mantle (PUM)-normalized trace element patterns of rounded (blue dots) and tabular (orange triangles) olivines in Almirez transitional Chl-harzburgite (sample AL14-06) from LA-ICP-MS analyses. Normalizing values from Sun and McDonough (1989). Compositional fields of rounded olivines in serpentinite and granofels Chl-harzburgite (green and blue shaded area, respectively) and tabular olivines in spinifex Chl-harzburgite (yellow shaded area) are shown for comparison (after Marchesi et al., 2013). (b) Tabular (orange triangles) olivines normalized to the average composition of the rounded ones from the Almirez transitional Chl-harzburgite. The standard deviation of the calculated average rounded olivine composition is given as blue shaded area in the background.*

Detailed LA-ICP-MS mapping of the Ti content in a composite olivine grain (shown in Fig. 6.2c) demonstrates that enrichment in these latter elements is restricted to the occurrence of tabular olivine morphology (Fig. 6.5).

6.4.3 Olivine microstructures and crystal morphologies

High-resolution EBSD map and crystal preferred orientation (CPO) data unveil that Ol_T and Ol_R in composite olivine porphyroblasts (Fig. 6.2b-c) share the same crystallographic orientation (Fig. 6.6). This crystallographic relationship implies epitaxial growth of tabular grains (Ol_T, outside white dashed line; orange and yellow squares; Fig. 6.6b-d) on rounded olivine seeds (Ol_R, inside white dashed line; purple and green squares Fig. 6.6b-d).

Combination of high-resolution µ-CT and EBSD data of composite olivine grains shows that the switch from rounded to tabular crystal habit was achieved by anisotropic growth parallel to the (100) face along [001] direction, resulting in olivine morphology tabular on (100) faces with [001] > [010] >> [100] (Fig. 6.7a-b). This morphology and orientation of tabular olivine in the transitional Chl-harzburgite is similar to those in spinifex Chl-harzburgite (Dilissen et al., 2018; Kahl et al., 2017).

6.5 Discussion

6.5.1 Origin of the compositional differences in olivine

The two main textural types of Chl-harzburgite in the Almirez ultramafic massif record different physical and fluid flux conditions during the dehydration of Atg-serpentinite: (1) antigorite breakdown at equilibrium and slow drain of fluids generated granofels Chl-harzburgite, and (2) fast crystal growth under high fluid-flux developed spinifex Chl-harzburgite in disequilibrium domains (Padrón-Navarta et al., 2011; Padrón-Navarta et al., 2010b). Mass balance calculations of fluid circulation in the Almirez paleo-subduction zone indicate that spinifex Chl-harzburgite crystallized in an open-system environment drained by volumes of external fluids up to 200 times greater than those produced by closed-system antigorite dehydration responsible for the formation of granofels Chl-harzburgite (Marchesi et al., 2013).

The varied-texture of transitional Chl-harzburgite captures the moment when physicochemical conditions during the Atg-serpentinite dehydration reaction have been changed, and Chl-harzburgite started to develop with spinifex olivine texture (Figs. 6.2 and 6.6). This observation is attested by the remarkable similarities in the major element

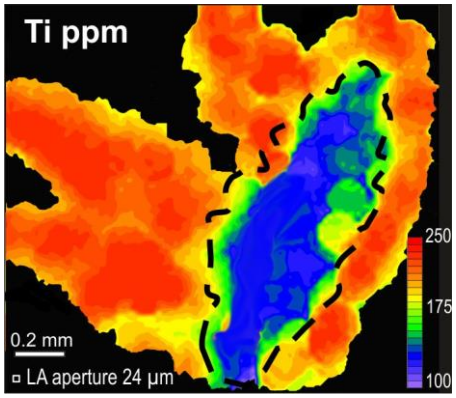

Figure 6.5. *Distribution of Ti (in ppm) in a composite olivine grain composed of rounded core mantled by tabular olivine crystals acquired by LA-ICP-MS mapping with a square-shaped aperture of 24 µm and an aperture overlap of 1 µm. The black dashed line indicates the border of rounded olivine core (see Fig. 6.2c for the optical image and Fig. 6.6c for crystal orientation of the composite grain). The scale bar of concentration is given in ppm.*

composition of rounded and tabular olivine grains in the varied-texture compared to those in well-developed granofels and spinifex Chl-harzburgite (Fig. 6.3), respectively (e.g., Bretscher et al., 2018; Marchesi et al., 2013; Padrón-Navarta et al., 2010a; Padrón-Navarta et al., 2011). The slightly lower X_{Mg} of some tabular olivine grains in the transitional Chl-harzburgite compared to those reported earlier from the Almirez spinifex Chl-harzburgite can be explained by the presence of microscopic and submicroscopic chromite and ilmenite inclusions, responsible for brown olivine pleochroism (cf. Ruiz Cruz et al., 1999; Trommsdorff et al., 1998). In the spinifex Chl-harzburgite, these Fe-Ti oxides are produced in part by titanian clinohumite breakdown to olivine, ilmenite and magnetite in the tabular olivines (López Sánchez-Vizcaíno et al., 2005). The almost constant X_{Mg} values in the composite grains are likely the consequence of the identical partitioning of Mg between olivine and orthopyroxene (K_D value for X_{Mg} close to 1, cf. Fig. 7 in Trommsdorff et al., 1998, and Fig. 7 in Padrón-Navarta et al., 2010a).

The granofels and spinifex Chl-harzburgite textural types in the Almirez ultramafic massif generally show similar trace element compositions (Marchesi et al., 2013), which are also recorded in the rounded and the tabular olivine crystals of the transitional Chl-harzburgite presented here (Fig. 6.4a). The remarkably similar trace element patterns in the rounded and the tabular olivines of the transitional Chl-harzburgite indicate that the geochemical nature of fluids in contact with them was essentially the same (Fig. 6.4b). The significantly higher trace element concentrations and the preferential partitioning of HFSE in the tabular olivines (Fig. 6.4b) are consistent with the arrival of external fluids in the system at the time of the morphological transition from rounded to tabular olivine. The rounded olivines in the transitional Chl-harzburgite therefore record processes

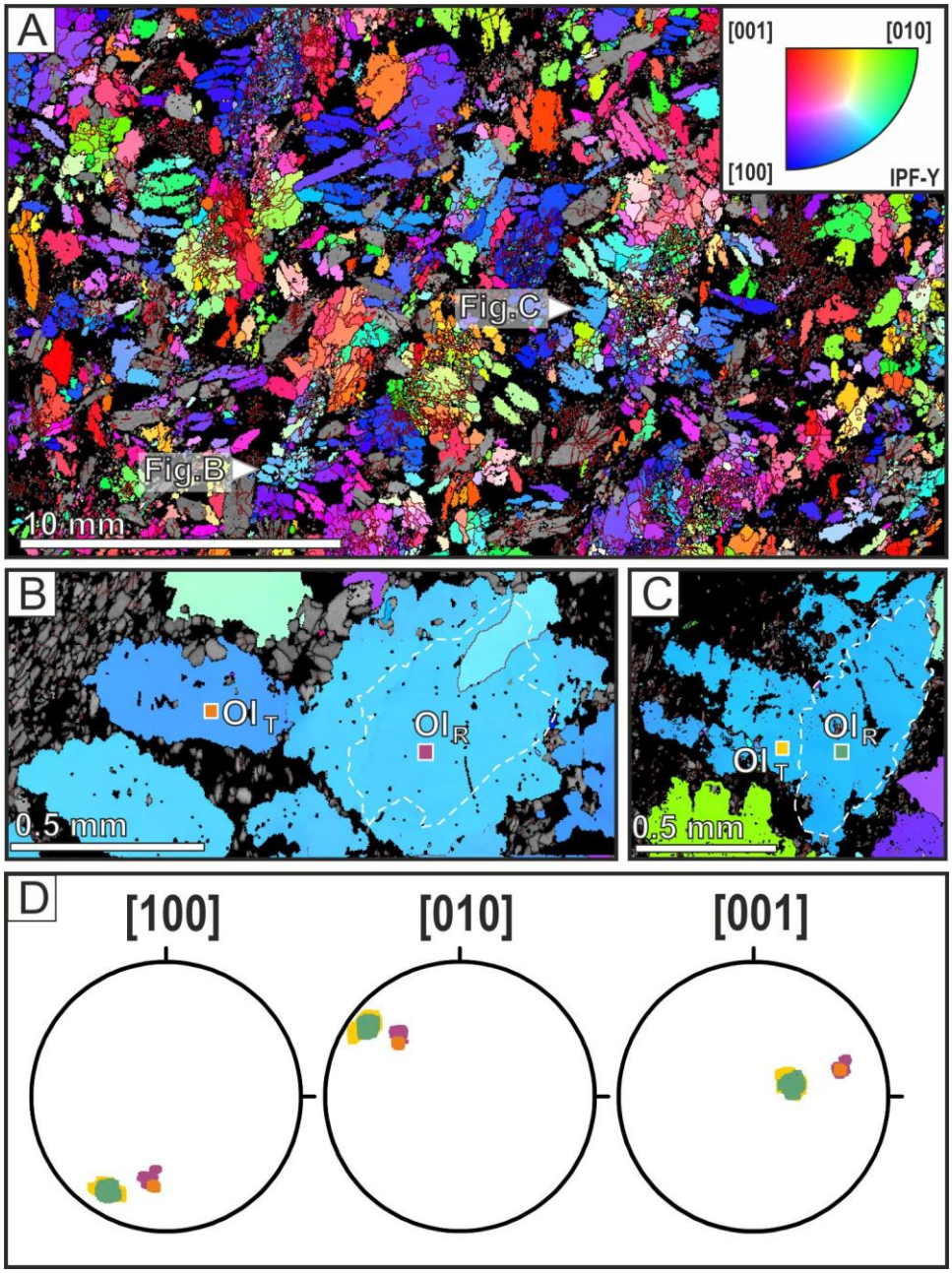

Figure 6.6. *(a-c) EBSD orientation map of olivines color-coded in the crystal reference frame (inverse pole figure, IPF). These are the complementary images of Fig. 6.2a-c. The inverse pole figure (IPF-Y) is shown in the upper right corner of (a), indicating that blue, green and red colored grains in the image have their [100], [010] or [001] crystallographic axis distributed parallel to the vertical in the image, respectively. Gray-shaded grains are different phases and have not been color-coded (e.g., Opx; compare to optical image in Fig. 6.2). (b-c) Close-up views on the representative composite olivine grains, with arrows pointing at the location of the grain assemblage in (a). White dashed line indicates the border of rounded olivine core (compare to Fig. 6.2b-c) and the square symbols are used for identification of the grains. (d) Orientation of [100], [010] and [001] of rounded and tabular olivine grains from (b) and (c) plotted in equal-area lower hemisphere stereographic projection in the sample reference frame.*

prevailing during the formation of granofels Chl-harzburgite, and the tabular olivines in this study correspond to those of spinifex Chl-harzburgite.

6.5.2 Cause of the morphological transition in olivine

6.5.2.1 The potential role of stress

In the granofels Chl-harzburgite, Padrón-Navarta et al. (2015) and Dilissen et al. (2018) have shown that the crystallographic orientation of rounded olivine is controlled by that of the precursor antigorite via topotactic relationship coupled to compaction. In the spinifex Chl-harzburgite, Dilissen et al. (2018) (cf. Ch. 5) demonstrated that crystallographic orientation of tabular olivines is not random but neither directly linked to the precursor antigorite; instead, the growth planes of tabular olivine populations are aligned with respect to the prevailing stress orientation. In the transitional Chl-harzburgite, the tabular olivines are smaller in size than those in the spinifex Chl-harzburgite, but they have the same morphology (i.e., olivine tabular on (100) and elongated along [001]; cf. Figs. 3.12, 3.13 and 5.8; Ch. 3 and 5; Kahl et al., 2017; Dilissen et al., 2018). However, if deviatoric stresses were responsible for the switch in the olivine morphology from rounded to tabular, the rather random growth direction of tabular olivines on rounded seeds in the transitional Chl-harzburgite (Figs. 6.2, 6.6 and 6.7) would indicate a near-hydrostatic condition. Such systematic heterogeneity of the stress state (i.e. hydrostatic vs. deviatoric) across contacts < 0.5 m thick between transitional Chl-harzburgite and well-developed spinifex Chl-harzburgite is highly unlikely to exist and/or result in identical crystal morphologies. In fact, the crystallographic orientation of the tabular morphology in transitional Chl-harzburgite is essentially controlled by epitaxial growth on rounded olivine seeds (Fig. 6.6b-c), excluding the possibility that deviatoric stresses had an important role in the morphological transition. These results suggest that deviatoric stresses may have controlled the direction of growth and the orientation of growth planes once tabular olivines are well-developed (i.e., in the spinifex Chl-harzburgite; Dilissen et al., 2018) but they cannot be responsible for triggering the observed morphological transition of olivine in the transitional Chl-harzburgite.

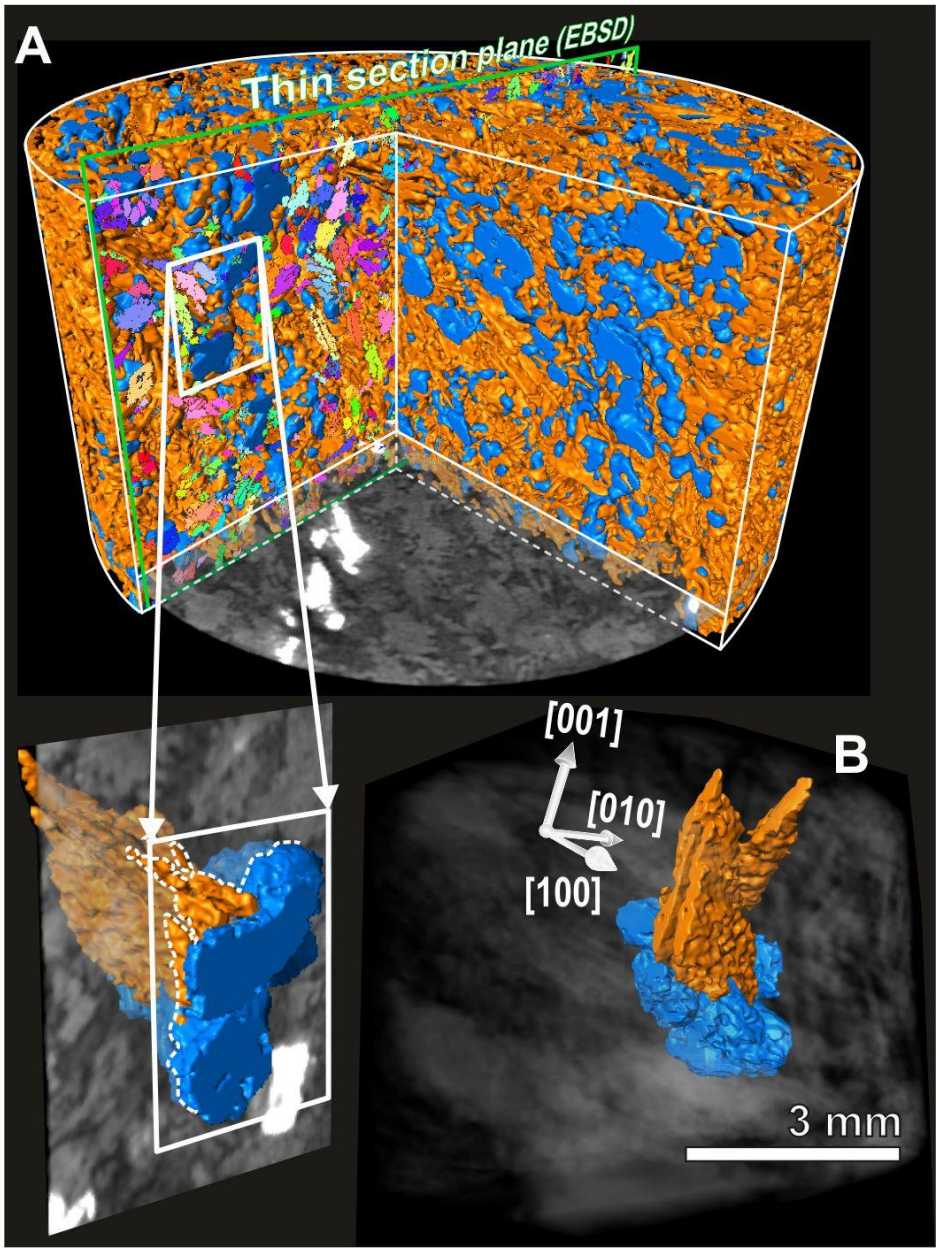

Figure 6.7. *(a) Crystal shape of rounded (rendered blue) and tabular (rendered orange) olivine grains in the µ-CT volume of the cylindrical, drill-pressed transitional Chl-harzburgite core (outlined white) with the crystallographic orientation of olivines shown in a vertical thin section plane (outlined green; EBSD data). Inset shows a composite grain in the µ-CT volume exposed in the vertical thin section (dashed line indicates the intersection of the assemblage with the thin section plane) with crystallographic axes annotated in (b). Except for a horizontal µ-CT slice and the grayscale background of the inset, only olivines are shown. For the sake of better visibility, EBSD data is thresholded for a minimum grain size of 3 mm (smaller grains and other phases are transparent); color-coding is the same as in Fig. 6.6a with vertical direction defined parallel to the axis of the cylindrical rock core. (b) 3-D view of the intergrowth of rounded and tabular olivines in a composite grain with the orientation of [100], [010] and [001] crystallographic axes. The composite grain is the same as shown in the inset of (a) but the assemblage has been rotated to have the best view on the tabular olivines. For more details on correlative µ-CT and EBSD analysis, see Methodology or Kahl et al. (2017).*

6.5.2.2 Is morphological transition driven by polysomes and the intergrowth of oxide bands?

The brown color of tabular olivine (Fig. 6.2) in spinifex Chl-harzburgite in the Almirez massif is due to the presence of submicron-sized magnetite and ferrian chromite micro-inclusions that form interconnected bands parallel to $[100]_{Ol}$ (Ruiz Cruz et al., 1999). In addition to oxide inclusions, tabular olivines also contain polysomatic titanian clinohumite (Ti-Chu) lamellae in the $(001)_{Ol}$ (López Sánchez-Vizcaíno et al., 2005, 2009).

If intergrowth of oxide bands and/or polysomatic Ti-Chu lamellae triggered the morphological switch from rounded to tabular morphologies, the expected olivine crystal habit would rather be tabular on $(001)_{Ol}$ and elongated along $[100]_{Ol}$ or $[010]_{Ol}$ directions. Such olivine morphology has not been described in the literature and it is not consistent with the observations showing Almirez olivine tabular on $(100)_{Ol}$ and elongated along $[001]_{Ol}$ (Fig. 6.7). We therefore suggest that the presence of oxide inclusions and polysomatic Ti-Chu lamellae has no impact on the morphology of tabular olivines.

6.5.2.3 Reaction affinity

The mechanisms and relative rates of nucleation and growth determine the number, size and shape of crystals during metamorphic crystallization. These rates are controlled by the affinity of the reaction (Donaldson, 1976; Ridley and Thompson, 1986). The varied-texture of olivine in the transitional Chl-harzburgite indicates that rounded olivine growth proceeded to some extent during the antigorite dehydration reaction and was followed by a phase of growth of tabular olivine until the completion of the reaction (e.g., Fig. 6.2, 6.6).

In the $MgO\text{-}SiO_2\text{-}H_2O$ (MSH) system, the antigorite dehydration reaction is:

$$Mg_3Si_2O_5(OH)_4 \rightarrow MgSiO_3 + Mg_2SiO_4 + 2H_2O \qquad (6.1)$$

(Antigorite → Enstatite + Forsterite + water)

Based on the modal abundance of rounded and tabular olivines in a representative transitional Chl-harzburgite (AL14-06: 74.0 and 26.0 area%, respectively), we estimate that at the time of morphological transition of olivine, the reaction progress was at approximately 74%. At 74% completion of the reaction, the molar unit of the rock was

composed of 27.7 cm^3 (72.0 g) antigorite, 23.2 cm^3 (74.3 g) enstatite, 31.8 cm^3 (104.1 g) forsterite, and 24.2 cm^3 (26.7 g) water (using density values of 2.6 g/cm^3, 3.2 g/cm^3, 3.3 g/cm^3 and 1.1 g/cm^3 for antigorite, enstatite, forsterite and water, respectively). Tabular olivines formed from the remaining antigorite in a subsequent stage (e.g., Dilissen et al., 2018; Padrón-Navarta et al., 2010a,b, 2011) following Eq. (6.1), Given that at the completion of the dehydration reaction water has gone, the present-day area of the water-free reaction products in the thin section (olivine and orthopyroxene; 3.5 cm^2 based on EBSD mapping) must be recalculated to a water-bearing system by a correction factor of 1.4 (i.e., total volume of reaction products divided by that of enstatite and forsterite at 74% completion of the reaction) to approximate the original area of antigorite (i.e. 5.0 cm^2). Rounded olivine crystals nucleated at this original area, whereas tabular ones nucleated in a much smaller surface (1.3 cm^2), which corresponds to the area of remaining antigorite at 74% completion of the reaction. In the thin section, we manually counted 54 rounded and 293 tabular olivine crystals (Fig. 6.8), which indicate nucleation frequency of 11 and 224 crystals per cm^2, respectively. The number of crystals per area can be converted to number per volume by raising the number of crystals per cm^2 to the power of 1.5 (cf. Roselle et al., 1997 and references therein). This calculation shows that the nucleation rate of tabular olivines is approximately two orders of magnitude higher than that of rounded ones (ca. 3355 vs. 35 crystals per cm^3, respectively). As nucleation rate is exponentially proportional to reaction affinity (e.g., Ridley and Thompson, 1986), the approximately two orders of magnitude higher nucleation rate of tabular olivines with respect to the rounded ones in the transitional Chl-harzburgite strongly supports non-equilibrium crystallization of Almirez tabular olivines compared to the rounded ones.

Previous studies in the Almirez massif agree that the equant, polyhedral morphology of rounded olivine formed at near-equilibrium in granofels Chl-harzburgite (Padrón-Navarta et al., 2011), and tabular olivine shape in spinifex Chl-harzburgite records growth at high reaction rate (Evans and Cowan, 2012; Padrón-Navarta et al., 2011). The high reaction rates are either accounted for during crystallization after a melt similarly to spinifex olivine in komatiites (Evans and Cowan, 2012), or during metamorphic dehydration of Atg-serpentinite (Padrón-Navarta et al., 2011). In either case, large olivine crystals with tabular morphology could only form if the growth rate was fast enough relative to the nucleation rate (e.g., Roselle et al., 1997 and references therein).

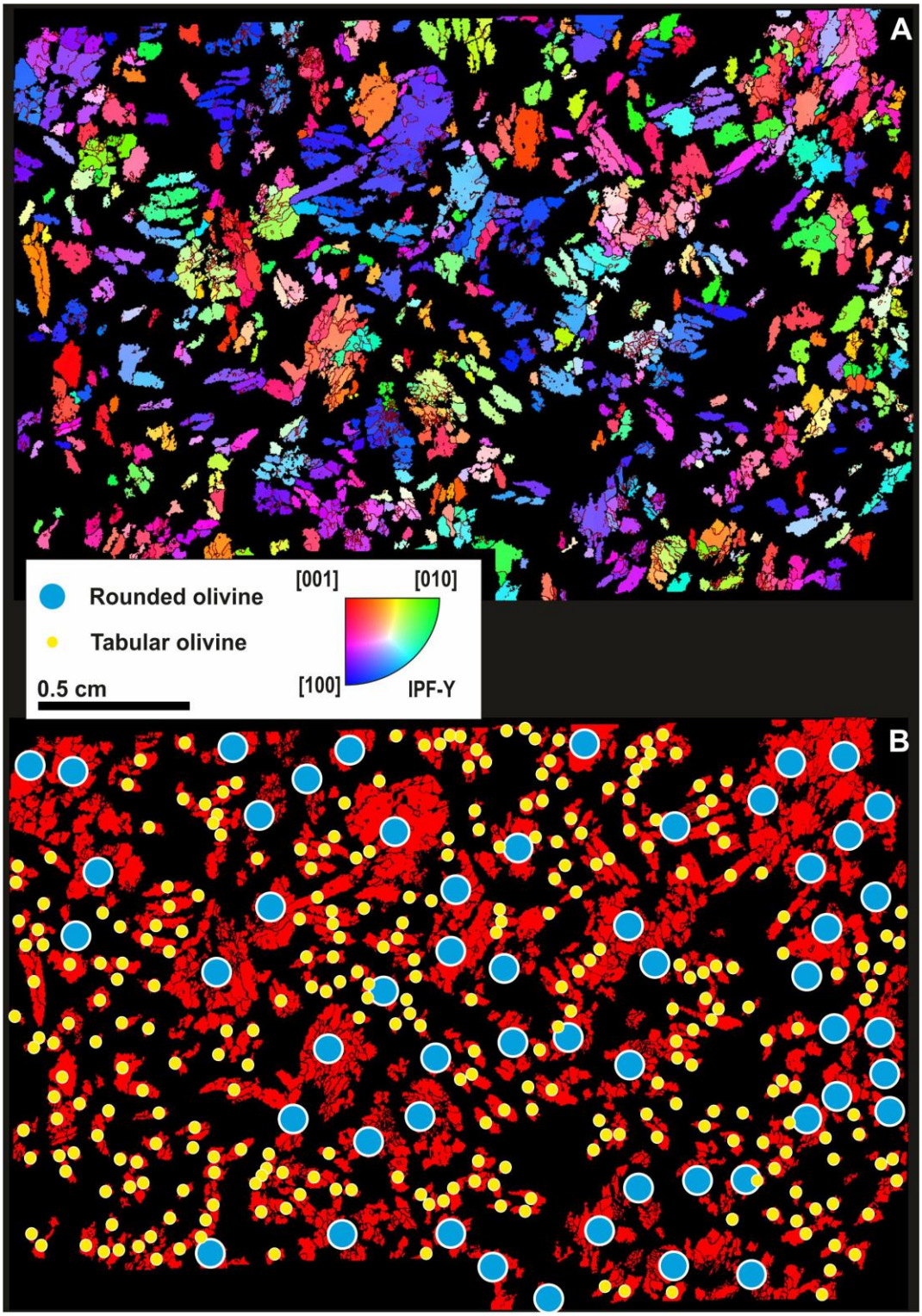

Figure 6.8. *Nucleation sites reconstructed in a thin section of Almirez transitional Chl-harzburgite based on petrographic and EBSD data analyses of sample AL14-06. (a) EBSD orientation map of olivines color-coded in the crystal reference frame (for the interpretation of color-coding, see Fig. 6.6a). Note that here the same grains are shown as in Fig. 6.6a, but for the clarity of the figure, we filtered olivines smaller than 3 mm equivalent diameter and other phases. (b) Nucleation sites of rounded (blue circle) and tabular (yellow circle) olivine varieties superposed on EBSD phase map. The same grains are shown as in (a).*

6.5.2.4 Diffusion versus interface-controlled growth of olivine

Tabular olivine crystals have been reported as the prime evolution towards rapid growth textures (Faure et al., 2003). However, at very high reaction affinities, growth is diffusion-controlled and morphologies are dominated by skeletal and dendritic crystals with hopper and swallowtail morphologies, respectively (Fig. 6.9; Donaldson, 1976; Faure et al., 2007; Shea and Hammer, 2013; Welsch et al., 2013). These crystal morphologies have not been reported from the Almirez massif in previous works, and our observations from optical microscopy (Fig. 6.2) and µ-CT 3-D images (Fig. 6.7) do not support the presence of non-faceted crystals either (i.e. there is lack of crystal cavities or holes in tabular olivine). We therefore suggest that despite the relatively high reaction affinity —indicated by the increased nucleation rate of tabular olivine (section 6.6.2.3)—

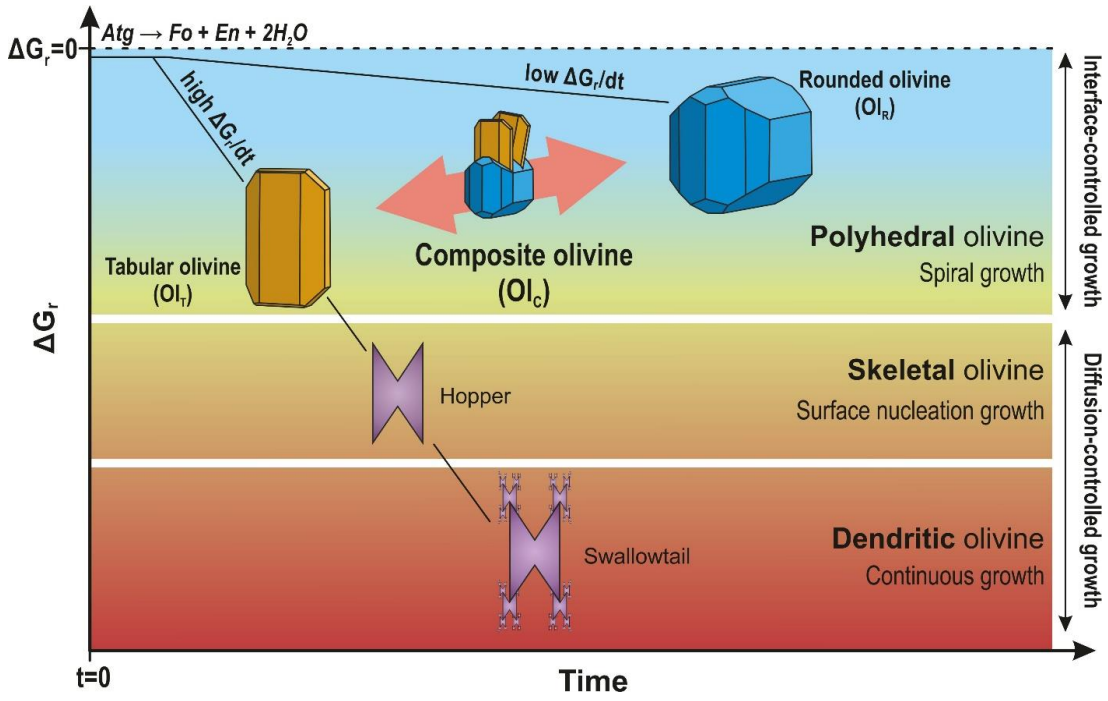

Figure 6.9. *Conceptual model for the evolution of olivine morphology as a function of Gibbs free energy of the dehydration reaction (ΔGr) and time (modified from Welsch et al., 2013 and references therein). The scales are arbitrary. The dehydration reaction is Antigorite (Atg) → Forsterite (Fo) + Enstatite (En) + 2H₂O in the MgO-SiO₂-H₂O (MSH) system. Reaction affinity increases downward the vertical axis of the diagram with increasing distance from the equilibrium condition (ΔGr=0, dashed horizontal line). Rates of change in reaction affinity are represented by gently and steeply dipping solid black lines that correspond to low ΔG/dt (i.e., slow near-equilibrium crystallization) and high ΔG/dt (i.e., rapid disequilibrium crystallization), respectively. The overstepping of the reaction is the distance between the crystallization paths and the equilibrium condition in vertical axis direction of the diagram (i.e., the small gap between the dashed and solid lines at t=0 and ΔGr<0). See text for further details.*

the growth of tabular olivine remained interface-controlled rather than diffusion-controlled (Fig. 6.9). These results show that, unlike the skeletal and dendritic growth of spinifex olivine in komatiites (e.g., Arndt et al., 2004; Dann, 2001; Donaldson, 1976; Faure et al., 2006; Shore and Fowler, 1999), reaction affinity alone cannot explain the tabular morphology of Almirez olivine.

High reaction affinity (i.e., $\Delta G_r << 0$, far from equilibrium conditions in Fig. 6.9) can exert a driving force for the dehydration reaction to proceed, resulting in increased metastability of antigorite. However, the polyhedral olivine morphologies rather suggest that rounded and tabular olivine in the transitional Chl-harzburgite record differences in the reaction kinetics, and hence the change of reaction affinity with time (i.e., low $\Delta G_r/dt$ vs. high $\Delta G_r/dt$ paths in Fig. 6.9) at similar or slightly different reaction affinities during interface-controlled crystallization. For such model to be efficient, physicochemical conditions must have been changed during crystallization because the Gibbs free energy (ΔG_r) of the system is a function of temperature (T), pressure (P) and composition (X). Therefore, these factors may have played an important role in shaping the morphology of growing crystals at enhanced growth rates during non-equilibrium crystallization (i.e., at increasing $\Delta G_r/dt$ rates in Fig. 6.9).

6.5.2.5 Morphological transition induced by temperature gradient?

Common dehydration reactions, including the Atg-dehydration reaction, are highly endothermic, and thus thermal perturbation during the development of reaction is unlikely. The increased nucleation rate of tabular olivines, nevertheless, might indicate that the morphological transition of olivine was due to changes in $\Delta G_r/dT$, eventually resulting in a steeper slope of $\Delta G_r/dt$ in Fig. 6.9.

Growth of spinifex olivine in komatiite is controlled by temperature gradients induced by conductive and radiative heat transfer, which enhance anisotropic growth along crystallographic directions with the highest thermal conductivity (Faure et al., 2006; Shore and Fowler, 1999). The highest thermal conductivity in olivine is along [100] (=a-axis; 5.9±0.1 $Wm^{-1}K^{-1}$), whereas the intermediate and slowest thermal diffusivities occur along [001] (=c-axis; 5.1±0.1 $Wm^{-1}K^{-1}$) and [010] (=b-axis; 3.4±0.06 $Wm^{-1}K^{-1}$), respectively (Shore and Fowler, 1999). As a consequence, komatiite spinifex olivines are elongated along [100] and tabular on (010) faces with a > c >> b (Fig. 6.10; Donaldson,

1976; Faure et al., 2003; Shore and Fowler, 1999). This crystal habit, however, is unlike the Almirez tabular olivines (c > b >> a; Fig. 6.10), which excludes that their morphology was controlled by conductive and radiative heat transfer gradients. Moreover, as the classical olivine crystal-structure analyses predict that enhanced growth rate results in tabular olivine morphologies with c ≈ a >> b (Donaldson, 1976; Wen et al., 2018), the Almirez tabular olivine morphology cannot be the result of enhanced growth rate along [100] direction.

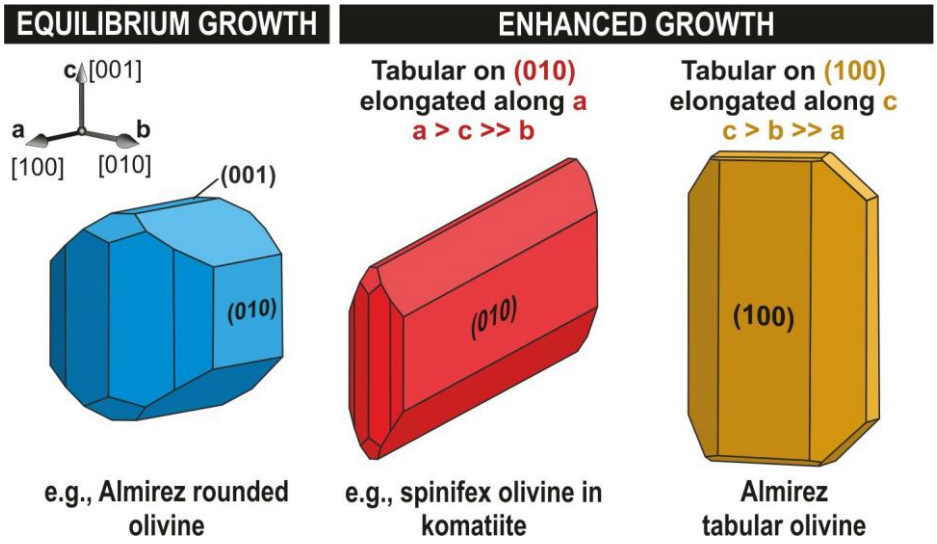

Figure 6.10. *Expected morphology of olivine in equilibrium crystallization (blue) and during enhanced growth resulting in tabular morphology based on literature data (red). The morphology of tabular Almirez olivine based on correlative EBSD and µ-CT (this study for transitional Chl-harzburgite and Dilissen et al., 2018 for spinifex Chl-harzburgite) is shown in orange color. See text for further details. Axes and crystal face orientations are the same for all represented crystals; crystallographic reference axes are shown in the top-left corner of the figure. Crystal shapes are modified from Deer et al. (1997).*

6.5.2.6 Morphological transition driven by a change in fluid chemistry

The strong dependence of nucleation rate on reaction affinity is classically ascribed to cooling but it can also be related to changing fluid composition due to infiltration (Ridley and Thompson, 1986). Migration of fluids in the dehydrating Almirez paleo-slab is supported by the presence of high-pressure hydrofractures in Chl-harzburgite, but these microcracks crosscut the already existing tabular olivines (Padrón-Navarta et al., 2010b). On the one hand, hydrofractures attest for the persistent build-up of fluid pressure even after the formation of spinifex Chl-harzburgite but, on the other hand, the sudden drop of

pressure associated with their formation cannot explain the morphological transition of olivine.

Thermodynamic modeling and geochemical data of spinifex Chl-harzburgite, dominated by tabular olivines, indicate a change in fluid composition with respect to the formation of granofels Chl-harzburgite, characterized by rounded olivines (Garrido et al., 2005; López Sánchez-Vizcaíno et al., 2005; Padrón-Navarta et al., 2011; Fig. 6.4). Compared to rounded olivine cores, tabular olivine in the Almirez transitional Chl-harzburgite has a distinctly higher Ti (up to 250-360 ppm) and other HFSE (e.g. U, Zr, Hf) content (Fig. 6.4b, 6.5; Table 6.1) in accordance with previous observations (e.g. Garrido et al., 2005; López Sánchez-Vizcaíno et al., 2005). The increasing Ti content of tabular olivine has been ascribed to the stability of titanian clinohumite during Atg-serpentinite dehydration that was open to external fluids (Garrido et al., 2005; López Sánchez-Vizcaíno et al., 2005; Marchesi et al., 2013). Such external supercritical aqueous fluids likely contained dissolved Na-Al silicates as it has been also documented in amphibole veins in meta-rodingites from the Almirez ultramafic massif (Laborda-López et al., 2018). Fluids with dissolved Na-Al silicates promote Ti solubility and fluid polymerization, which can function as important material-transport agents in subduction zones (Manning, 2004a, b). In the deep crust and mantle, polymer complexes predominate relative to monomeric species and control the chemical interaction of fluids with crustal and mantle rocks (Manning, 2004b). The correlation between olivine morphology and composition suggests that the morphological transition was triggered by these external, Ti-bearing, polymerized aqueous fluids.

Crystallization experiments show that addition of dissolved components to a solution causes morphological transition in growing crystals due to the formation of surface-active molecules (i.e., surfactants) that inhibit growth on specific crystal-solution interfaces (e.g., Bakshi, 2016; Kumari et al., 2009; Qazi et al., 2017; Townsend et al., 2015). Surfactants control the crystal nucleation and growth through different surface adsorption on certain crystal planes (Bakshi, 2016; Canselier, 1993). The presence of polymers in the fluid increases significantly the habit modification effect of surfactants (Kumari et al., 2009; Townsend et al., 2015). In Almirez, the arrival of Ti-bearing, polymerized aqueous fluids may have formed surfactant-like polymers that inhibited growth on certain olivine

interfaces and switched olivine habit from rounded to tabular during Atg-serpentinite dehydration.

As surfactant adsorption is governed both by the nature of the surfactant and the surface, water adsorption mechanisms at olivine-fluid interfaces can readily account for the morphological transition. The shortest [100]-axes of the Almirez tabular olivines correspond to growth on (100) interfaces where ordered water monolayers are strongly bonded by dissociative adsorption, the intermediate [010]-axes match (010) interfaces where only weak molecular (associative) adsorption occurs, and the growth of the longest [001]-axes is not inhibited due to unfavorable water molecule interactions (i.e., steric hindrance) at the (001) interface (King et al., 2010; Muralidharan et al., 2008; Prigiobbe et al., 2013; Stimpfl et al., 2006). The Ti-bearing polymeric silicate complexes in the infiltrating external aqueous fluids therefore likely acted as surfactants during fluid-solid interaction, and resulted in Almirez olivine morphologies that are tabular on (100) and elongated along [001] (Figs. 6.6 and 6.7b) by selectively inhibiting growth on (100) and, to a lesser extent on (010) olivine interfaces. Considering that tabular olivines in transitional Chl-harzburgite record identical physicochemical conditions to those prevailing during the formation of spinifex Chl-harzburgite, open-system fluid circulation resulted in not only trace element transport, but was also responsible for the development of tabular olivine morphologies during the high-pressure metamorphic dehydration reaction of Atg-serpentinite in the Almirez ultramafic massif.

6.6 Appendices

6.A EPMA analyses

EPMA analysis of major elements (in wt%) and calculated cation numbers (in atoms per formula unit) in olivines from Almirez transitional Chl-harzburgite. FeO* and Fe*: all iron reported as Fe2+; XMg=Mg/(Mg+Fe) expressed in cation numbers per formula units; nd: not detected; Fo: forsterite; Fa: Fayalite.

Morphology	Rounded											
Sample	AL14-06						AL14-07					
Label	C1-Ol1	C1-Ol2	C2-Ol1	C2-Ol2	C3-Ol1	C3-Ol2	C1-Ol1	C1-Ol2	C2-Ol1	C2-Ol2	C3-Ol1	C3-Ol2
Site	core	rim	core	rim	core	rim	core	rim	core	rim	core	rim
SiO_2 (±0.1)	40,4	40,4	40,3	40,0	40,4	40,4	40,1	40,3	40,2	40,2	40,3	40,2
TiO_2 (±0.01)	nd	0,01	nd	0,02	nd	nd	nd	0,01	nd	0,01	nd	0,01
Cr_2O_3 (±0.01)	nd	0,01	nd	0,14	nd	nd	nd	nd	nd	nd	nd	0,01
FeO* (±0.15)	9,99	9,68	10,0	10,3	10,1	10,0	10,1	10,2	10,1	10,0	10,3	9,82
MnO (±0.02)	0,13	0,11	0,14	0,17	0,14	0,12	0,10	0,15	0,16	0,13	0,17	0,11
NiO (±0.03)	0,38	0,42	0,44	0,37	0,34	0,39	0,42	0,38	0,26	0,37	0,25	0,42
MgO (±0.2)	49,4	49,5	49,1	49,0	49,4	49,4	49,0	48,9	49,0	49,0	49,0	49,2
CaO (±0.01)	0,01	nd	nd	nd	nd	nd	nd	nd	nd	nd	0,01	nd
Na_2O (±0.01)	nd	nd	nd	nd	0,01	nd	nd	nd	nd	nd	0,01	0,01
Total	100,3	100,2	100,1	100,1	100,4	100,4	99,8	99,9	99,7	99,8	100,0	99,9
X_{Mg}	0,898	0,901	0,897	0,895	0,897	0,898	0,896	0,895	0,897	0,897	0,895	0,899
Si	0,9901	0,9904	0,9904	0,9863	0,9893	0,9897	0,9899	0,9929	0,9911	0,9907	0,9914	0,9906
Fe*	0,2048	0,1986	0,2061	0,2116	0,2071	0,2060	0,2086	0,2094	0,2077	0,2070	0,2117	0,2021
Cr		0,0001		0,0027				0,0000		0,0000		0,0001
Ti		0,0001		0,0004				0,0002		0,0002		0,0001
Mn	0,0026	0,0022	0,0029	0,0036	0,0028	0,0025	0,0020	0,0030	0,0034	0,0028	0,0035	0,0022
Mg	1,8048	1,8098	1,8014	1,7999	1,8047	1,8044	1,8011	1,7938	1,8015	1,8011	1,7967	1,8056
Ca	0,0001										0,0002	
Na					0,0003						0,0003	0,0003
Ni	0,0074	0,0082	0,0087	0,0074	0,0067	0,0076	0,0083	0,0075	0,0052	0,0072	0,0050	0,0083
Total	3,01	3,01	3,01	3,01	3,01	3,01	3,01	3,01	3,01	3,01	3,01	3,01
Fo	0,898	0,901	0,897	0,895	0,897	0,898	0,896	0,895	0,897	0,897	0,895	0,899
Fa	0,102	0,099	0,103	0,105	0,103	0,102	0,104	0,105	0,103	0,103	0,105	0,101

Morphology	Tabular										
Sample	AL14-06					AL14-07					
Label	C1-Ol4	C2-Ol3	C2-Ol4	C3-Ol3	C3-Ol4	C1-Ol3	C1-Ol4	C2-Ol3	C2-Ol4	C3-Ol3	C3-Ol4
Site	core	rim	rim	rim	core	core	rim	rim	rim	rim	rim
SiO_2 (±0.1)	40,0	40,1	40,0	39,6	40,2	40,5	40,3	40,4	40,0	40,4	40,1
TiO_2 (±0.01)	0,09	0,06	0,03	0,07	0,03	0,02	nd	nd	0,14	0,01	0,06
Cr_2O_3 (±0.01)	0,26	0,29	0,08	0,40	0,19	0,23	0,01	0,01	0,14	0,04	0,14
FeO* (±0.15)	10,4	10,2	10,2	10,7	10,2	10,3	9,88	10,0	10,1	10,0	10,3
MnO (±0.02)	0,13	0,14	0,12	0,15	0,14	0,11	0,12	0,11	0,13	0,11	0,11
NiO (±0.03)	0,41	0,41	0,43	0,40	0,44	0,40	0,39	0,39	0,41	0,41	0,43
MgO (±0.2)	49,2	49,0	49,3	48,5	49,0	48,6	49,2	49,1	49,0	49,1	49,1
CaO (±0.01)	0,01	nd	0,02	nd	nd	nd	nd	nd	nd	nd	0,01
Na_2O (±0.01)	nd	0,01	0,01	0,01	nd	nd	0,01	nd	nd	0,01	0,01
Total	100,6	100,2	100,2	99,9	100,3	100,2	100,0	100,1	100,0	100,2	100,4
X_{Mg}	0,894	0,896	0,896	0,890	0,896	0,893	0,899	0,897	0,896	0,897	0,895
Si	0,9826	0,9861	0,9843	0,9813	0,9878	0,9948	0,9907	0,9928	0,9866	0,9919	0,9860
Fe*	0,2140	0,2090	0,2098	0,2208	0,2092	0,2123	0,2033	0,2058	0,2081	0,2058	0,2113
Cr	0,0051	0,0056	0,0015	0,0078	0,0038	0,0046	0,0001	0,0002	0,0027	0,0008	0,0028
Ti	0,0017	0,0012	0,0006	0,0014	0,0006	0,0004			0,0026	0,0002	0,0012
Mn	0,0028	0,0029	0,0026	0,0032	0,0028	0,0023	0,0025	0,0024	0,0027	0,0023	0,0024
Mg	1,7985	1,7970	1,8064	1,7907	1,7968	1,7804	1,8047	1,7982	1,7986	1,7982	1,7991
Ca	0,0001		0,0004								0,0002
Na		0,0003	0,0005	0,0002			0,0005			0,0005	0,0003
Ni	0,0082	0,0080	0,0086	0,0080	0,0086	0,0079	0,0077	0,0078	0,0082	0,0080	0,0085
Total	3,01	3,01	3,01	3,01	3,01	3,00	3,01	3,01	3,01	3,01	3,01
Fo	0,894	0,896	0,896	0,890	0,896	0,893	0,899	0,897	0,896	0,897	0,895
Fa	0,106	0,104	0,104	0,110	0,104	0,107	0,101	0,103	0,104	0,103	0,105

6.B LA-ICP-MS analysis of trace elements

LA-ICP-MS analysis of trace elements (in ppm) in olivines from Almirez transitional Chl-harzburgite sample AL14-06.

Morphology	*Rounded*						
Grain	Ol1	Ol2	Ol3		Ol4		Ol5
Spot	OL1-3	OL2-3	OL3-2	OL3-3	OL4-1	OL4-2	OL5-3
Cs(ppm)	*bdl*	0,0094	0,009	*bdl*	*bdl*	*bdl*	*bdl*
Rb	0,0087	0,049	0,0193	0,016	0,037	0,034	*bdl*
Ba	0,3	0,94	0,2	0,328	0,6	0,53	0,064
Th	0,006	0,0086	0,0033	0,0161	0,0031	0,0058	0,00871
U	0,0101	0,016	0,009	0,032	0,0078	0,0091	0,0089
Nb	0,182	0,218	0,202	0,22	0,372	0,18	0,3229
Ta	0,0063	0,0086	0,0058	0,0082	0,0103	0,0047	0,0144
La	0,0091	0,0205	0,021	0,0183	0,0112	0,0112	0,0049
Ce	0,023	0,0357	0,043	0,047	0,024	0,0262	0,0149
Pb	0,026	0,124	0,09	0,026	0,048	0,079	0,0087
Pr	0,003	0,0033	0,0051	0,0039	0,00224	0,00221	0,00122
Sr	0,42	3	0,96	0,91	2,8	1,6	0,16
Nd	0,013	0,0106	0,019	0,022	0,0061	0,0126	*bdl*
Zr	0,045	0,095	0,0401	0,026	0,045	0,0247	0,056
Hf	0,0046	0,005	0,0014	0,0017	0,0025	*bdl*	0,007
Sm	0,0027	0,0035	0,0037	0,01	*bdl*	*bdl*	0,0063
Eu	0,0013	0,0027	0,003	0,0012	0,00103	0,00126	0,002
Gd	0,0044	0,003	0,0051	0,0119	0,0053	0,0044	0,0025
Ti	28,5	47	26,5	47	47	33,3	64
Tb	0,00066	0,00132	0,0018	0,0017	0,00068	0,00116	0,0013
Dy	0,0079	0,0176	0,017	0,03	0,0086	0,0129	0,01
Y	0,076	0,148	0,16	0,257	0,069	0,09	0,082
Ho	0,00316	0,007	0,0063	0,0065	0,00258	0,0037	0,0041
Er	0,013	0,027	0,02	0,0387	0,0171	0,0172	0,0199
Tm	0,0044	0,0054	0,0036	0,0076	0,0035	0,00468	0,0046
Yb	0,046	0,068	0,054	0,072	0,052	0,055	0,047
Lu	0,0141	0,0188	0,0126	0,0157	0,0161	0,0147	0,0165

bdl = below detection limit

Morphology	*Tabular*				
Grain	Ol2	Ol4		Ol5	
Spot	OL2-1	OL4-3	OL4-4	OL5-5	OL5-6
Cs(ppm)	*bdl*	0,017	0,0107	0,013	0,029
Rb	0,0255	0,07	0,026	0,077	0,23
Ba	0,694	2	1,41	1,7	3,8
Th	0,0258	0,051	0,042	0,0865	0,0826
U	0,238	0,178	0,151	0,19	0,215
Nb	1,36	1,17	1,43	0,946	1,17
Ta	0,02024	0,0422	0,0368	0,044	0,041
La	0,042	0,105	0,048	0,0851	0,0813
Ce	0,079	0,217	0,101	0,181	0,181
Pb	0,034	0,33	0,163	0,35	0,45
Pr	0,0082	0,02455	0,0129	0,0164	0,02
Sr	0,82	2,8	2	1,7	13,3
Nd	0,0401	0,101	0,0472	0,086	0,087
Zr	1,1	0,565	0,722	0,577	0,637
Hf	0,0742	0,051	0,077	0,044	0,0592
Sm	0,0153	0,0429	0,0188	0,0195	0,042
Eu	0,00102	0,0058	0,0035	0,0029	0,0062
Gd	0,0236	0,049	0,023	0,049	0,048
Ti	398	298,2	578	260	266
Tb	0,0078	0,01067	0,0073	0,0084	0,0124
Dy	0,1	0,121	0,094	0,1077	0,114
Y	0,9	0,936	0,831	0,863	0,95
Ho	0,0377	0,039	0,0362	0,0395	0,043
Er	0,1966	0,193	0,185	0,1828	0,182
Tm	0,0422	0,0447	0,0431	0,0374	0,0446
Yb	0,348	0,356	0,392	0,344	0,356
Lu	0,076	0,077	0,089	0,066	0,0699

bdl = below detection limit

Part III

CONCLUSIONS

7 Conclusions

The present thesis has provided new insights into the dynamics and mechanisms of high-pressure Atg-serpentinite dehydration at sub-arc depth in subduction zones as recorded in the Almirez ultramafic massif. Combined field, textural, petrological and geochemical studies at different length scales in the Almirez rocks have shed new light on: (i) the mechanism and episodic nature of fluid release during high-P Atg-serpentinite dehydration; (ii) the dynamics of Atg-serpentinite dehydration and its relation to the orientation of stresses and the kinematics of subducting slabs; and (iii) the physicochemical factors that govern the texture and morphology of olivine during metamorphic crystallization of prograde Chl-harzburgite after Atg-serpentinite.

The detailed textural mapping of the Chl-harzburgite section in the Almirez massif reveals a sequence of lenses of Chl-harzburgite with granofels and spinifex textures that crystallized at different extent of overstepping of the Atg-serpentinite dehydration reaction (Ch. 4). The Chl-harzburgite lenses have a similar mean average thickness, volume, and calculated time-integrated water volume, suggesting that their crystallization was controlled by episodic fluid release triggered by an instability with a length scale of ~ 15 – 35 m. This range of length scales agrees well with length scale expected for the development of porosity wave instabilities by viscous compaction (i.e., the compaction length) for typical values of the permeability and viscosity of Atg-serpentinite. We estimate that the minimum timescale of compaction-driven fluid expulsion from 15 – 35 m thick Atg-serpentinite lenses was 10 – 23 yrs. This estimate can increase up to three orders of magnitude depending on fluid production rates. Stress-transfer instabilities that likely formed spinifex textures occurred in the order of 12–70 or 0.5–4 days considering linear and non-linear kinetics, respectively. Time-integrated fluid fluxes associated with the development of these episodic events and formation of Chl-harzburgite ranged between 1 – 4 $m^3\ m^{-2}$ for unfocused flow through half-surface of lenses, or $10^1\ m^3\ m^{-2}$ and $3{\cdot}10^3\ m^3\ m^{-2}$ for focused flow in narrower cracks. If formation of granofels and spinifex Chl-harzburgite records fluxes associated with fluid draining by porosity waves and cracks, respectively, the alternating lenses mapped in Almirez correspond to cyclic events of low and high fluxes varying up to three orders of magnitude. This unique natural

record of the Almirez thus provides the first evidence supporting the episodic nature of fluid release during high-P serpentinite dehydration.

The correlative study of μ-CT and EBSD oriented samples across the Atg-serpentinite dehydration isograd of the Almirez massif has provided a detailed account of the textural evolution during high-P Atg-serpentinite dehydration to peridotite (Ch. 5). This comprehensive study offers new insights into the mechanisms of dehydration and their relation with the stress orientation at the intermediate-depth of subducting slabs. The texture of Atg-serpentinite records the long-term shear deformation with the main compressive stress (σ_1) at an angle of c. 30°±15° to the foliation within the plane of the oxide stretching lineation. The foliation and stretching lineation were, respectively, broadly parallel to the slab interface and the slab-entrained flow direction. Crystallization of granofels and spinifex Chl-harzburgite records, respectively, a sequence of slow and fast fluid draining events during serpentinite dehydration under the same orientation of the principal stresses that resulted in the Atg-serpentinite shear deformation. During slow fluid draining events, granofels Chl-harzburgite crystallized after Atg-serpentinite by a topotactic dehydration reaction coupled to compaction. During fast draining events, dehydration of serpentinite resulted in spinifex Chl-harzburgite with tabular olivine SPOs and CPOs that show a remarkable correlation with the orientation of paleostresses. The dominant orientation group lies on the maximum compression plane (σ_2–σ_3) and can be accounted for by the oriented growth of platy crystals perpendicular to σ_1. The ultimate cause for the oriented crystallization of tabular olivine in other planes is uncertain. The ESE–WNW oxide aggregate lineation of spinifex and granofels Chl-harzburgites and the $[001]_{Ol}$ platelet lineation of the spinifex tabular olivines subparallel to σ_2 could mark the along strike paleoflow direction of fluids below the Atg-out dehydration front. The coupling among markers of slab kinematics, the stress field, and fluid flow in the Almirez paleo-subduction terrane suggests these factors exert a dynamic control during Atg-serpentinite dehydration in subduction zones.

The physicochemical factors that govern the texture and morphology of olivine during metamorphic crystallization of prograde Chl-harzburgite from Atg-serpentinite have been investigated in a sample of transitional Chl-harzburgite recording the morphological transition from rounded to tabular olivine (Ch. 6). In transitional Chl-harzburgite, composite olivine porphyroblasts occur that are composed of large equant and colorless

cores mantled by brown crystals. Composite porphyroblasts provide a snapshot of a morphological transition induced by the shift of physicochemical conditions during Atg-serpentinite dehydration. Quantitative textural calculations attest for approximately two-orders of magnitude greater time-integrated nucleation rate for the formation of tabular olivines compared to rounded ones, suggesting a sudden shift to an increasing reaction affinity during interface-controlled crystallization. Correlative X-ray μ-CT and EBSD shows that the morphology of brown olivine is tabular on (100) with $c > b >> a$. Because olivine growth is slower growth along [010] relative to the [001] and [100] directions, this morphology is inconsistent with the theoretical equilibrium morphology of Mg-rich olivine that has a tabular habit on (010) with $a > c >> b$ or $a \approx c >> b$. The tabular olivine shape on (100) in Almirez Chl-harzburgite is consistent with inhibited growth of olivine on (100) and, to a lesser amount, on (010). First-principle modeling in polymerized fluids predicts inhibited growth of olivine on (100) due to the formation of surfactants along these fluid-olivine interfaces during growth. Changes in the physicochemical nature of fluids might have triggered then the morphological transition from rounded to tabular olivine. The arrival of external, Ti-bearing, highly polymerized aqueous fluids during Atg-serpentinite dehydration could account for the morphological transition from rounded to tabular growth of olivine at an increasing affinity of the Atg-serpentinite dehydration reaction. If so, these results show that, in addition to the reaction affinity, polymerized fluids may play a fundamental role in shaping the morphology of crystals during metamorphic crystallization.

Part IV

REFERENCES

References

Abers, G.A., van Keken, P.E., Kneller, E.A., Ferris, A., Stachnik, J.C., 2006. The thermal structure of subduction zones constrained by seismic imaging: Implications for slab dehydration and wedge flow. *Earth and Planetary Science Letters* 241, 387–397.

Abramson, E.H., 2007. Viscosity of water measured to pressures of 6 GPa and temperatures of 300 °C. *Physical Review E* 76, 051203.

Abramson, E.H., Brown, J.M., 2004. Equation of state of water based on speeds of sound measured in the diamond-anvil cell. *Geochimica et Cosmochimica Acta*, 68, 1827–1835.

Ague, J.J., 2007. Models of permeability contrasts in subduction zone mélange: Implications for gradients in fluid fluxes, Syros and Tinos Islands, Greece. *Chemical Geology* 239, 217–227.

Ague, J.J., Park, J., Rye, D.M., 1998. Regional metamorphic dehydration and seismic hazard. *Geophysical Research Letters* 25, 4221–4224.

Alt, J.C., Garrido, C.J., Shanks, W.C., Turchyn, A., Padrón-Navarta, J.A., López Sánchez-Vizcaíno, V., Gómez-Pugnaire, M.T., Marchesi, C., 2012. Recycling of water, carbon, and sulfur during subduction of serpentinites: A stable isotope study of Cerro del Almirez, Spain. *Earth and Planetary Science Letters* 327, 50–60.

Alt, J.C., Schwarzenbach, E.M., Frueh-Green, G.L., Shanks, W.C., Bernasconi, S.M., Garrido, C.J., Crispini, L., Gaggero, L., Padron-Navarta, J.A., Marchesi, C., 2013. The role of serpentinites in cycling of carbon and sulfur: Seafloor serpentinization and subduction metamorphism. *Lithos* 178, 40–54.

Amiguet, E., Van De Moortèle, B., Cordier, P., Hilairet, N., Reynard, B., 2014. Deformation mechanisms and rheology of serpentines in experiments and in nature. *Journal of Geophysical Research– Solid Earth* 119, 4640–4655.

Appoloni, C.R., Macedo, Á., Fernandes, C.P., Philippi, P.C., 2002. Characterization of porous microstructure by X-ray microtomography. *X-Ray Spectrometry* 31, 124–127.

Arndt, N.T., Lesher, C.M., Houlé, M.G., Lewin, E., Lacaze, Y., 2004. Intrusion and crystallization of a spinifex-textured komatiite sill in Dundonald Township, Ontario. *Journal of Petrology* 45, 2555–2571.

Augier, R., Agard, P., MoniÉ, P., Jolivet, L., Robin, C., Booth-Rea, G., 2005. Exhumation, doming and slab retreat in the Betic Cordillera (SE Spain): in situ $^{40}Ar/^{39}Ar$ ages and P–T–d–t paths for the Nevado-Filabride complex. Journal of Metamorphic *Geology* 23, 357–381.

Auzende, A.L., Escartin, J., Walte, N.P., Guillot, S., Hirth, G., Frost, D.J., 2015. Deformation mechanisms of antigorite serpentinite at subduction zone conditions determined from experimentally and naturally deformed rocks. *Earth and Planetary Science Letters* 411, 229–240.

Bach, W., Garrido, C.J., Paulick, H., Harvey, J., Rosner, M., 2004. Seawater-peridotite interactions: First insights from ODP Leg 209, MAR 15°N. *Geochemistry, Geophysics, Geosystems* 5, 9. doi:10.1029/2004GC000744

Bach, W., Paulick, H., Garrido, C.J., Ildefonse, B., Meurer, W.P., Humphris, S.E., 2006. Unraveling the sequence of serpentinization reactions: petrography, mineral chemistry, and petrophysics of serpentinites from MAR 15°N (ODP Leg 209, Site 1274). *Geophysical Research Letters* 33, L13306, doi:10.1029/2006GL025681

Bachmann, F., Hielscher, R., Schaeben, H., 2010. Texture analysis with MTEX – free and open source software toolbox. *Diffusion and Defect Data part B (Solid State Phenomena)* 160, 63–68.

Bachmann, R., Oncken, O., Glodny, J., Seifert, W., Georgieva, V., Sudo, M., 2009. Exposed plate interface in the European Alps reveals fabric styles and gradients related to an ancient seismogenic coupling zone. *Journal of Geophysical Research–Solid Earth* 114, B05402, doi:10.1029/2008JB005927.

Baker, D.R., Mancini, L., Polacci, M., Higgins, M.D., Gualda, G., Hill, R., Rivers, M., 2012. An introduction to the application of X-ray microtomography to the three-dimensional study of igneous rocks. *Lithos* 148, 262–276.

Bakshi, M.S., 2016. How surfactants control crystal growth of nanomaterials. *Crystal Growth and Design* 16, 1104–1133.

Balanyá, J.C., García-Dueñas, V., Azañón, J.M., Sánchez-Gómez, M., 1997. Alternating contractional and extensional events in the Alpujarride nappes of the Alboran Domain (Betics, Gibraltar Arc). *Tectonics* 16, 226–238.

Bastos, A., Zaefferer, S., Raabe, D., 2008. Three-dimensional EBSD study on the relationship between triple junctions and columnar grains in electrodeposited Co–Ni films. *Journal of Microscopy* 230, 487–498.

Bebout, G.E., Penniston-Dorland, S.C., 2016. Fluid and mass transfer at subduction interfaces – The field metamorphic record. *Lithos* 240, 228–258.

Behr, W., Platt, J., 2012. Kinematic and thermal evolution during two-stage exhumation of a Mediterranean subduction complex. *Tectonics* 31, TC4025, doi:10.1029/2012TC003121

Behr, W.M., Platt, J.P., 2013. Rheological evolution of a Mediterranean subduction complex. *Journal of Structural Geology* 54, 136–155.

Berger, A., Herwegh, M., Schwarz, J.-O., Putlitz, B., 2011. Quantitative analysis of crystal/grain sizes and their distributions in 2D and 3D. *Journal of Structural Geology* 33, 1751–1763.

Bezacier, L., Reynard, B., Bass, J.D., Sanchez-Valle, C., Van de Moortele, B.V., 2010. Elasticity of antigorite, seismic detection of serpentinites, and anisotropy in subduction zones. *Earth and Planetary Science Letters* 289, 198–208.

Bird, P., 2003. An updated digital model of plate boundaries. *Geochemistry, Geophysics, Geosystems* 4, 3, doi:10.1029/2001GC000252.

Bloch, W., John, T., Kummerow, J., Salazar, P., Krüger, O.S., Shapiro, S.A., 2018. Watching dehydration: seismic indication for transient fluid pathways in the oceanic mantle of the subducting Nazca slab. *Geochemistry, Geophysics, Geosystems* 19, 3189–3207.

Booth-Rea, G., Azañón, J., Martínez-Martínez, J., Vidal, O., García-Dueñas, V., 2005. Contrasting structural and P-T evolution of tectonic units in the southeastern Betics: Key for understanding the exhumation of the Alboran Domain HP/LT crustal rocks (western Mediterranean). *Tectonics* 24, 2, doi.org/10.1029/2004TC001640.

Booth-Rea, G., Martínez-Martínez, J., Giaconia, F., 2015. Continental subduction, intracrustal shortening, and coeval upper-crustal extension: PT evolution of subducted south Iberian paleomargin metapelites (Betics, SE Spain). *Tectonophysics* 663, 122–139.

Booth-Rea, G., Ranero, C.R., Martínez-Martínez, J., Grevemeyer, I., 2007. Crustal types and Tertiary tectonic evolution of the Alborán sea, western Mediterranean. *Geochemistry, Geophysics, Geosystems* 8, 10, doi.org/10.1029/2007GC001639.

Boudier, F., Baronnet, A., Mainprice, D., 2010. Serpentine mineral replacements of natural olivine and their seismic implications: oceanic lizardite versus subduction-related antigorite. *Journal of Petrology* 51, 495–512.

Brace, W.F., 1980. Permeability of crystalline and argillaceous rocks. *International Journal of Rock Mechanics* 17, 241–251.

Brantut, N., Stefanou, I., Sulem, J., 2017. Dehydration-induced instabilities at intermediate depths in subduction zones. *Journal of Geophysical Research– Solid Earth* 122, 6087–6107.

Breeding, C.M., Ague, J.J., 2002. Slab-derived fluids and quartz-vein formation in an accretionary prism, Otago Schist, *New Zealand. Geology* 30, 499–502.

Bretscher, A., Hermann, J., Pettke, T., 2018. The influence of oceanic oxidation on serpentinite dehydration during subduction. *Earth and Planetary Science Letters* 499, 173–184.

Bromiley, G.D., Pawley, A.R., 2003. The stability of antigorite in the systems MgO-SiO_2-H_2O (MSH) and MgO-Al_2O_3-SiO_2-H_2O (MASH): The effects of Al^{3+} substitution on high-pressure stability. *American Mineralogist* 88, 99–108.

Brown, K.M., Tryon, M.D., DeShon, H.R., Dorman, L.M., Schwartz, S.Y., 2005. Correlated transient fluid pulsing and seismic tremor in the Costa Rica subduction zone. *Earth and Planetary Science Letters* 238, 189–203.

Brown, M., 2013. Granite: From genesis to emplacement. *Geological Society of America Bulletin* 125, 1079–1113.

Burnett, T., Kelley, R., Winiarski, B., Contreras, L., Daly, M., Gholinia, A., Burke, M., Withers, P., 2016. Large volume serial section tomography by Xe Plasma FIB dual beam microscopy. *Ultramicroscopy* 161, 119–129.

Calcagnotto, M., Ponge, D., Demir, E., Raabe, D., 2010. Orientation gradients and geometrically necessary dislocations in ultrafine grained dual-phase steels studied by 2D and 3D EBSD. *Materials Science and Engineering*: *A* 527, 2738–2746.

Canselier, J.P., 1993. The effects of surfactants on crystallization phenomena. *Journal of Dispersion Science and Technology* 14, 625–644.

Carlson, W.D., 2006. Three-dimensional imaging of earth and planetary materials. *Earth and Planetary Science Letters* 249, 133–147.

Carlson, W.D., Pattison, D.R., Caddick, M.J., 2015. Beyond the equilibrium paradigm: How consideration of kinetics enhances metamorphic interpretation. *American Mineralogist* 100, 1659-1667.

Chauve, T., Montagnat, M., Barou, F., Hidas, K., Tommasi, A., Mainprice, D., 2017. Investigation of nucleation processes during dynamic recrystallization of ice using cryo-EBSD. *Philosophical Transactions* 375, doi:10.1098/rsta.2015.0345.

Clément, M., Padrón-Navarta, J.A., Tommasi, A., Mainprice, D., 2018. Non-hydrostatic stress field orientation inferred from orthopyroxene (Pbca) to low-clinoenstatite (P 21/c) inversion in partially dehydrated serpentinites. *American Mineralogist* 103, 993–1001.

Cnudde, V., Boone, M.N., 2013. High-resolution X-ray computed tomography in geosciences: A review of the current technology and applications. *Earth-Science Reviews* 123, 1–17.

Comas, M., Platt, J., Soto, J., Watts, A., 1999. 44. The origin and tectonic history of the Alboran Basin: insights from Leg 161 results, *Proceedings of the Ocean Drilling Program Scientific Results*, pp. 555–580.

Connolly, J., 2009. The geodynamic equation of state: what and how. *Geochemistry, Geophysics, Geosystems* 10, 10, doi:10.1029/2009GC002540

Connolly, J.A.D., Podladchikov, Y.Y., 2013. A Hydromechanical Model for Lower Crustal Fluid Flow, in: Harlov, D.E., Austrheim, H. (Eds.), *Metasomatism and the Chemical Transformation of Rock: The Role of Fluids in Terrestrial and Extraterrestrial Processes*. Springer Berlin Heidelberg, Berlin, Heidelberg, pp. 599–658.

Connolly, J.A., 2005. Computation of phase equilibria by linear programming: a tool for geodynamic modeling and its application to subduction zone decarbonation. *Earth and Planetary Science Letters* 236, 524–541.

Connolly, J.A.D., 1997. Devolatilization-generated fluid pressure and deformation-propagated fluid flow during prograde regional metamorphism. *Journal of Geophysical Research–Solid Earth* 102, 18149–18173.

Connolly, J.A.D., 2010. The mechanics of metamorphic fluid expulsion. *Elements* 6, 165–172.

Connolly, J.A.D., Podladchikov, Y.Y., 1998. Compaction-driven fluid flow in viscoelastic rock. *Geodinamica Acta* 11, 55–84.

Conrad, C.P., Lithgow-Bertelloni, C., 2002. How mantle slabs drive plate tectonics. *Science* 298, 207–209.

Crespo-Blanc, A., Balanyá, J., Expósito, I., Luján, M., Suades, E., 2012. Crescent-like large-scale structures in the external zones of the western Gibraltar Arc (Betic–Rif orogenic wedge). *Journal of the Geological Society* 169, 667–679.

Dann, J.C., 2001. Vesicular komatiites, 3.5-Ga Komati Formation, Barberton Greenstone Belt, South Africa: inflation of submarine lavas and origin of spinifex zones. *Bulletin of Volcanology* 63, 462–481.

Dautriat, J., Gland, N., Guelard, J., Dimanov, A., Raphanel, J.L., 2009. Axial and radial permeability evolutions of compressed sandstones: end effects and shear-band induced permeability anisotropy. *Pure and Applied Geophysics* 166, 1037–1061.

Davies, G.F., 2001. Dynamic Earth: Plates, plumes and mantle convection. *American Journal of Physics* 69, 620–621.

Davies, G.F., Richards, M.A., 1992. Mantle convection. *The Journal of Geology* 100, 151–206.

de Lis Mancilla, F., Booth-Rea, G., Stich, D., Pérez-Peña, J.V., Morales, J., Azañón, J.M., Martin, R., Giaconia, F., 2015. Slab rupture and delamination under the Betics and Rif constrained from receiver functions. *Tectonophysics* 663, 225–237.

Debret, B., Bolfan-Casanova, N., Padrón-Navarta, J.A., Martin-Hernandez, F., Andreani, M., Garrido, C.J., López Sánchez-Vizcaíno, V., Gómez-Pugnaire, M.T., Muñoz, M., Trcera, N., 2015. Redox state of iron during high-pressure serpentinite dehydration. *Contributions to Mineralogy and Petrology* 169, 36, doi: 10.1007/s00410-015-1130-y

Debret, B., Sverjensky, D.A., 2017. Highly oxidising fluids generated during serpentinite breakdown in subduction zones. *Scientific Reports* 7, 10351, doi:10.1038/s41598-017-09626-y.

Deer, W.A., Howie, R.A., Zussman, J., 1997. *Rock-forming minerals: Orthosilicates*. Volume 1A, 2nd edition. Geological Society, London, 936 pp.

Deschamps, F., Godard, M., Guillot, S., Chauvel, C., Andreani, M., Hattori, K., Wunder, B., France, L., 2012. Behavior of fluid-mobile elements in serpentines from abyssal to subduction environments: Examples from Cuba and Dominican Republic. *Chemical Geology* 312, 93–117.

Deschamps, F., Godard, M., Guillot, S., Hattori, K., 2013. Geochemistry of subduction zone serpentinites: A review. *Lithos* 178, 96–127.

Deschamps, F., Guillot, S., Godard, M., Andreani, M., Hattori, K., 2011. Serpentinites act as sponges for fluid-mobile elements in abyssal and subduction zone environments. *Terra Nova* 23, 171–178.

Dickey, J.S., 1972. A primary peridotite magma-revisited: olivine quench crystals in a peridotite lava. *Geological Society of America Memoirs* 132, 289–297.

Dilissen, N., Hidas, K., Garrido, C.J., Kahl, W.-A., López Sánchez-Vizcaíno, V., Padrón-Navarta, J.A., 2018. Textural evolution during high-pressure dehydration of serpentinite to peridotite and its relation to stress orientations and kinematics of subducting slabs: Insights from the Almirez ultramafic massif. *Lithos* 320–321, 470–489.

Donaldson, C.H., 1976. An experimental investigation of olivine morphology. *Contributions to Mineralogy and Petrology* 57, 187–213.

Doo, W.-B., Kuo-Chen, H., Brown, D., Lo, C.-L., Hsu, S.-K., Huang, Y.-S., 2016. Serpentinization of the fore-arc mantle along the Taiwan arc-continent collision of the northern Manila subduction zone inferred from gravity modeling. *Tectonophysics* 691, 282–289.

Dymkova, D., Gerya, T., 2013. Porous fluid flow enables oceanic subduction initiation on Earth. *Geophysical Research Letters* 40, 5671–5676.

Echlin, M.P., Mottura, A., Wang, M., Mignone, P.J., Riley, D.P., Franks, G.V., Pollock, T.M., 2014. Three-dimensional characterization of the permeability of W–Cu composites using a new "TriBeam" technique. *Acta Materialia* 64, 307–315.

Eggler, D.H., Ehmann, A.N., 2010. Rate of antigorite dehydration at 2 GPa applied to subduction zones. *American Mineralogist* 95, 761–769.

Evans, B.W., 1976. Stability of chrysotile and antigorite in serpentinite multisystem. *Schweizerische Mineralogische und Petrographische Mitteilungen* 56, 79–93.

Evans, B.W., Cowan, D.S., 2012. A Melt origin for spinifex-textured metaperidotite in the Cerro del Almirez massif, southern Spain. *American Journal of Science* 312, 967–993.

Exner, H.E., 2011. Stereology and 3D microscopy: useful alternatives or competitors in the quantitative analysis of microstructures? *Image Analysis and Stereology* 23, 73–82.

Faccenda, M., 2014. Water in the slab: A trilogy. *Tectonophysics* 614, 1–30.

Faure, F., Arndt, N., Libourel, G., 2006. Formation of spinifex texture in komatiites: an experimental study. *Journal of Petrology* 47, 1591–1610.

Faure, F., Schiano, P., Trolliard, G., Nicollet, C., Soulestin, B., 2007. Textural evolution of polyhedral olivine experiencing rapid cooling rates. *Contributions to Mineralogy and Petrology* 153, 405–416.

Faure, F., Trolliard, G., Soulestin, B., 2003. TEM investigation of forsterite dendrites. *American Mineralogist* 88, 1241–1250.

Feldkamp, L.A., Davis, L., Kress, J.W., 1984. Practical cone-beam algorithm, *Journal of the Optical Society of America A: Optics, Image Science, and Vision* 1, 612–619.

Ferrand, T.P., Hilairet, N., Incel, S., Deldicque, D., Labrousse, L., Gasc, J., Renner, J., Wang, Y., Green Ii, H.W., Schubnel, A., 2017. Dehydration-driven stress transfer triggers intermediate-depth earthquakes. *Nature Communications* 8, 15247, doi: 10.1038/ncomms15247.

Ferry, J.M., 1994. A historical review of metamorphic fluid-flow. *Journal of Geophysical Research–Solid Earth* 99, 15487–15498.

Ferry, J.M., Gerdes, M.L., 1998. Chemically reactive fluid flow during metamorphism. *Annual Review of Earth and Planetary Sciences* 26, 255–287.

Flukiger, F., Bernard, D., 2009. A new numerical model for pore scale dissolution of calcite due to CO2 saturated water flow in 3D realistic geometry: Principles and first results. *Chemical Geology* 265, 171–180.

Forsyth, D., 1975. On the relative importance of the driving forces of plate motion. *Geophysical Journal International* 43, 163–200.

Frohlich, C., 1989. Earthquakes – new rumbles on deep sources. *Nature* 341, 687–688.

Früh-Green, G.L., Connolly, J.A., Plas, A., Kelley, D.S., Grobéty, B., 2004. Serpentinization of oceanic peridotites: implications for geochemical cycles and biological activity. *The subseafloor biosphere at mid-ocean ridges* 144, 119–136.

Fryer, P., 2002. Recent Studies of Serpentinite Occurrences in the Oceans: Mantle-Ocean Interactions in the Plate Tectonic Cycle. *Chemie der Erde – Geochemistry* 62, 257–302.

Fukao, Y., Hori, S., Ukawa, M., 1983. A seismological constraint on the depth of basalt–eclogite transition in a subducting oceanic crust. *Nature* 303, 413–415.

Furukawa, Y., 1993. Depth of the decoupling plate interface and thermal structure under arcs. *Journal of Geophysical Research– Solid Earth* (1978–2012) 98, 20005–20013.

Garrido, C.J., Gueydan, F., Booth-Rea, G., Precigout, J., Hidas, K., Padrón-Navarta, J.A., Marchesi, C., 2011. Garnet lherzolite and garnet-spinel mylonite in the Ronda peridotite: Vestiges of Oligocene backarc mantle lithospheric extension in the western Mediterranean. *Geology* 39, 927–930.

Garrido, C.J., López Sánchez–Vizcaíno, V., Gómez-Pugnaire, M.T., Trommsdorff, V., Alard, O., Bodinier, J.L., Godard, M., 2005. Enrichment of HFSE in chlorite-harzburgite produced by high-pressure dehydration of antigorite-serpentinite: Implications for subduction magmatism. *Geochemistry Geophysics Geosystems* 6, 1, doi:10.1029/2004GC000791

Gerya, T.V., Stöckhert, B., Perchuk, A.L., 2002. Exhumation of high-pressure metamorphic rocks in a subduction channel: A numerical simulation. *Tectonics* 21, 6, 1056, doi:10.1029/2002TC001406

Gerya, T.V., Yuen, D.A., 2003. Rayleigh-Taylor instabilities from hydration and melting propel 'cold plumes' at subduction zones. *Earth and Planetary Science Letters* 212, 47–62.

Goldsmith, R., 1959. Granofels, a new metamorphic name. *Journal of Geology* 67, 109–110.

Gómez-Pugnaire, M., Rubatto, D., Fernández-Soler, J., Jabaloy, A., López Sánchez-Vizcaíno, V., González-Lodeiro, F., Galindo-Zaldívar, J., Padrón-Navarta, J., 2012. Late Variscan magmatism in the Nevado-Filábride Complex: U-Pb geochronologic evidence for the pre-Mesozoic nature of the deepest Betic complex (SE Spain). *Lithos* 146, 93–111.

Gómez-Pugnaire, M.T., Galindo-Zaldívar, J., Rubatto, D., González-Lodeiro, F., López Sánchez-Vizcaíno, V., Jabaloy, A., 2004. A reinterpretation of the Nevado-Filábride and Alpujárride complexes (Betic Cordillera): field, petrography and U-Pb ages from orthogneisses (western Sierra Nevada, S Spain). *Schweizerische Mineralogische und Petrographische Mitteilungen* 84, 303–322.

Gómez-Pugnaire, M.T., Ulmer, P., López-Sánchez-Vizcaíno, V., 2000. Petrogenesis of the mafic igneous rocks of the Betic Cordilleras: A field, petrological and geochemical study. *Contributions to Mineralogy and Petrology* 139, 436–457.

Grevemeyer, I., Ranero, C.R., Ivandic, M., 2018. Structure of oceanic crust and serpentinization at subduction trenches. *Geosphere* 14, 395–418.

Grove, T.L., Till, C.B., Krawczynski, M.J., 2012. The Role of H_2O in Subduction Zone Magmatism. *Annual Review of Earth and Planetary Sciences* 40, 413–439.

Guerrera, F., Martín-Martín, M., Perrone, V., Tramontana, M., 2005. Tectono-sedimentary evolution of the southern branch of the Western Tethys (Maghrebian Flysch Basin and Lucanian Ocean): consequences for Western Mediterranean geodynamics. *Terra Nova* 17, 358–367.

Guillot, S., Schwartz, S., Reynard, B., Agard, P., Prigent, C., 2015. Tectonic significance of serpentinites. *Tectonophysics* 646, 1–19.

Hacker, B.R., 1997. Diagenesis and fault valve seismicity of crustal faults. Journal of *Geophysical Research– Solid Earth* 102, 24459–24467.

Hacker, B.R., 2008. H_2O subduction beyond arcs. *Geochemistry, Geophysics, Geosystems* 9, doi:10.1029/2007GC001707

Hacker, B.R., Abers, G.A., Peacock, S.M., 2003. Subduction factory 1. Theoretical mineralogy, densities, seismic wave speeds, and H_2O contents. *Journal of Geophysical Research– Solid Earth* (1978–2012) 108(B1), 2029, doi:10.1029/2001JB001127

Hacker, B.R., Peacock, S.M., Abers, G.A., Holloway, S.D., 2003. Subduction factory – 2. Are intermediate-depth earthquakes in subducting slabs linked to metamorphic dehydration reactions? *Journal of Geophysical Research* 108, 1–16.

Hager, B.H., O'Connell, R.J., 1981. A simple global model of plate dynamics and mantle convection. *Journal of Geophysical Research– Solid Earth* 86, 4843–4867.

Harrigan, T., Mann, R., 1984. Characterization of microstructural anisotropy in orthotropic materials using a second rank tensor. *Journal of Materials Science* 19, 761–767.

Harvey, J., Garrido, C.J., Savov, I., Agostini, S., Padrón-Navarta, J.A., Marchesi, C., López Sánchez-Vizcaíno, V., Gómez-Pugnaire, M.T., 2014. B^{11}-rich fluids in subduction zones: The role of antigorite dehydration in subducting slabs and boron isotope heterogeneity in the mantle. *Chemical Geology* 376, 20–30.

Hatakeyama, K., Katayama, I., Hirauchi, K.-I., Michibayashi, K., 2017. Mantle hydration along outer-rise faults inferred from serpentinite permeability. *Scientific Reports* 7, 13870, doi:10.1038/s41598-017-14309-9

Hattori, K.H., Guillot, S., 2003. Volcanic fronts form as a consequence of serpentinite dehydration in the forearc mantle wedge. *Geology* 31, 525–528.

Hattori, K.H., Guillot, S., 2007. Geochemical character of serpentinites associated with high-to ultrahigh-pressure metamorphic rocks in the Alps, Cuba, and the Himalayas: Recycling of elements in subduction zones. *Geochemistry, Geophysics, Geosystems* 8, 9, doi:10.1029/2007GC001594

Healy, D., Reddy, S.M., Timms, N.E., Gray, E.M., Brovarone, A.V., 2009. Trench-parallel fast axes of seismic anisotropy due to fluid-filled cracks in subducting slabs. *Earth and Planetary Science Letters* 283, 75–86.

Hermann, J., Müntener, O., Scambelluri, M., 2000. The importance of serpentinite mylonites for subduction and exhumation of oceanic crust. *Tectonophysics* 327, 225–238.

Hermann, J., Spandler, C., Hack, A., Korsakov, A.V., 2006. Aqueous fluids and hydrous melts in high-pressure and ultra-high pressure rocks: implications for element transfer in subduction zones. *Lithos* 92, 399–417.

Hidas, K., Booth-Rea, G., Garrido, C.J., Martínez-Martínez, J.M., Padrón-Navarta, J.A., Konc, Z., Giaconia, F., Frets, E., Marchesi, C., 2013. Backarc basin inversion and subcontinental mantle emplacement in the crust: kilometre-scale folding and shearing at the base of the proto-Alborán lithospheric mantle (Betic Cordillera, southern Spain). *Journal of the Geological Society* 170, 47–55.

Hidas, K., Tommasi, A., Garrido, C.J., Padrón-Navarta, J.A., Mainprice, D., Vauchez, A., Barou, F., Marchesi, C., 2016. Fluid-assisted strain localization in the shallow subcontinental lithospheric mantle. *Lithos* 262, 636–650.

Hidas, K., Tommasi, A., Mainprice, D., Chauve, T., Barou, F., Montagnat, M., 2017. Microstructural evolution during thermal annealing of ice-Ih. *Journal of Structural Geology* 99, 31–44.

Hidas, K., Varas-Reus, M.I., Garrido, C.J., Marchesi, C., Acosta-Vigil, A., Padrón-Navarta, J.A., Targuisti, K., Konc, Z., 2015. Hyperextension of continental to oceanic-like lithosphere: The record of late gabbros in the shallow subcontinental lithospheric mantle of the westernmost Mediterranean. *Tectonophysics* 650, 65–79.

Hielscher, R., Schaeben, H., 2008. A novel pole figure inversion method: specification of the MTEX algorithm. *Journal of Applied Crystallography* 41, 1024–1037.

Higgins, M.D., 2006. *Quantitative Textural Measurements in Igneous and Metamorphic Petrology*. Cambridge University Press, Cambridge, 276 pp.

Hilairet, N., Daniel, I., Reynard, B., 2006. Equation of state of antigorite, stability field of serpentines, and seismicity in subduction zones. *Geophysical Research Letters* 33, L02302, doi:10.1029/2005GL024728

Hilairet, N., Reynard, B., Wang, Y., Daniel, I., Merkel, S., Nishiyama, N., Petitgirard, S., 2007. High-pressure creep of serpentine, interseismic deformation, and initiation of subduction. *Science* 318, 1910–1913.

Hildebrand, T., Rüegsegger, P., 1997. A new method for the model-independent assessment of thickness in three-dimensional images. *Journal of Microscopy* 185, 67–75.

Hildyard, R., Prior, D., Mariani, E., Faulkner, D., 2009. Crystallographic preferred orientation (CPO) of gypsum measured by electron backscatter diffraction (EBSD). *Journal of Microscopy* 236, 159–164.

Hirth, G., Guillot, S., 2013. Rheology and tectonic significance of serpentinite. *Elements* 9, 107–113.

Hofmann, A., 1997. Mantle geochemistry: the message from oceanic volcanism. *Nature* 385, 219–229.

Holland, T., Powell, R., 1991. A Compensated-Redlich-Kwong (CORK) equation for volumes and fugacities of CO_2 and H_2O in the range 1 bar to 50 kbar and 100–1600 °C. *Contributions to Mineralogy and Petrology* 109, 265–273.

Holland, T., Powell, R., 1998. An internally consistent thermodynamic data set for phases of petrological interest. *Journal of Metamorphic Geology* 16, 309–343.

Horiuchi, S.-S., Iwamori, H., 2016. A consistent model for fluid distribution, viscosity distribution, and flow-thermal structure in subduction zone. *Journal of Geophysical Research– Solid Earth* 121, 3238–3260.

Houston, H., 2015. *Deep Earthquakes*, in: Elsevier (Ed.), Schubert, Gerald, Treatise on Geophysics (Second Edition), Oxford, pp. 329–354.

Hyndman, R.D., Peacock, S.M., 2003. Serpentinization of the forearc mantle. *Earth and Planetary Science Letters* 212, 417–432.

Inoue, T., 1994. Effect of water on melting phase relations and melt composition in the system Mg_2SiO_4 - $MgSiO_3$ - H_2O up to 15 GPa. *Physics of the Earth and Planetary Interiors* 85, 237–263.

Iyer, K., Austrheim, H., John, T., Jamtveit, B., 2008. Serpentinization of the oceanic lithosphere and some geochemical consequences: Constraints from the Leka Ophiolite Complex, Norway. *Chemical Geology* 249, 66–90.

Iyer, K., Jamtveit, B., Mathiesen, J., Malthe-Sørenssen, A., Feder, J., 2008. Reaction-assisted hierarchical fracturing during serpentinization. *Earth and Planetary Science Letters* 267, 503–516.

Iyer, K., Ruepke, L.H., Morgan, J.P., Grevemeyer, I., 2012. Controls of faulting and reaction kinetics on serpentinization and double Benioff zones. *Geochemistry Geophysics Geosystems* 13, 9, doi:10.1029/2012GC004304

Jabaloy-Sánchez, A., Gómez-Pugnaire, M.T., Padrón-Navarta, J.A., López Sánchez-Vizcaíno, V., Garrido, C.J., 2015. Subduction- and exhumation-related structures preserved in metaserpentinites and associated metasediments from the Nevado–Filábride Complex (Betic Cordillera, SE Spain). *Tectonophysics* 644–645, 40–57.

Jabaloy-Sánchez, A., Talavera, C., Gómez-Pugnaire, M.T., López-Sánchez-Vizcaíno, V., Vázquez-Vílchez, M., Rodríguez-Peces, M.J., Evans, N.J., 2018. U-Pb ages of detrital zircons from the Internal Betics: A key to deciphering paleogeographic provenance and tectono-stratigraphic evolution. *Lithos* 318-319, 244–266.

Jamtveit, B., Andersen, T.B., 1992. Morphological instabilities during rapid growth of metamorphic garnets. *Physics and Chemistry of Minerals* 19, 176–184.

Jarrard, R.D., 1986. Relations among subduction parameters. *Reviews of Geophysics* 24, 217–284.

Jerram, D.A., Higgins, M.D., 2007. 3D Analysis of rock textures: quantifying igneous microstructures. *Elements* 3, 239-245.

Jerram, D.A., Mock, A., Davis, G.R., Field, M., Brown, R.J., 2009. 3D crystal size distributions: A case study on quantifying olivine populations in kimberlites. *Lithos* 112, 223–235.

John, T., Gussone, N., Podladchikov, Y.Y., Bebout, G.E., Dohmen, R., Halama, R., Klemd, R., Magna, T., Seitz, H.-M., 2012. Volcanic arcs fed by rapid pulsed fluid flow through subducting slabs. *Nature Geoscience* 5, 489–492.

Jung, H., 2011. Seismic anisotropy produced by serpentine in mantle wedge. *Earth and Planetary Science Letters* 307, 535–543.

Jung, H., Karato, S., 2001. Water-induced fabric transitions in olivine. *Science* 293, 1460–1463.

Kahl, W.A., Dilissen, N., Hidas, K., Garrido, C.J., López Sánchez-Vizcaíno, V., Román-Alpiste, M.J., 2017. 3-D microstructure of olivine in complex geological materials reconstructed by correlative X-ray μ-CT and EBSD analyses. *Journal of Microscopy* 268, 193–207.

Kahl, W.-A., Hinkes, R., Feeser, V., Holzheid, A., 2013. Microfabric and anisotropy of elastic waves in sandstone–an observation using high-resolution X-ray microtomography. *Journal of Structural Geology* 49, 35–49.

Karson, J.A., 1998. Internal structure of oceanic lithosphere: A perspective from tectonic windows. *Geophysical Monograph–American Geophysical Union* 106, 177–218.

Katayama, I., Hirauchi, H., Michibayashi, K., Ando, J., 2009. Trench-parallel anisotropy produced by serpentine deformation in the hydrated mantle wedge. *Nature* 461, 1114–U1209.

Kawano, S., Katayama, I., Okazaki, K., 2011. Permeability anisotropy of serpentinite and fluid pathways in a subduction zone. *Geology* 39, 939–942.

Ketcham, R.A., 2005. Three-dimensional grain fabric measurements using high-resolution X-ray computed tomography. *Journal of Structural Geology* 27, 1217–1228.

Ketcham, R.A., Carlson, W.D., 2001. Acquisition, optimization and interpretation of X-ray computed tomographic imagery: applications to the geosciences. *Computers & Geosciences* 27, 381–400.

King, H.E., Stimpfl, M., Deymier, P., Drake, M.J., Catlow, C.R.A., Putnis, A., de Leeuw, N.H., 2010. Computer simulations of water interactions with low-coordinated forsterite surface sites: Implications for the origin of water in the inner solar system. *Earth and Planetary Science Letters* 300, 11–18.

Kirby, S., 1995. Interslab earthquakes and phase changes in subducting lithosphere. *Reviews of Geophysics* 33, 287–297.

Kirby, S.H., Stern, L.A., Durham, W.B., 1991. Mantle phase changes and deep-earthquake faulting in subducting lithosphere. *Science* 252, 216–225.

Kirchner, K.L., Behr, W.M., Loewy, S., Stockli, D.F., 2016. Early Miocene subduction in the western Mediterranean: Constraints from Rb-Sr multimineral isochron geochronology. *Geochemistry, Geophysics, Geosystems* 17, 1842–1860.

Kita, S., Ferrand, T.P., 2018. Physical mechanisms of oceanic mantle earthquakes: Comparison of natural and experimental events. *Scientific Reports* 8, 17049, doi:10.1038/s41598-018-35290-x

Kita, S., Okada, T., Nakajima, J., Matsuzawa, T., Hasegawa, A., 2006. Existence of a seismic belt in the upper plane of the double seismic zone extending in the along-arc direction at depths of 70–100 km beneath NE Japan. *Geophysical Research Letters* 33, https://doi.org/10.1029/2006GL028239|

Ko, S.C., Olgaard, D.L., Wong, T.F., 1997. Generation and maintenance of pore pressure excess in a dehydrating system .1. Experimental and microstructural observations. *Journal of Geophysical Research–Solid Earth* 102, 825–839.

Komabayashi, T., 2006. Phase relations of hydrous peridotite: implications for water circulation in the Earth's mantle. *Earth's Deep Water Cycle*, 29–43.

Komabayashi, T., Hirose, K., Funakoshi, K.-I., Takafuji, N., 2005. Stability of phase A in antigorite (serpentine) composition determined by in situ X-ray pressure observations. *Physics of the Earth and Planetary Interiors* 151, 276–289.

Konzett, J., Ulmer, P., 1999. The stability of hydrous potassic phases in lherzolitic mantle—an experimental study to 9.5 GPa in simplified and natural bulk compositions. *Journal of Petrology* 40, 629–652.

Kovalenko, V.I., Naumov, V.B., Girnis, A.V., Dorofeeva, V.A., Yarmolyuk, V.V., 2010. Average composition of basic magmas and mantle sources of island arcs and active continental margins estimated from the data on melt inclusions and quenched glasses of rocks. *Petrology* 18, 1–26.

Kumari, L., Li, W., Kulkarni, S., Wu, K., Chen, W., Wang, C., Vannoy, C.H., Leblanc, R.M., 2009. Effect of surfactants on the structure and morphology of magnesium borate hydroxide nanowhiskers synthesized by hydrothermal route. *Nanoscale Research Letters* 5, 149–157, doi: 10.1007/s11671-009-9457-9

Kunze, G., 1956. Die gewellte struktur des antigorits, I. *Zeitschrift für Kristallographie* 108, 82-107.

Kunze, G., 1958. Die gewellte Struktur des Antigorits. II. *Zeitschrift für Kristallographie–Crystalline Materials* 110, 282–320.

Kunze, G., 1961. Antigorit. *Fortschritte der Mineralogie* 39, 206–324.

Laborda-López, C., López Sánchez-Vizcaíno, V., Marchesi, C., Gómez-Pugnaire: M. T., Garrido C. J., Jabaloy-Sánchez, A., Padrón-Navarta J. A., Hidas, K., 2018. High pressure metamorphism of rodingites during serpentinite dehydration (Cerro del Almirez, southern Spain): implications for the redox state in subduction zones. *Journal of Metamorphic Geology* 36, 1141–1173

Lafay, R., Deschamps, F., Schwartz, S., Guillot, S., Godard, M., Debret, B., Nicollet, C., 2013. High-pressure serpentinites, a trap-and-release system controlled by metamorphic conditions: Example from the Piedmont zone of the western Alps. *Chemical Geology* 343, 38–54.

Lamadrid, H.M., Rimstidt, J.D., Schwarzenbach, E.M., Klein, F., Ulrich, S., Dolocan, A., Bodnar, R.J., 2017. Effect of water activity on rates of serpentinization of olivine. *Nature Communications* 8, 16107, doi: 10.1038/ncomms16107

Leeman, W.P., 1996. Boron and other fluid-mobile elements in volcanic arc lavas: implications for subduction processes. Washington DC *American Geophysical Union Geophysical Monograph Series*, 96, 269–276

Lenoir, X., Garrido, C.J., Bodinier, J.-L., Dautria, J.-M., Gervilla, F., 2001. The recrystallization front of the Ronda peridotite: evidence for melting and thermal erosion of subcontinental lithospheric mantle beneath the Alboran Basin. *Journal of Petrology* 42, 141–158.

Lillie, R.J., 2005. *Parks and Plates: The Geology of our National Parks, Monuments, and Seashores*. WW Norton, 298 pp.

Lonergan, L., White, N., 1997. Origin of the Betic-Rif mountain belt. *Tectonics* 16, 504–522.

Long, H., Swennen, R., Foubert, A., Dierick, M., Jacobs, P., 2009. 3D quantification of mineral components and porosity distribution in Westphalian C sandstone by microfocus X-ray computed tomography. *Sedimentary Geology* 220, 116–125.

López Sánchez-Vizcaíno, V., Gómez-Pugnaire, M.T., in press. *Alpine Metamorphism. Metamorphism of the Nevado-Filábride Complex*. in: Quesada, C., Oliveira, J.T. (Eds.), The Geology of Iberia: a Geodynamic Approach.

López Sánchez-Vizcaíno, V., Gómez-Pugnaire, M.T., Garrido, C.J., Padrón-Navarta, J.A., Mellini, M., 2009. Breakdown mechanisms of titanclinohumite in antigorite serpentinite (Cerro del Almirez massif, S. Spain): A petrological and TEM study. *Lithos* 107, 216–226.

López Sánchez-Vizcaíno, V., Rubatto, D., Gómez-Pugnaire, M.T., Trommsdorff, V., Müntener, O., 2001. Middle Miocene high-pressure metamorphism and fast exhumation of the Nevado-Filábride Complex, SE Spain. *Terra Nova* 13, 327-332.

López Sánchez-Vizcaíno, V., Trommsdorff, V., Gómez-Pugnaire, M.T., Garrido, C., Müntener, O., Connolly, J.A.D., 2005. Petrology of titanian clinohumite and olivine at the high-pressure breakdown of antigorite serpentinite to chlorite harzburgite (Almirez Massif, S. Spain). *Contributions to Mineralogy and Petrology* 149, 627–646.

Louis, L., Baud, P., Wong, T.-F., 2007. Characterization of pore-space heterogeneity in sandstone by X-ray computed tomography. *Geological Society, London, Special Publications* 284, 127–146.

Louis, L., Baud, P., Wong, T.-F., 2009. Microstructural inhomogeneity and mechanical anisotropy associated with bedding in Rothbach sandstone. *Pure and Applied Geophysics* 166, 1063–1087.

Luján, M., Crespo-Blanc, A., Balanyá, J.C., 2006. The Flysch Trough thrust imbricate (Betic Cordillera): A key element of the Gibraltar Arc orogenic wedge. *Tectonics* 25, 10.1029/2005TC001910

Manning, C., 2004. Polymeric silicate complexing in aqueous fluids at high pressure and temperature, and its implications for water-rock interaction, in Wanty, R. B., and Seal, R. R., II, eds., *Water-rock interaction, proceedings of the eleventh international symposium on water-rock interaction*. Taylor & Francis Group, London, pp. 45–49.

Manning, C.E., 2004. The chemistry of subduction-zone fluids. *Earth and Planetary Science Letters* 233, 1–16.

Manning, C.E., Ingebritsen, S.E., 1999. Permeability of the continental crust: Implications of geothermal data and metamorphic systems. *Reviews of Geophysics* 37, 127–150.

Marchesi, C., Garrido, C.J., Padrón-Navarta, J.A., López Sánchez-Vizcaíno, V., Gómez-Pugnaire, M.T., 2013. Element mobility from seafloor serpentinization to high-pressure dehydration of antigorite in subducted serpentinite: Insights from the Cerro del Almirez ultramafic massif (southern Spain). *Lithos* 178, 128–142.

Martínez-Martínez, J.M., Booth-Rea, G., Azañón, J.M., Torcal, F., 2006. Active transfer fault zone linking a segmented extensional system (Betics, southern Spain): Insight into heterogeneous extension driven by edge delamination. *Tectonophysics* 422, 159–173.

Martínez-Martínez, J.M., Soto, J.I., Balanyá, J.C., 2002. Orthogonal folding of extensional detachments: Structure and origin of the Sierra Nevada elongated dome (Betics, SE Spain). *Tectonics* 21, 3, 1012, 10.1029/2001TC001283

McDonough, W.F., 2001. The composition of the Earth. Earthquake thermodynamics and phase transformations in the Earth's interior 76, 80077-80072.

McKenzie, D., 1984. The generation and compaction of partially molten rock. *Journal of Petrology* 25, 713–765.

McMahon, C., Soe, B., Loeb, A., Vemulkar, A., Ferry, M., Bassman, L., 2013. Boundary identification in EBSD data with a generalization of fast multiscale clustering. *Ultramicroscopy* 133, 16–25.

Means, W.D., Paterson, M.S., 1966. Experiments on preferred orientation of platy minerals. *Contributions to Mineralogy and Petrology* 13, 108–133.

Mei, S., Bai, W., Hiraga, T., Kohlstedt, D.L., 2002. Influence of melt on the creep behavior of olivine-basalt aggregates under hydrous conditions. *Earth and Planetary Science Letters* 201, 491–507.

Mellini, M., Trommsdorff, V., Compagnoni, R., 1987. Antigorite polysomatism: behaviour during progressive metamorphism. *Contributions to Mineralogy and Petrology* 97, 147–155.

Mével, C., 2003. Serpentinization of abyssal peridotites at mid-ocean ridges. *Comptes Rendus Geoscience* 335, 825–852.

Miller, S.A., van der Zee, W., Olgaard, D.L., Connolly, J.A.D., 2003. A fluid-pressure feedback model of dehydration reactions: experiments, modelling, and application to subduction zones. *Tectonophysics* 370, 241–251.

Molnar, P., Freedman, D., Shih, J.S., 1979. Lengths of intermediate and deep seismic zones and temperatures in downgoing slabs of lithosphere. *Geophysical Journal International* 56, 41–54.

Morales, L.F., Mainprice, D., Kern, H., 2018. Olivine-antigorite orientation relationships: Microstructures, phase boundary misorientations and the effect of cracks in the seismic properties of serpentinites. *Tectonophysics* 724–725, 93–115.

Mullin, J.W., 2001. *Crystal Growth*, in: Mullin, J.W. (Ed.), Crystallization (Fourth Edition). Butterworth-Heinemann, Oxford, pp. 216–288.

Muralidharan, K., Deymier, P., Stimpfl, M., de Leeuw, N.H., Drake, M.J., 2008. Origin of water in the inner Solar System: A kinetic Monte Carlo study of water adsorption on forsterite. *Icarus* 198, 400–407.

Nagaya, T., Wallis, S.R., Seto, Y., Miyake, A., Soda, Y., Uehara, S., Matsumoto, M., 2017. Minimizing and quantifying mis-indexing in electron backscatter diffraction (EBSD) determinations of antigorite crystal directions. *Journal of Structural Geology* 95, 127–141.

Naliboff, J.B., Billen, M.I., Gerya, T., Saunders, J., 2013. Dynamics of outer-rise faulting in oceanic-continental subduction systems. *Geochemistry, Geophysics, Geosystems* 14, 2310–2327.

Nicolas, A., Poirier, J.P., 1976. *Crystalline Plasticity and Solid State Flow in Metamorphic Rocks*. John Wiley & Sons. London; New York, 246 pp.

Noiriel, C., 2015. Resolving time-dependent evolution of pore-scale structure, permeability and reactivity using X-ray microtomography. *Reviews in Mineralogy and Geochemistry* 80, 247–285.

Noiriel, C., Bernard, D., Gouze, P., Thibault, X., 2005. Hydraulic properties and microgeometry evolution accompanying limestone dissolution by acidic water. *Oil & Gas Science and Technology* 60, 177–192.

Noiriel, C., Luquot, L., Madé, B., Raimbault, L., Gouze, P., Van Der Lee, J., 2009. Changes in reactive surface area during limestone dissolution: An experimental and modelling study. *Chemical Geology* 265, 160–170.

Noll, P., Newsom, H., Leeman, W., Ryan, J.G., 1996. The role of hydrothermal fluids in the production of subduction zone magmas: evidence from siderophile and chalcophile trace elements and boron. *Geochimica et Cosmochimica Acta* 60, 587–611.

Nur, A., Walder, J., 1992. *Hydraulic Pulses in the Earth's Crust*, in: Evans, B., Wong, T.-F. (Eds.), Fault Mechanics and Transport Properties of Rocks. Academic Press, London, pp. 461–473.

Odgaard, A., 1997. Three-dimensional methods for quantification of cancellous bone architecture. *Bone* 20, 315–328.

Okazaki, K., Noda, H., Uehara, S., Shimamoto, T., 2014. Permeability, porosity and pore geometry evolution during compaction of Neogene sedimentary rocks. *Journal of Structural Geology* 62, 1–12.

O'Neill, C., Jellinek, A., Lenardic, A., 2007. Conditions for the onset of plate tectonics on terrestrial planets and moons. *Earth and Planetary Science Letters* 261, 20–32.

Padrón Navarta, J.A., 2010. *A coupled petrological and petrophysical study of high pressure dehydration reactions in subduction settings. Insights from the Betic Cordillera and the Kohistan Paleo-arc*. Ph.D. Thesis, University of Granada.

Padron-Navarta, J., Garrido, C., Sanchez-Navas, A., Tommasi, A., López Sánchez-Vizcaíno, V., Gómez-Pugnaire, M., Hussain, S.S., 2008. Oriented growth of garnet by topotactic reactions and epitaxy in high-pressure, mafic garnet granulite formed by dehydration melting of metastable hornblende-gabbronorite (Jijal Complex, Kohistan Complex, north Pakistan). *Journal of Metamorphic Geology* 26, 855–870.

Padrón-Navarta, J.A., Hermann, J., Garrido, C.J., López Sánchez-Vizcaíno, V., Gómez-Pugnaire, M.T., 2010. An experimental investigation of antigorite dehydration in natural silica-enriched serpentinite. *Contributions to Mineralogy and Petrology* 159, 25–42.

Padrón-Navarta, J.A., López Sánchez-Vizcaíno, V., Garrido, C.J., Gómez-Pugnaire, M.T., 2011. Metamorphic record of high-pressure dehydration of antigorite serpentinite to chlorite harzburgite in a subduction setting (Cerro del Almirez, Nevado-Filábride Complex, southern Spain). *Journal of Petrology* 52, 2047–2078.

Padrón-Navarta, J.A., López Sánchez-Vizcaíno, V., Garrido, C.J., Gómez-Pugnaire, M.T., Jabaloy, A., Capitani, G.C., Mellini, M., 2008. Highly ordered antigorite from Cerro del Almirez HP-HT serpentinites, SE Spain. *Contributions to Mineralogy and Petrology* 156, 679–688.

Padrón-Navarta, J.A., López Sanchez-Vizcaino, V., Hermann, J., Connolly, J.A.D., Garrido, C.J., Gomez-Pugnaire, M.T., Marchesi, C., 2013. Tschermak's substitution in antigorite and consequences for phase relations and water liberation in high-grade serpentinites. *Lithos* 178, 186–196.

Padrón-Navarta, J.A., Tommasi, A., Garrido, C.J., López Sánchez-Vizcaíno, V., 2012. Plastic deformation and development of antigorite crystal preferred orientation in high-pressure serpentinites. *Earth and Planetary Science Letters* 349, 75–86.

Padrón-Navarta, J.A., Tommasi, A., Garrido, C.J., López Sánchez-Vizcaíno, V., Gómez-Pugnaire, M.T., Jabaloy, A., Vauchez, A., 2010. Fluid transfer into the wedge controlled by high-pressure hydrofracturing in the cold top-slab mantle. *Earth and Planetary Science Letters* 297, 271–286.

Padrón-Navarta, J.A., Tommasi, A., Garrido, C.J., Mainprice, D., 2015. On topotaxy and compaction during antigorite and chlorite dehydration: an experimental and natural study. *Contributions to Mineralogy and Petrology* 169, 1–20.

Pattison, D.R.M., De Capitani, C., Gaidies, F., 2011. Petrological consequences of variations in metamorphic reaction affinity. *Journal of Metamorphic Geology* 29, 953–977.

Paulatto, M., Laigle, M., Galve, A., Charvis, P., Sapin, M., Bayrakci, G., Evain, M., Kopp, H., 2017. Dehydration of subducting slow-spread oceanic lithosphere in the Lesser Antilles. *Nature Communications* 8, 15980, 10.1038/ncomms15980

Peacock, S.M., 1990. Fluid processes in subduction zones. *Science* 248, 329–337.

Peacock, S.M., 2001. Are the lower planes of double seismic zones caused by serpentine dehydration in subducting oceanic mantle? *Geology* 29, 299–302.

Peacock, S.M., 2003. Thermal structure and metamorphic evolution of subducting slabs. Inside the subduction factory, *Geophysical Monograph–American Geophysical Union*, 138, 7–22.

Peacock, S.M., Wang, K., 1999. Seismic consequences of warm versus cool subduction metamorphism: Examples from southwest and northeast Japan. *Science* 286, 937–939.

Peng, S., Hu, Q., Dultz, S., Zhang, M., 2012. Using X-ray computed tomography in pore structure characterization for a Berea sandstone: Resolution effect. *Journal of Hydrology* 472, 254–261.

Penniston-Dorland, S.C., Ferry, J.M., 2008. Element mobility and scale of mass transport in the formation of quartz veins during regional metamorphism of the Waits River Formation, east-central Vermont. *American Mineralogist* 93, 7–21.

Perrillat, J.P., Daniel, I., Koga, K.T., Reynard, B., Cardon, H., Crichton, W.A., 2005. Kinetics of antigorite dehydration: A real-time X-ray diffraction study. *Earth and Planetary Science Letters* 236, 899–913.

Philippot, P., Rumble, D., 2000. Fluid-rock interactions during high-pressure and ultrahigh-pressure metamorphism. *International Geology Review* 42, 312–327.

Piazolo, S., Montagnat, M., Blackford, J., 2008. Sub-structure characterization of experimentally and naturally deformed ice using cryo-EBSD. *Journal of Microscopy* 230, 509–519.

Piazolo, S., Passchier, C.W., 2002. Controls on lineation development in low to medium grade shear zones: a study from the Cap de Creus peninsula, NE Spain. *Journal of Structural Geology* 24, 25–44.

Platt, J.P., Anczkiewicz, R., Soto, J.-I., Kelley, S.P., Thirlwall, M., 2006. Early Miocene continental subduction and rapid exhumation in the western Mediterranean. *Geology* 34, 981–984.

Platt, J.P., Behr, W.M., Cooper, F.J., 2015. Metamorphic core complexes: windows into the mechanics and rheology of the crust. *Journal of the Geological Society* 172, 9–27.

Platt, J.P., Behr, W.M., Johanesen, K., Williams, J.R., 2013. The Betic-Rif arc and its orogenic hinterland: a review. *Annual Review of Earth and Planetary Sciences* 41, 313–357.

Plümper, O., John, T., Podladchikov, Y.Y., Vrijmoed, J.C., Scambelluri, M., 2017. Fluid escape from subduction zones controlled by channel-forming reactive porosity. *Nature Geoscience* 10, 150–156.

Plümper, O., Piazolo, S., Austrheim, H., 2012. Olivine pseudomorphs after serpentinized orthopyroxene record transient oceanic lithospheric mantle dehydration (Leka Ophiolite Complex, Norway). *Journal of Petrology* 53, 1943–1968.

Pogge von Strandmann, P.A., Dohmen, R., Marschall, H.R., Schumacher, J.C., Elliott, T., 2015. Extreme magnesium isotope fractionation at outcrop scale records the mechanism and rate at which reaction fronts advance. *Journal of Petrology* 56, 33–58.

Poli, S., Schmidt, M.W., 2002. Petrology of subducted slabs. *Annual Review of Earth and Planetary Sciences* 30, 207–235.

Précigout, J., Gueydan, F., Garrido, C.J., Cogné, N., Booth-Rea, G., 2013. Deformation and exhumation of the Ronda peridotite (Spain). *Tectonics* 32, 1011–1025.

Prigiobbe, V., Suarez Negreira, A., Wilcox, J., 2013. Interaction between olivine and water based on density functional theory calculations. *The Journal of Physical Chemistry C* 117, 21203–21216.

Prior, D., Lilly, K., Seidemann, M., Vaughan, M., Becroft, L., Easingwood, R., Diebold, S., Obbard, R., Daghlian, C., Baker, I., 2015. Making EBSD on water ice routine. *Journal of Microscopy* 259, 237–256.

Puga, E., de Federico, A.D., Nieto, J., Puga, M.D., Martínez-Conde, J.R., 2009. The Betic ophiolitic association: a very significant geological heritage that needs to be preserved. *Geoheritage* 1, 11.

Puga, E., Fanning, M., de Federico, A.D., Nieto, J.M., Beccaluva, L., Bianchini, G., Puga, M.A.D., 2011. Petrology, geochemistry and U–Pb geochronology of the Betic Ophiolites: inferences for Pangaea break-up and birth of the westernmost Tethys Ocean. *Lithos* 124, 255–272.

Puga, E., Nieto, J., Dıaz de Federico, A., Bodinier, J., Morten, L., 1999. Petrology and metamorphic evolution of ultramafic rocks and dolerite dykes of the Betic Ophiolitic Association (Mulhacén Complex, SE Spain): evidence of eo-Alpine subduction following an ocean-floor metasomatic process. *Lithos* 49, 23–56.

Qazi, M.J., Liefferink, R.W., Schlegel, S.J., Backus, E.H., Bonn, D., Shahidzadeh, N., 2017. Influence of surfactants on sodium chloride crystallization in confinement. *Langmuir* 33, 4260–4268.

Raleigh, C.B., Paterson, M.S., 1965. Experimental deformation of serpentinite and its tectonic implications. *Journal of Geophysical Research* 70, 3965–3985.

Ranero, C.R., Morgan, J.P., McIntosh, K., Reichert, C., 2003. Bending-related faulting and mantle serpentinization at the Middle America trench. *Nature* 425, 367–373.

Remeysen, K., Swennen, R., 2008. Application of microfocus computed tomography in carbonate reservoir characterization: possibilities and limitations. *Marine and Petroleum Geology* 25, 486–499.

Renard, F., 2012. Microfracturation in rocks: from microtomography images to processes. *The European Physical Journal–Applied Physics*. doi.org/10.1051/epjap/2012120093

Ridley, J., Thompson, A.B., 1986. *The Role of Mineral Kinetics in the Development of Metamorphic Microtextures*. in: Walther J.V., Wood B.J. (eds) Fluid—Rock Interactions during Metamorphism. Advances in Physical Geochemistry, vol 5. Springer, New York, NY, pp. 154–193.

Robyr, M., Vonlanthen, P., Baumgartner, L.P., Grobety, B., 2007. Growth mechanism of snowball garnets from the Lukmanier Pass area (Central Alps, Switzerland): a combined μCT/EPMA/EBSD study. *Terra Nov*a 19, 240–244.

Roselle, G.T., Baumgartner, L.P., Chapman, J.A., 1997. Nucleation-dominated crystallization of forsterite in the Ubehebe Peak contact aureole, California. *Geology* 25, 823–826.

Rudnick, R.L., Gao, S., 2003. *Composition of the Continental Crust*, in: Holland, H.D., Turekian, K.K. (Eds.), Treatise on Geochemistry. Pergamon, Oxford, pp. 1–64.

Ruiz Cruz, M.D., Puga, E., Nieto, J.M., 1999. Silicate and oxide exsolution in pseudo-spinifex olivine from metaultramafic rocks of the Betic Ophiolitic Association: A TEM study. *American Mineralogist* 84, 1915–1924.

Rüpke, L.H., Morgan, J.P., Hort, M., Connolly, J.A., 2004. Serpentine and the subduction zone water cycle. *Earth and Planetary Science Letters* 223, 17–34.

Rutter, E., Llana-Funez, S., Brodie, K., 2009. Dehydration and deformation of intact cylinders of serpentinite. *Journal of Structural Geology* 31, 29–43.

Rutter, E.H., Brodie, K.H., 1988. Experimental "syntectonic" dehydration of serpentinite under conditions of controlled pore water pressure. *Journal of Geophysical Research– Solid Eart*h 93, 4907–4932.

Ryan, J.G., Morris, J., Tera, F., Leeman, W.P., Tsvetkov, A., 1995. Cross-arc geochemical variations in the Kurile arc as a function of slab depth. *Science* 270, 625–627.

Saowadee, N., Agersted, K., Ubhi, H., Bowen, J.R., 2013. Ion beam polishing for three-dimensional electron backscattered diffraction. *Journal of Microscopy* 249, 36–40.

Sawyer, E.W., Cesare, B., Brown, M., 2011. When the continental crust melts. *Elements* 7, 229–233.

Sayab, M., Suuronen, J.-P., Hölttä, P., Aerden, D., Lahtinen, R., Kallonen, A.P., 2015. High-resolution X-ray computed microtomography: A holistic approach to metamorphic fabric analyses. *Geology* 43, 55–58.

Sayab, M., Suuronen, J.-P., Molnár, F., Villanova, J., Kallonen, A., O'Brien, H., Lahtinen, R., Lehtonen, M., 2016. Three-dimensional textural and quantitative analyses of orogenic gold at the nanoscale. *Geology* 44, 739–742.

Scambelluri, M., Bottazzi, P., Trommsdorff, V., Vannucci, R., Hermann, J., Gómez-Pugnaire, M.T., López Sánchez-Vizcaíno, V., 2001. Incompatible element-rich fluids released by antigorite breakdown in deeply subducted mantle. *Earth and Planetary Science Letters* 192, 457–470.

Scambelluri, M., Fiebig, J., Malaspina, N., Muntener, O., Pettke, T., 2004. Serpentinite subduction: Implications for fluid processes and trace-element recycling. *International Geology Review* 46, 595–613.

Scambelluri, M., Pettke, T., Cannaò, E., 2015. Fluid-related inclusions in Alpine high-pressure peridotite reveal trace element recycling during subduction-zone dehydration of serpentinized mantle (Cima di Gagnone, Swiss Alps). *Earth and Planetary Science Letters* 429, 45–59.

Scambelluri, M., Pettke, T., Rampone, E., Godard, M., Reusser, E., 2014. Petrology and trace element budgets of high-pressure peridotites indicate subduction dehydration of serpentinized mantle (Cima di Gagnone, Central Alps, Switzerland). *Journal of Petrology* 55, 459–498.

Scambelluri, M., Philippot, P., 2001. Deep fluids in subduction zones. *Lithos* 55, 213–227.

Scambelluri, M., Strating, E.H., Piccardo, G., Vissers, R., Rampone, E., 1991. Alpine olivine-and titanian clinohumite-bearing assemblages in the Erro-Tobbio peridotite (Voltri Massif, NW Italy). *Journal of Metamorphic Geology* 9, 79–91.

Schmidt, M.W., Poli, S., 1998. Experimentally based water budgets for dehydrating slabs and consequences for arc magma generation. *Earth and Planetary Science Letters* 163, 361–379.

Schmidt, M.W., Poli, S., 2014. *Devolatilization during Subduction*. Holland, Heinrich D, in: Turekian, K.K. (Ed.), Treatise on Geochemistry (Second Edition). Elsevier, Oxford, pp. 669–701.

Schmitt, M., Halisch, M., Müller, C., Fernandes, C.P., 2016. Classification and quantification of pore shapes in sandstone reservoir rocks with 3-D X-ray micro-computed tomography. *Solid Earth* 7, 285–300.

Schroeder, T., John, B., Frost, B.R., 2002. Geologic implications of seawater circulation through peridotite *exposed* at slow-spreading mid-ocean ridges. *Geology* 30, 367–370.

Schubert, G., Turcotte, D.L., Olson, P., 2001. *Mantle Convection in the Earth and Planets*. Cambridge University Press, Cambridge, 2001, 956 pp.

Seno, T., Yamanaka, Y., 1996. Double Seismic Zones, Compressional deep trench-outer rise events, and superplumes. In: *Subduction Top to Bottom*, *AGU Special Publications* 347–355.

Shea, T., Hammer, J.E., 2013. Kinetics of cooling- and decompression-induced crystallization in hydrous mafic-intermediate magmas. *Journal of Volcanology and Geothermal Research* 260, 127–145.

Shore, M., Fowler, A.D., 1999. The origin of spinifex texture in komatiites. *Nature* 397, 691–694.

Sibson, R.H., 1996. Structural permeability of fluid-driven fault-fracture meshes. *Journal of Structural Geology* 18, 1031–1042.

Sibson, R.H., 2017. The edge of failure: critical stress overpressure states in different tectonic regimes. *Geological Society, London, Special Publications* 458, 131–141.

Skarbek, R.M., Rempel, A.W., 2016. Dehydration-induced porosity waves and episodic tremor and slip. *Geochemistry, Geophysics, Geosystems* 17, 442–469.

Soustelle, V., Tommasi, A., Demouchy, S., Ionov, D.A., 2010. Deformation and fluid-rock interaction in the supra-subduction mantle: microstructures and water contents in peridotite xenoliths from the Avacha Volcano, Kamchatka. *Journal of Petrology* 51, 363–394.

Spandler, C., Pettke, T., Rubatto, D., 2011. Internal and external fluid sources for eclogite-facies veins in the Monviso meta-ophiolite, Western Alps: implications for fluid flow in subduction zones. *Journal of Petrology* 52, 1207–1236.

Spence, W., 1987. Slab pull and the seismotectonics of subducting lithosphere. *Reviews of Geophysics* 25, 55–69.

Spowart, J.E., 2006. Automated serial sectioning for 3-D analysis of microstructures. *Scripta Materialia* 55, 5–10.

Stern, R.J., 2002. Subduction zones. *Reviews of Geophysics* 40, 4, 1012, doi:10.1029/2001RG000108

Stern, R.J., 2004. Subduction initiation: spontaneous and induced. *Earth and Planetary Science Letters* 226, 275–292.

Stimpfl, M., Walker, A.M., Drake, M.J., de Leeuw, N.H., Deymier, P., 2006. An ångström-sized window on the origin of water in the inner solar system: Atomistic simulation of adsorption of water on olivine. *Journal of Crystal Growth* 294, 83–95.

Sun, S.-S., McDonough, W.F., 1989. Chemical and isotopic systematics of oceanic basalts: implications for mantle composition and processes. *Geological Society, London, Special Publications* 42, 313–345.

Syracuse, E.M., van Keken, P.E., Abers, G.A., 2010. The global range of subduction zone thermal models. *Physics of the Earth and Planetary Interiors* 183, 73–90.

Tenthorey, E., Hermann, J.r., 2004. Composition of fluids during serpentinite breakdown in subduction zones: Evidence for limited boron mobility. *Geology* 32, 865–868.

Tian, M., Ague, J.J., Chu, X., Baxter, E.F., Dragovic, N., Chamberlain, C.P., Rumble, D., 2018. The potential for metamorphic thermal pulses to develop during compaction-driven fluid flow. *Geochemistry, Geophysics, Geosystems* 19, 232–256.

Torne, M., Fernandez, M., Comas, M., Soto, J., 2000. Lithospheric structure beneath the Alboran Basin: results from 3D gravity modeling and tectonic relevance. Journal of *Geophysical Research–Solid Earth* 105, 3209–3228.

Townsend, E.R., van Enckevort, W.J., Meijer, J.A., Vlieg, E., 2015. Polymer versus monomer action on the growth and habit modification of sodium chloride crystals. *Crystal Growth & Design* 15, 5375–5381.

Trommsdorff, V., López Sánchez-Vizcaíno, V., Gómez-Pugnaire, M.T., Müntener, O., 1998. High pressure breakdown of antigorite to spinifex-textured olivine and orthopyroxene, SE Spain. *Contributions to Mineralogy and Petrology* 132, 139–148.

Tubía, J., Cuevas, J., Navarro-Vilá, F., Alvarez, F., Aldaya, F., 1992. Tectonic evolution of the Alpujárride complex (Betic cordillera, southern Spain). *Journal of Structural Geology* 14, 193–203.

Turcotte, D., Schubert, G., 2014. *Geodynamics*. Cambridge University Press, Cambridge, 848 pp.

Turcotte, D.L., Schubert, G., 1982. *Geodynamics: Applications of Continuum Physics to Geological Problems*, John Wiley, New York, 450 pp.

Uchic, M., Groeber, M., Shah, M., Callahan, P., Shiveley, A., Scott, M., Chapman, M., Spowart, J., 2012. An automated multi-modal serial sectioning system for characterization of grain-scale microstructures in engineering materials, *Proceedings of the 1st International Conference on 3D Materials Science*. Springer, pp. 195–202.

Uehara, S., 1998. TEM and XRD study of antigorite superstructures. *The Canadian Mineralogist* 36, 1595–1605.

Uesugi, M., Uesugi, K., Oka, M., 2010. Non-destructive observation of meteorite chips using quantitative analysis of optimized X-ray micro-computed tomography. *Earth and Planetary Science Letters* 299, 359–367.

Ulmer, P., Trommsdorff, V., 1995. Serpentine stability to mantle depths and subduction-related magmatism. *Science* 168, 858-861.

Ulmer, P., Trommsdorff, V., 1999. *Phase relations of hydrous mantle subducting to 300 km*, in: Mantle Petrology: Field observations and High Pressure Experimentation, 259–281.

Uyeda, S., Kanamori, H., 1979. Back-arc opening and the mode of subduction. Journal of *Geophysical Research–Solid Earth* 84, 1049–1061.

Van de Moortèle, B., Bezacier, L., Trullenque, G., Reynard, B., 2010. Electron back-scattering diffraction (EBSD) measurements of antigorite lattice-preferred orientations (LPO). *Journal of Microscopy* 239, 245–248.

Van Grieken, R., Markowicz, A., 2001. *Handbook of X-ray Spectrometry*. CRC press. 1016 pp.

van Keken, P.E., Hacker, B.R., Syracuse, E.M., Abers, G.A., 2011. Subduction factory: 4. Depth-dependent flux of H_2O from subducting slabs worldwide. *Journal of Geophysical Research–Solid Earth* 116, B01401, doi:10.1029/2010JB007922

van Keken, P.E., Wada, I., Abers, G.A., Hacker, B.R., Wang, K., 2018. Mafic high-pressure rocks are preferentially exhumed from warm subduction settings. *Geochemistry, Geophysics, Geosystems* 19, 2934–2961.

Van Marcke, P., Verleye, B., Carmeliet, J., Roose, D., Swennen, R., 2010. An improved pore network model for the computation of the saturated permeability of porous rock. *Transport in Porous Media* 85, 451–476.

Vaughan, P.J., Green, H.W., Coe, R.S., 1984. Anisotropic growth in the olivine-spinel transformation of Mg_2GeO_4 under nonhydrostatic stress. *Tectonophysics* 108, 299–322.

Voltolini, M., Zandomeneghi, D., Mancini, L., Polacci, M., 2011. Texture analysis of volcanic rock samples: quantitative study of crystals and vesicles shape preferred orientation from X-ray microtomography data. *Journal of Volcanology and Geothermal Research* 202, 83–95.

Vonlanthen, P., Rausch, J., Ketcham, R.A., Putlitz, B., Baumgartner, L.P., Grobéty, B., 2015. High-resolution 3D analyses of the shape and internal constituents of small volcanic ash particles: the contribution of SEM micro-computed tomography (SEM micro-CT). *Journal of Volcanology and Geothermal Research* 293, 1–12.

Walowski, K.J., Wallace, P.J., Hauri, E.H., Wada, I., Clynne, M.A., 2015. Slab melting beneath the Cascade Arc driven by dehydration of altered oceanic peridotite. *Nature Geoscience* 8, 404–408.

Water and Steam, 2008. http://iapws.org/relguide/visc.pdf.

Weber, J.N., Greer, R.T., 1965. Dehydration of serpentinite – Heat of reaction and kinetics at PH_2O = 1 atm. *American Mineralogist* 50, 450–464.

Wedepohl, K. H., 1995. The composition of the continental crust. *Geochimica et Cosmochimica Acta* 59, 1217–1232.

Wei, S.S., Wiens, D.A., van Keken, P.E., Cai, C., 2017. Slab temperature controls on the Tonga double seismic zone and slab mantle dehydration. *Science Advances* 3, 1, 10.1126/sciadv.1601755

Weinberg, R.F., Hasalová, P., 2015. Water-fluxed melting of the continental crust: A review. *Lithos* 212, 158–188.

Welsch, B., Faure, F., Famin, V., Baronnet, A., Bachelery, P., 2013. Dendritic crystallization: A single process for all the textures of olivine in basalts? *Journal of Petrology* 54, 539–574.

Wen, D.-P., Wang, Y.-F., Zhang, J.-F., Jin, Z.-M., 2018. Anisotropic growth of olivine during crystallization in basalts from Hawaii: Implications for olivine fabric development. *American Mineralogist* 103, 735–741.

Wenk, H.-R., Kanitpanyacharoen, W., Voltolini, M., 2010. Preferred orientation of phyllosilicates: Comparison of fault gouge, shale and schist. *Journal of Structural Geology* 32, 478–489.

West, G., Thomson, R., 2009. Combined EBSD/EDS tomography in a dual-beam FIB/FEG–SEM. *Journal of Microscopy* 233, 442–450.

Whitney, D.L., Evans, B.W., 2010. Abbreviations for names of rock-forming minerals. *American Mineralogist* 95, 185–187.

Whitney, J.A., 1988. The origin of granite: The role and source of water in the evolution of granitic magmas. *Geological Society of America Bulletin* 100, 1886–1897.

Wicks, F., O'Hanley, D., 1988. Serpentine Minerals: structures and petrology. in: Hydrous Phyllosilicates (exclusive of Micas)(SW Bailey, editor). *Reviews in Mineralogy* 19, 91–167.

Wiesmaier, S., Morgavi, D., Renggli, C., Perugini, D., De Campos, C., Hess, K., Ertel-Ingrisch, W., Lavallée, Y., Dingwell, D., 2015. Magma mixing enhanced by bubble segregation. *Solid Earth*, 3, 1007–1023.

Wilson, M., 1993. Plate-moving mechanisms: constraints and controversies. *Journal of the Geological Society* 150, 923–926.

Worden, R., Droop, G., Champness, P., 1991. The reaction antigorite → olivine + talc + H_2O in the Bergell aureole, N. Italy. *Mineralogical Magazine* 55, 367–377.

Wunder, B., Schreyer, W., 1997. Antigorite: High-pressure stability in the system MgO-SiO_2-H_2O (MSH). *Lithos* 41, 213–227.

Wunder, B., Wirth, R., Gottschalk, M., 2001. Antigorite pressure and temperature dependence of polysomatism and water content. *European Journal of Mineralogy* 13, 485–496.

Yardley, B.W., 1989. *An introduction to metamorphic petrology.* Harlow, Essex, England: Longman Scientific & Technical, 248 pp.

Zack, T., John, T., 2007. An evaluation of reactive fluid flow and trace element mobility in subducting slabs. *Chemical Geology* 239, 199–216.

Zaefferer, S., Wright, S., Raabe, D., 2008. Three-dimensional orientation microscopy in a focused ion beam–scanning electron microscope: A new dimension of microstructure characterization. *Metallurgical and Materials Transactions A* 39, 374–389.

Zucali, M., Voltolini, M., Ouladdiaf, B., Mancini, L., Chateigner, D., 2014. The 3D quantitative lattice and shape preferred orientation of a mylonitised metagranite from Monte Rosa (Western Alps): Combining neutron diffraction texture analysis and synchrotron X-ray microtomography. *Journal of Structural Geology* 63, 91–105.

Zussman, J., 1954. Investigation of the crystal structure of antigorite. *Mineralogical Magazine* 30, 498–512.




Subduction zones are the main sites of water recycling on Earth. At intermediate depth of subducting slabs, metamorphic devolatilization reactions are the principal source of fluids. Despite their fundamental role in subduction dynamics, the time, flux and nature of deserpentinization fluid release are poorly constrained. A key metamorphic devolatilization reaction in these settings is the discontinuous dehydration of antigorite serpentinite because it liberates the largest amount of fluid at the intermediate depths of subducting slabs.

The main aim of the present Ph.D. thesis is to constrain the dynamics and mechanisms of fluid release during high-pressure antigorite serpentinite dehydration from observations in the Almirez ultramafic massif (Betic Cordillera, Nevado-Filábride Complex, SE Spain). This ultramafic massif —exhumed from a paleo-subduction zone during the Alpine orogeny—preserves a unique record of the dehydration of antigorite serpentinite to chlorite harzburgite occurring at the subarc depths of subduction zones. Combining field and petrological observations with innovative textural and microstructural characterization via μ-CT and EBSD-SEM and geochemical data, the present Ph.D. thesis sheds new light on (i) the mechanism and episodic nature of fluid release during high-pressure dehydration of antigorite serpentinite, (ii) the dynamics of serpentinite dehydration and its relation to the orientation of stresses and the kinematics of subducting slabs, and (iii) the physicochemical factors that govern the texture and morphology of olivine during metamorphic crystallization of prograde chlorite harzburgite after antigorite serpentinite.

IACT
INSTITUTO ANDALUZ DE CIENCIAS DE LA TIERRA
Research Group on
Petrology, Geochemistry and Geochronology
Thesis Memoir n°8

MARIE CURIE ACTIONS
CSIC
Consejo Superior de Investigaciones Científicas
ugr Universidad de Granada